ARMY RESEARCH LABORATORY

# An Experiment, Analysis, and Model of Ballistic Shock

by J. Terrence Klopcic, Walton T. Robinson,
Donald W. Petty, and Michael R. Sivack

ARL-MR-368 November 1997

The findings in this report are not to be construed as an official Department of the Army position unless so designated by other authorized documents.

Citation of manufacturer's or trade names does not constitute an official endorsement or approval of the use thereof.

Destroy this report when it is no longer needed. Do not return it to the originator.

**Army Research Laboratory**
Aberdeen Proving Ground, MD 21005-5068

**ARL-MR-368** **November 1997**

# An Experiment, Analysis, and Model of Ballistic Shock

J. Terrence Klopcic, Walton T. Robinson, Donald W. Petty, Michael R. Sivack
Survivability/Lethality Analysis Directorate, ARL

# Abstract

This study deals with the propagation of the leading, high-frequency edge of the shock wave emanating from an impact point on an armored vehicle, specifically, in an experiment on an M113 armored personnel carrier subjected to explosive charges.

The amplitude of the transverse wave can be well fit by a semiempirical equation, which accounts for both longitudinal and transverse waves, exponential decrease with distance, mixing of waves at edges, and amplification at points near edges. Comparison of wave speeds with published data confirms the roles of longitudinal and transverse disturbances.

# Acknowledgments

The authors wish to acknowledge the superb guidance and support given to us by Mr. Joseph Collins of the U.S. Army Research Laboratory (ARL). Joe provided not only the software, but also the dedicated training on that software, which allowed us to conduct the analysis presented here.

The willingness and expertise of Dr. Barry Bodt of ARL to supply guidance on statistical matters, on this project as well as on many others over the years, are gratefully acknowledged.

This page intentionally left blank

# Contents

This page intentionally left blank

# List of Figures

# List of Tables

This page intentionally left blank

# I. Introduction

When a significant amount of energy is deposited onto a small area (or into a small volume) of a structure, a physical phenomenon known as ballistic shock may occur. In this phenomenon, a portion of the deposited energy is transmitted away from the immediate region of deposition through the violent vibration of the structure. In the case of armored vehicles and other structures made of resilient materials, this energy may be transmitted (dispersed) throughout the structure including areas far removed from and not exposed to the incident agent. Thus, if transmitted to vibration-sensitive components, a system may undergo failure via damage that occurs far removed from the point of impact.

Note that this phenomenon can occur whether or not the incident agent (*e.g.*, a kinetic energy penetrator or shaped charge jet) perforates the structure.

For the balance of this discussion, we shall assume that the target is an armored vehicle which is struck on its integral, metallic hull.

Target response to ballistic shock is conveniently divided, by vibrational modes (and associated frequencies), into two markedly different physical domains. The lower frequency domain – up to approximately 1 kHz – is dominated by large-scale flexural vibrations, which include by far the majority of the energy imparted by the incident agent. This is distinguished from the higher domain (above 1 kHz) by relatively larger deflections but relatively lower accelerations. As vibrational frequencies increase above 1 kHz, the dominant mechanism for the propagation of vibrational energy changes from flexural vibration of the system as a whole to stress waves in the material itself. It is not surprising, therefore, that the two domains manifest significantly different damage mechanisms. Energy in the lower frequency domain tends to produce structural damage, such as the failure of plates and edge joints (welds). In the higher frequency domain, the energy tends to produce damage of light, intricate, frequency-sensitive components such as electronics and optics.

This report deals exclusively with the measurement and analysis of ballistic shock in the higher frequency domain (above 1 kHz).

A salient characteristic was observed by Petty[1] in experiments involving high-frequency ballistic shock. In measurements taken with accelerometers (see below), it was observed that the initial, transient, high-frequency pulse of

[1]Petty, D. Private communication. U.S. Army Research Laboratory, Aberdeen Proving Ground, MD, 1997

energy that first reaches any given point inevitably included the highest of the high-frequency amplitudes. That is, in actual ballistic shock events, the leading (transient) pulse is always the strongest – and hence, presumably, the most damaging. Thus, it appears justified to confine the analysis of the higher frequency domain to this "leading edge". This simplification is important for two reasons. First, measurements of vibrations in the high-frequency domain are eventually overwhelmed by the large amplitude, low-frequency motions of the target. However, these low-frequency motions become apparent only after several milliseconds, by which time the high-frequency leading edge has passed and been recorded.

In addition, the ability to concentrate on the passage of the leading edge results in a significantly simplified analysis. Rather than tracking all vibrations throughout a vehicle until all energy has been dissipated, it is reasonable to model the spread of high-frequency energy as a single wavefront that propagates outward from the source. (First-order corrections at boundaries are discussed in Section III.) This allows formulation of a linear model in which the propagation of energy from point to point is characterized by "transfer functions". Such a model is amenable to incorporation into the production-grade computer codes that are used for routine vulnerability analyses and the generation of large amounts of vulnerability data.

This report presents data, data analysis, and attempts at deriving a semi-empirical model of the high-frequency ballistic shock phenomenon. In this limited study, only one set of experiments on one relatively simple vehicle (M113 armored personnel carrier) is presented. Other data taken by Petty and others remain to be fully analyzed. It is also recognized that newer vehicles, with composite and/or double hulls, will introduce further complications into this treatment. Application of the findings of this study to such cases is discussed in Section IV.

# II. Experimental Procedure and Results

In the experiment analyzed herein, an M113 armored personnel carrier (a vehicle with monolithic aluminum exterior walls and top) was instrumented as shown in Figures 1 and 2. Gauges consisted of single directional (perpendicular to mounting surface) accelerometers, made and calibrated by PCB Piezotronics, Inc. Advertised operating range was 0.1–20 kHz, with a rise time of 5 $\mu$s. All gauges were screwed into holes that had been drilled and tapped directly into the aluminum hull of the test vehicle. Outputs were digitally recorded.

In these experiments, the input shock was produced by detonating a bare charge of pentolite that was fixed to a 30.5-cm $\times$ 30.5-cm $\times$ 2.54-cm (12-in $\times$ 12-in $\times$ 1-in) aluminum plate (the "charge plate") mounted on the vehicle where shown in Figure 2. In all cases, the charge weight was 56.7 g (1/8th lb). Gauge distances from charge-center and number of intervening edges vs. gauge numbers are given in Table 1.

Table 1: Gauge Distances and Intervening Edges.

| Gauge No. | Distance (in.) from Charge | Intervening Edges |
|---|---|---|
| 1 | 48 | 0 |
| 2 | 48 | 0 |
| 3 | 25 | 0 |
| 4 | 27 | 1 |
| 5 | 50.5 | 1 |
| 6 | 75.1 | 1 |
| 7 | 99.6 | 1 |
| 8 | 123.1 | 1 |
| 9 | 125.1 | 2 |
| 10 | 150.1 | 2 |
| 11 | 161 | 2 |
| 12 | 161 | 2 |

The experimental series consisted of eight data shots herein referred to by their range sequence numbers, as given in Table 2.

Table 2: Shot Numbers of Data Included in This Analysis.

| 695 | 698 | 708 | 709 | 712 | 713 | 714 | 719 |
|---|---|---|---|---|---|---|---|

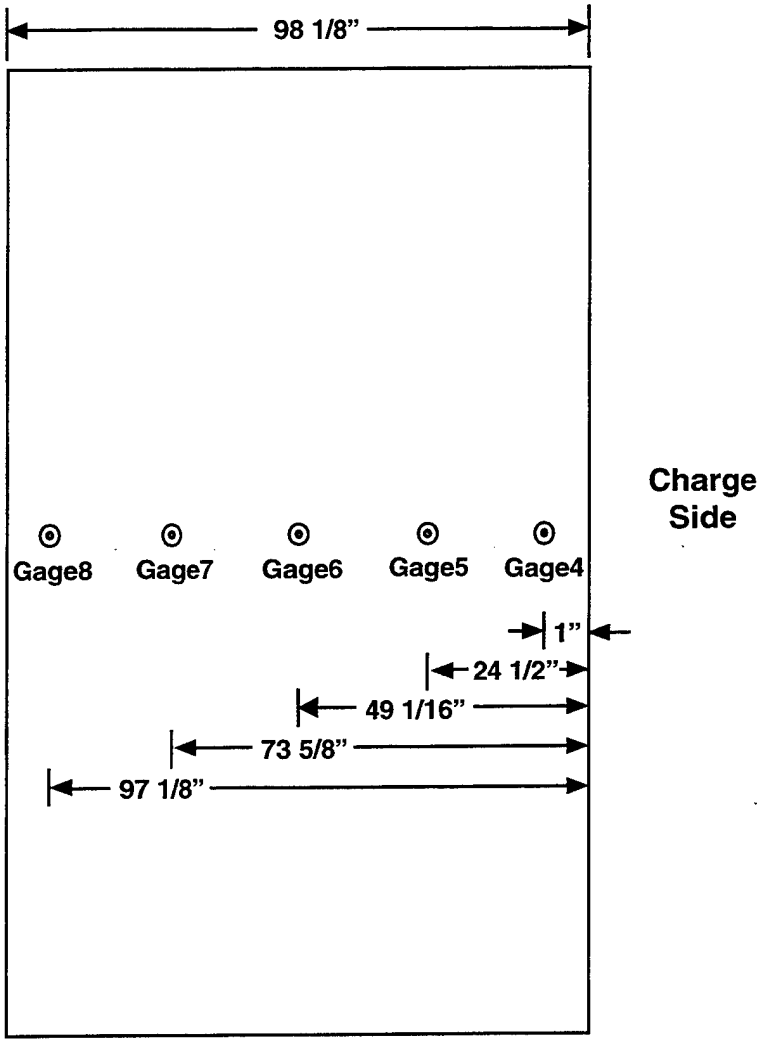


Figure 1: Gauge Positions on M113, Top View.

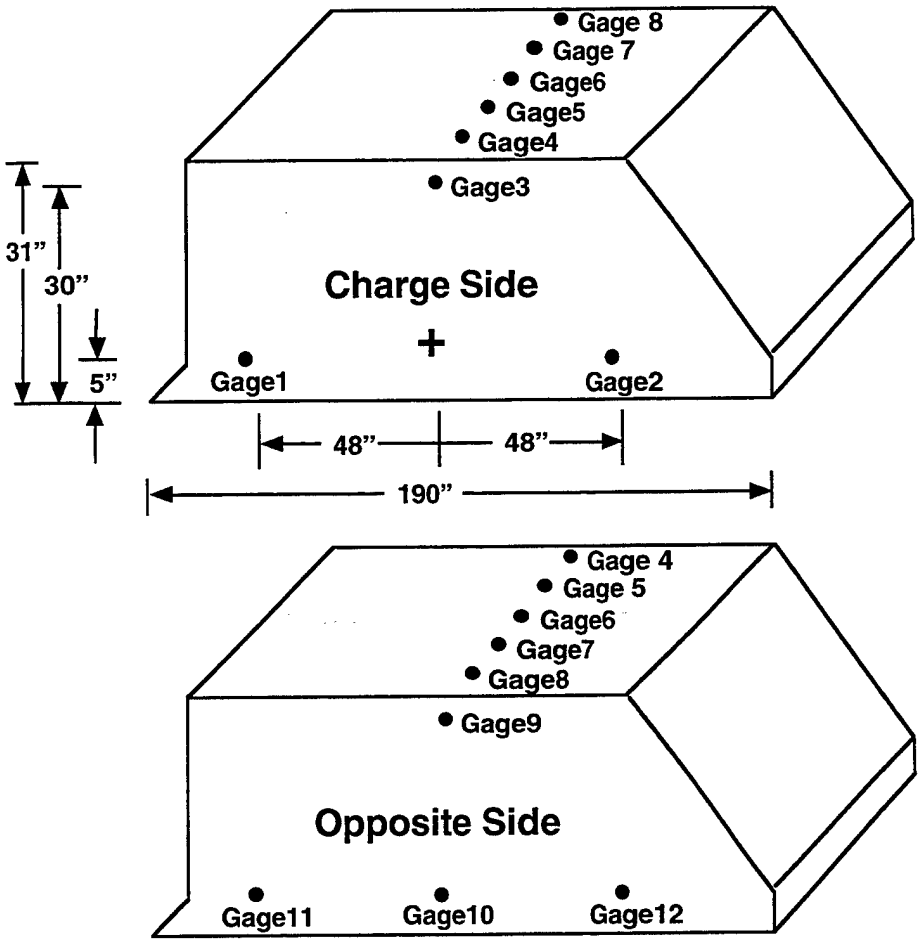


Figure 2: Gauge Positions on M113, Side Views.

The output of each gauge, scaled by its calibration, is presented in Appendix A. A typical plot, that of Gauge #6 in shot #709, is presented in Figure 3. The following characteristics are noted:

a. First, two ultrahigh frequency "spikes" riding on the initial quiescent signal.

b. After another quiescent period, a series of low-amplitude "ripples".

c. Then, a mass of high amplitude oscillations – in this case, at about 3 kHz.

d. Degradation into a more noisy appearing, lower amplitude signal.

e. Although not apparent in Figure 3, there is also the beginning of a longer time period baseline shift incorporated in the noisy tail of the plot.

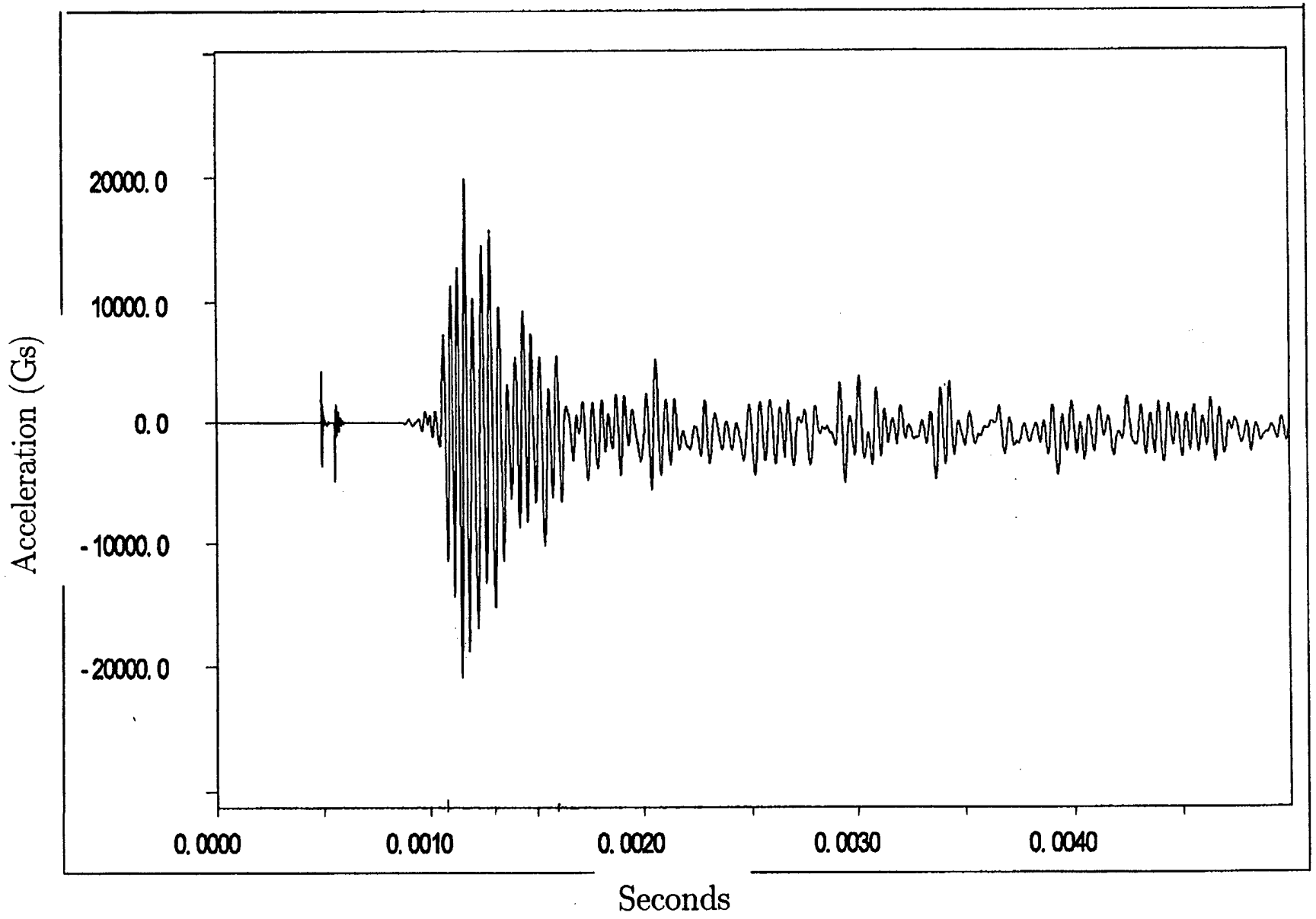


Figure 3: Calibrated Output of Gauge #6, Shot #709.

# III. Analysis

## A. Extraction of Metrics.

### 1. Pulse Shape Analysis.

Analysis of the calibrated data traces resulted in the following conclusions. (Italicized terms are defined for use in subsequent discussions.)

First, the leading ultrahigh frequency spikes are caused by the *trigger pulse*, the electrical signal that initiated the detonation of the shock-producing charge. Since this pulse is simultaneously recorded on the output of every detector, this ultrahigh frequency spike can serve as a zero-time marker on every detector record.

Following detonation, there is a quiescent period at the detector sites during which the ballistic shock is forming and propagating outward from the shock point. The subsequent low-amplitude ripples indicate the arrival of a longitudinal vibration spreading out from the shock point through the vehicle hull. The speed of a longitudinal vibration is higher than that of a transverse one, explaining its early arrival. However, since the detectors were designed to respond to transverse vibrations, the amplitude of detector response to the longitudinal vibration is low. We refer to this set of early, low-amplitude ripples as the *precursor pulse.*

This is followed by the arrival of and detector response to the transverse vibration, herein referred to as the *main pulse.* As reported by Petty, the response is most severe within the first few milliseconds: within ten ms, the amplitude has decreased significantly, with only isolated subsequent cycles reaching 20% of the highest peaks. This lower amplitude "noise" continues throughout the remainder of the measurement period.

Longer term data traces exhibit marked low-frequency rises and falls of the baseline on which this noise rides; these low-frequency oscillations are the response of the vehicle as a whole to the low-frequency portion of the shock.

Using this analysis of the characteristics of each detector output, it was possible to define and extract metrics that characterize the data of interest for this study.

## 2. Arrival Time Analysis.

First, in order to verify the above analysis, it was illustrative to extract from each data record the times between the trigger pulse, the arrival of the first low-amplitude oscillation, and the arrival of the first high amplitude oscillation. To do this, a computer program was written that distinguished signals above appropriate thresholds, sensed frequency by the number of consecutive readings above threshold, and counted data points in the intervals. From this two sets of timing data were extracted: trigger-pulse-to-arrival-time for the precursor pulse (*T1 data*) and trigger-pulse-to-arrival-time for the main pulse (*T2 data*).

Analysis of these data follows. In this analysis and all that follow, functions were fit to the data using the S-PLUS[†] statistical software analysis package.

First, from a plot of the T1 data for the gauges on top of the M113 (*top gauges*) vs. distance from the charge point (Figure 4), the precursor pulse speed can be calculated. Fitting the T1 data with a straight line yields a slope of 0.20 in/$\mu$s which equates to a speed of 5080 m/s, somewhat less than the published speed[2] of a longitudinal wave in bulk rolled aluminum (6420 m/s), but slightly greater than the speed of a longitudinal wave in an aluminum rod (5000 m/s) which, as in the present case, exhibits boundary effects upon wave speed. We conclude that the measured speed is consistent with the existence of a longitudinal wave.

Similarly, a plot of the T2 data for the top gauges (Figure 5) yields a slope of 0.12 in/$\mu$s which equates to a speed of 3055 m/s, in excellent agreement with the published value of a transverse wave in rolled aluminum (3040 m/s).

We conclude that the observed data traces are caused by the arrival of a longitudinal disturbance followed by a transverse one.

In the analysis of the T2 data, a phenomenon was noted which gave important guidance to the amplitude analyses presented in the next section of this report. A plot of T2 data that includes both the front surface and the top surface reveals an interesting paradox. As seen in Figure 6, the arrival of the transverse pulse at points on the top surface actually occurs before the arrival of the pulse at equal distances on the front surface – even though the pulse arriving at the

[†]S-PLUS is a software product of Statistical Sciences, Inc., 1700 Westlake Ave. N.,Suite 500, Seattle, WA 98109.

[2] *Handbook of Chemistry and Physics, Forty-Fourth Edition*, Chemical Rubber Publishing Company, Cleveland, OH, 1963.

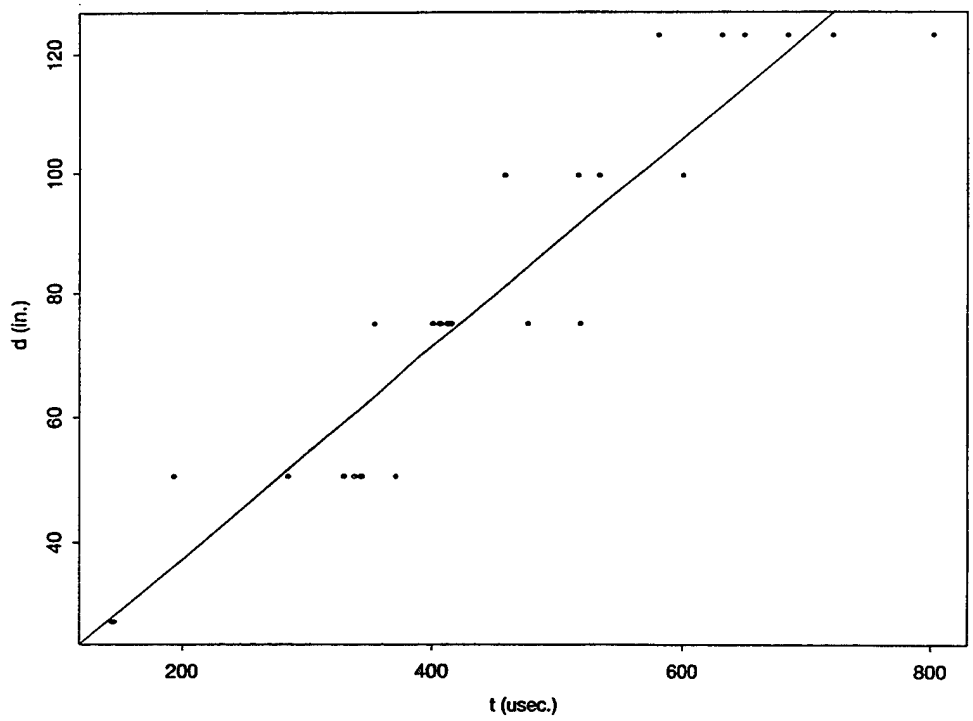


Figure 4: Arrival Time of Precursor Pulse – Top Gauges.

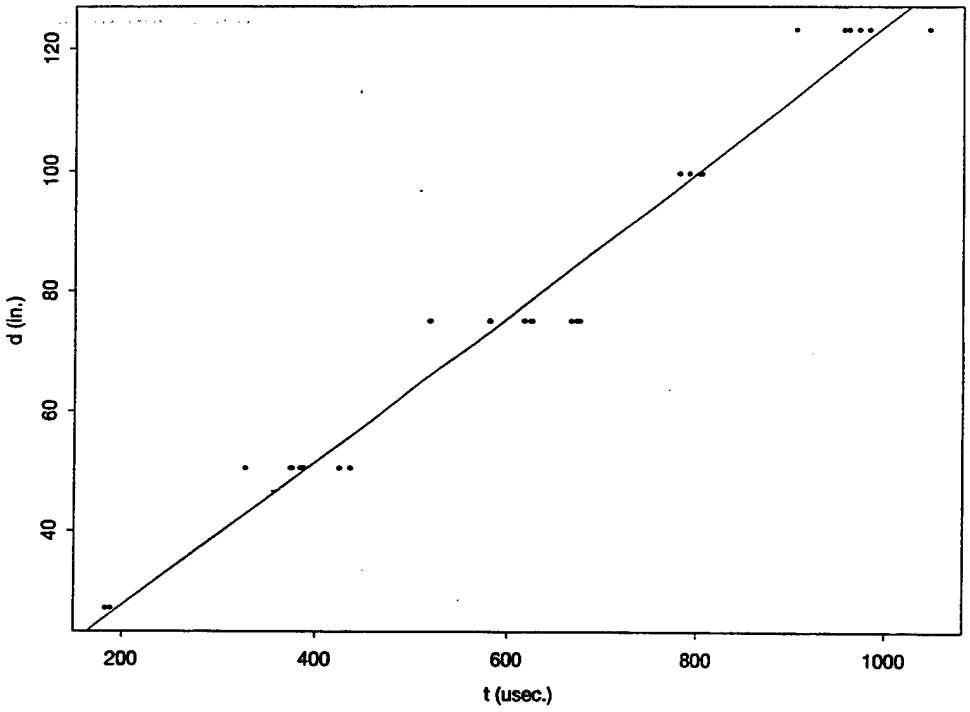


Figure 5: Arrival Time of Main Pulse – Top Gauges.

top points must negotiate the intervening edge. From the intercepts of the two lines plotted in Figure 6, the time difference is found to be 67 $\mu$s.

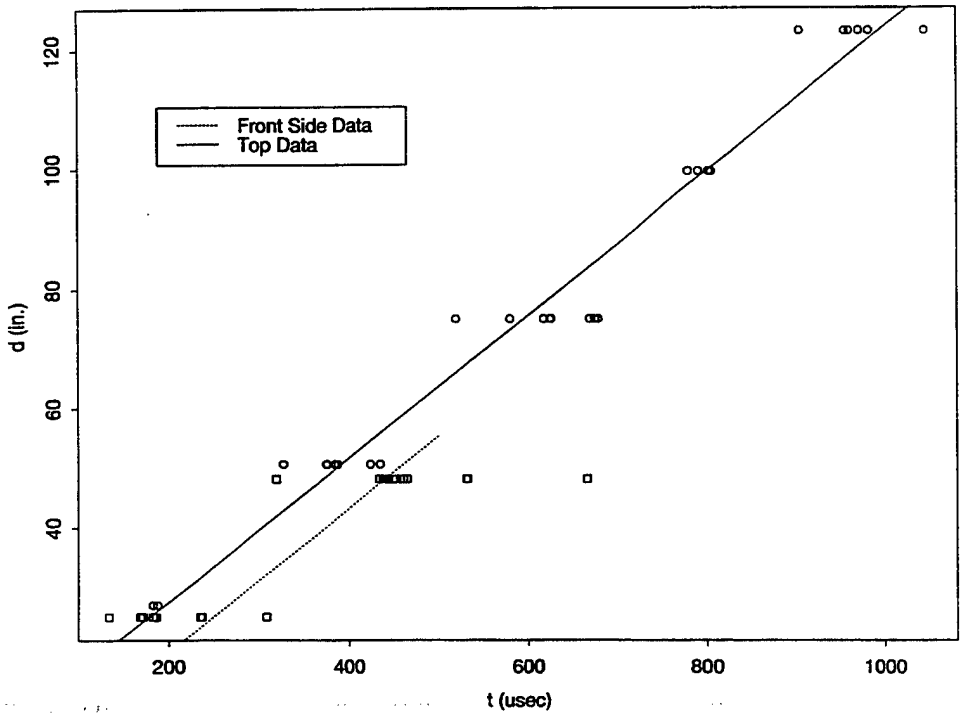


Figure 6: Arrival Time of Main Pulse – Front and Top Gauges.

Analysis led to the following explanation. Detonation of the charge results in the creation of both longitudinal and transverse disturbances on the front side which propagate outward from the edge of the charge plate, with the longitudinal disturbance traveling faster as indicated above. Upon reaching the edge, the longitudinal disturbance generates both a longitudinal and a transverse disturbance on the top side (as well as reflected disturbances on the front). It is this transverse disturbance on the top surface, created by the longitudinal disturbance on the front, that first reaches the top surface gauges.

For this explanation to hold true, the difference between the time of arrival of the longitudinal disturbance at the top edge and the time for a transverse disturbance to travel the same distance – approximately 50.8 cm (20 in) – must account for the time difference noted in Figure 6. Using the speeds measured from Figures 4 and 5, we find

$$\text{Time Difference} = \frac{20}{0.12} - \frac{20}{0.20} = 67\ \mu\text{s}$$

in remarkable agreement with the 67 $\mu$s measured in Figure 6.

We conclude that the initial portion (approximately 70 $\mu$s) of the transverse vibrations measured on the top surface is generated at the intervening edge by the arrival of the longitudinal disturbance on the front side. As shown below, this conclusion dictates the form of the functions used to fit the amplitude data in Section 4.

## 3. Amplitude Metrics.

Inspection of the calibrated data traces (Appendix A) reveals a great deal of chaos in the high-frequency vibration record, as is to be expected in a shock environment. In order to characterize the amplitude of each trace in a consistent manner, the following technique was used.

First, visual analysis of the data traces was made. This analysis identified and removed those traces in which obvious experimental difficulties were experienced. For example, the data trace for Gauge #4 in Shot #713 (Figure 7) is clearly oversaturated, as – somewhat more subtly – is the same gauge in Shot #708 (Figure 8). (The behavior of Gauge #4 in general is discussed below.) The data so removed are listed in Table 3.

A utility code was written to conduct the data extraction. Operating on the complete files of calibrated data, this code removed the data listed in Table 3, extracted the arrival times presented in the preceding section, and also performed amplitude characterization. This characterization consisted of identifying peaks in each data trace by comparing the values of adjacent data points. For each trace, peak amplitudes were then tabulated. In order to "smooth out" the chaos evident in the traces, the N highest peaks were then averaged. Clearly, larger values of N tend to give smoother data, but also dilute the differences between gauge outputs. After trying several values of N, it was decided to characterize the output of each gauge for each shot by the average of the four highest peaks in the corresponding data trace. We refer to these averages as the "top4" metric. Thus, the magnitude of the shock measured by each gauge for each shot is represented by a single top4 number.

It was recognized that, in order to include data from different shots into a single analysis, it would be necessary to normalize all data records to remove shot-to-shot variations. Thus, as a final step in the extraction of top4 data, all top4 numbers from each shot were normalized. Two normalization schemes were investigated. In the first scheme, each top4 value for each gauge for a given shot was normalized to the average of the top4 numbers of all gauges

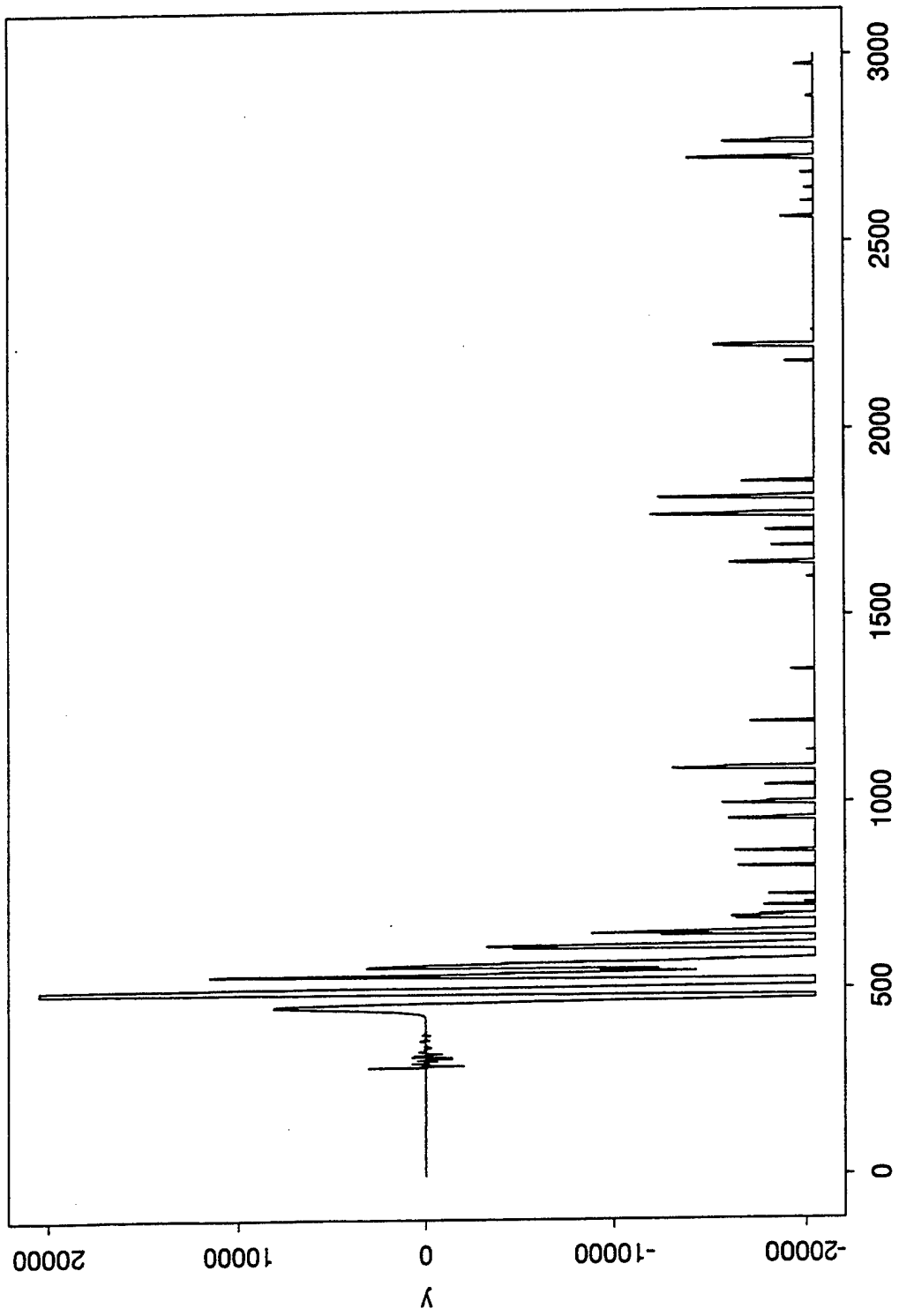


Figure 7: Calibrated Output of Gauge #4, Shot #713.

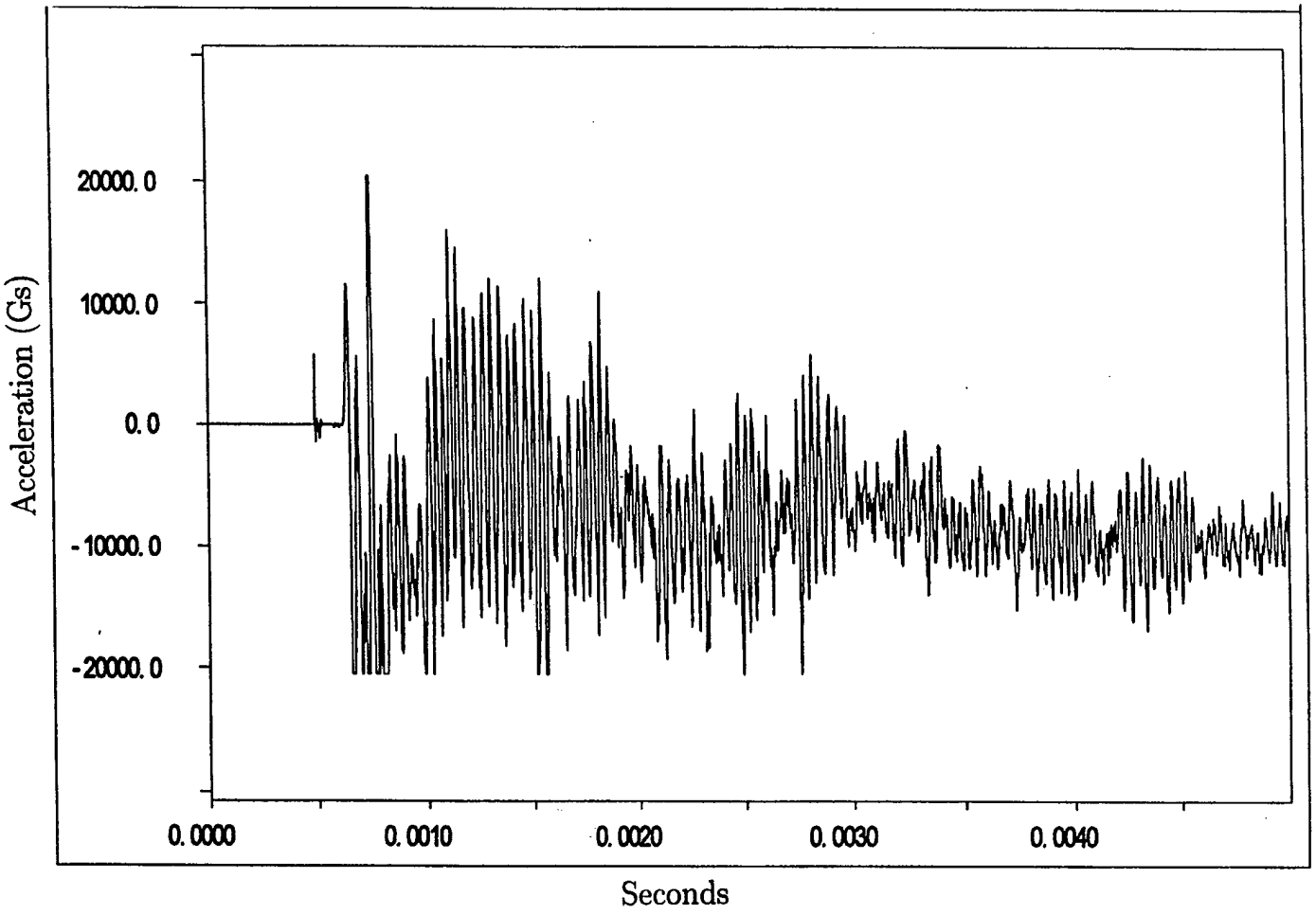


Figure 8: Calibrated Output of Gauge #4, Shot #708.

Table 3: Data Removed from Analysis.

| Shot # | Gauge # |
|---|---|
| 695 | 1 |
| 698 | 1 |
| 698 | 7 |
| 708 | 4 |
| 708 | 7 |
| 708 | 9 |
| 709 | 4 |
| 709 | 7 |
| 709 | 8 |
| 712 | 4 |
| 712 | 8 |
| 713 | 4 |
| 713 | 11 |
| 714 | 4 |
| 714 | 11 |
| 719 | 2 |
| 719 | 7 |
| 719 | 8 |
| 719 | 11 |

for that shot. The second scheme used the output of only the distant front-face gauges (gauges #1 and #2) as the normalization constant for each shot. Since the second scheme was found to introduce less scatter into the data than the first, the analyses reported below were done using data normalized by use of the second scheme. Note that normalization loses any information on the absolute acceleration of any point, which was not of interest in this study. Preserved is the relative acceleration of each point with respect to that of the other points for that shot. This normalization allowed data from the eight shots listed in Table 2 to be combined into a single analysis even though experimental vagaries resulted in different initial shock levels for the various shots.

A utility code then gathered the normalized numbers, associated them with the corresponding distances from the shock point and numbers of intervening edges, and formed matrices for the analysis presented in the next section. A plot of the combined normalized data, by distance from the shock point, is presented in Figure 9. Similar plots, containing the normalized data from each shot individually, are presented in Appendix B. In these plots, squares represent data from front face gauges, circles from top face gauges, and triangles from rear face gauges.

Recall that there were two gauges on the front face at 48 in from the charge, the average of which was used to normalize all data from a particular shot. This averaging accounts for the spread in the points at 48 in from the charge. Had there only been one gauge at 48 in, all points at that abscissa would fall exactly at a normalized amplitude of 1, of course.

## 4. Semi-empirical Equation Development.

The approach taken to fitting the M113 ballistic shock data in Figure 9 was to hypothesize various physical phenomena which could be important in the propagation of the leading edge of the high-frequency shock wave to the various gauges over the vehicle. The expected behavior of each of these phenomena was parameterized and included in a comprehensive function which was then fit to the data. This resulted in the systematic set of progressively more complex semi-empirical fits. Goodness of fit was assessed via the residual sum of squares calculated by the S-PLUS statistical software analysis package.

In this section, we present the final equation used to fit the data in Figure 9.

Modeling of the following physical phenomena effected the best fit:

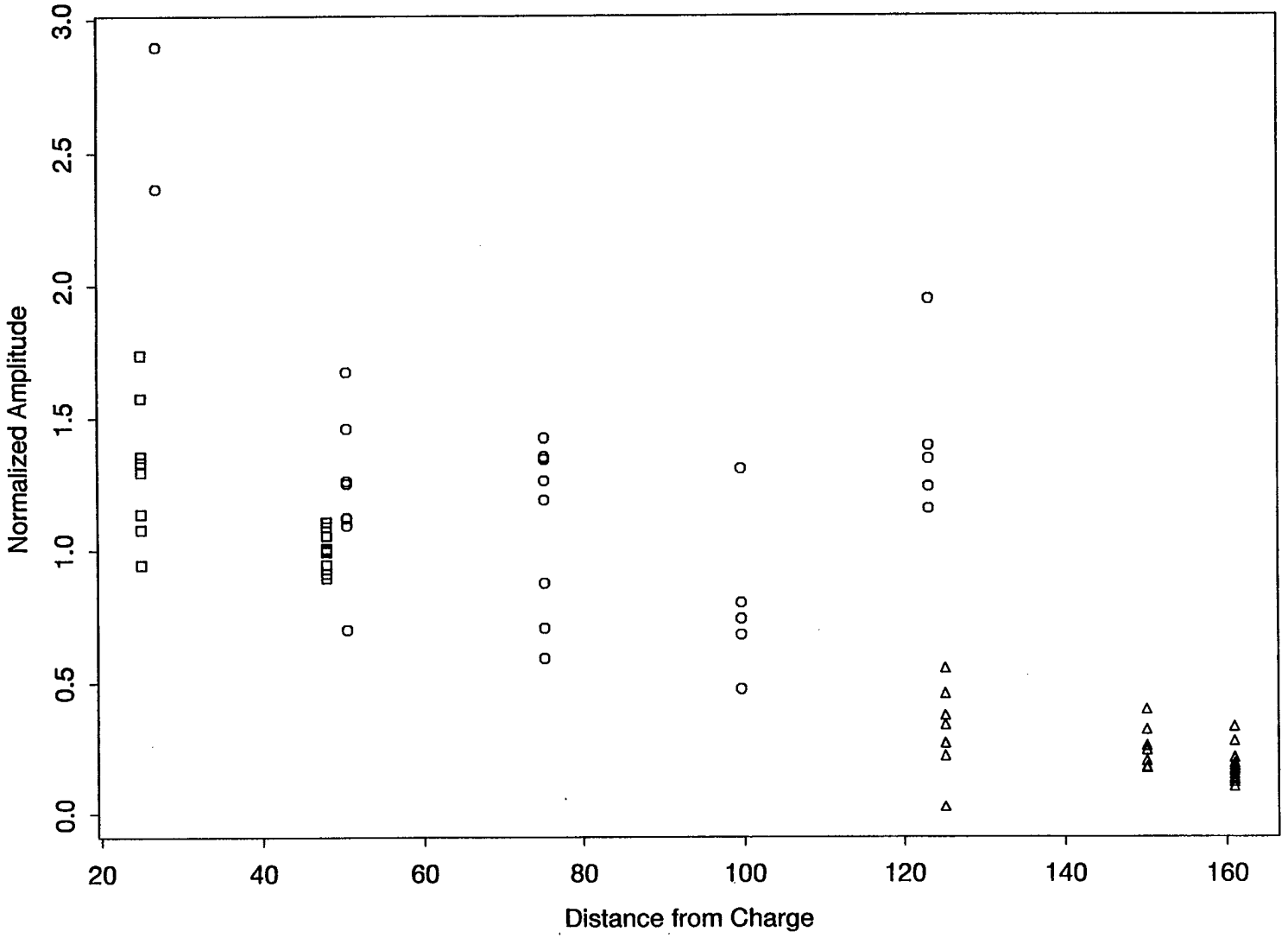


Figure 9: Pulse Amplitudes by Distance From Shock Point.

- The existence of two wave modes, longitudinal and transverse, denoted by subscripts 1 and 2, respectively.
- The mixing of modes, as modeled by parameters $C_{ij}, i, j = 1, 2$.
- Mode-dependent exponential decrease in amplitude with distance.
- Amplitude enhancements at points close to an edge, with differentiation between points before an edge (*subsequent edge*) and points beyond an edge (*preceding edges*) (as viewed from the source).

The resulting equation can be succinctly written as follows.

$$Y_i = A_i \times e^{-b_i \cdot x} \times (1 + D \times e^{-d \cdot r}) \times (1 + F \times e^{-f \cdot s}) \quad (1)$$

$$A_i\,(new\ face) = C_{ij} \times Y_j\,(edge\ of\ preceding\ face)$$

where

$Y_i$ = Amplitude of the disturbance
$i$ = Subscript indicating longitudinal (1) or transverse (2)
$A_i$ = Amplitude at charge point/each succeeding edge
$b_i$ = Decrease with distance (exponential parameter)
x = Distance from charge point to measurement point
D = Enhancement due to proximity of subsequent edge
d = Decrease in D with distance from subsequent edge
r = Distance from subsequent edge
F = Enhancement due to proximity of preceding edge
f = Decrease in F with distance from preceding edge
s = Distance from preceding edge

The ability of Equation 1 to fit the Figure 9 data is shown in Figure 10. The data set consists of 75 points. However, it must be pointed out that the available data were not sufficient to determine all of the above parameters. For example, the $C_{ij}$ were found to be irresolvable. Two $C_{ij}$ could be freed to fit to the data only if the $A_i$ were fixed; however, attempts to free both the $A_i$ and $C_{ij}$ or to free more than two $C_{ij}$ led to "singular gradient matrix" errors in the fitting routine, an indication that the fitting parameters are not independent with respect to the available data. Similarly, it must be noted that the value of $A_2$ was effectively set by normalizing to a front face point. Hence, in the actual fitting equation, there were six free (fitting) parameters, viz:

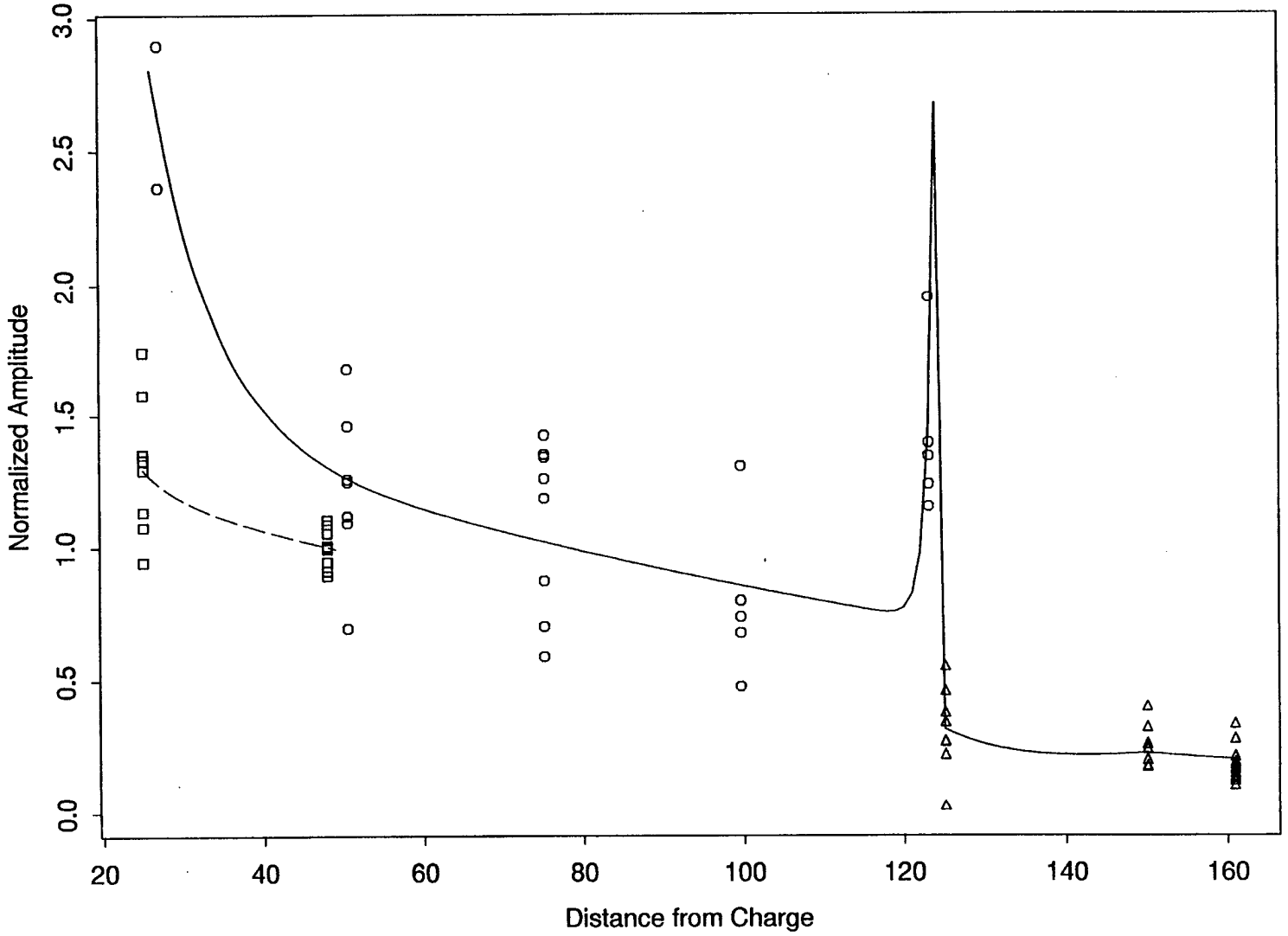


Figure 10: Fit to Pulse Amplitudes by Distance From Shock Point.

$A_1$ – Amplitude at charge point/each succeeding edge
$b_1$ – Decrease with distance (exponential parameter)
$b_2$ – Decrease with distance (exponential parameter)
D – Enhancement due to proximity of subsequent edge
d – Decrease in D with distance from subsequent edge
F – Enhancement due to proximity of preceding edge

## 5. Goodness of Fit.

Evaluation of the goodness of fit of a non-linear equation is generally problematic. However, the following technique, adopted from Draper and Smith[3] provides a reasonable (practical) measure. Effectively, the technique compares the intrinsic scatter in the data from their means to the scatter of the data from the fit at each measurement point.

Note that the technique for estimating intrinsic scatter requires more than one independent measurement be taken at some or all of the measurement points, a condition assured from the beginning in this analysis by combining the (normalized) data from the eight shots listed in Table 2. (See Section III.A.3.)

The intrinsic scatter is characterized as follows: The "pure error sum of squares", $S^2$, in a data set containing more than one value at each point in the independent variables, is defined as

$$S^2 = \sum_{k=1}^{K} \sum_{j=1}^{n_k} (Y_{kj} - \overline{Y}_k)^2, \tag{2}$$

where $n_k$ are the number of values at each of K measurement points, $Y_{kj}$ are the data and $\overline{Y}_k$ are the means at each measurement point. Since K means have been computed, the total degrees of freedom in computing $S^2$ is given by N-K, where N is the total number of data. Thus, the "mean square for pure error" is given by

$$s_e^2 = \frac{\sum_{k=1}^{K} \sum_{j=1}^{n_k} (Y_{kj} - \overline{Y}_k)^2}{N - K}. \tag{3}$$

[3]Draper, N. R., and H. Smith. *Applied Regression Analysis.* New York: John Wiley & Sons, Inc., 1966

The scatter of the data from the fit is characterized by

$$\hat{S}^2 = \sum_{i=1}^{N} (Y_i - \hat{Y}_i)^2, \tag{4}$$

where $\hat{Y}_i$ is the fitted value corresponding to the $i^{th}$ datum. The number of degrees of freedom in $\hat{S}^2$ is the number of data, N, minus the number of fitting parameters, m, in the equation for $\hat{S}^2$. Thus, the mean square scatter of the data from the fit is given by

$$\hat{s}_e^2 = \frac{\sum_{i=1}^{N} (Y_i - \hat{Y}_i)^2}{N - m}. \tag{5}$$

For the data in this analysis, we find

| Parameter | Value | Statistic | Value |
|---|---|---|---|
| N | 75 | $S^2$ | 3.00035 |
| m | 6 | $s_e^2$ | 0.04616 |
| K | 10 | $\hat{S}^2$ | 3.08613 |
| | | $\hat{s}_e^2$ | 0.04473 |

Note that $\hat{s}_e^2$ is less than $s_e^2$.

Heuristically, one can think of this goodness of fit analysis as follows. In addition to the underlying physical phenomena which we wish to model, the data contain indeterminate contributions ("pure error") from experimental vagaries, measurement error, and other sources. We assume that the indeterminate contributions are randomly distributed about the mean at each measurement point and therefore that the mean at each measurement point is the best estimate of the true value at that point. The fit (Equation 1) attempts to produce the true values via a parametric equation. We therefore ask to what

degree does the intrinsic scatter of the data about each best estimate compare to the scatter about the fitted value.

Bodt[4] notes that the complexities in nonlinear modeling do not support the same statistical tests that linear modeling supports. However, similar test constructions as in the linear case are still often used, but with the *caveat* that the actual distribution of the test statistic is unknown.

Even with that *caveat*, Bodt points out that the use of the F-statistic to compare $\hat{s}_e^2$ and $s_e^2$ would be unwarranted. An F random variable is the ratio of two independent Chi-Square random variables. But, the Chi-Square variate based on the residual mean square ($\hat{s}_e^2$) and the Chi-Square variate based on the pure error mean square ($s_e^2$) are not independent.

However, the Chi-Square variate based on the residual mean square with the pure error mean square removed is independent of the Chi-Square variate based on the pure error mean square. In this spirit, Draper and Smith suggest the following statistic to gain "an approximate idea of possible lack of fit":

$$GoF \equiv \frac{(\hat{S}^2 - S^2)/(K-m)}{S^2/(N-K)} = 0.4645 \qquad (6)$$

which they compare to

$$F(K-m, N-K, 0.95) \approx 2.5 >> GoF.$$

The comparison here is significantly better than the example which, according to Draper and Smith,[3] "would make us tentatively feel that the model does not fit badly". We thus conclude that Equation 1 accounts very well for the non-random behavior of the data.

[4]Bodt, Barry A., Private communication. U.S. Army Research Laboratory, APG, MD, 1997

[3]Draper, N. R., and H. Smith. *Applied Regression Analysis.* New York: John Wiley & Sons, Inc., 1966

# IV. Summary and Discussion

This study has dealt with the propagation of only the leading, high-frequency edge of the shock wave emanating from an impact point on an armored vehicle. Since the data show that this leading edge invariably contains the highest amplitude disturbances in the frequency range of interest, concentration on this phenomenon is warranted. Specifically, this study has analyzed the data taken in an experiment in which the vehicle was an M113 armored personnel carrier and the mechanism of shock production was an explosive charge placed on a striker plate which was in contact with the hull of the M113.

This study has shown that the amplitude of the transverse wave can be well fit by a semi-empirical equation (Equation 1) which accounts for both a longitudinal and a transverse wave, exponential decrease with distance, mixing of waves at edges, and amplification at points near edges. Since this analysis dealt only with the propagation of the leading edge of longitudinal and transverse disturbances within the hull material itself, the flexural response of the system as a whole was irrelevant.

Comparison of the leading edge velocities with data published for rolled aluminum confirms the analysis of longitudinal and transverse disturbances. No further attempt was made to relate the results to material properties. Attempts to do so will require data taken on structures made of other materials. Similarly, resolution of certain semi-empirical parameters, such as the mode mixing ratios, will require additional data from experiments specifically designed for such measurements.

It is seen that Equation 1 constitutes an algorithm that is suitable for incorporation into vulnerability analysis codes. Such a code must propagate both the longitudinal and transverse waves through the hull material from point of impact to point of interest. At each intervening edge, amplitudes must be calculated for use as starting values for propagation on the succeeding face.

It is recognized that the above algorithm addresses only one of the three major factors in the analysis of the high-frequency portion of ballistic shock. Significant work is required on shock generation upon impact and upon component failure due to high frequency acceleration before a useful ballistic shock methodology can be assembled.

It is also recognized that newer vehicles, with composite and/or double hulls, will introduce further complications into this treatment. However, the results presented herein give a reasonable starting point for future development.

This page intentionally left blank

# Appendix A

# Calibrated Data

This page intentionally left blank

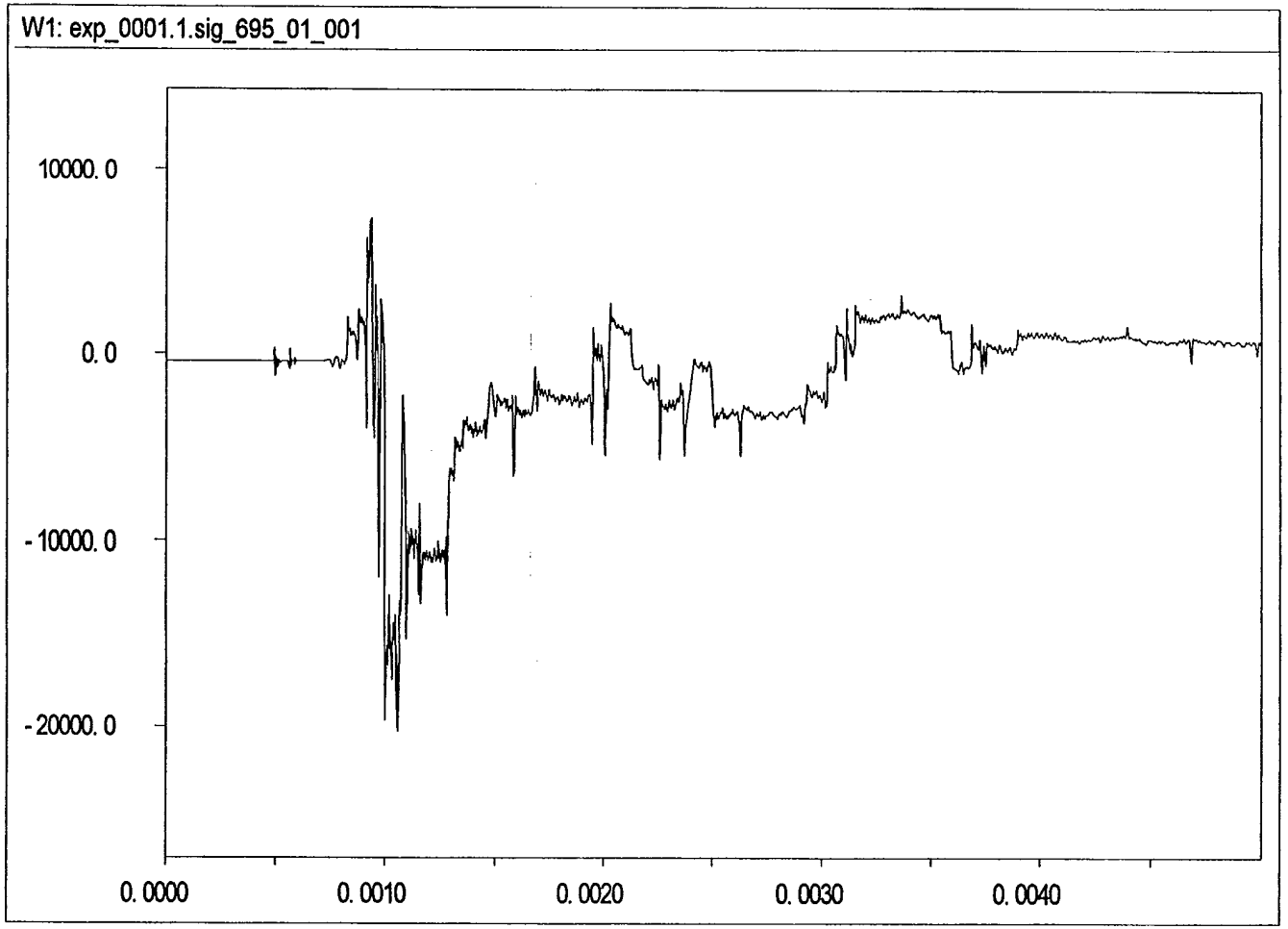


Figure A-1: Calibrated Output of Gauge #1, Shot #695.

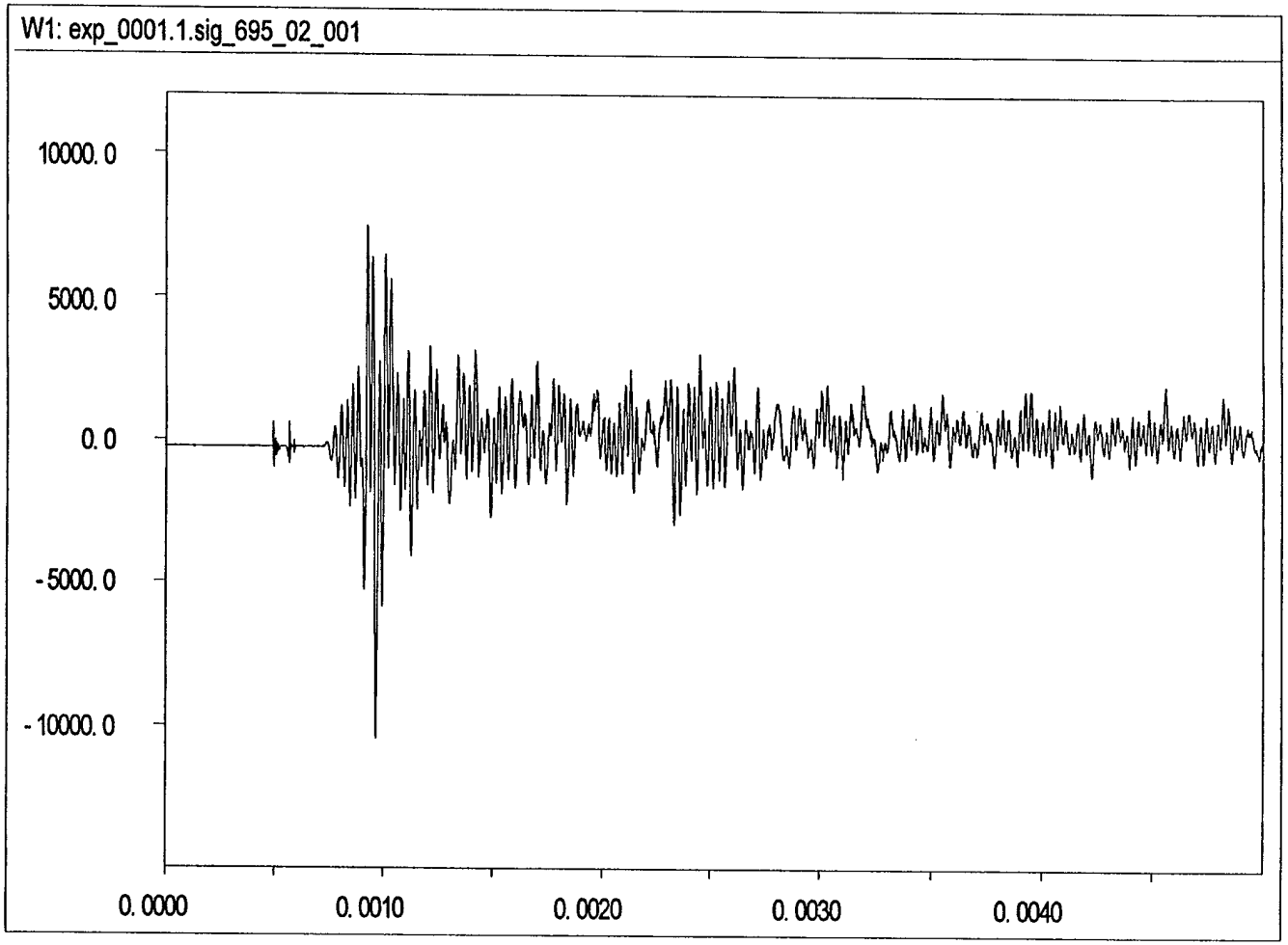


Figure A-2: Calibrated Output of Gauge #2, Shot #695.

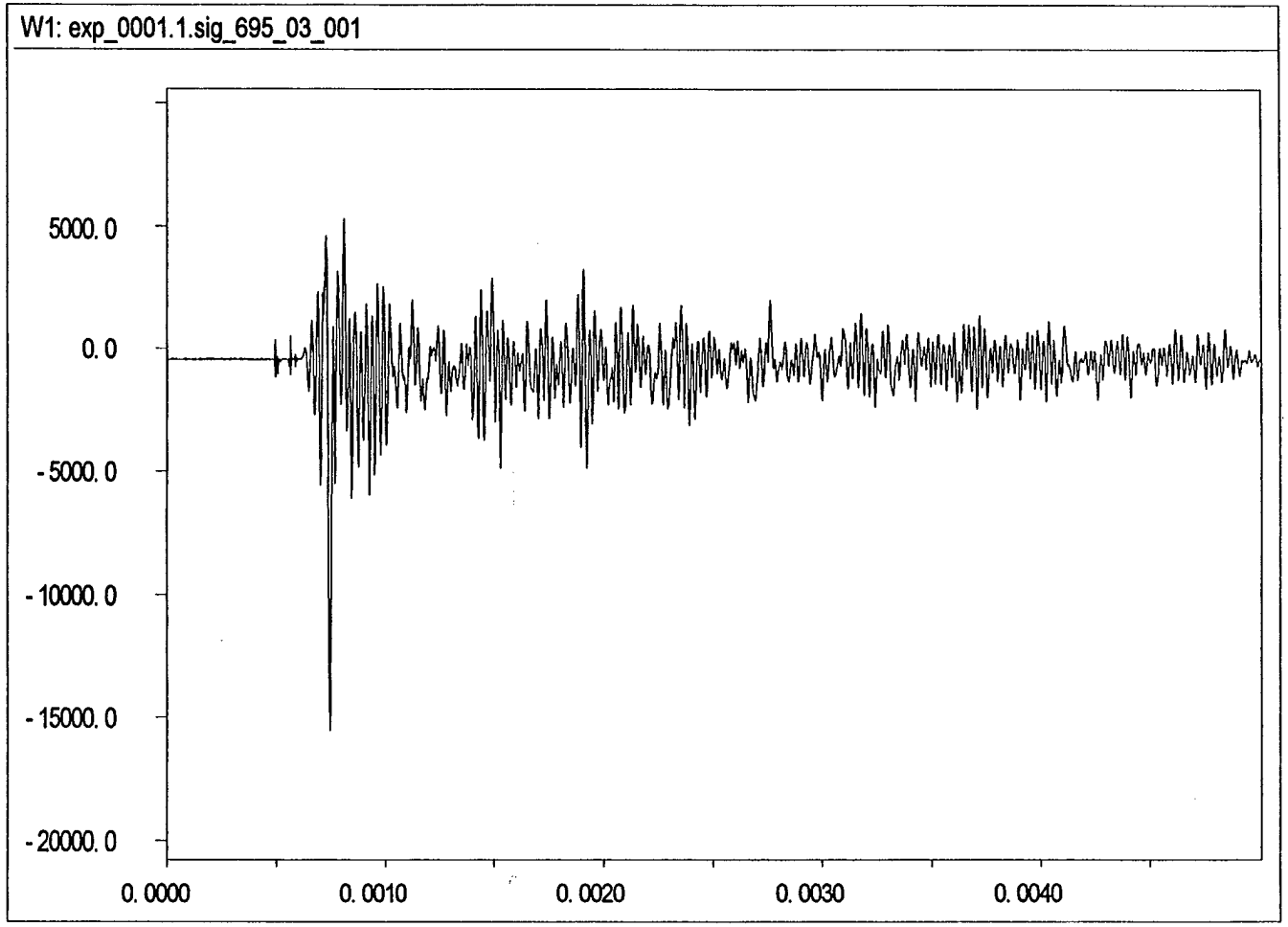


Figure A-3: Calibrated Output of Gauge #3, Shot #695.

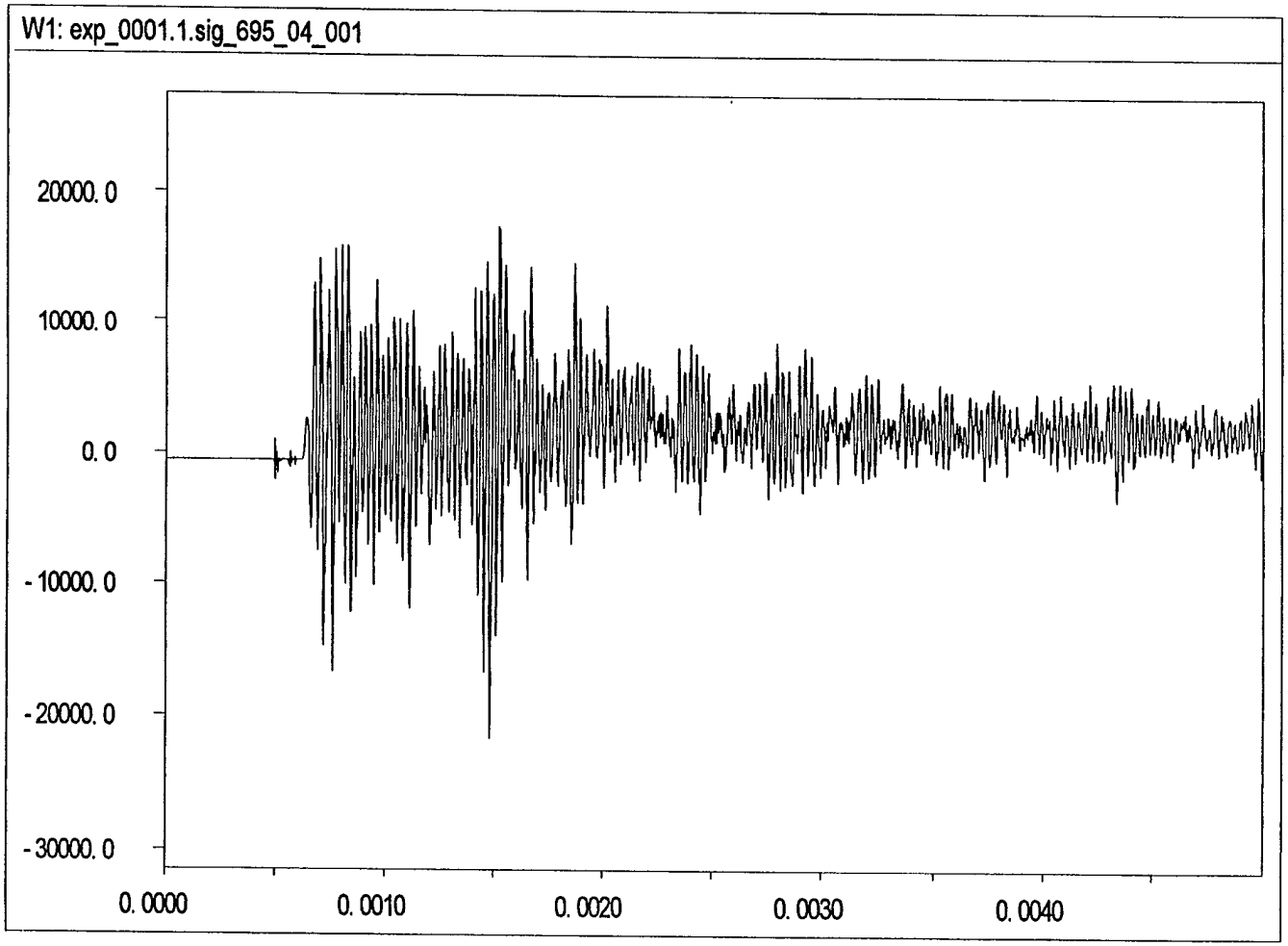


Figure A-4: Calibrated Output of Gauge #4, Shot #695.

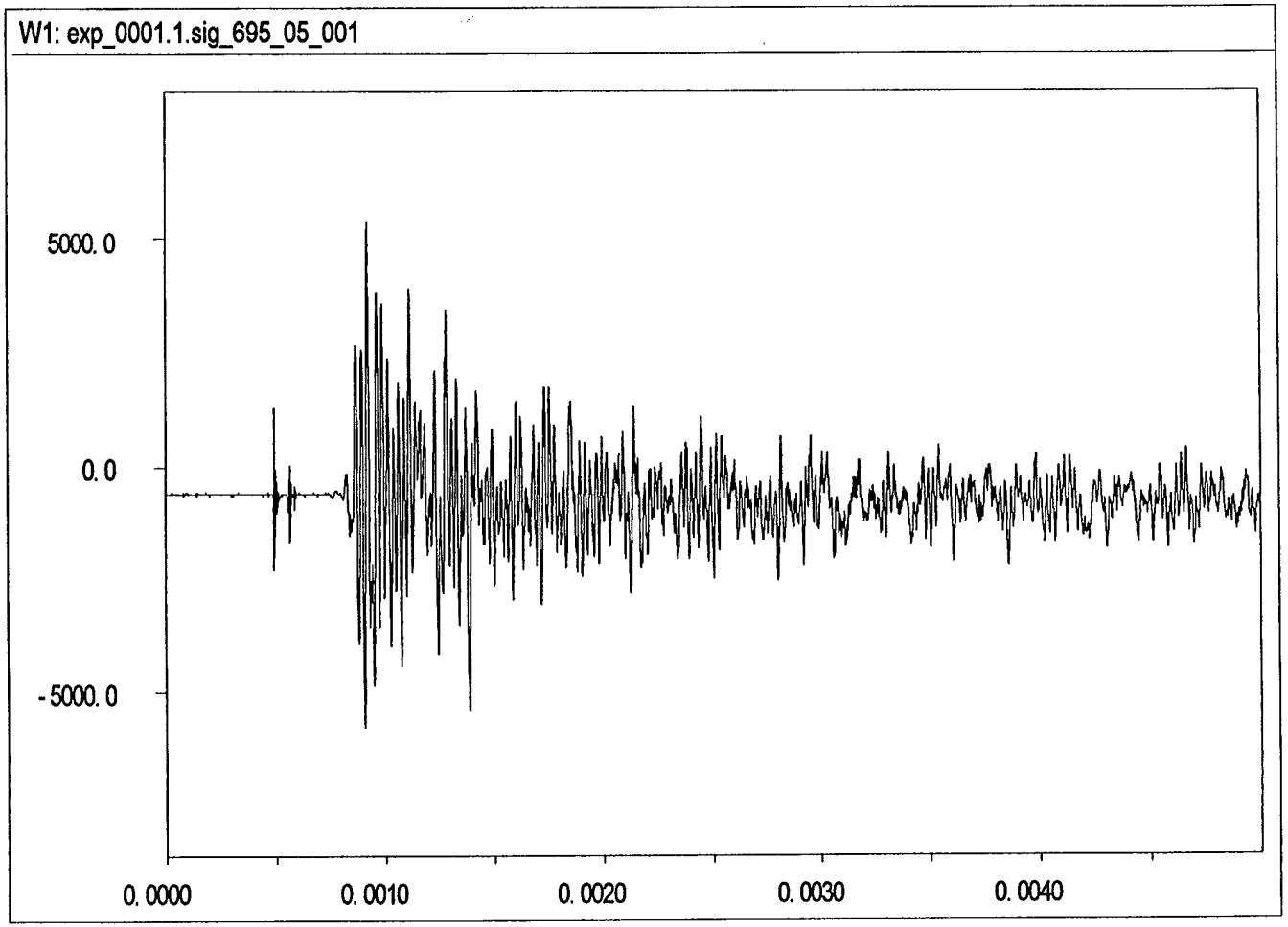


Figure A-5: Calibrated Output of Gauge #5, Shot #695.

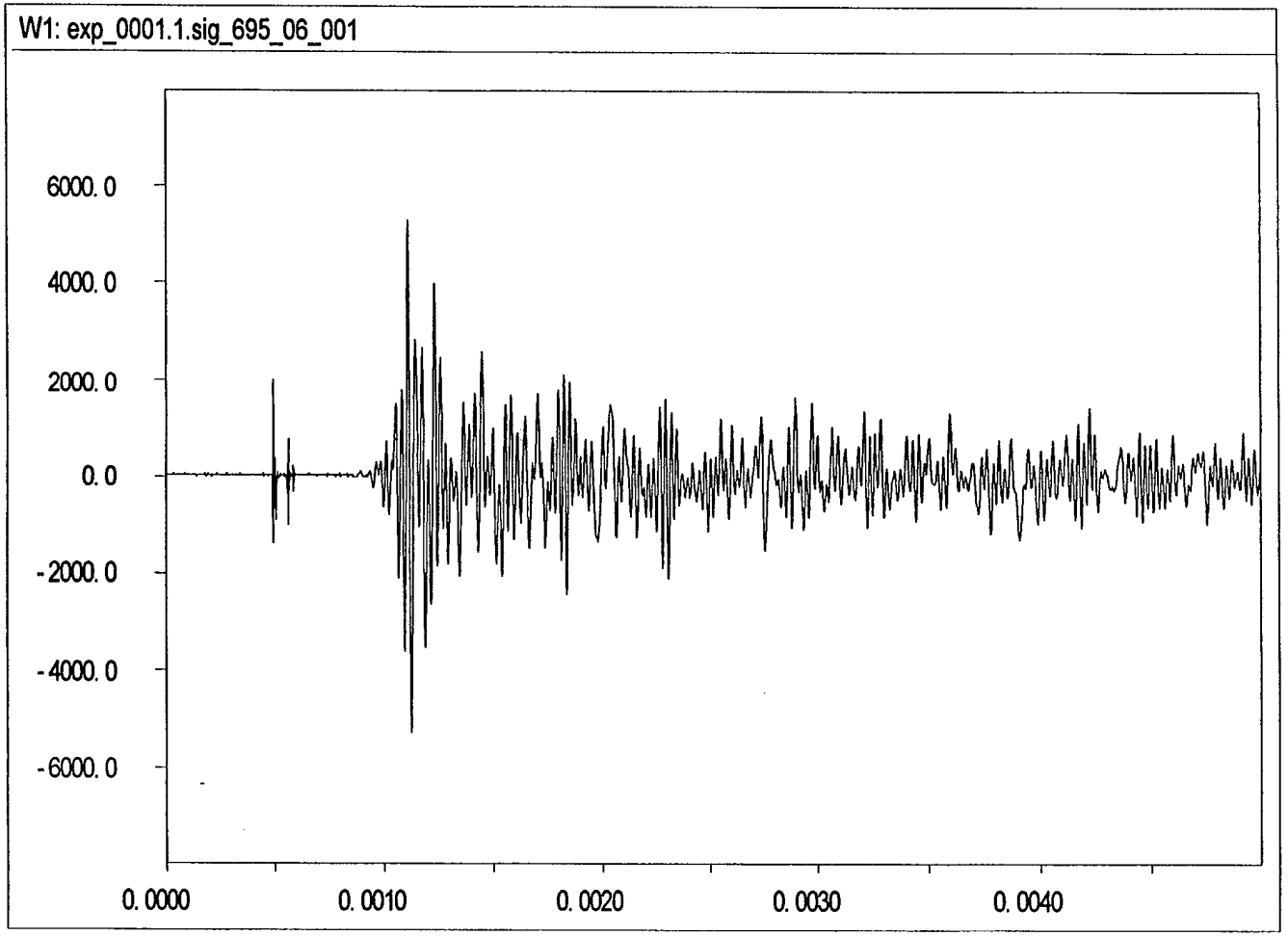


Figure A-6: Calibrated Output of Gauge #6, Shot #695.

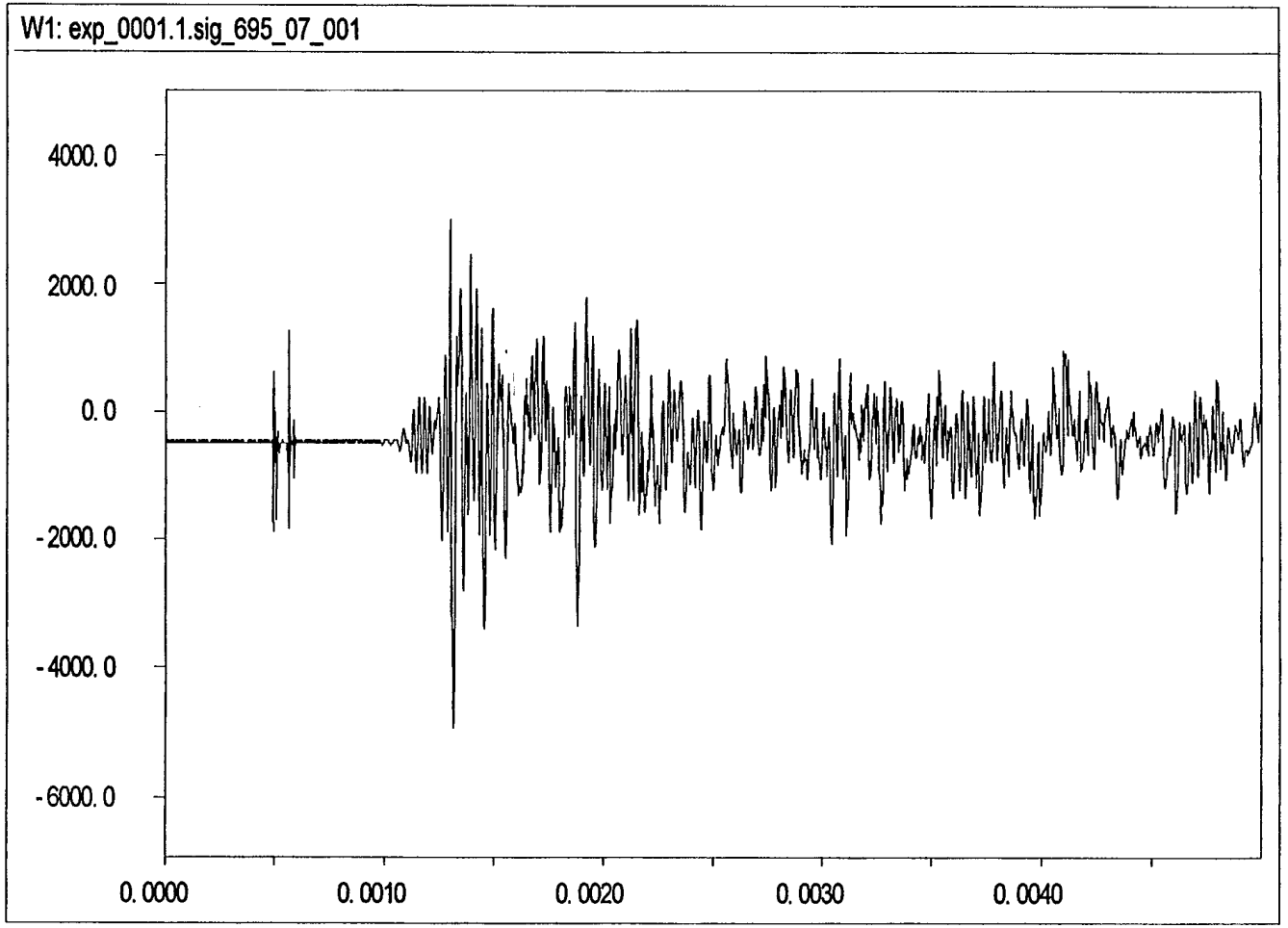


Figure A-7: Calibrated Output of Gauge #7, Shot #695.

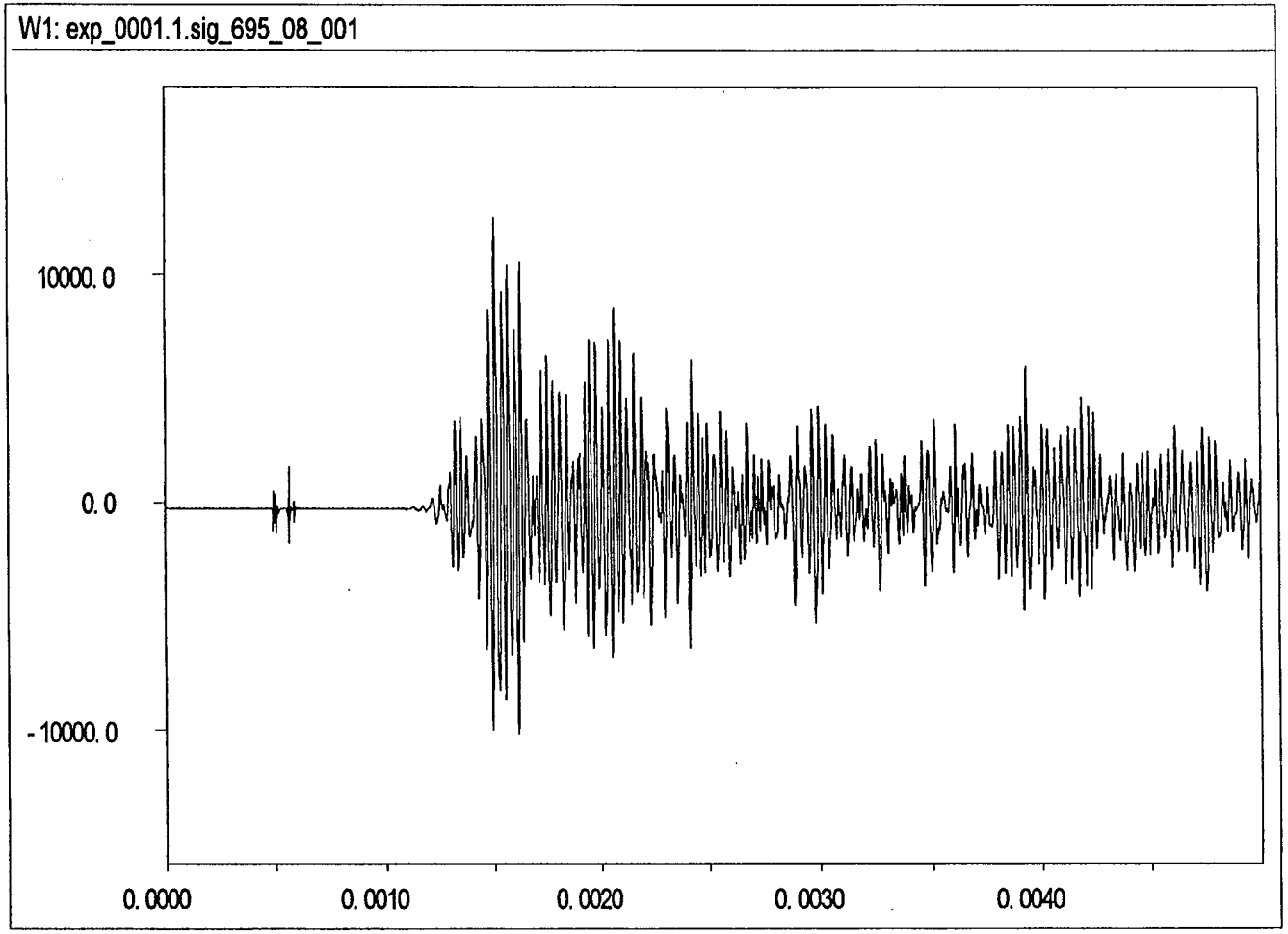


Figure A-8: Calibrated Output of Gauge #8, Shot #695.

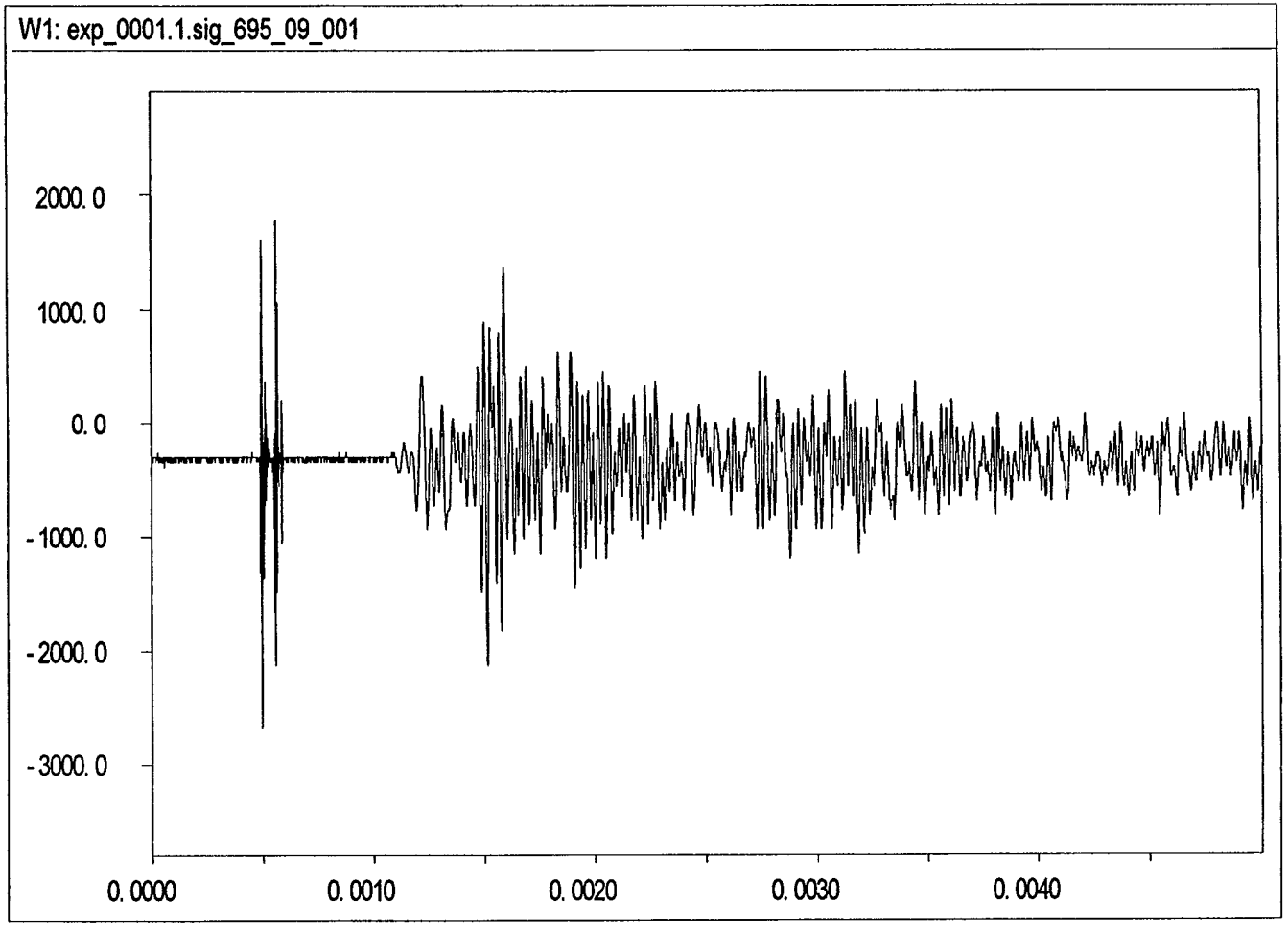


Figure A-9: Calibrated Output of Gauge #9, Shot #695.

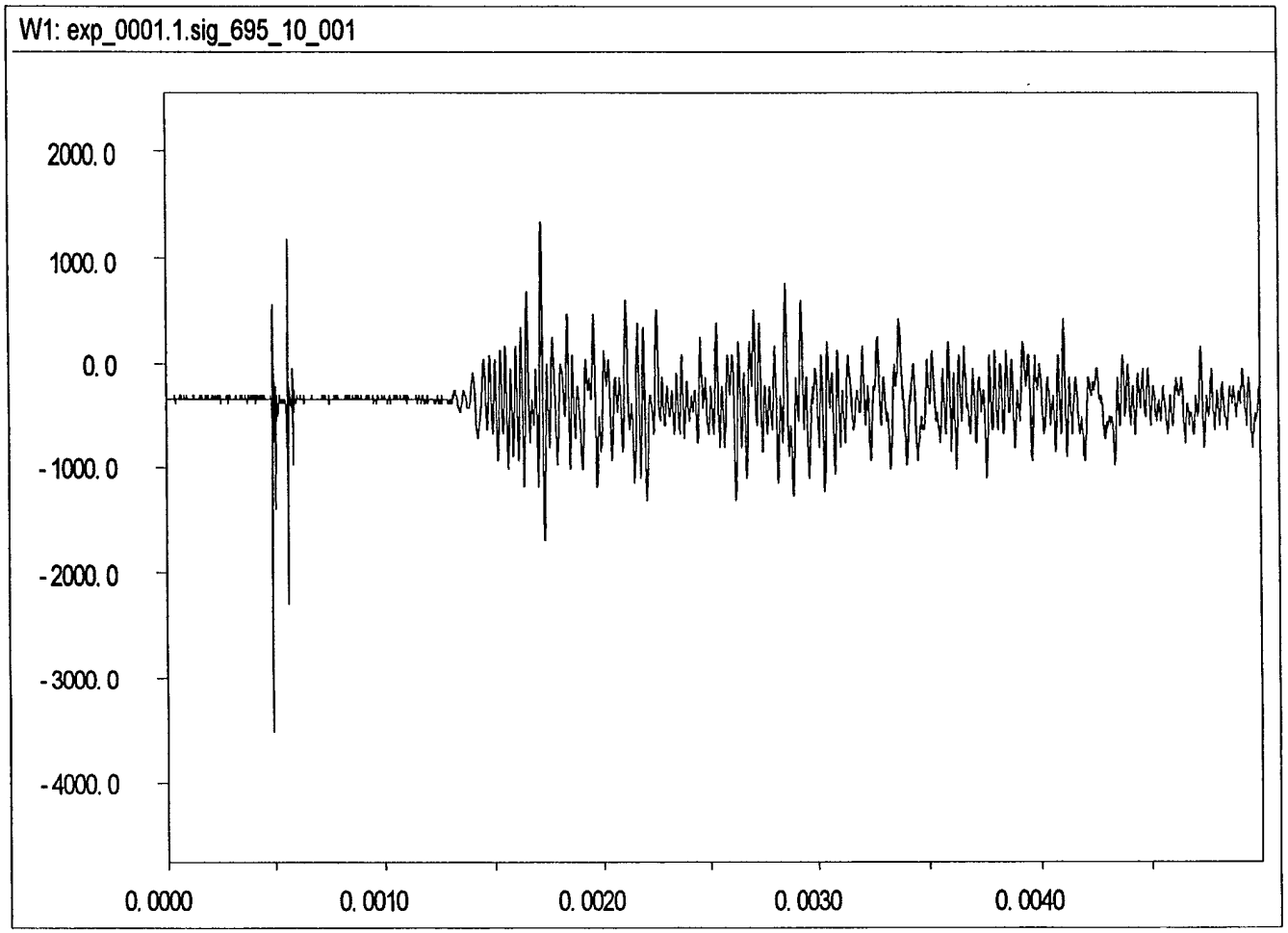


Figure A-10: Calibrated Output of Gauge #10, Shot #695.

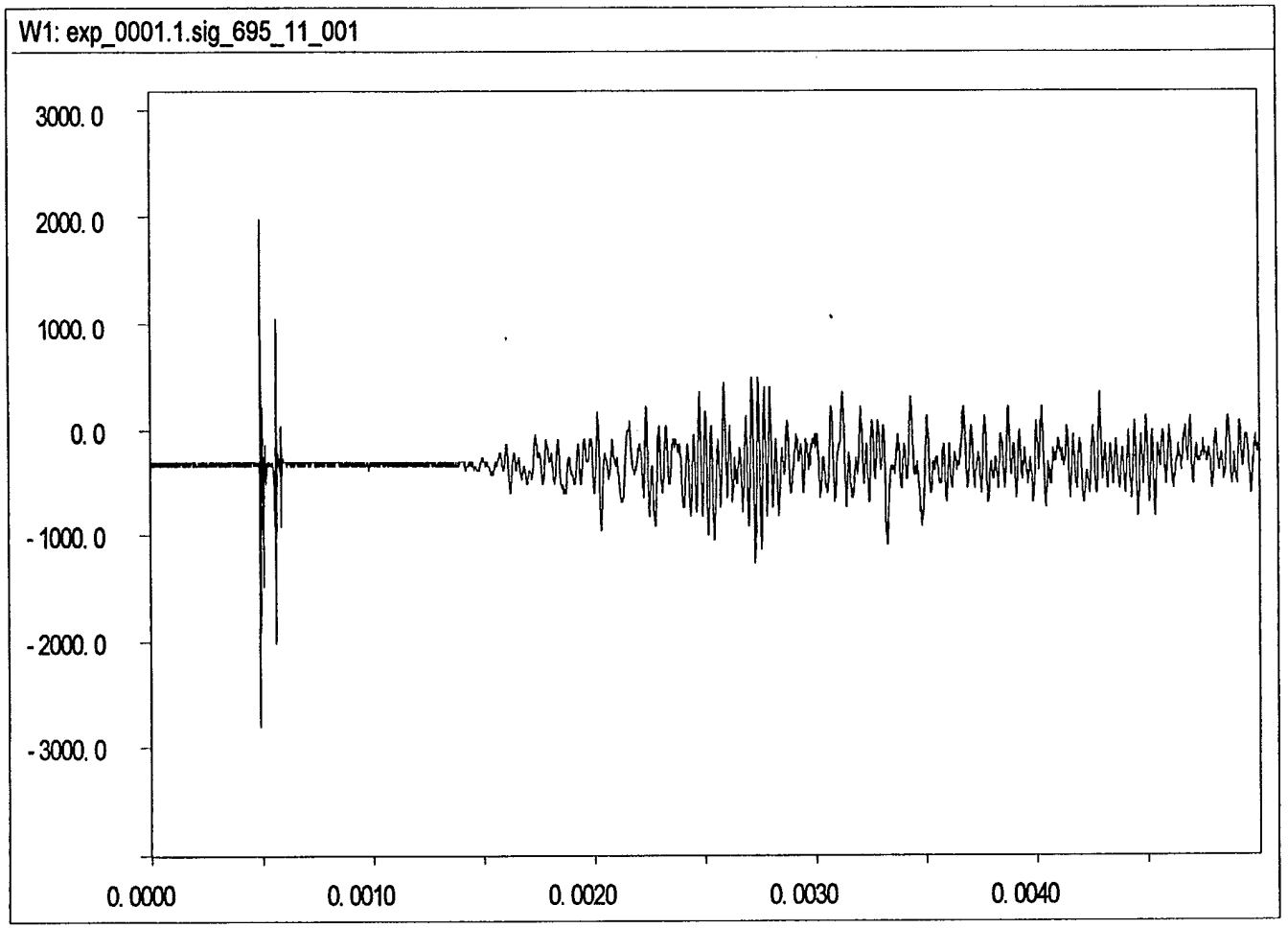


Figure A-11: Calibrated Output of Gauge #11, Shot #695.

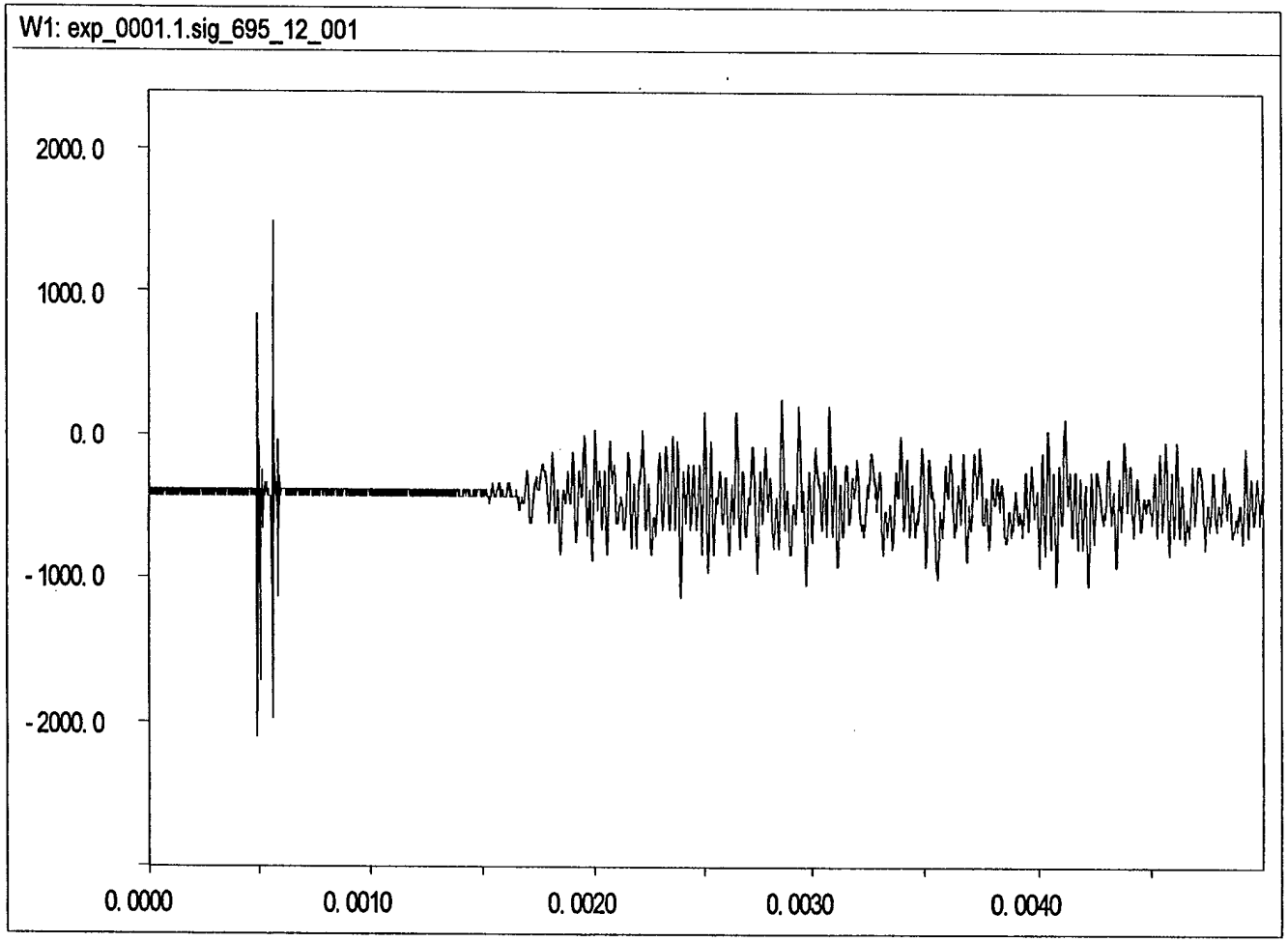


Figure A-12: Calibrated Output of Gauge #12, Shot #695.

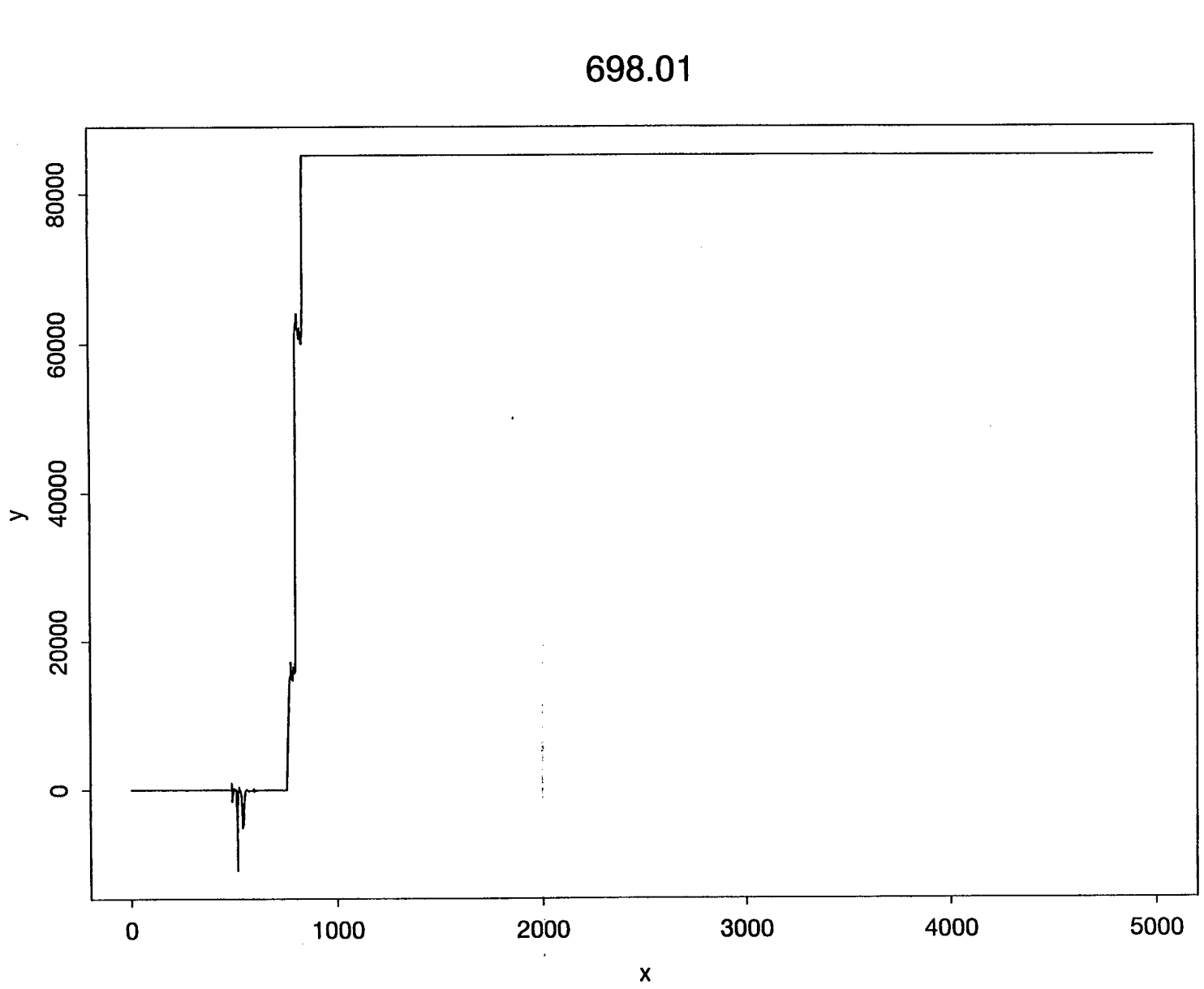


Figure A-13: Calibrated Output of Gauge #1, Shot #698.

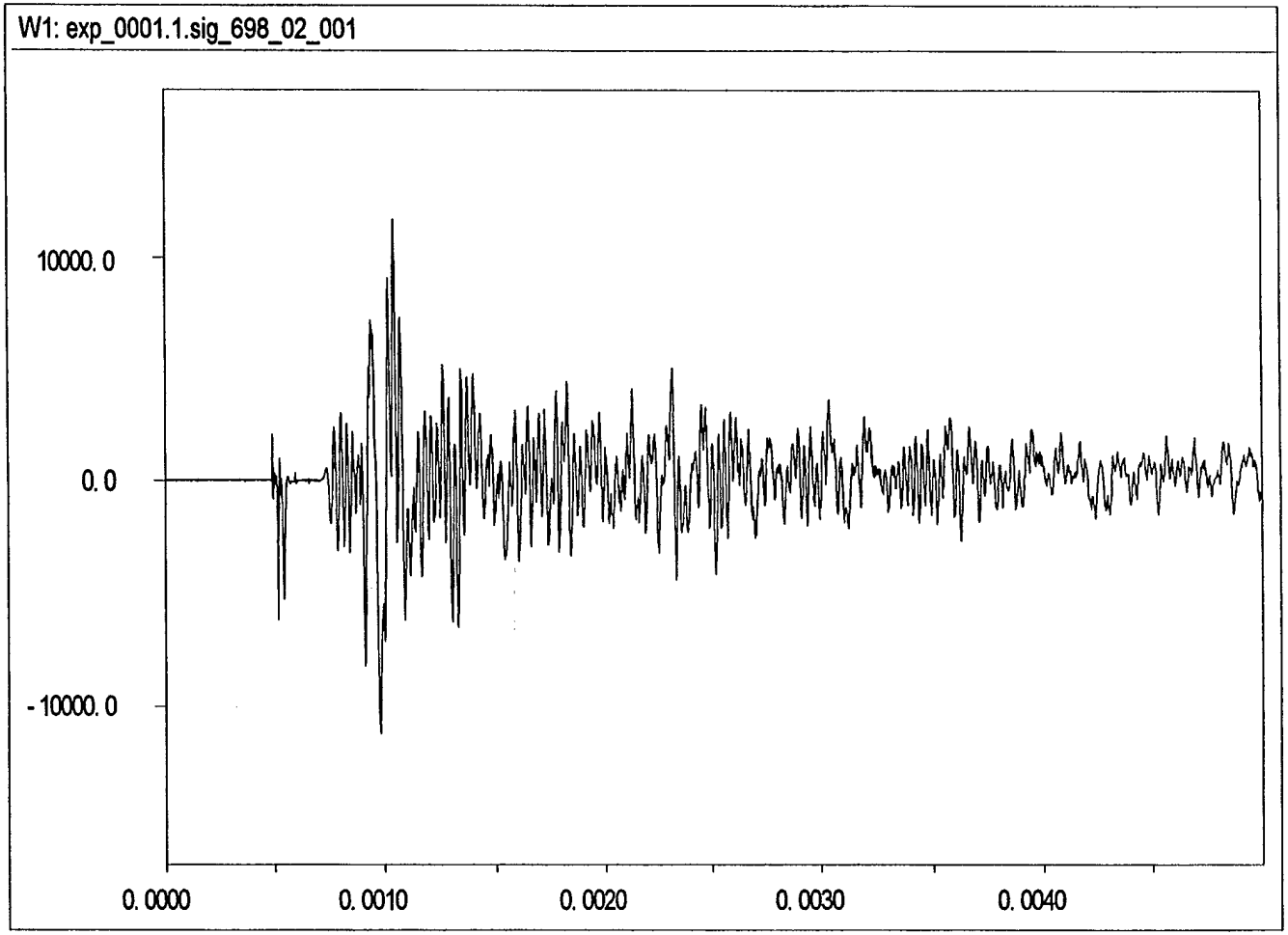


Figure A-14: Calibrated Output of Gauge #2, Shot #698.

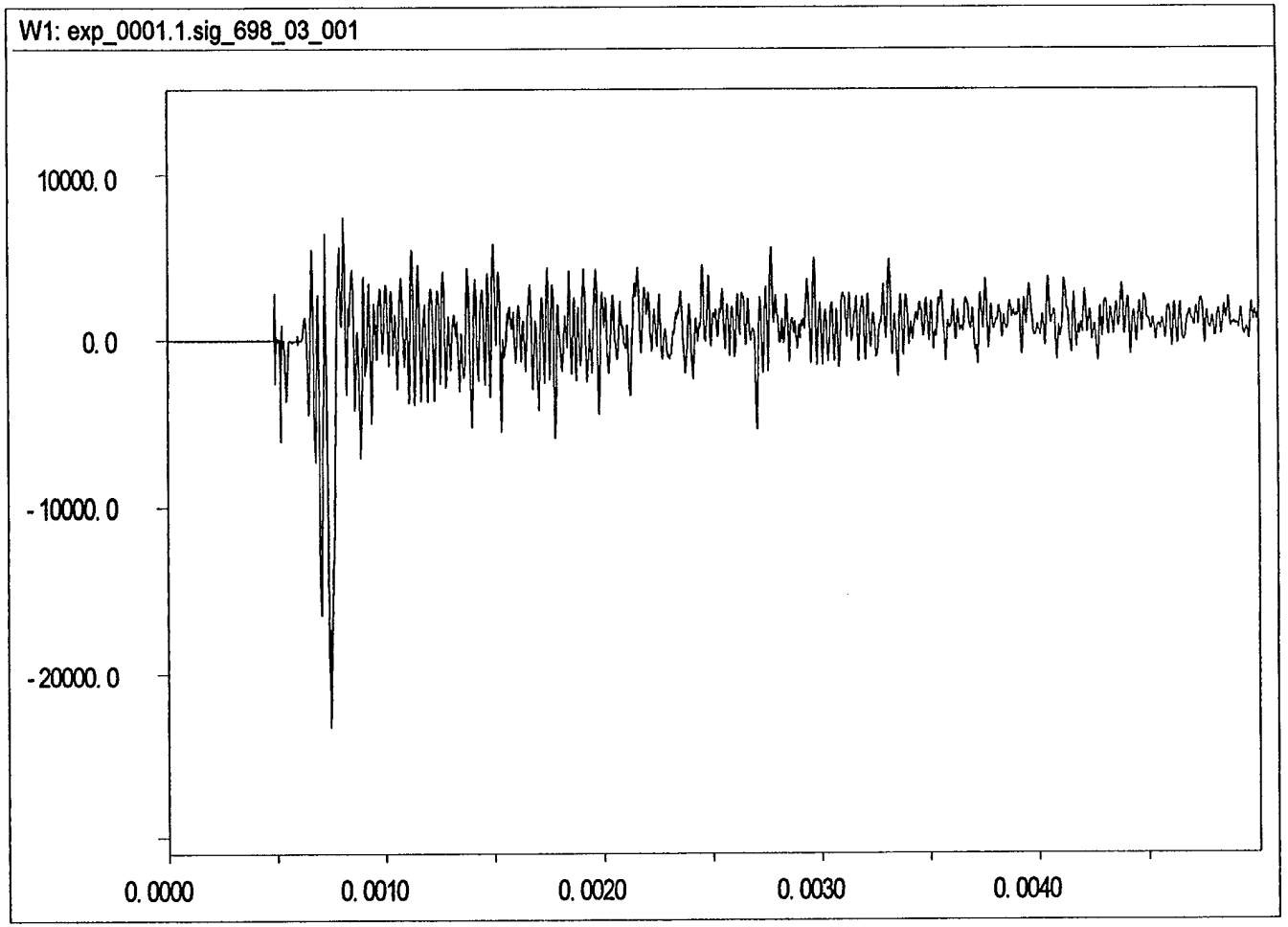


Figure A-15: Calibrated Output of Gauge #3, Shot #698.

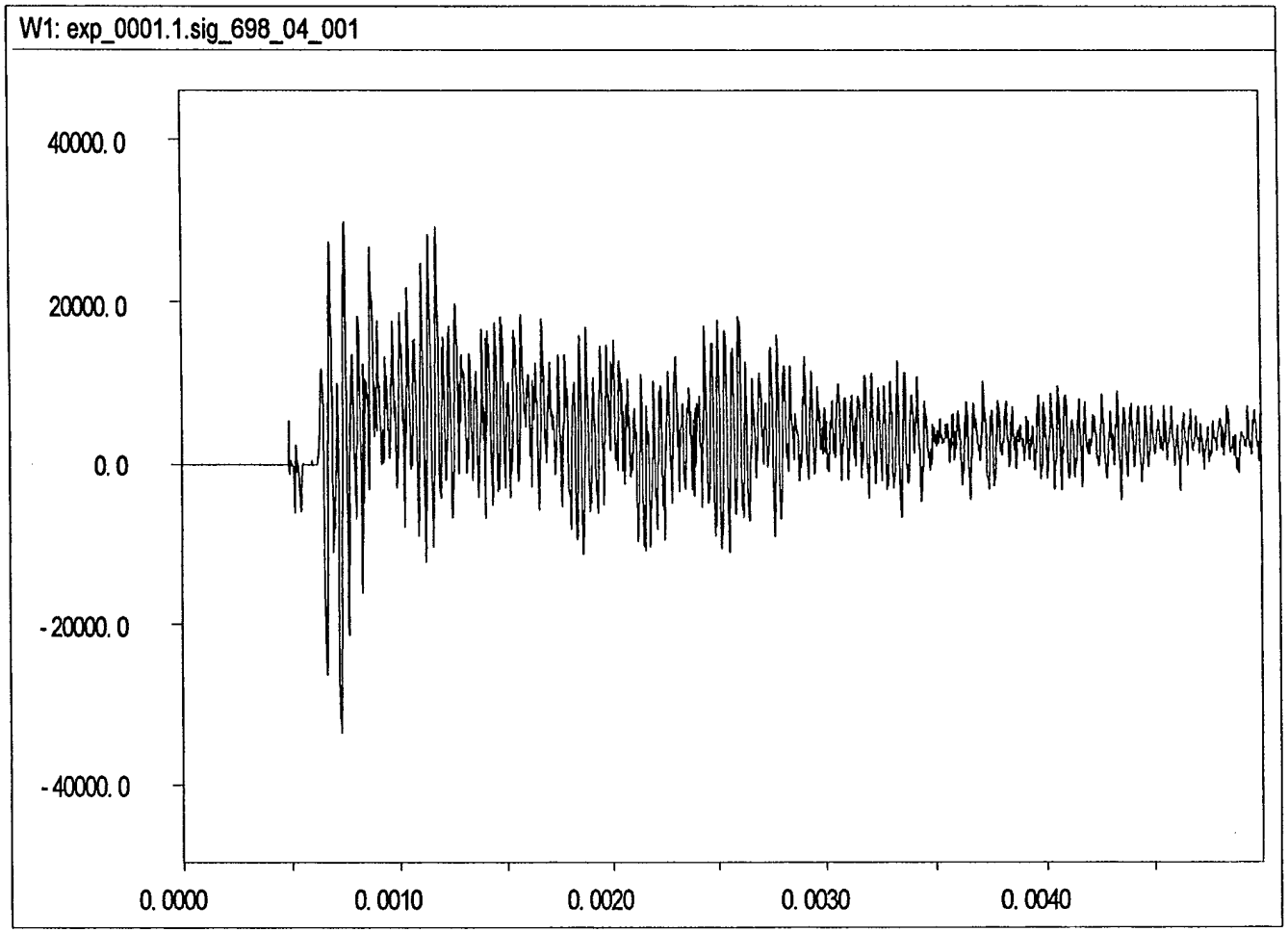


Figure A-16: Calibrated Output of Gauge #4, Shot #698.

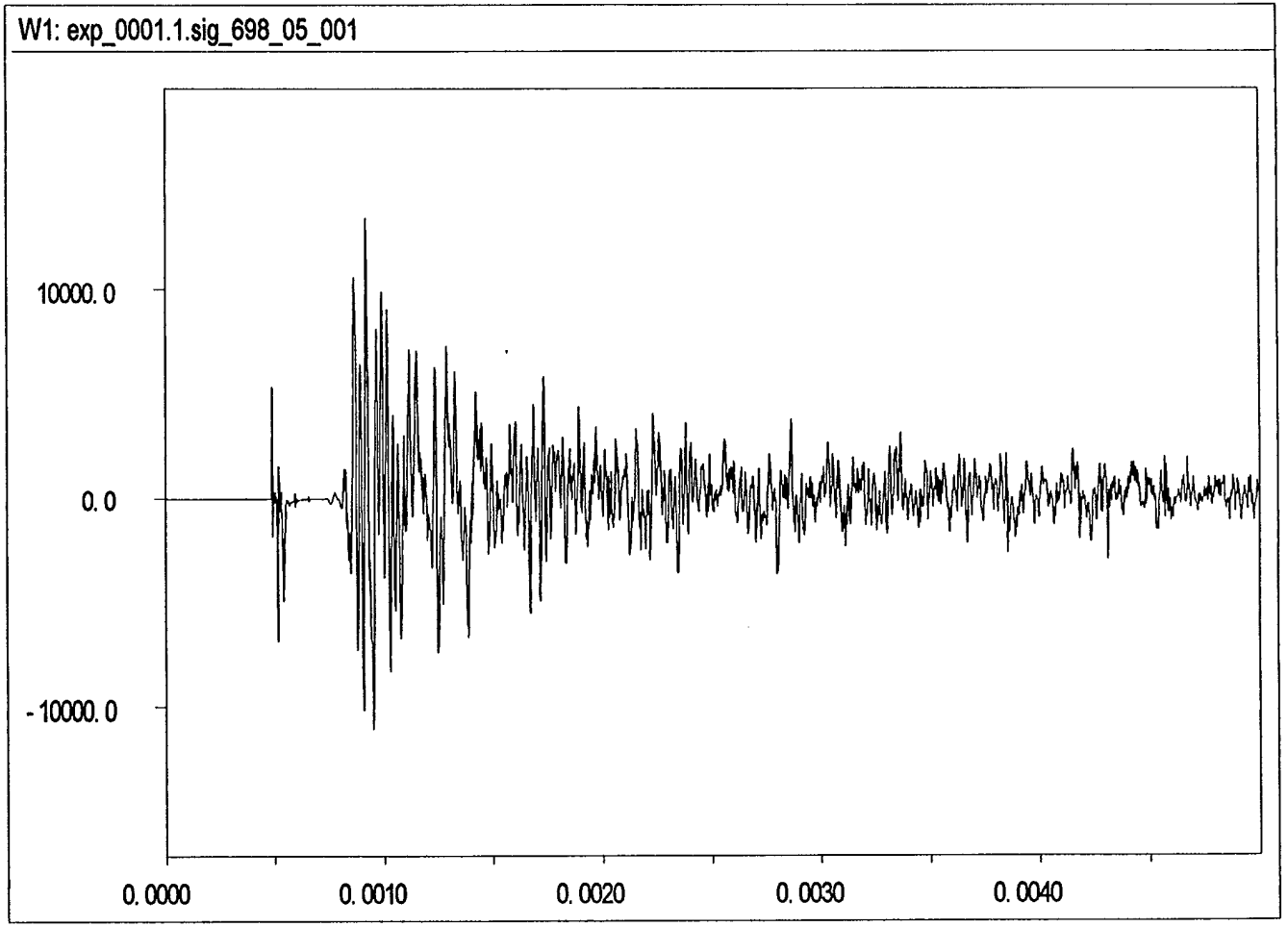


Figure A-17: Calibrated Output of Gauge #5, Shot #698.

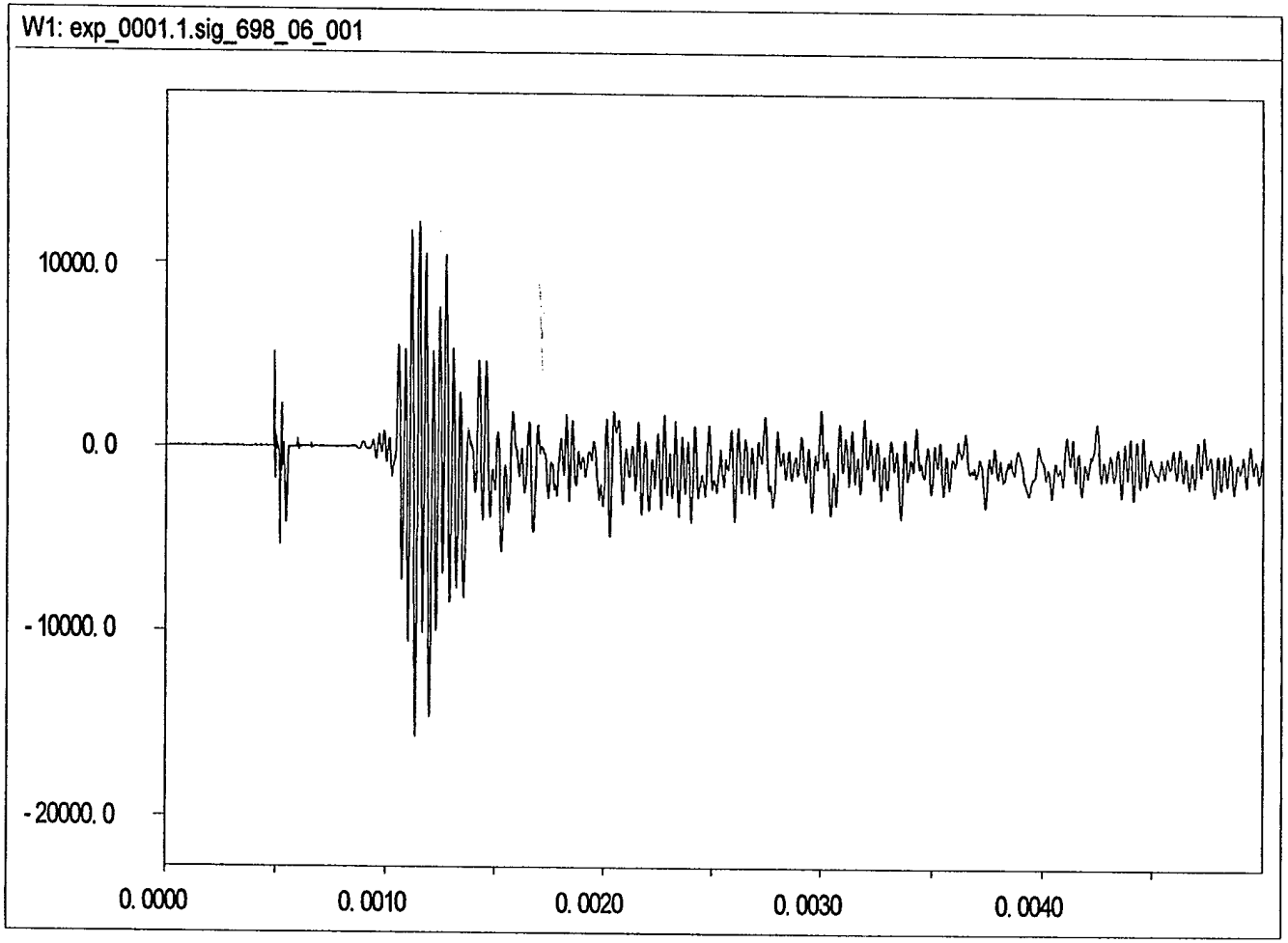


Figure A-18: Calibrated Output of Gauge #6, Shot #698.

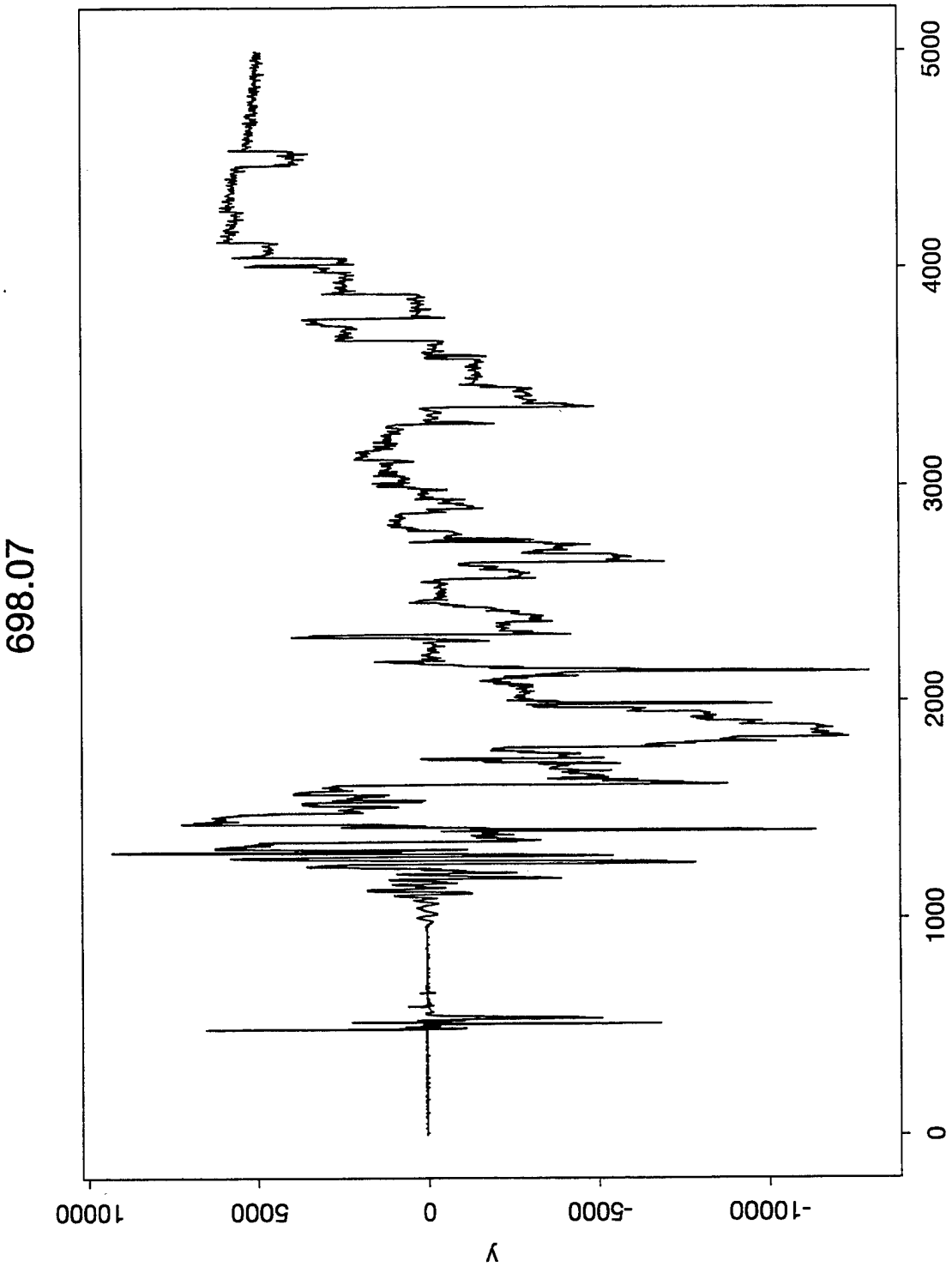


Figure A-19: Calibrated Output of Gauge #7, Shot #698.

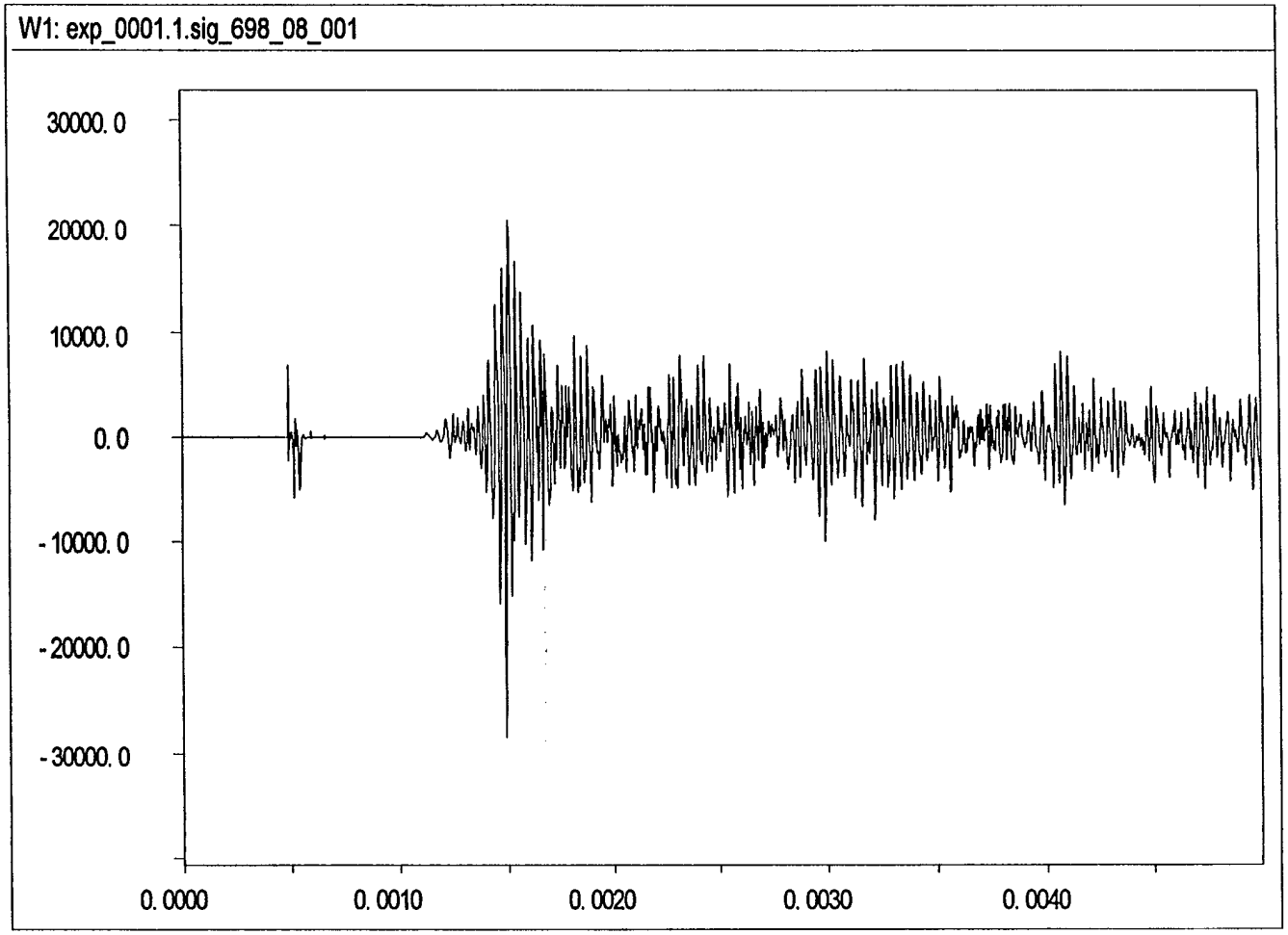


Figure A-20: Calibrated Output of Gauge #8, Shot #698.

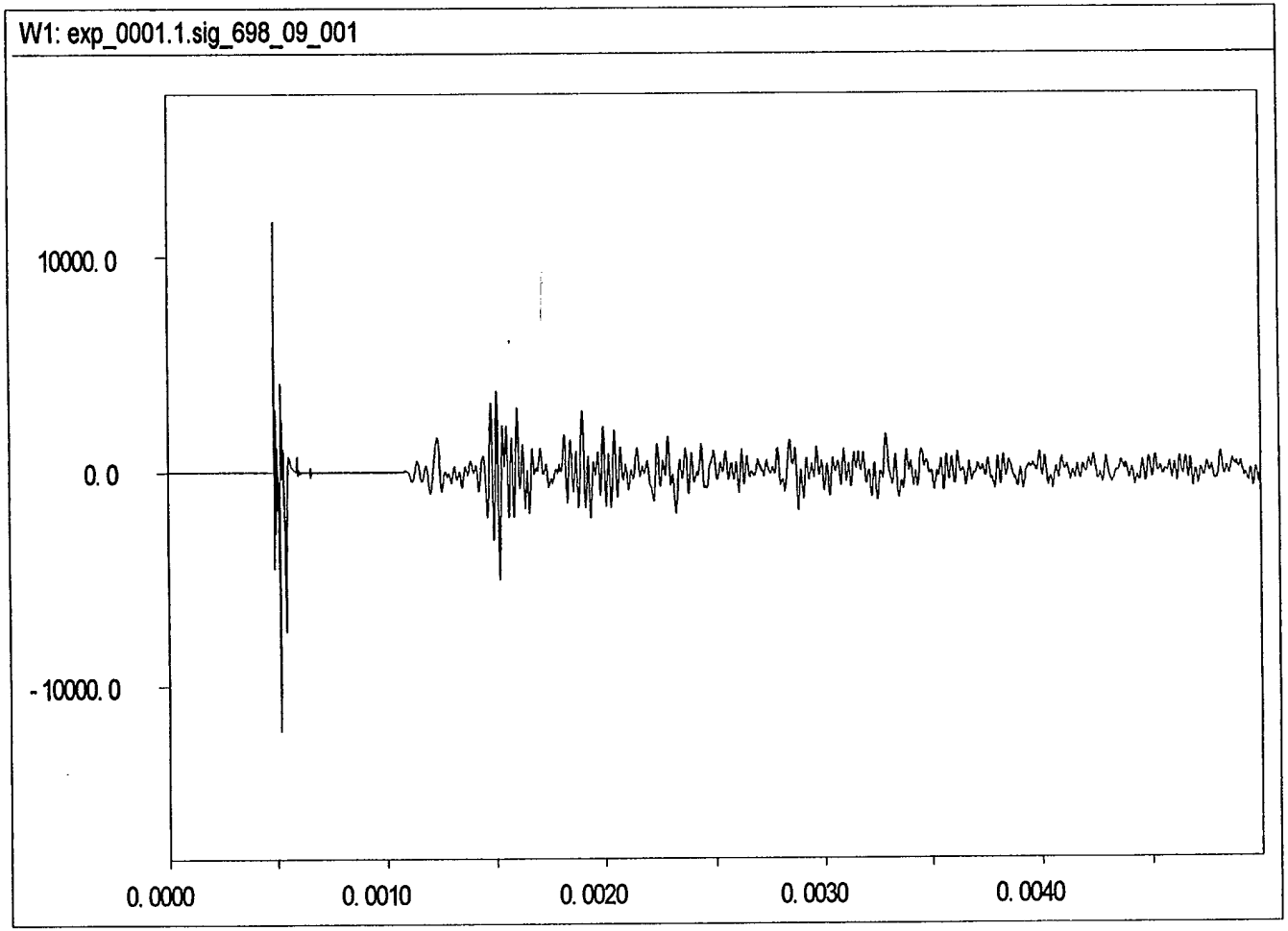


Figure A-21: Calibrated Output of Gauge #9, Shot #698.

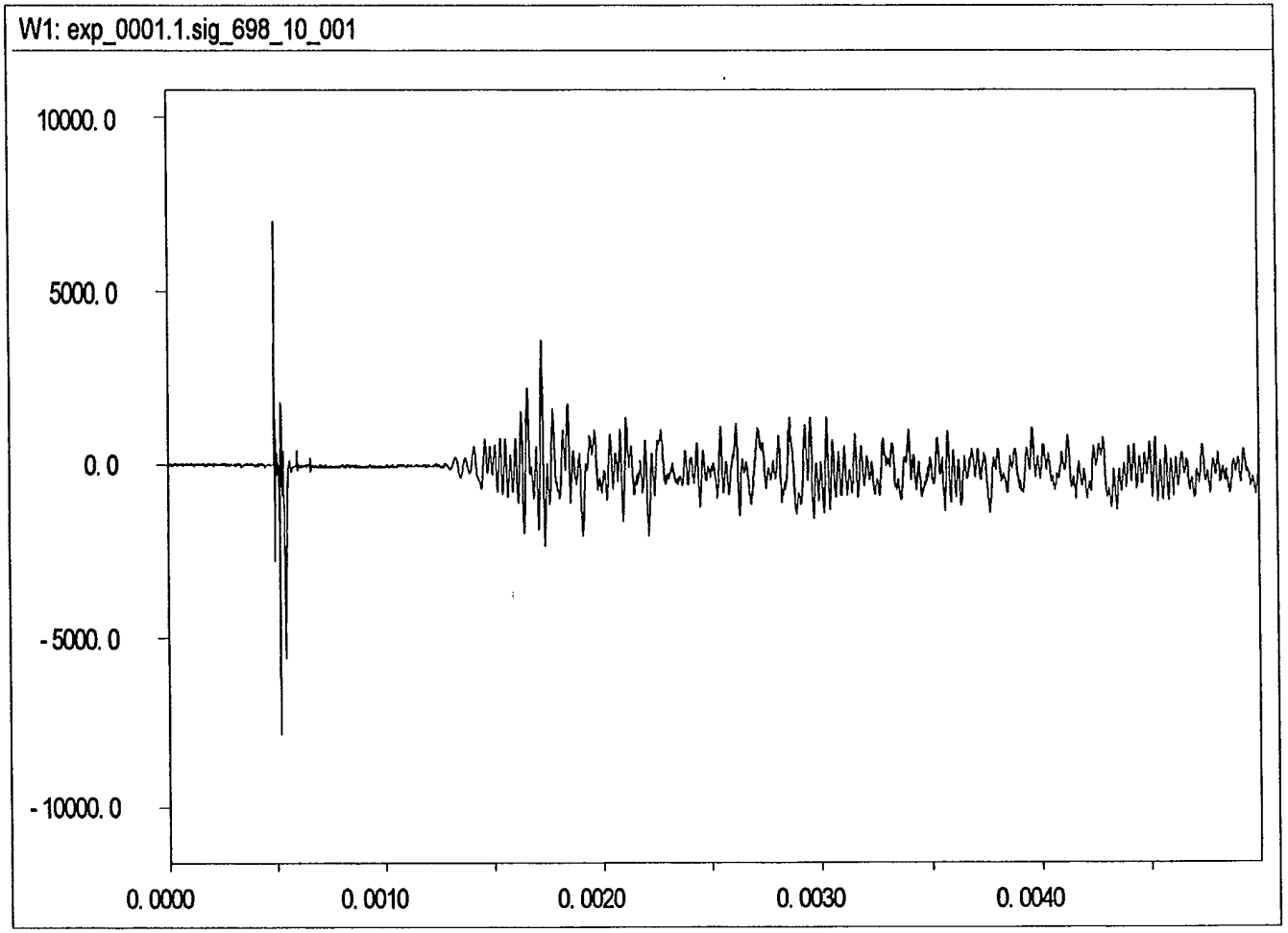


Figure A-22: Calibrated Output of Gauge #10, Shot #698.

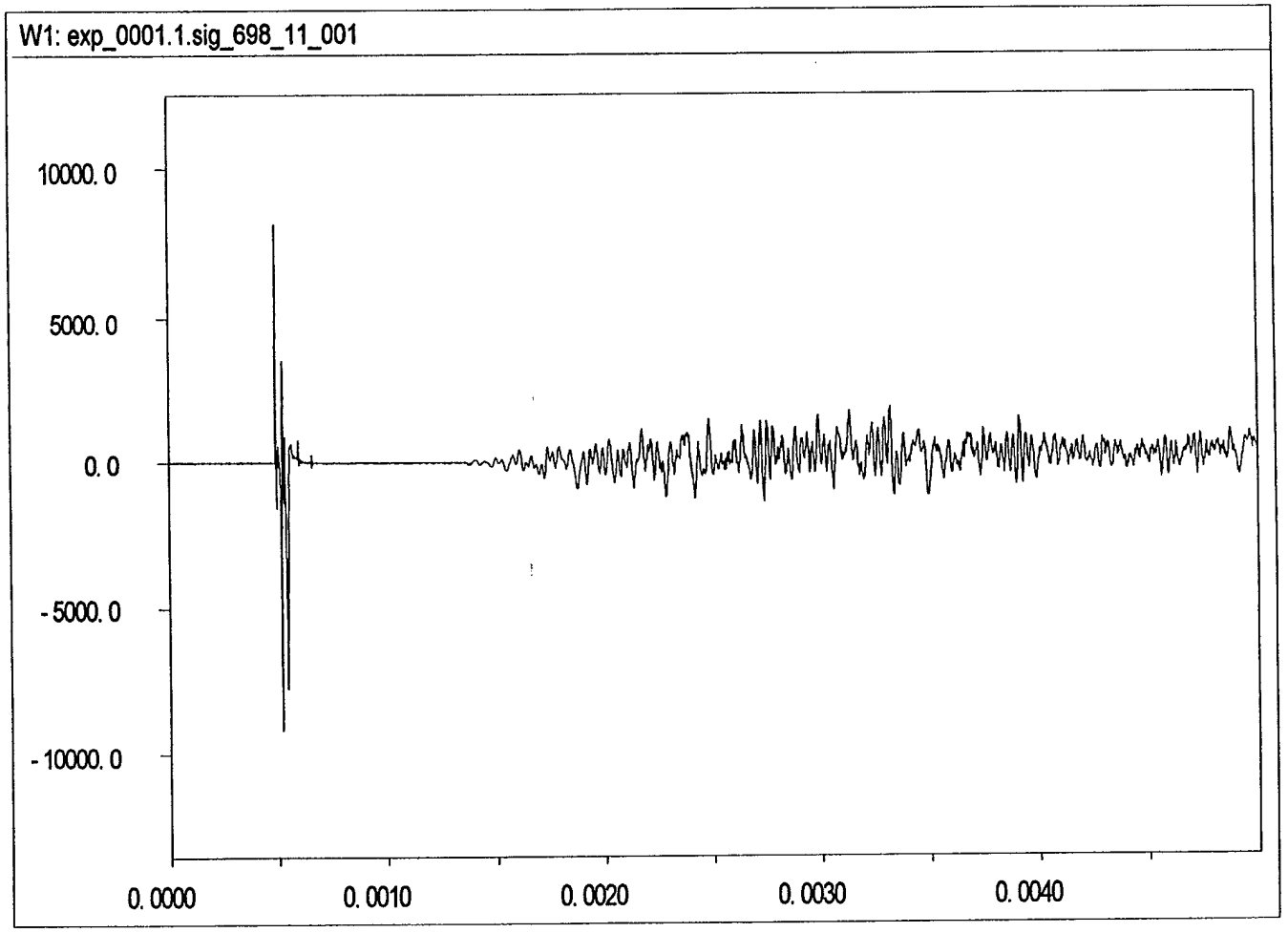


Figure A-23: Calibrated Output of Gauge #11, Shot #698.

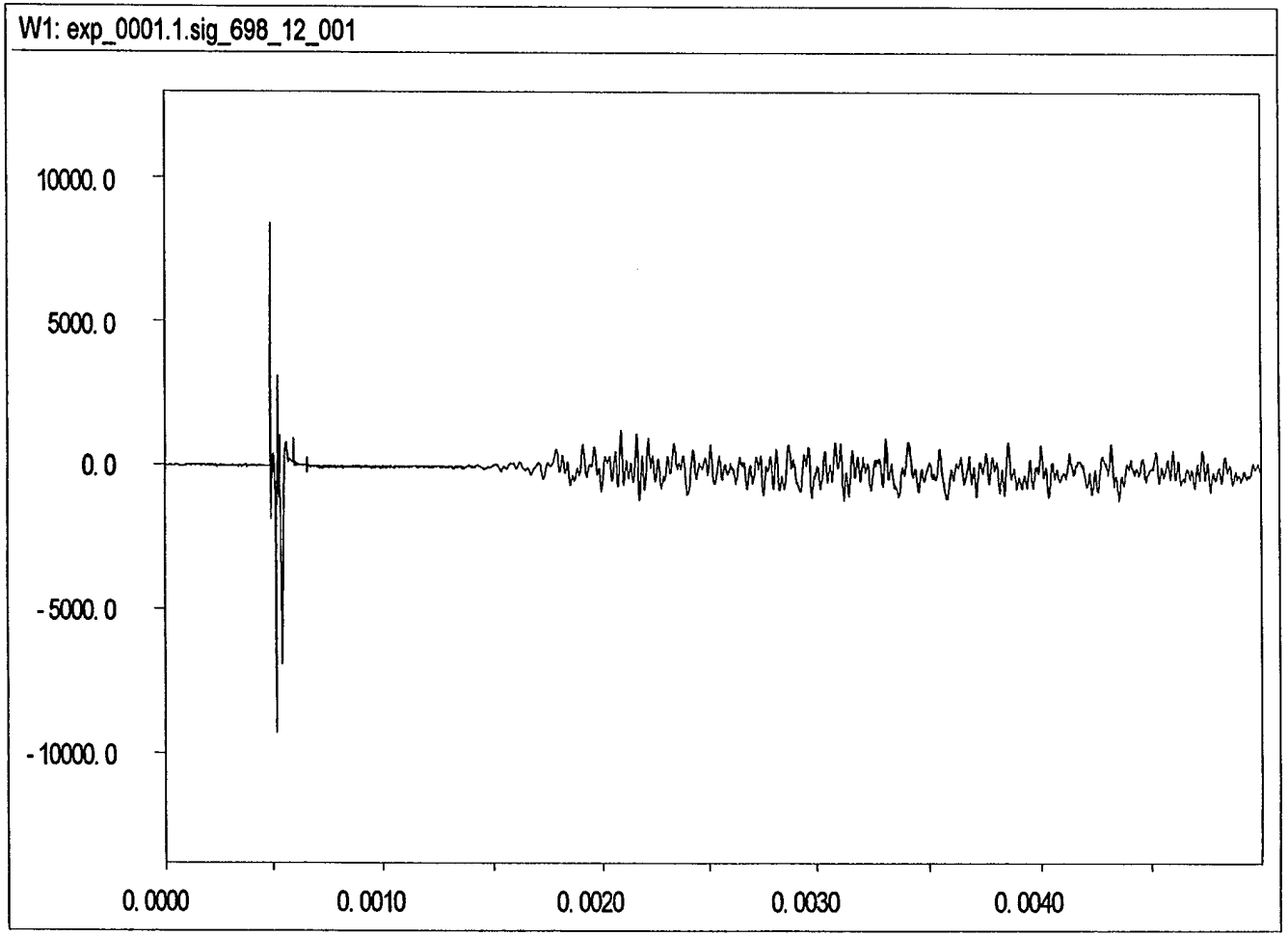


Figure A-24: Calibrated Output of Gauge #12, Shot #698.

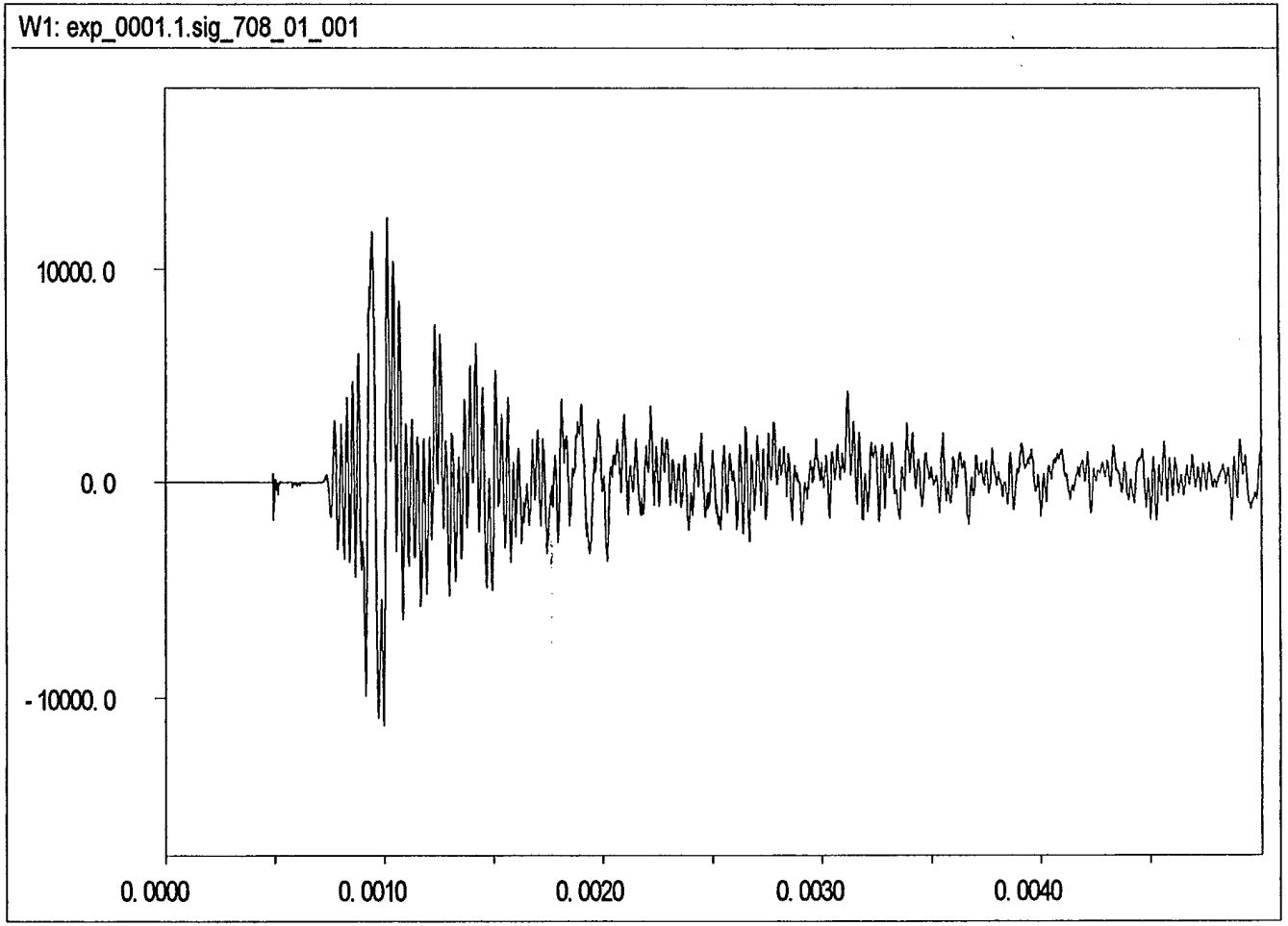


Figure A-25: Calibrated Output of Gauge #1, Shot #708.

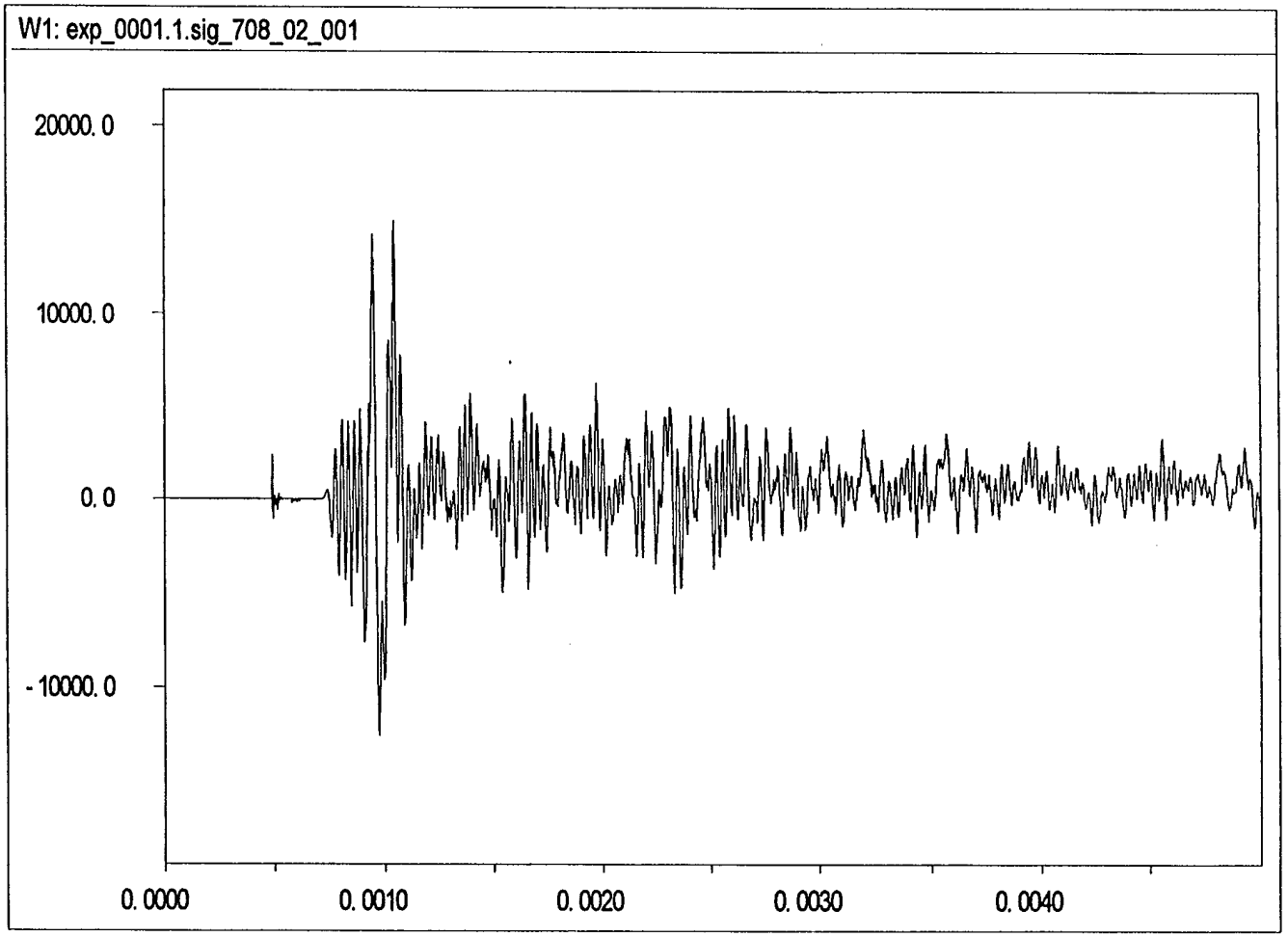


Figure A-26: Calibrated Output of Gauge #2, Shot #708.

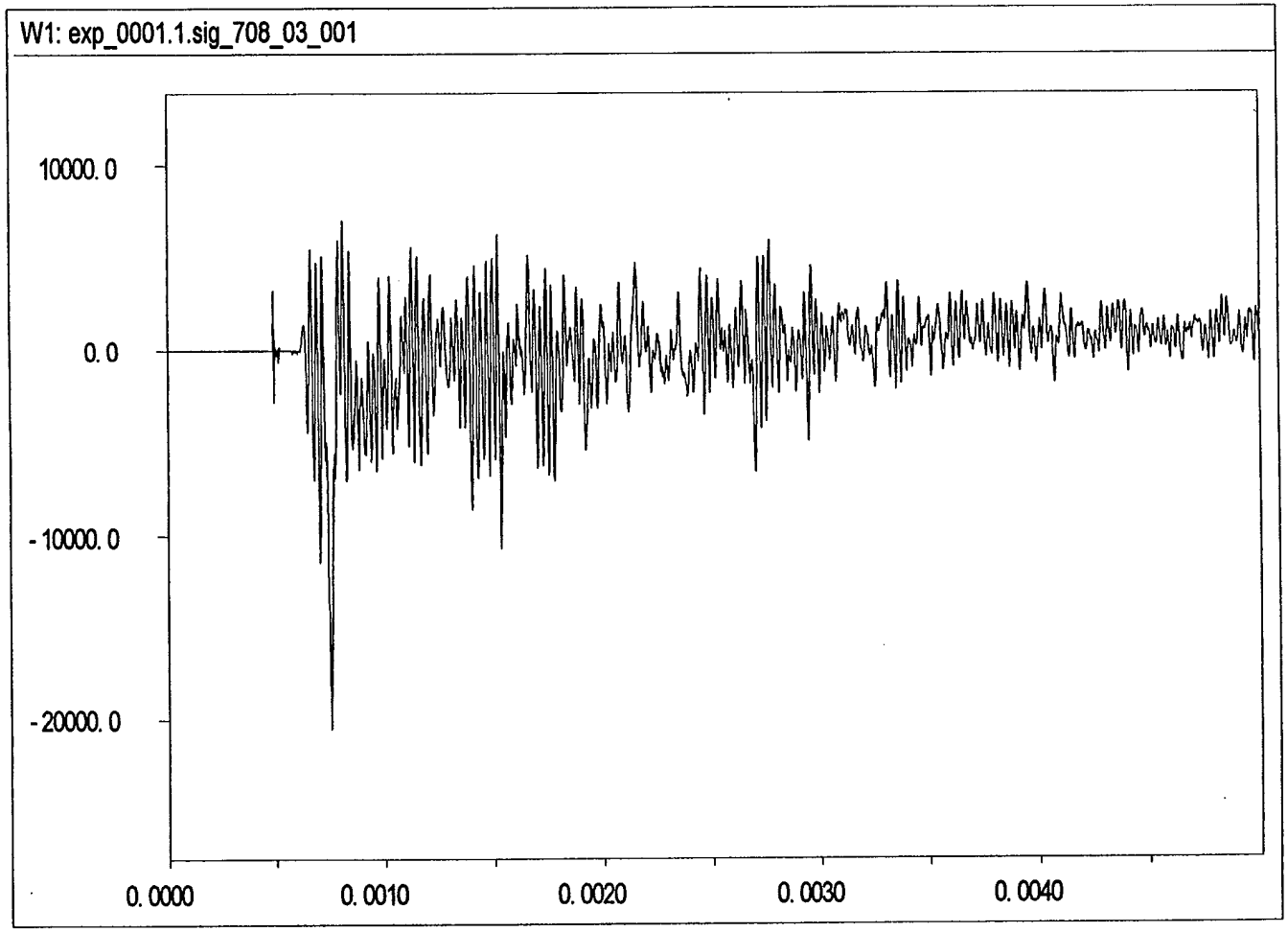


Figure A-27: Calibrated Output of Gauge #3, Shot #708.

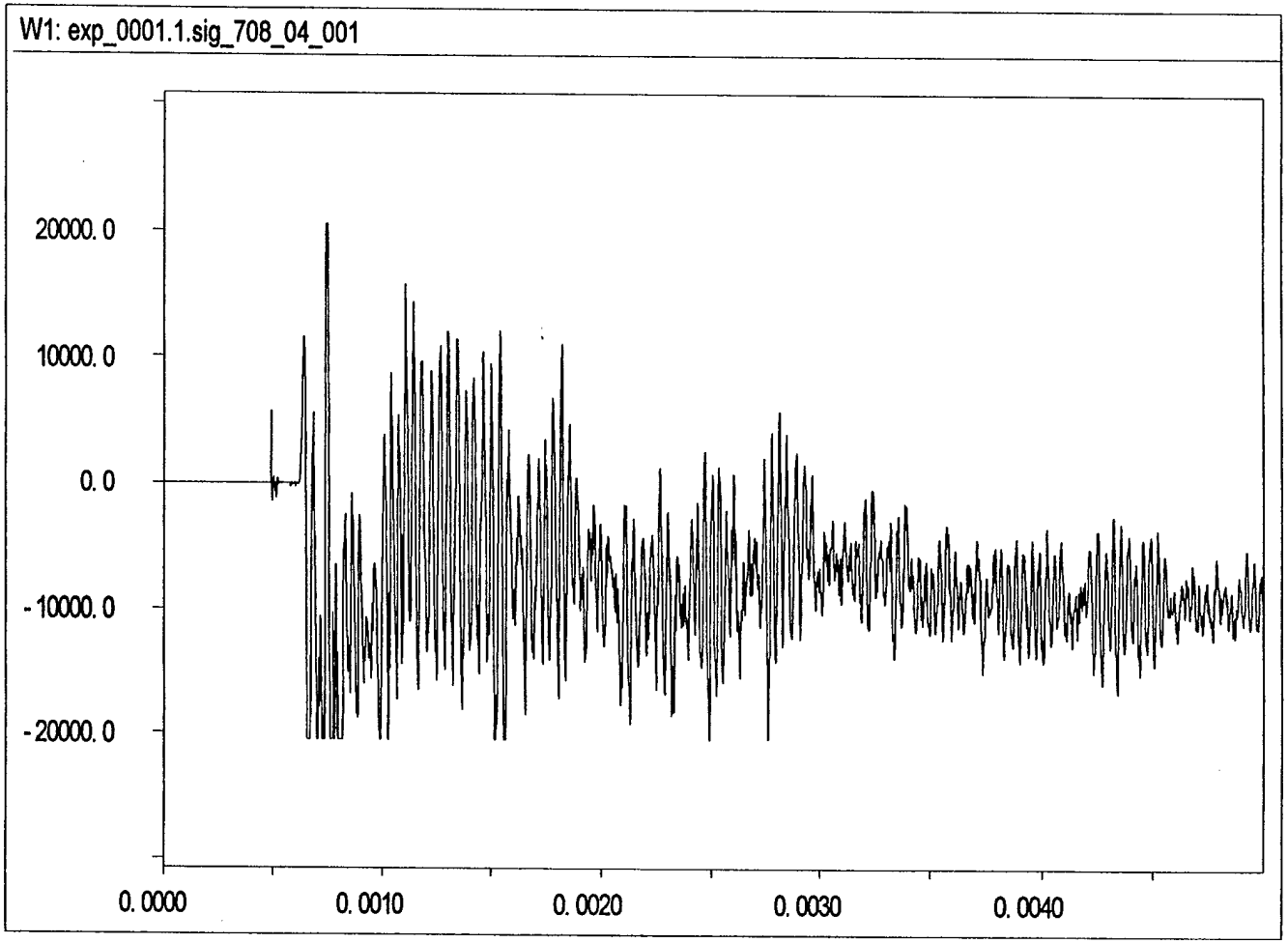


Figure A-28: Calibrated Output of Gauge #4, Shot #708.

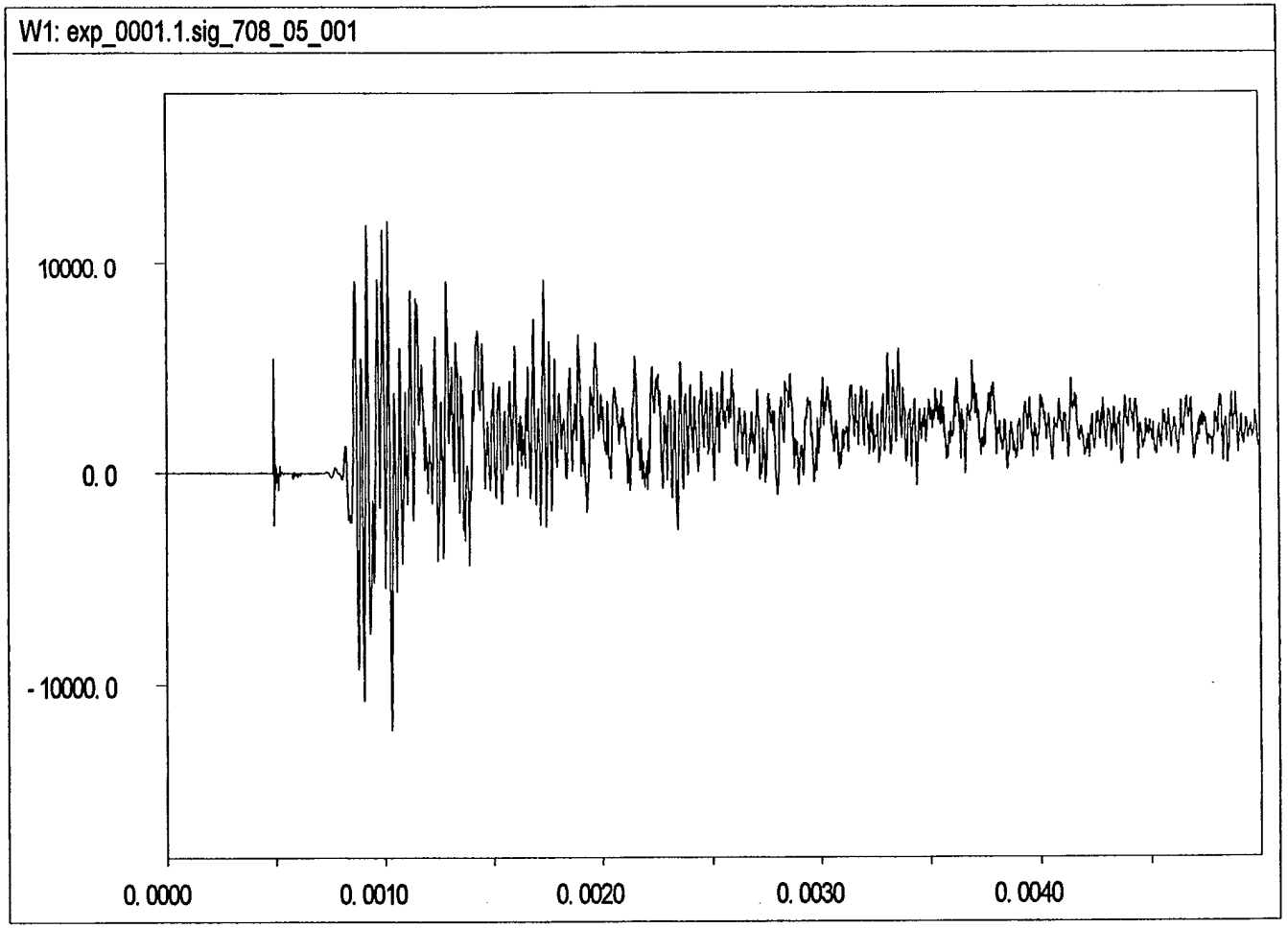


Figure A-29: Calibrated Output of Gauge #5, Shot #708.

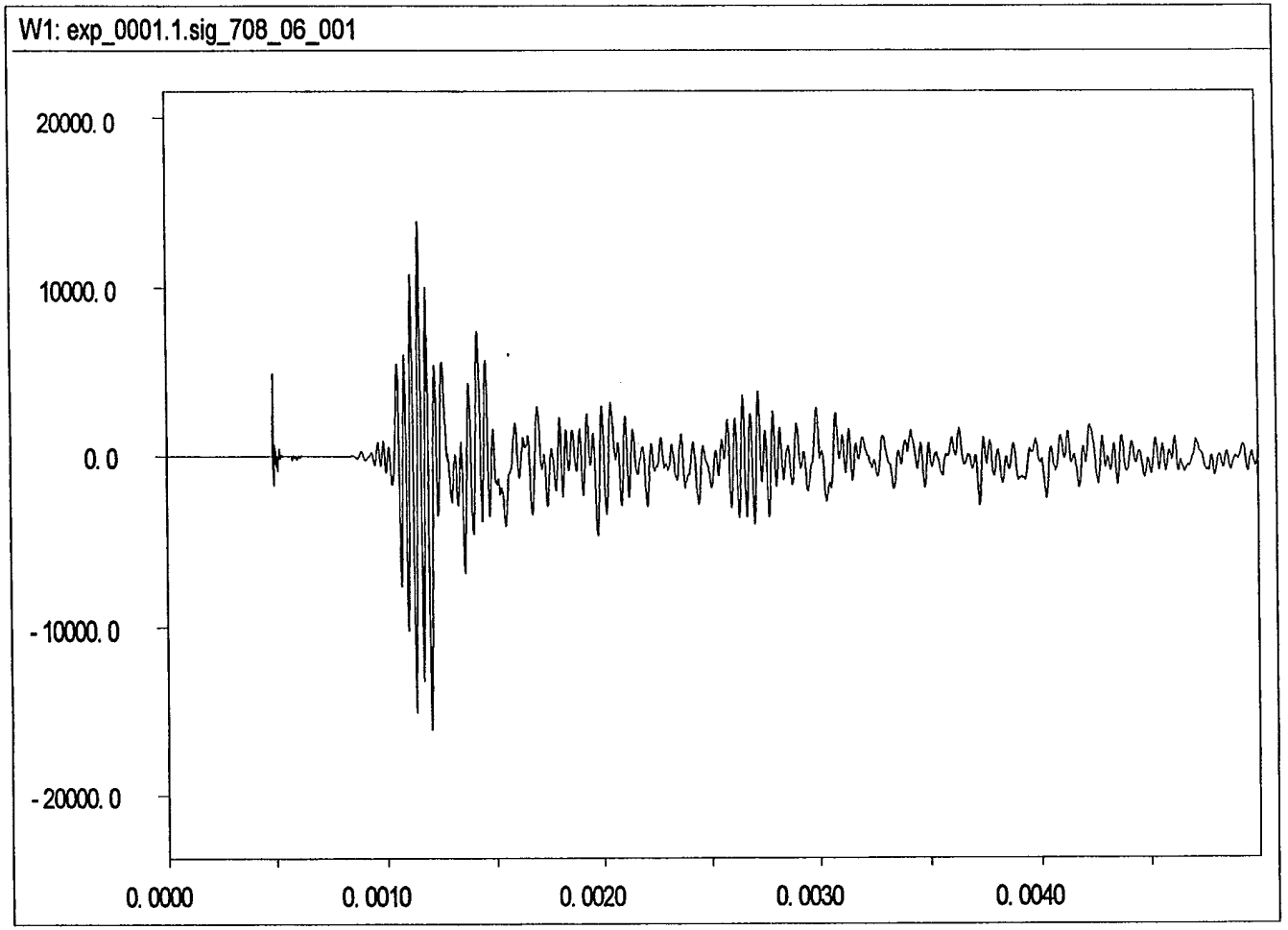


Figure A-30: Calibrated Output of Gauge #6, Shot #708.

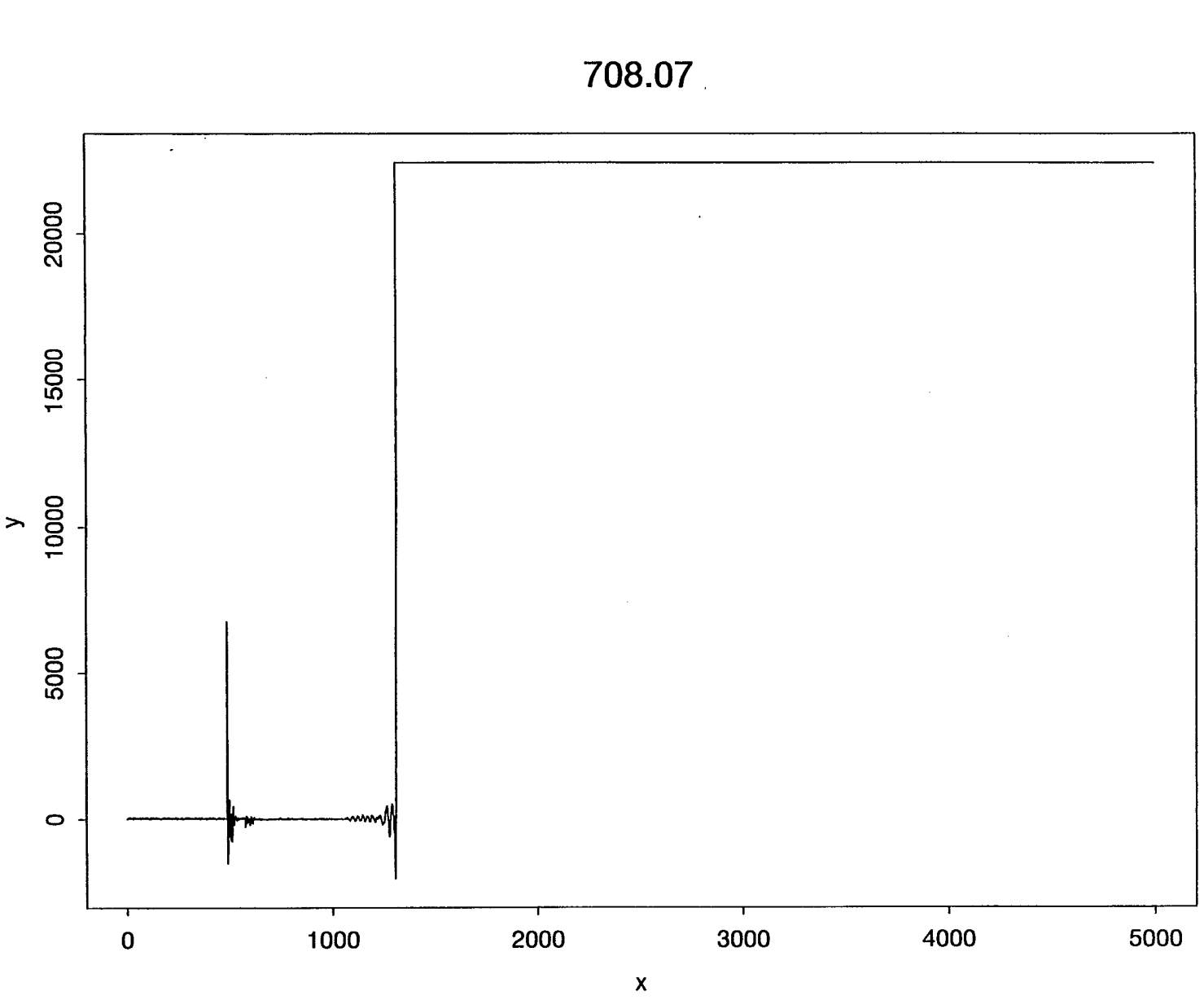


Figure A-31: Calibrated Output of Gauge #7, Shot #708.

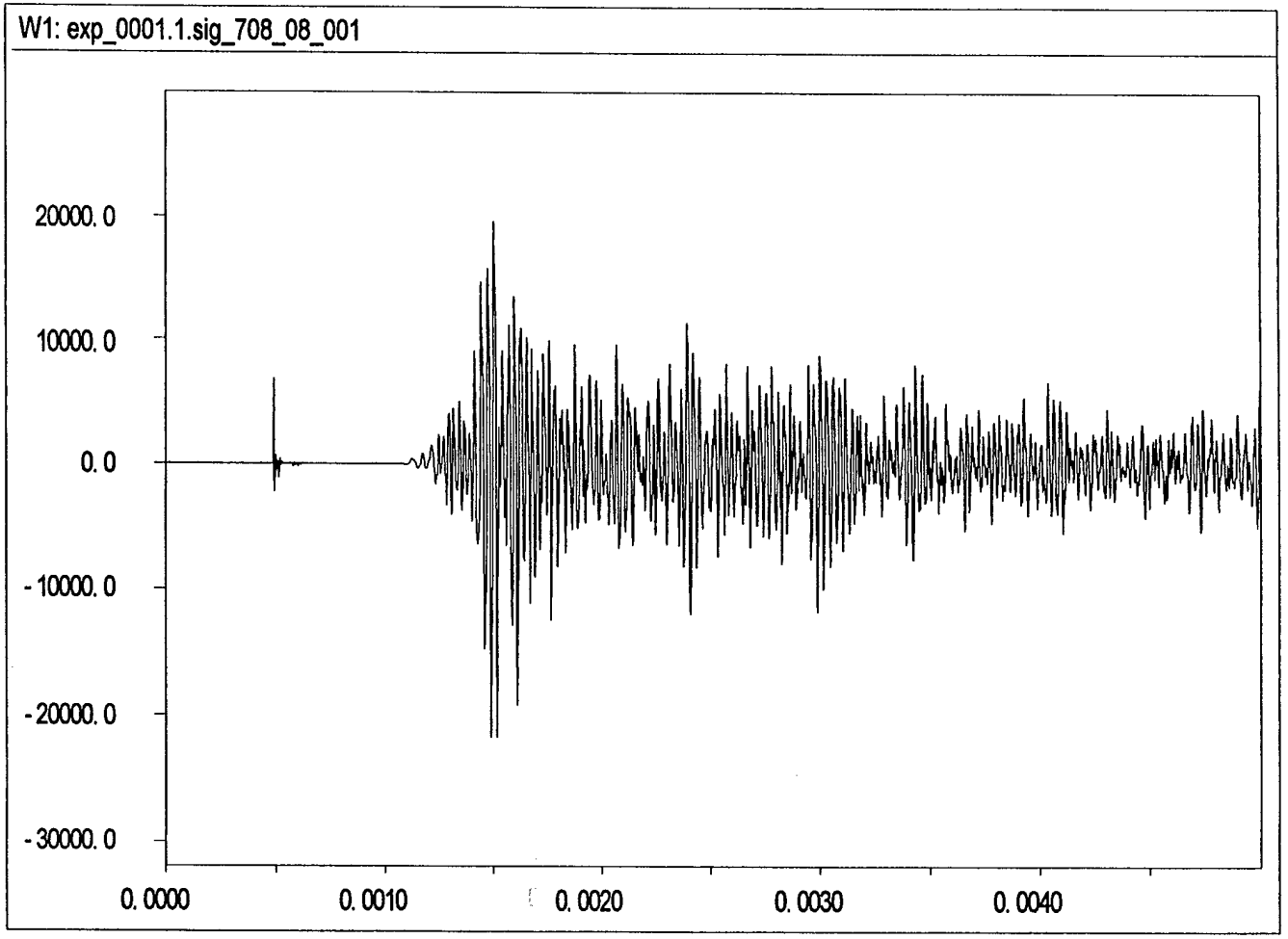


Figure A-32: Calibrated Output of Gauge #8, Shot #708.

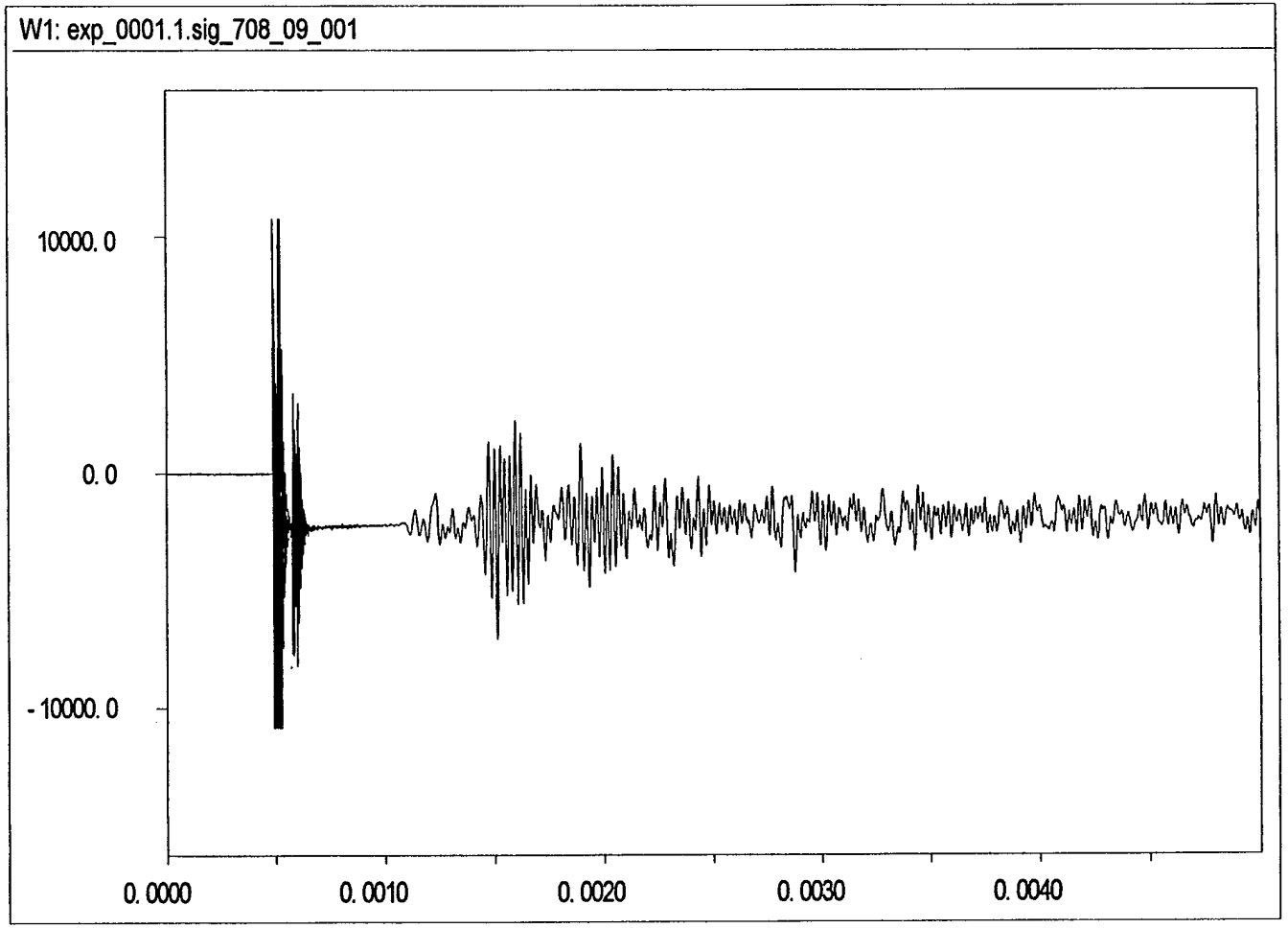


Figure A-33: Calibrated Output of Gauge #9, Shot #708.

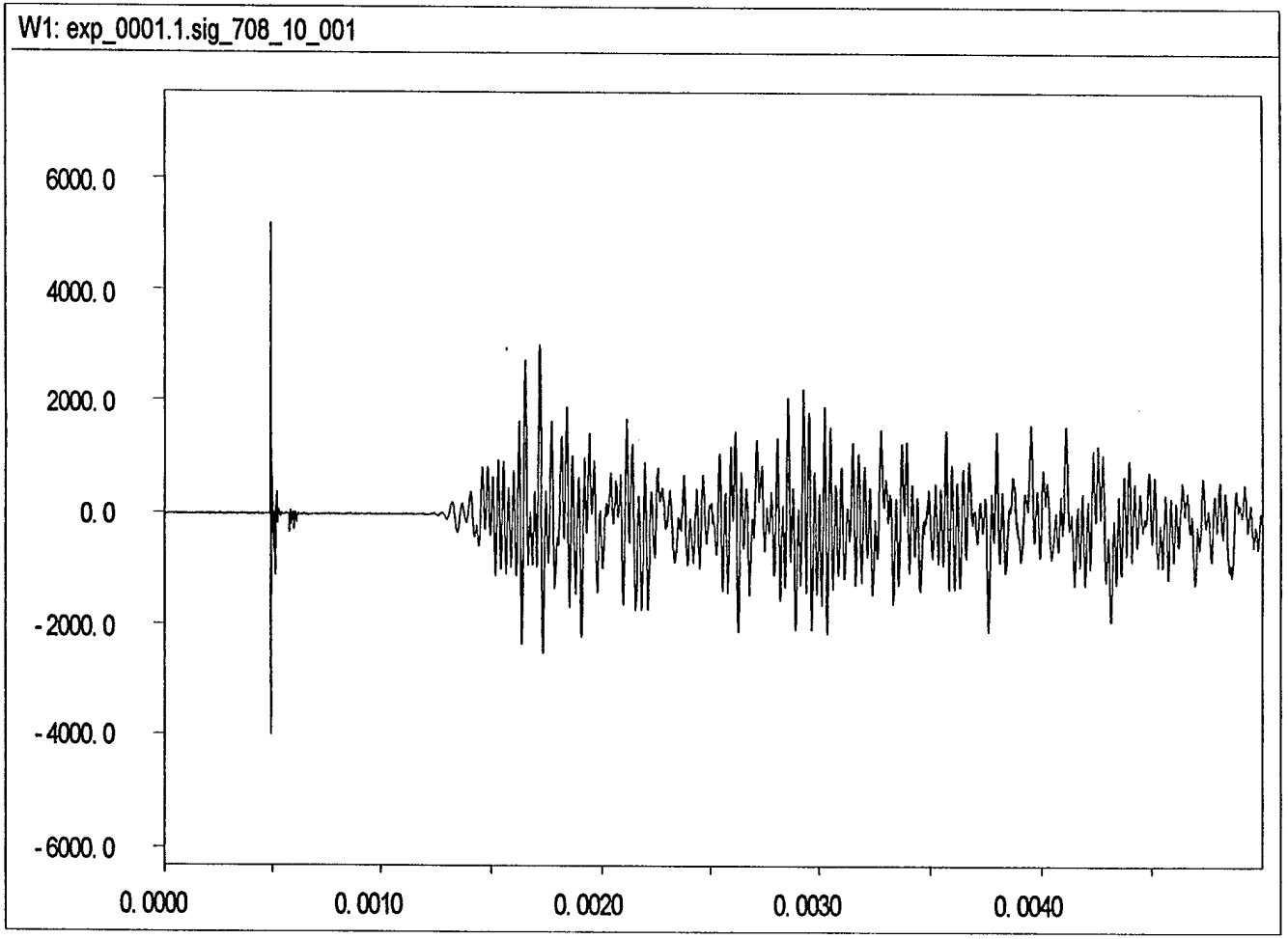


Figure A-34: Calibrated Output of Gauge #10, Shot #708.

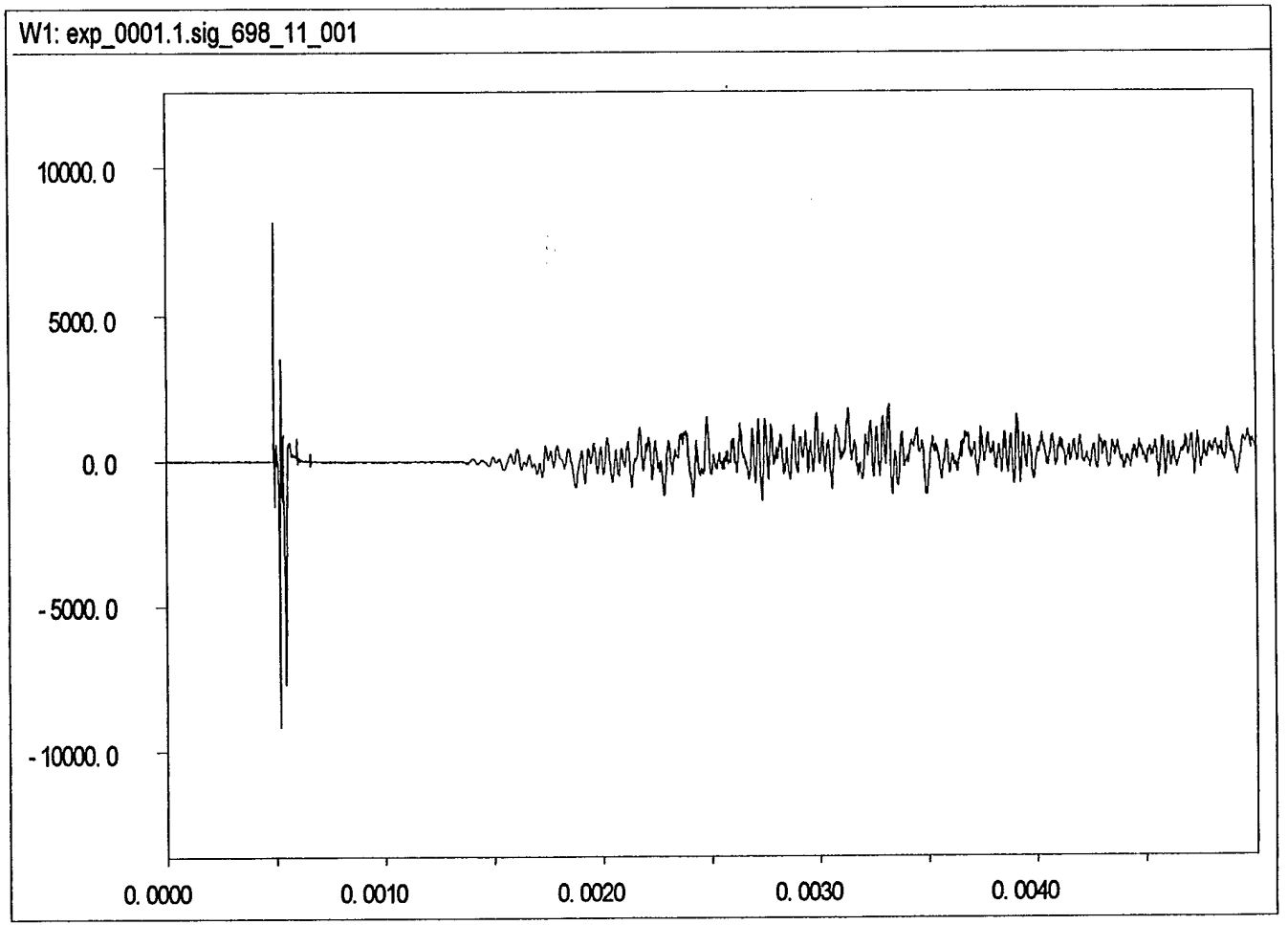


Figure A-35: Calibrated Output of Gauge #11, Shot #708.

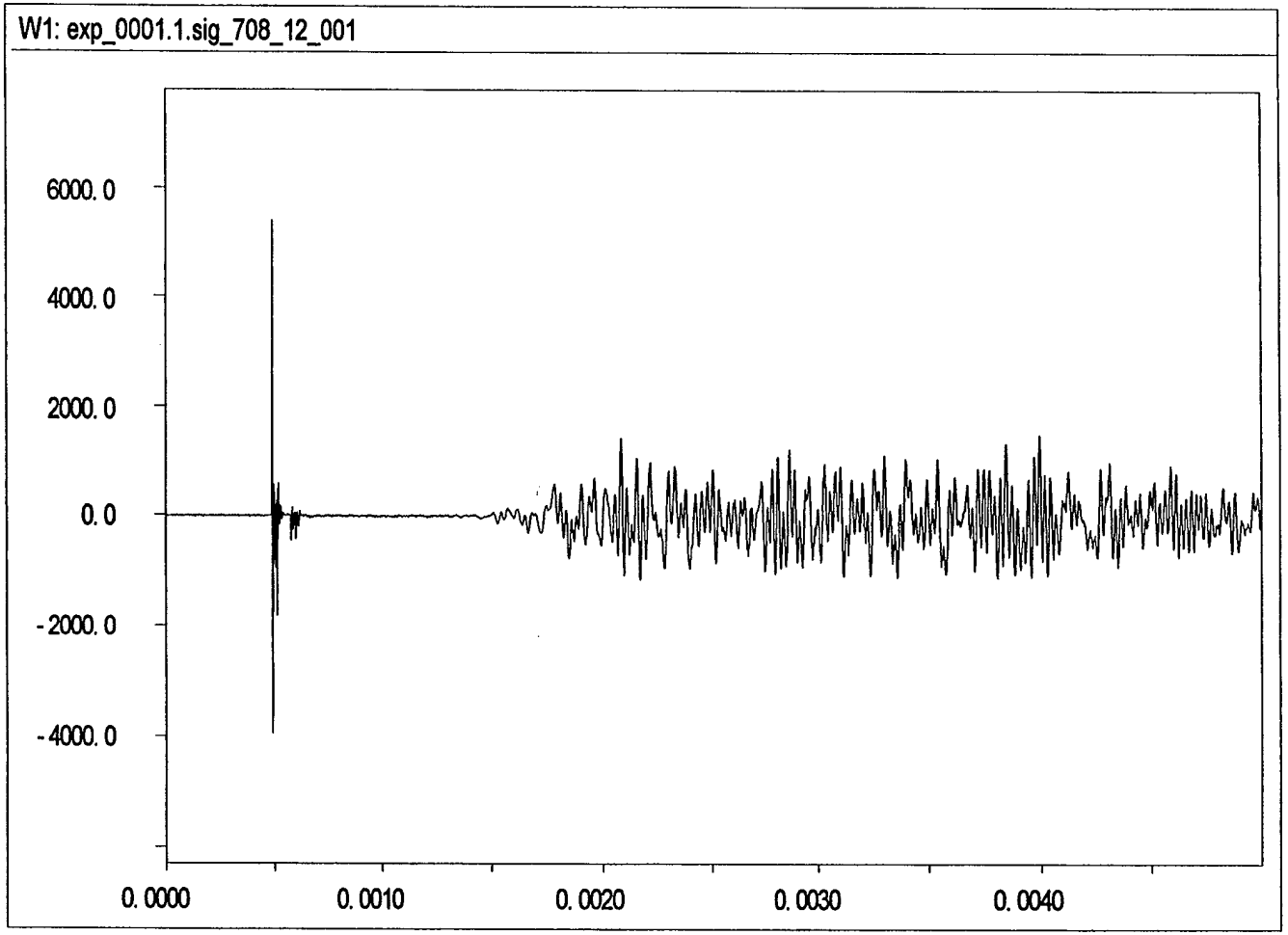


Figure A-36: Calibrated Output of Gauge #12, Shot #708.

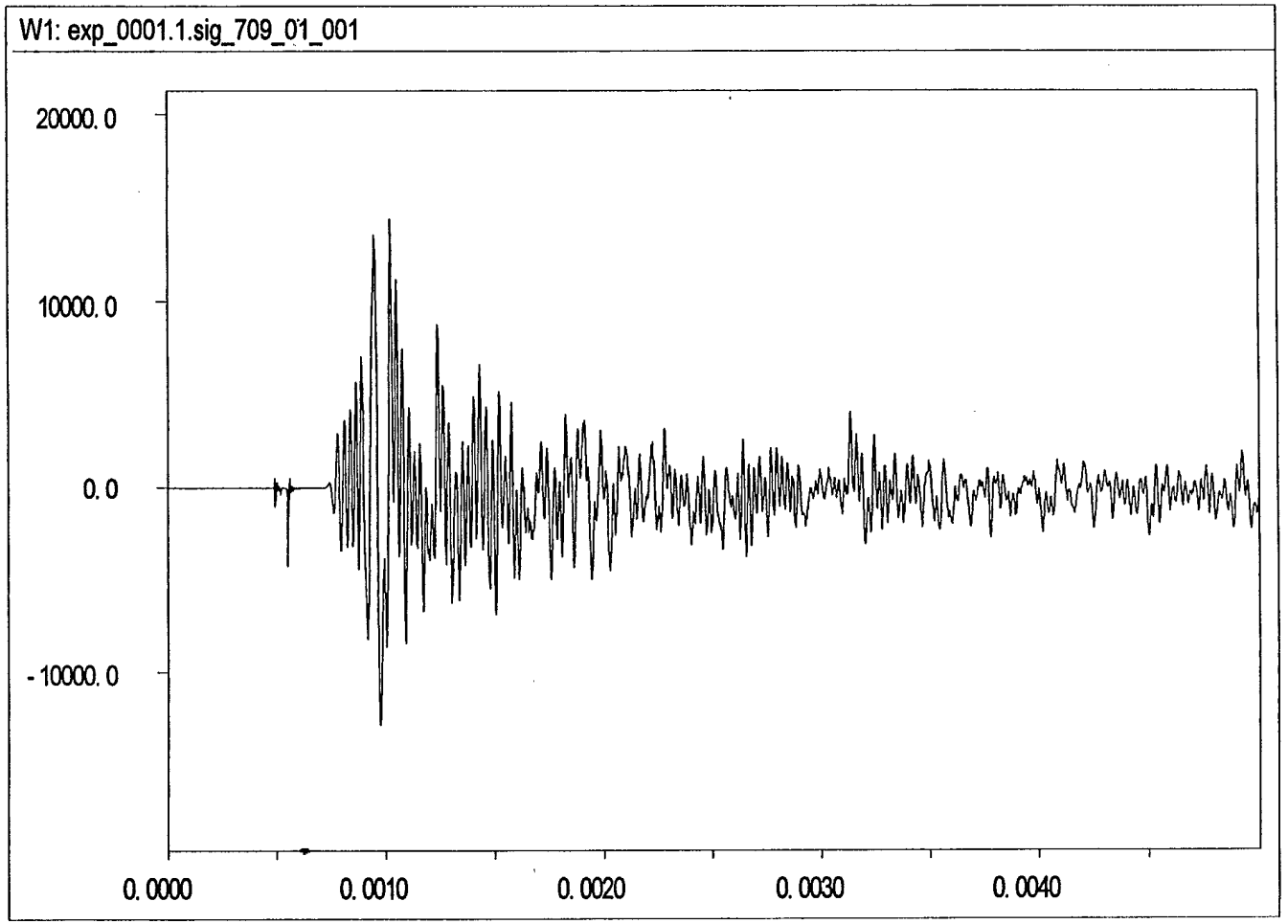


Figure A-37: Calibrated Output of Gauge #1, Shot #709.

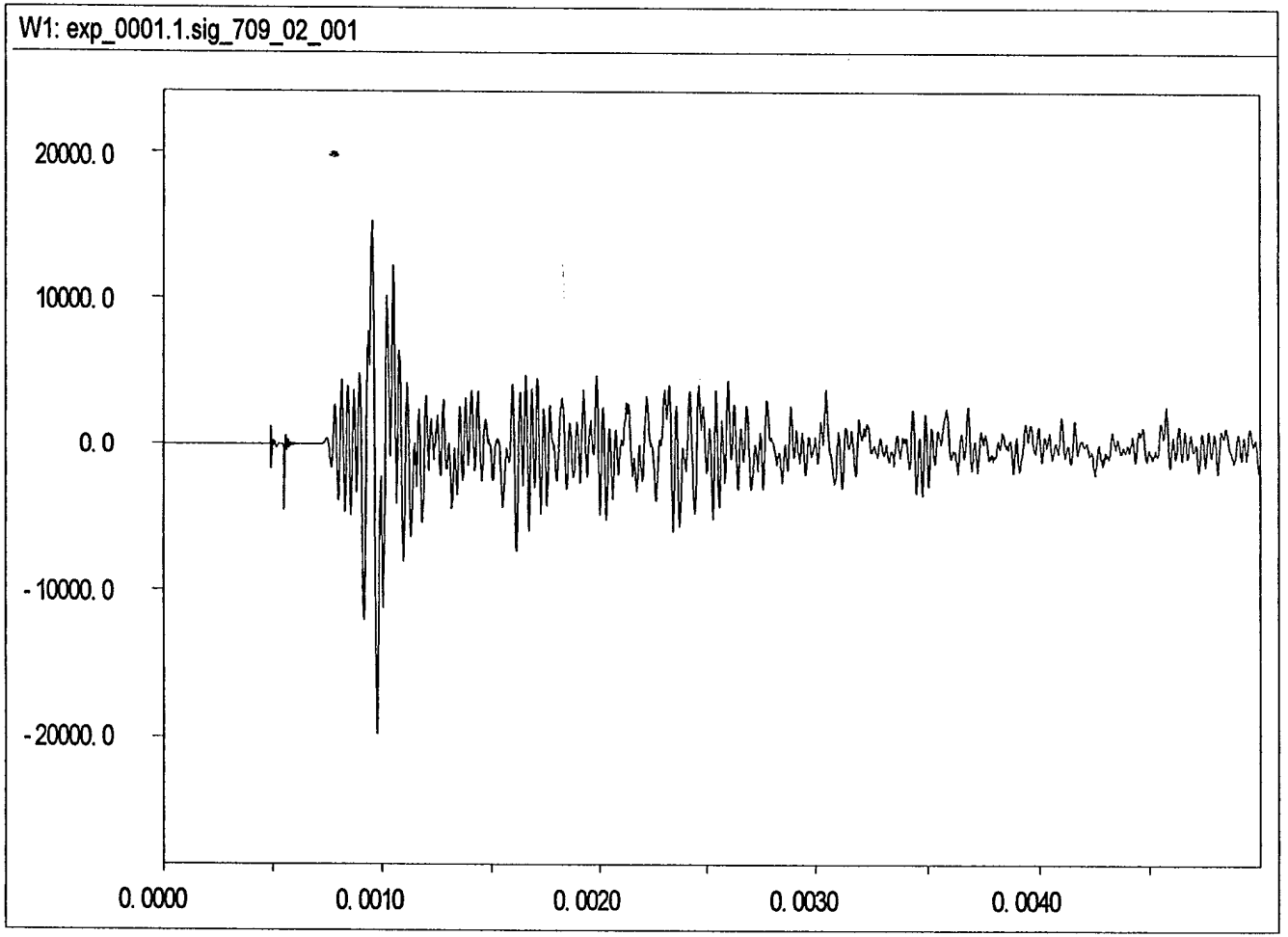


Figure A-38: Calibrated Output of Gauge #2, Shot #709.

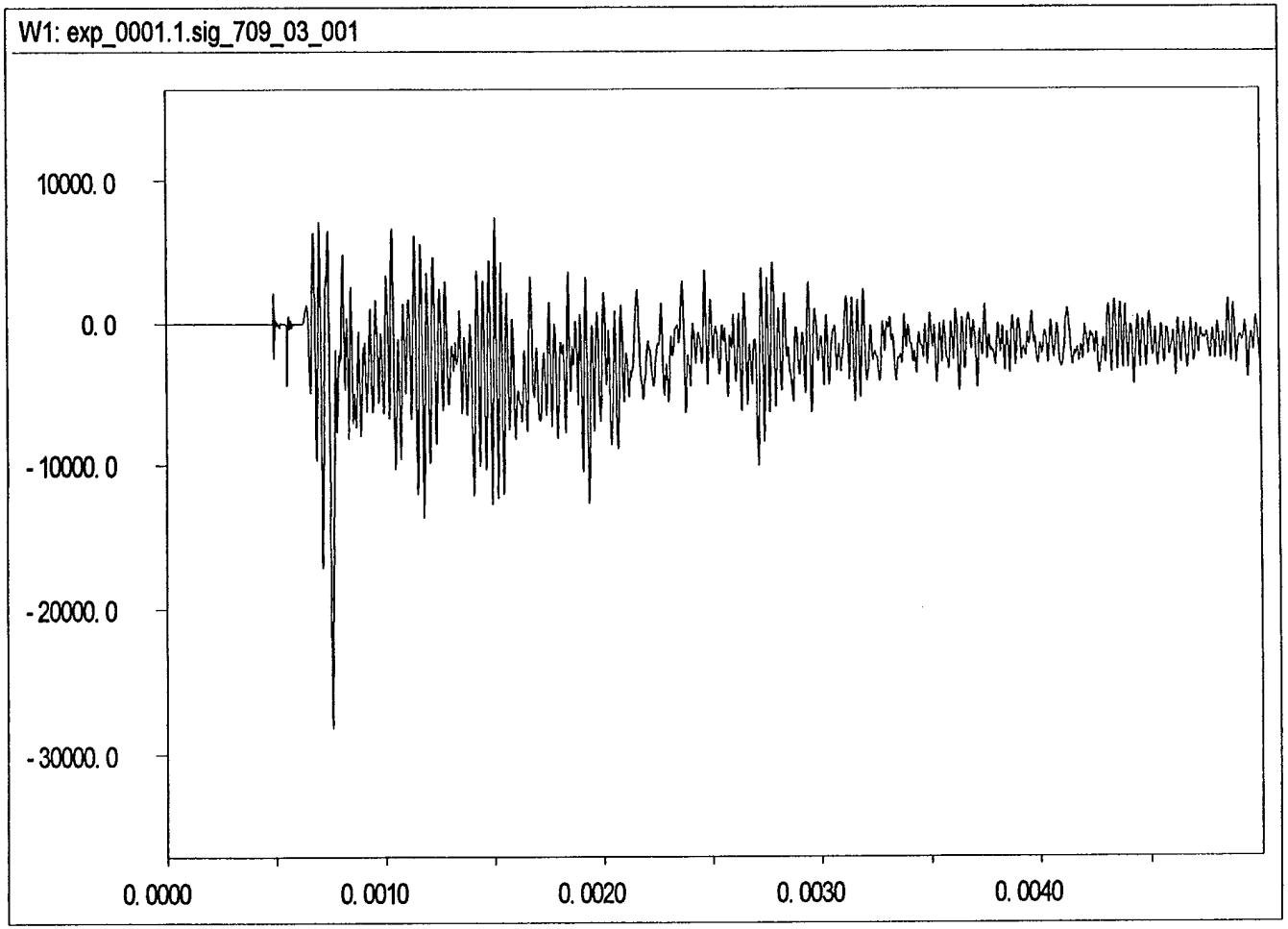


Figure A-39: Calibrated Output of Gauge #3, Shot #709.

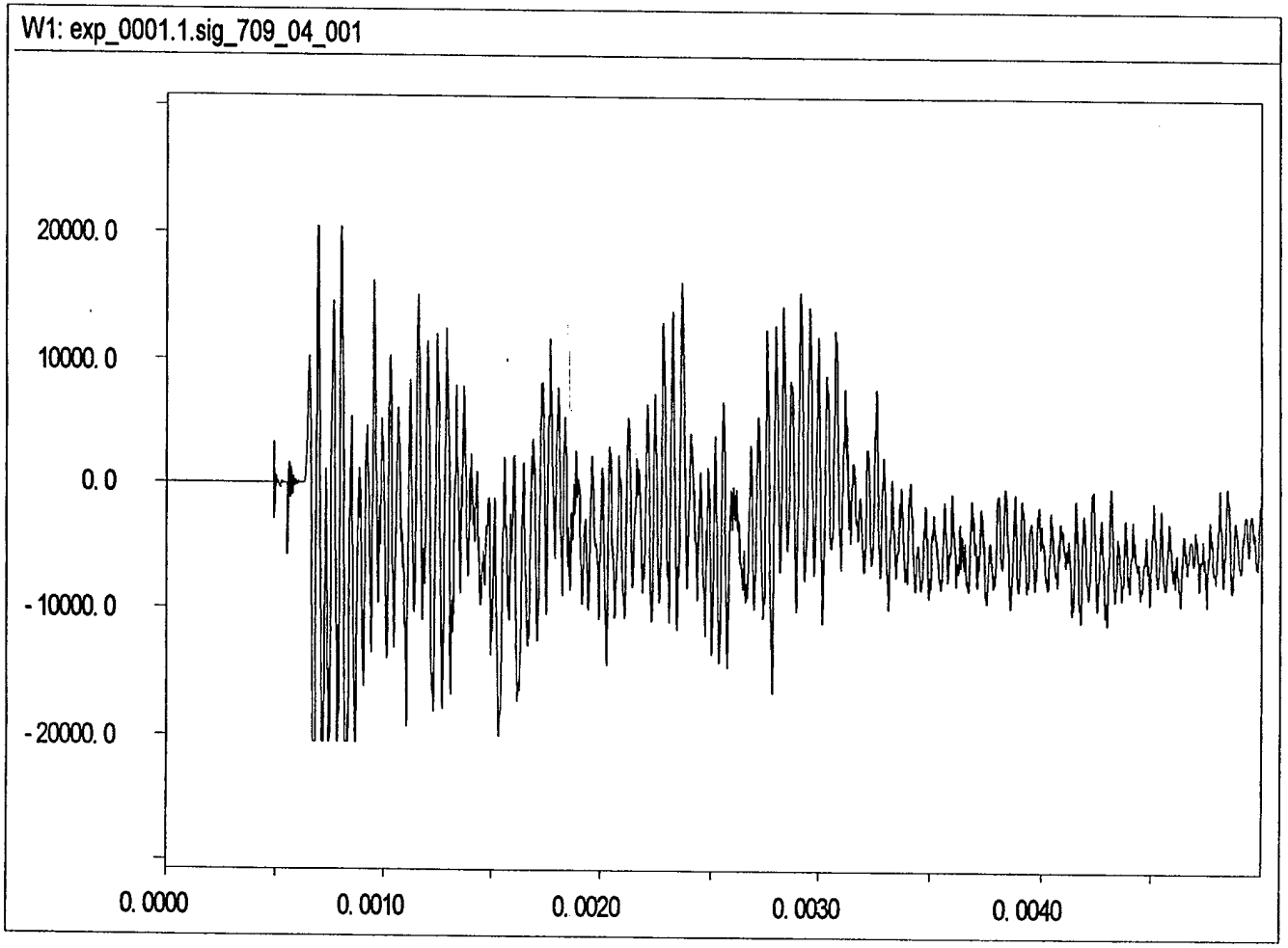


Figure A-40: Calibrated Output of Gauge #4, Shot #709.

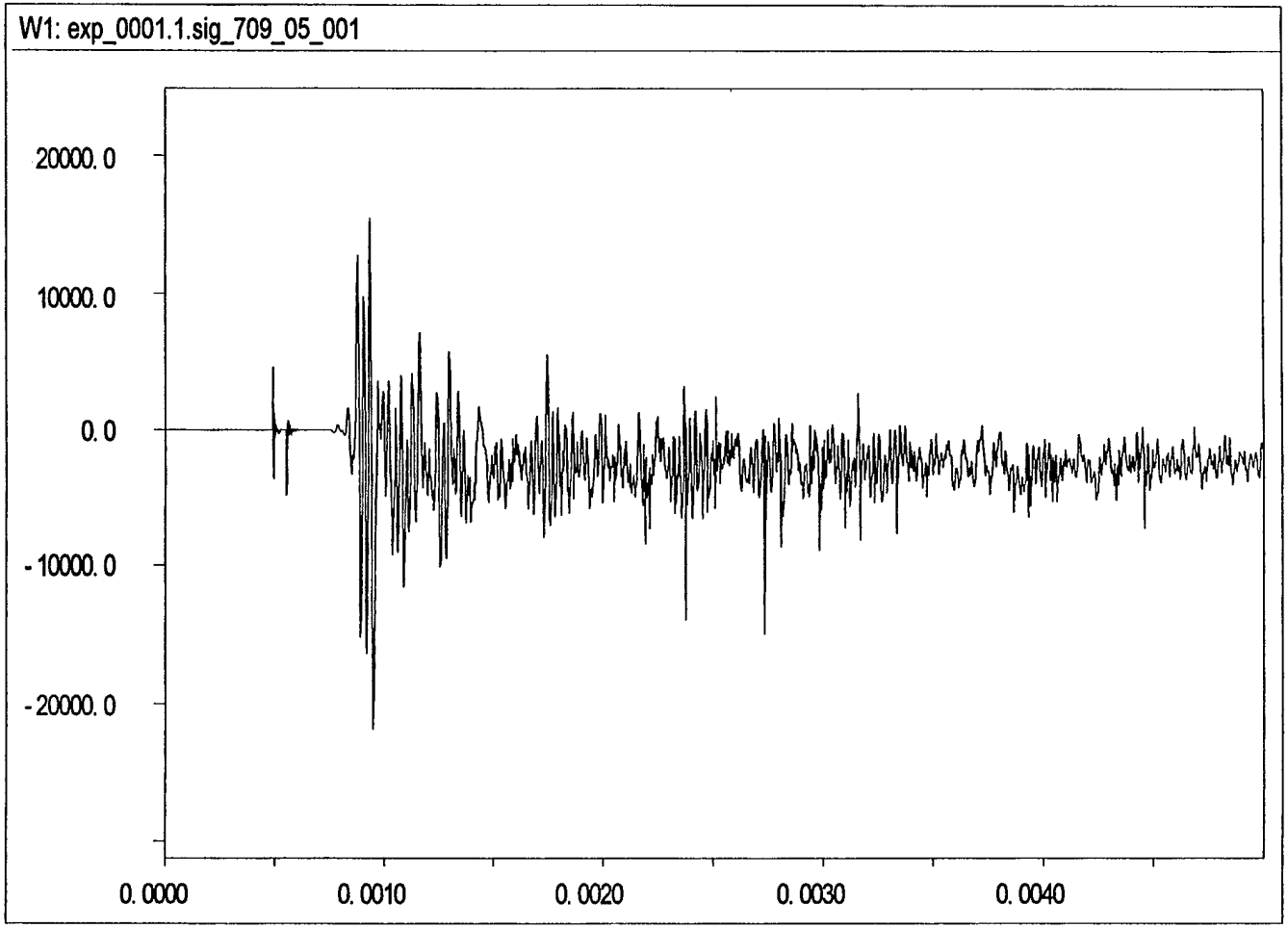


Figure A-41: Calibrated Output of Gauge #5, Shot #709.

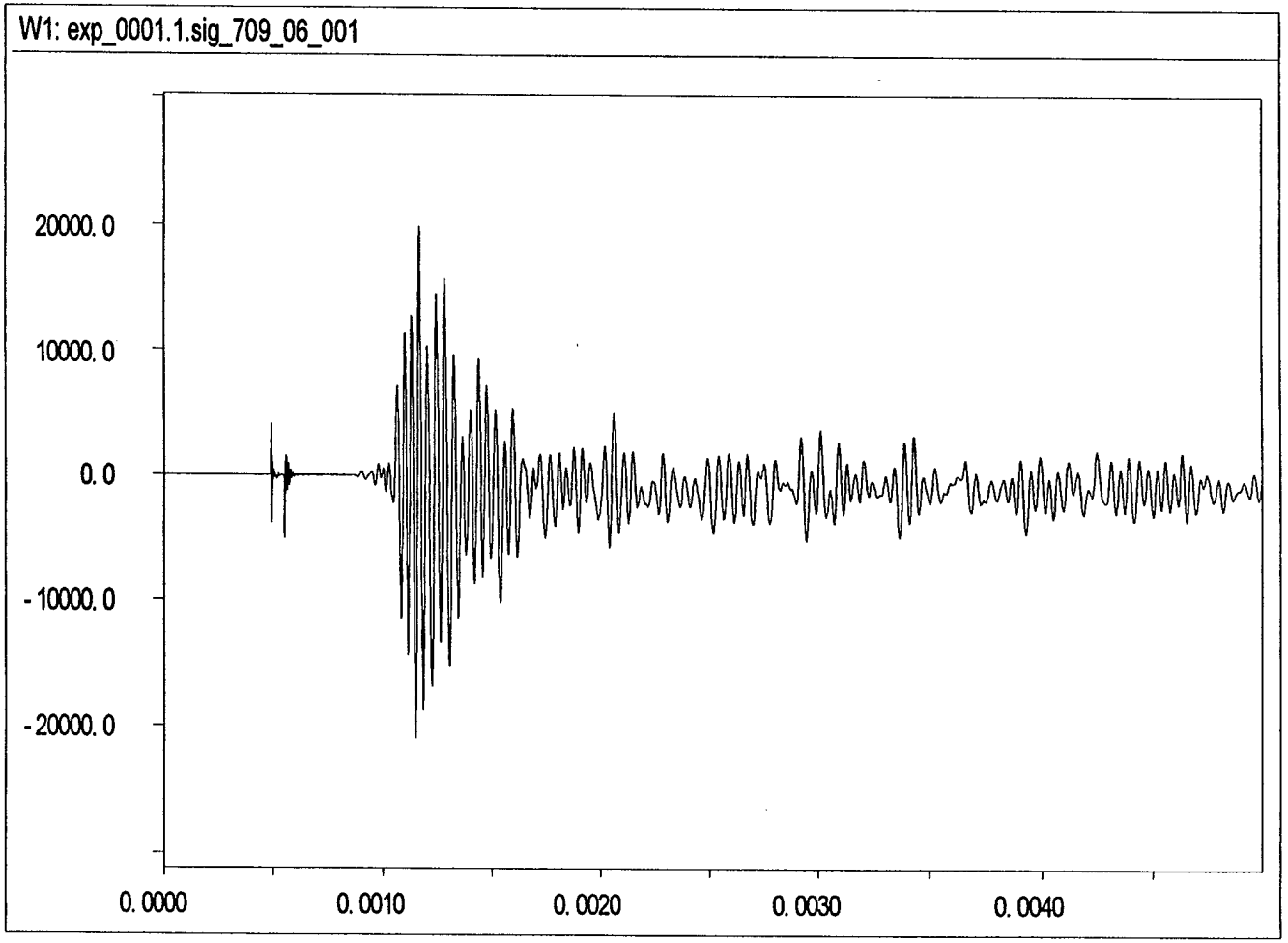


Figure A-42: Calibrated Output of Gauge #6, Shot #709.

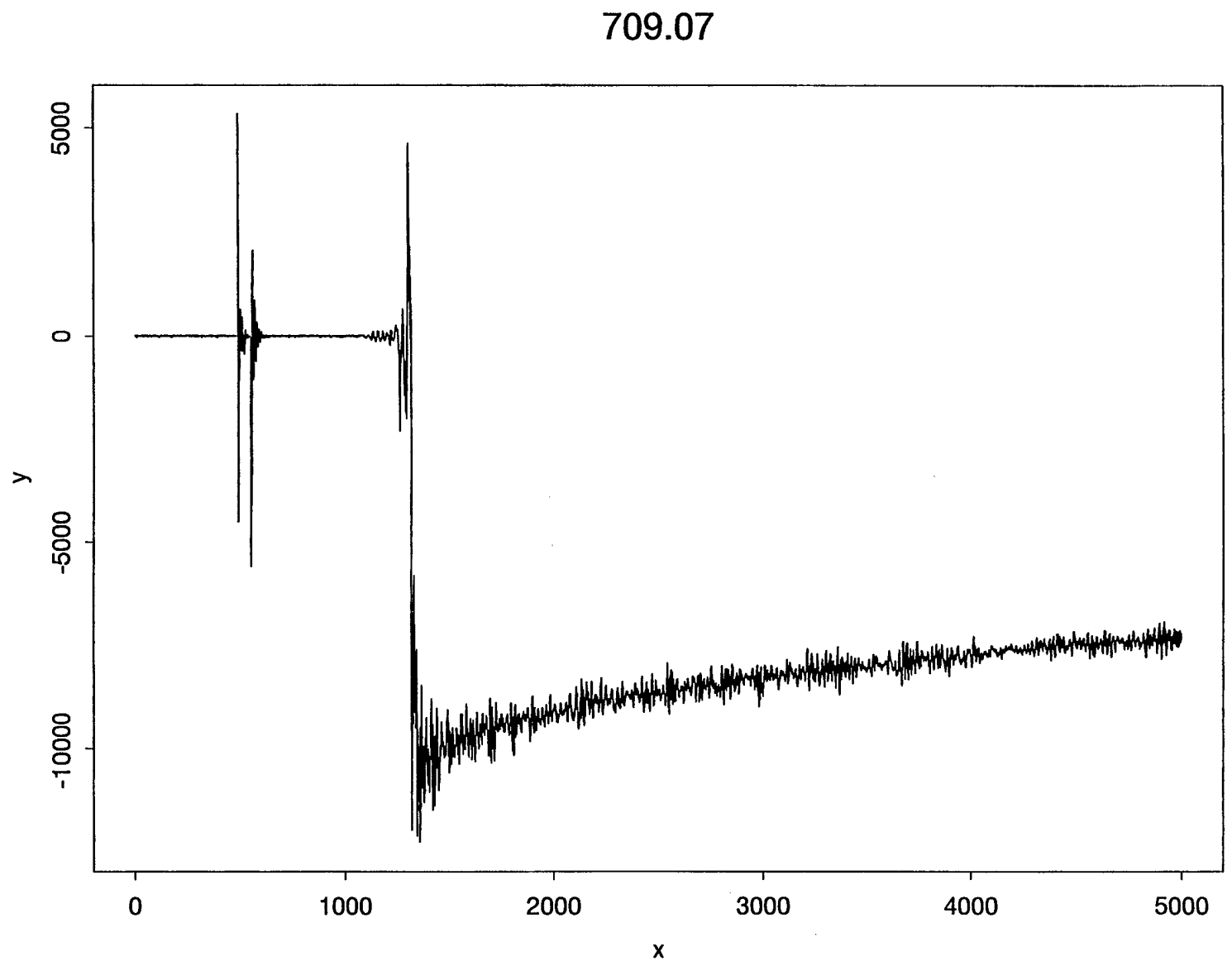


Figure A-43: Calibrated Output of Gauge #7, Shot #709.

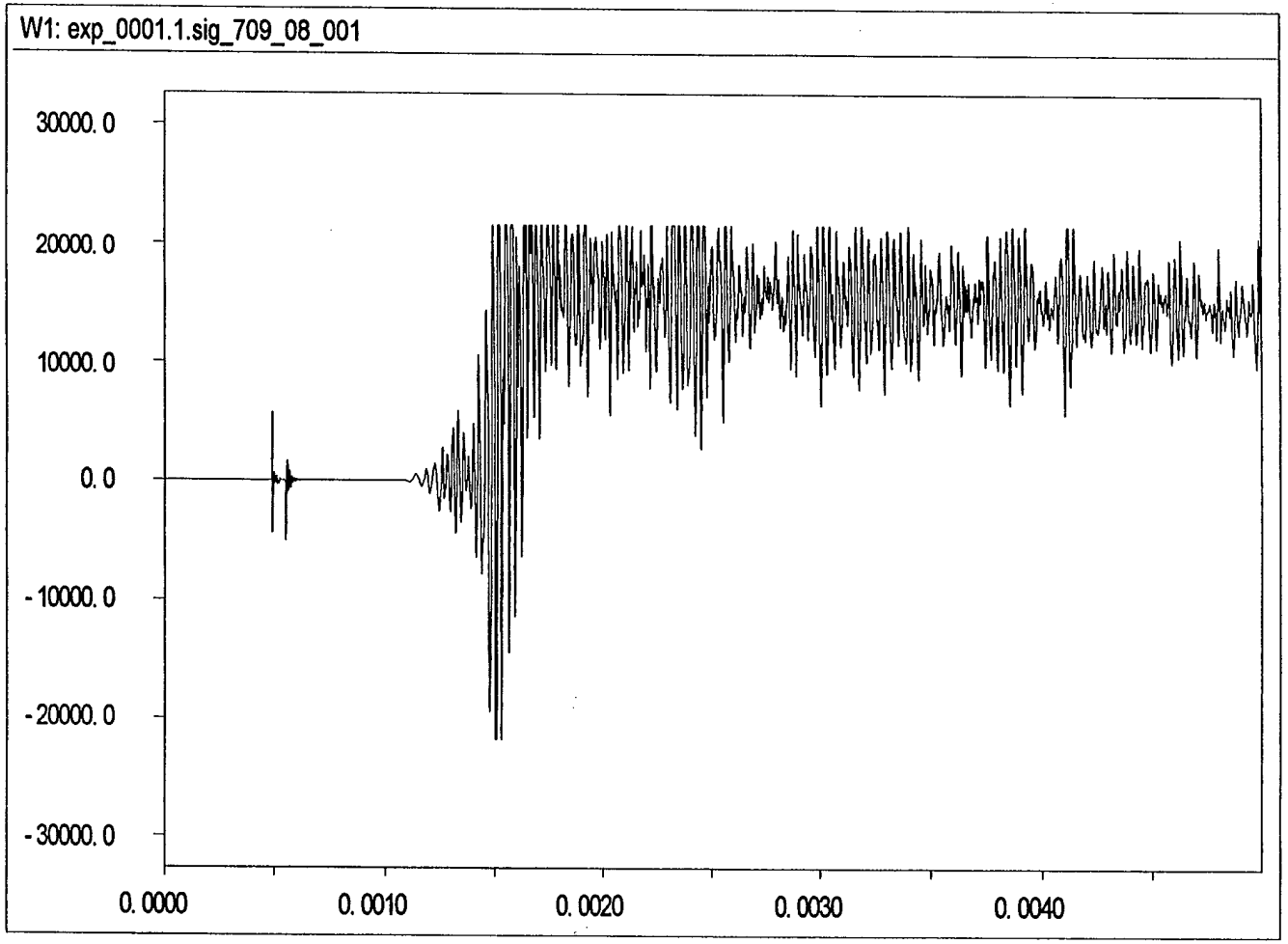


Figure A-44: Calibrated Output of Gauge #8, Shot #709.

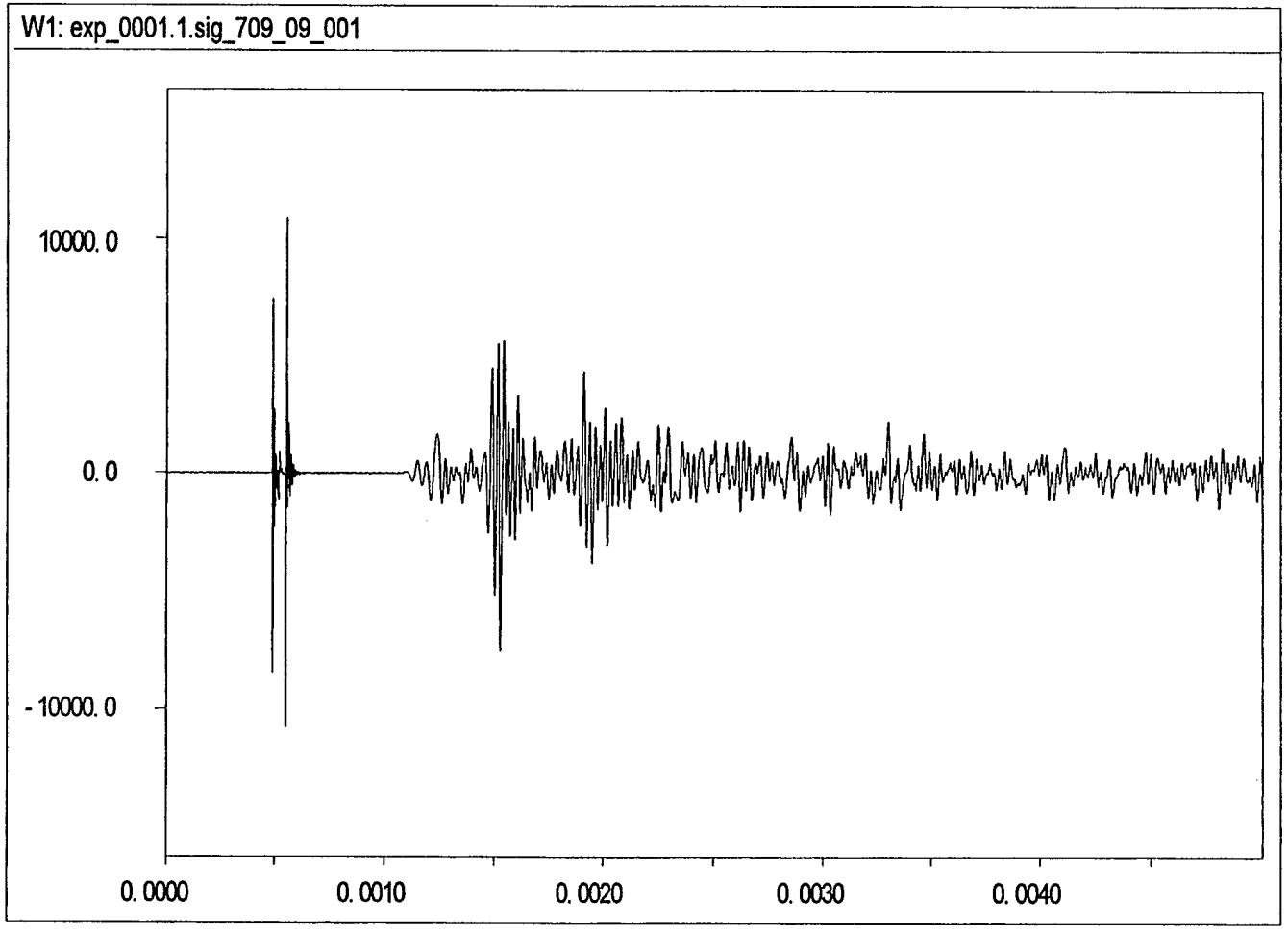


Figure A-45: Calibrated Output of Gauge #9, Shot #709.

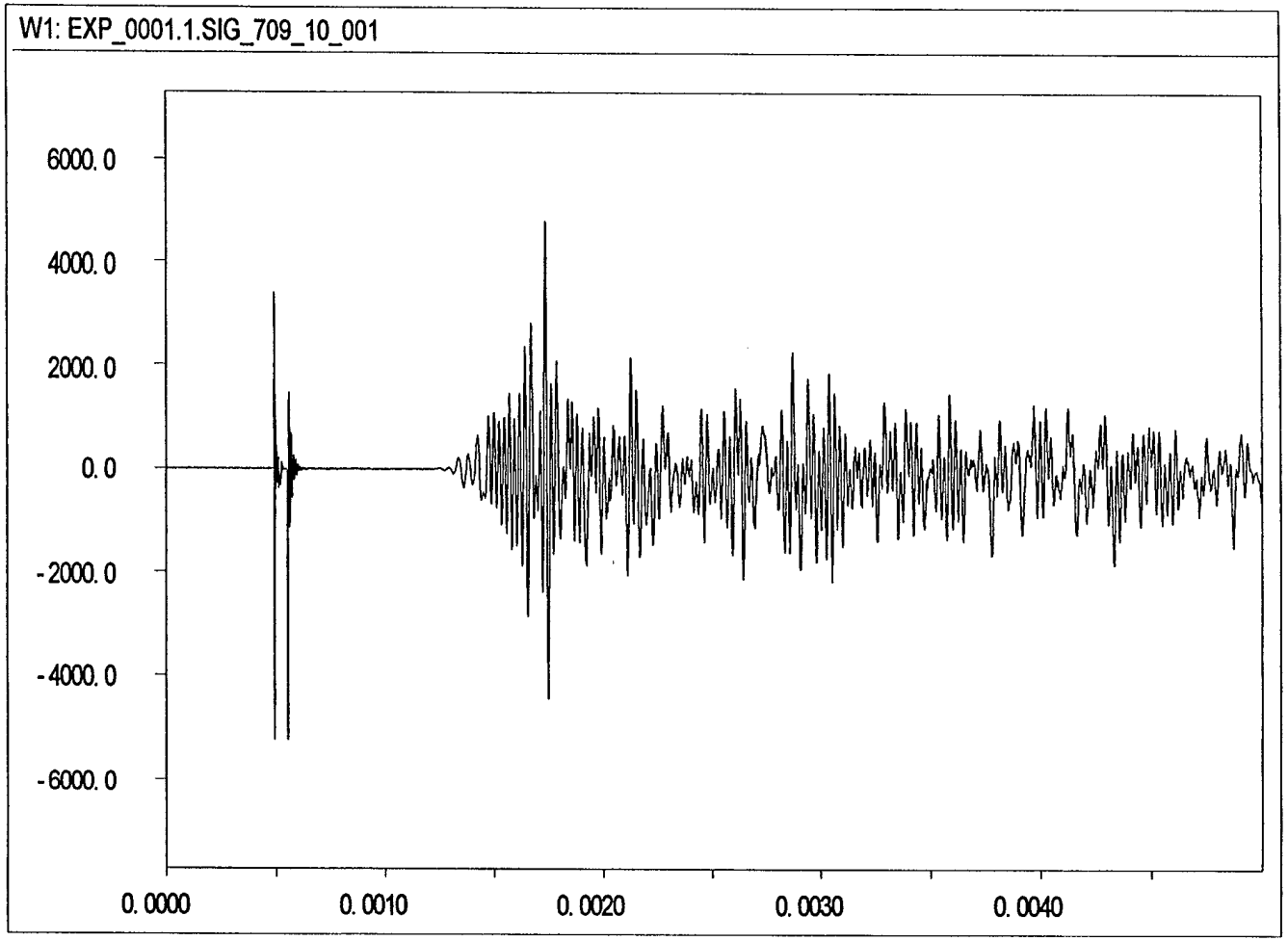


Figure A-46: Calibrated Output of Gauge #10, Shot #709.

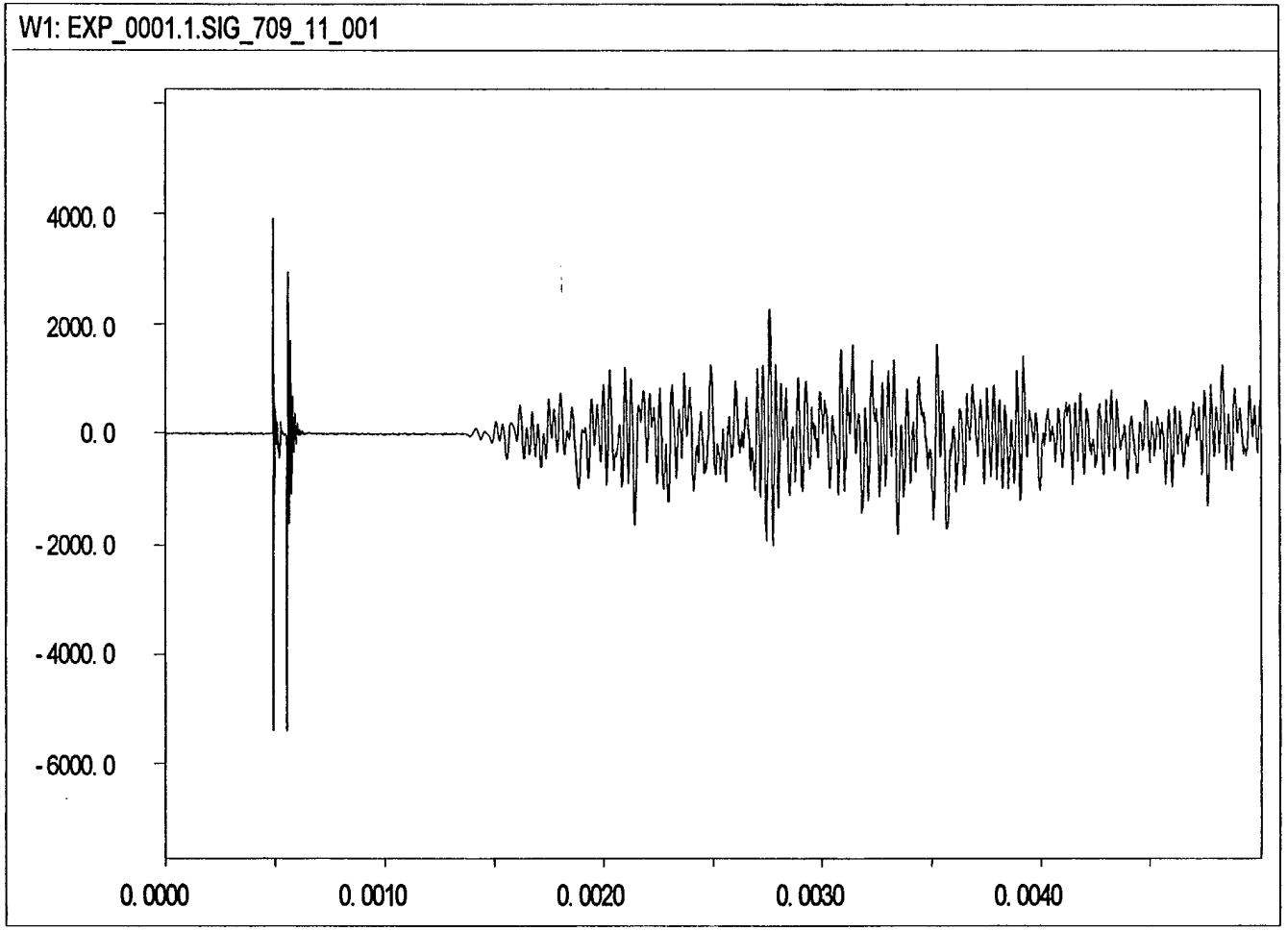


Figure A-47: Calibrated Output of Gauge #11, Shot #709.

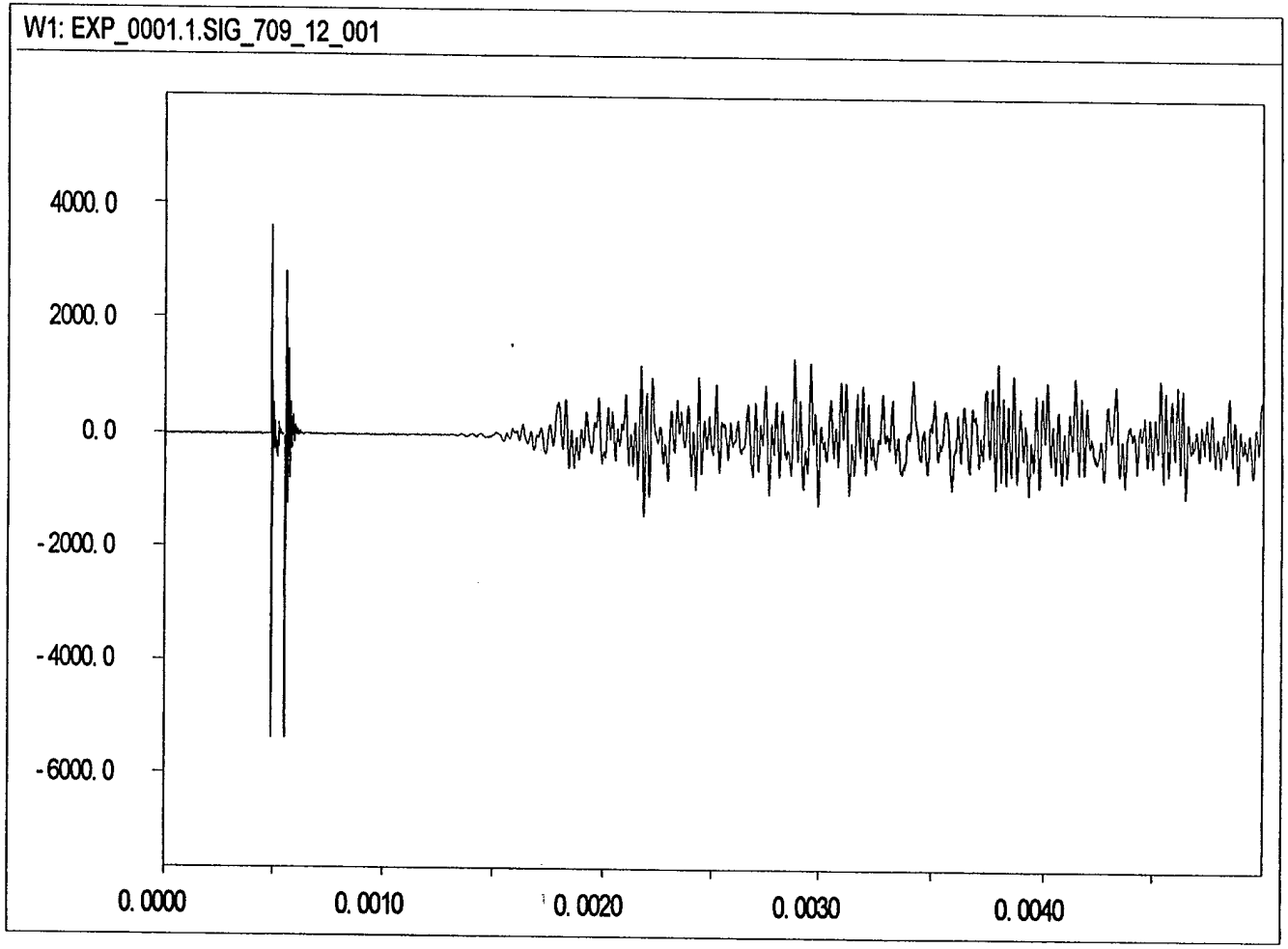


Figure A-48: Calibrated Output of Gauge #12, Shot #709.

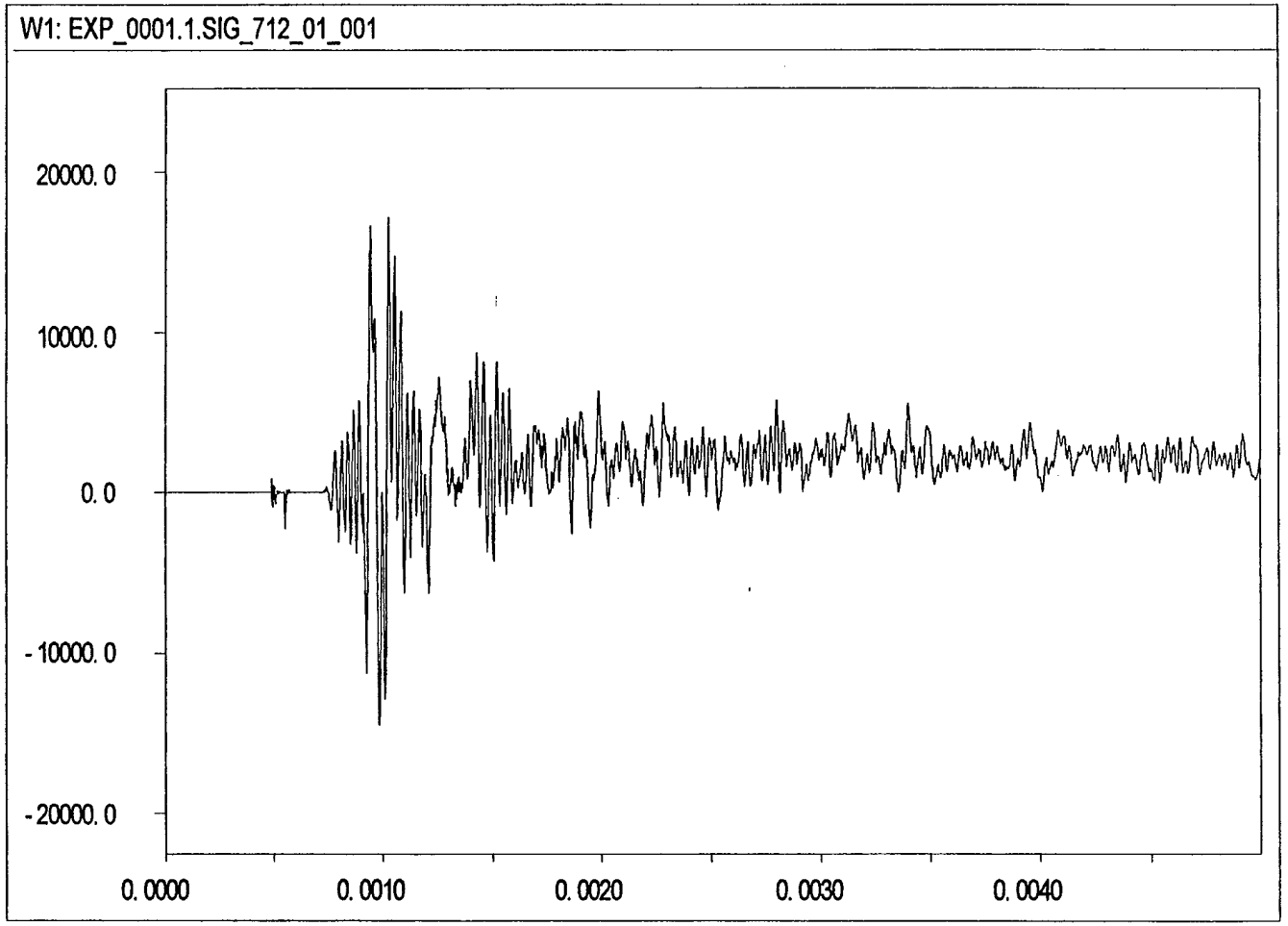


Figure A-49: Calibrated Output of Gauge #1, Shot #712.

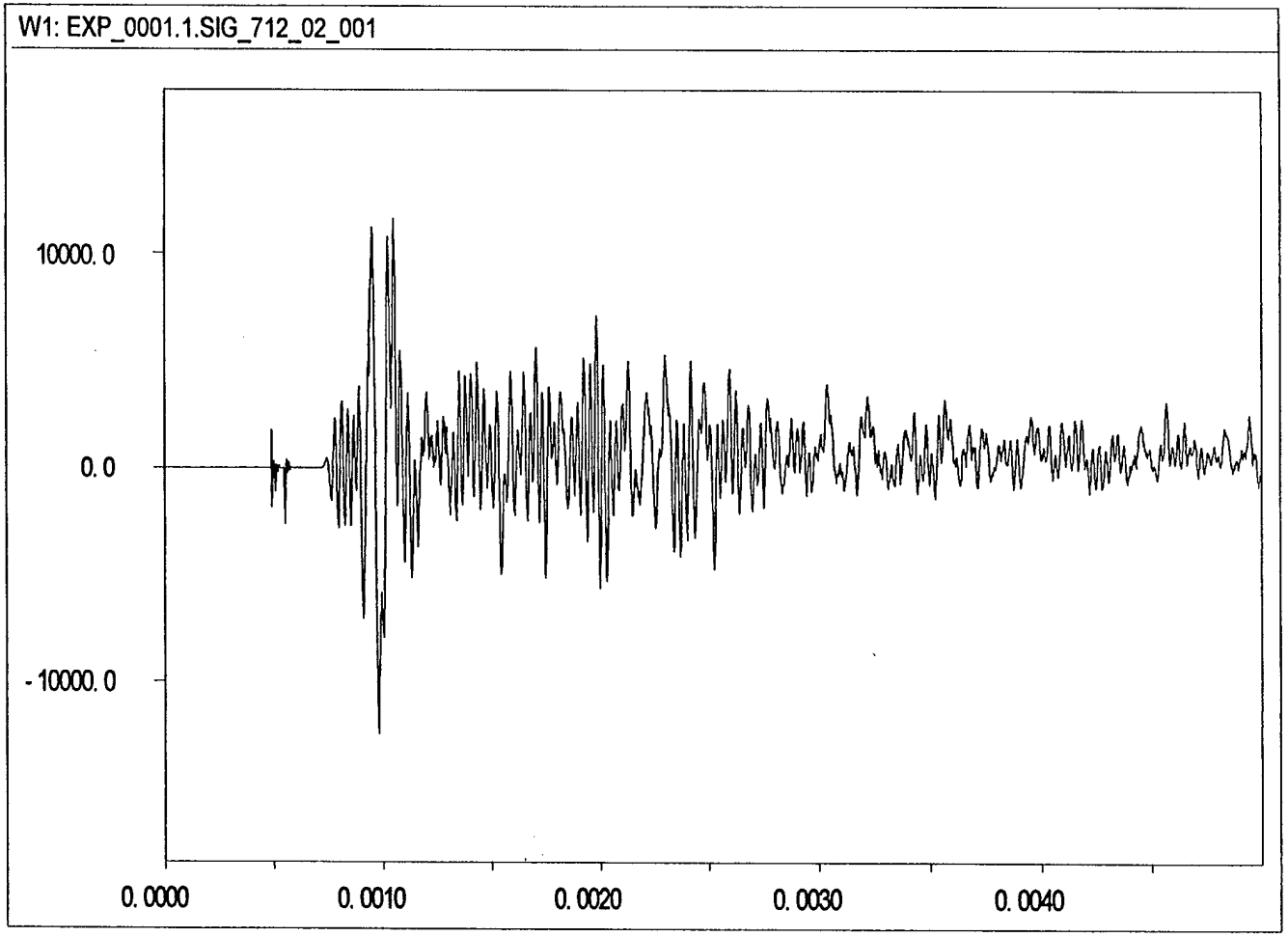


Figure A-50: Calibrated Output of Gauge #2, Shot #712.

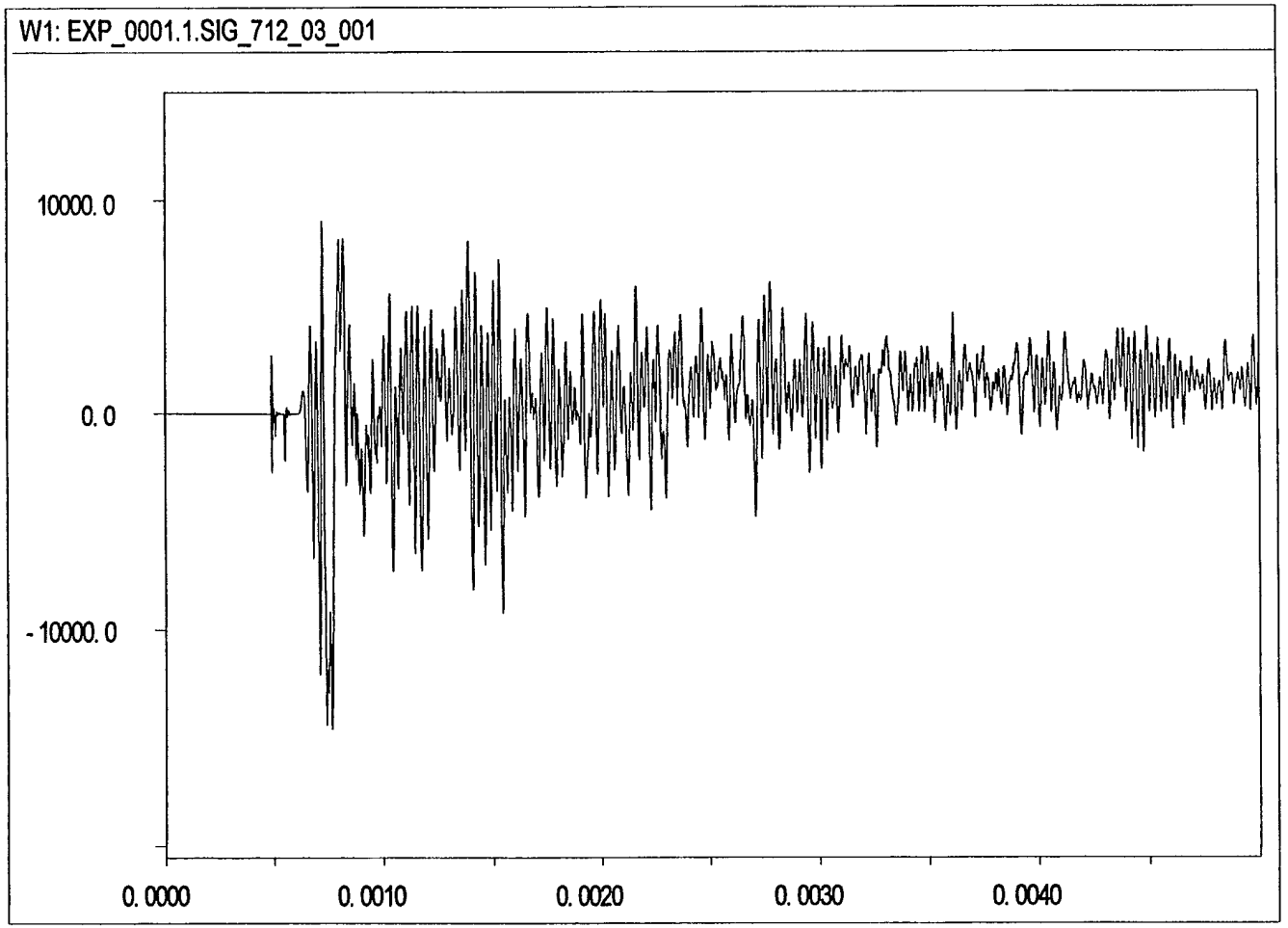


Figure A-51: Calibrated Output of Gauge #3, Shot #712.

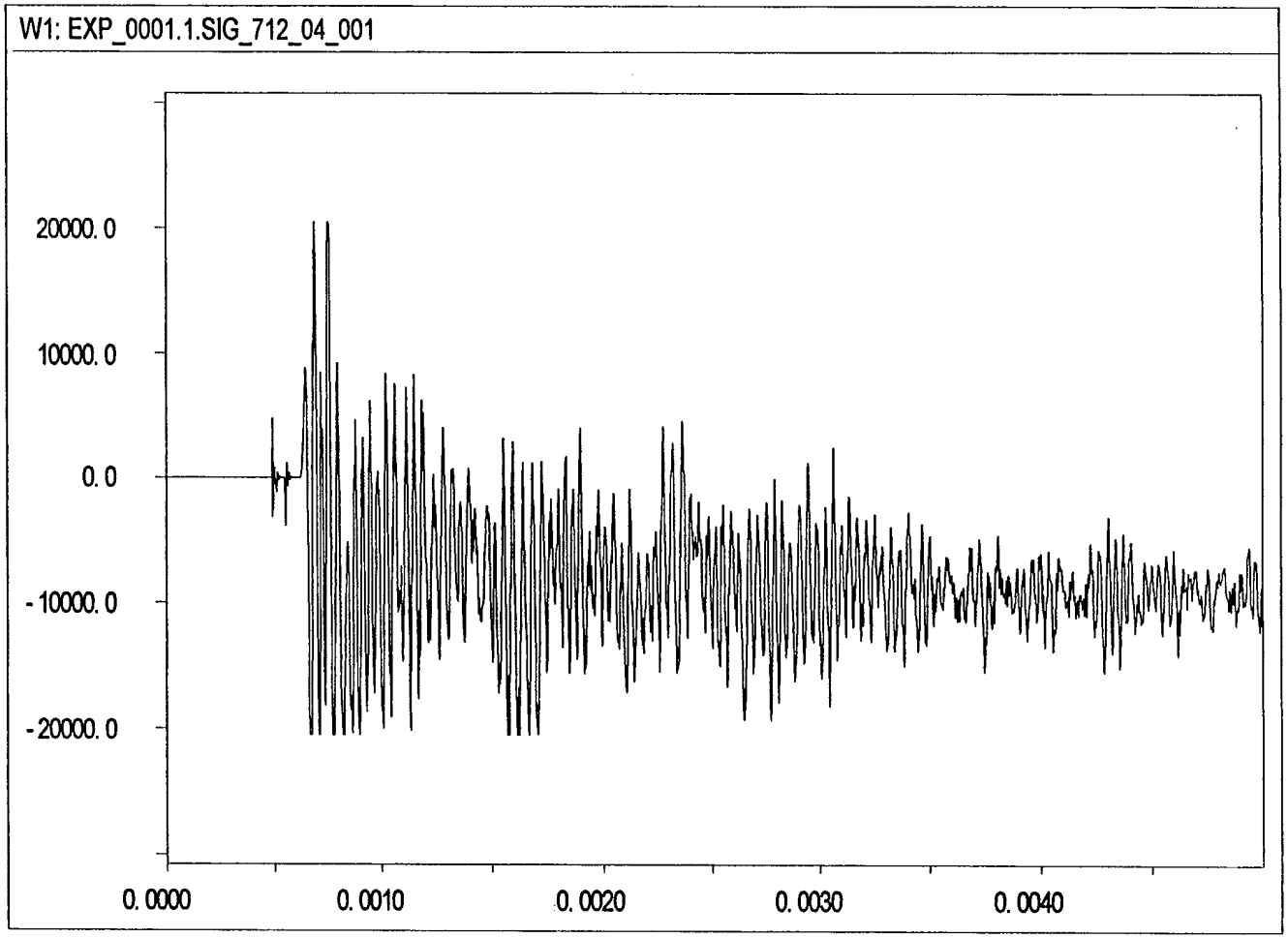


Figure A-52: Calibrated Output of Gauge #4, Shot #712.

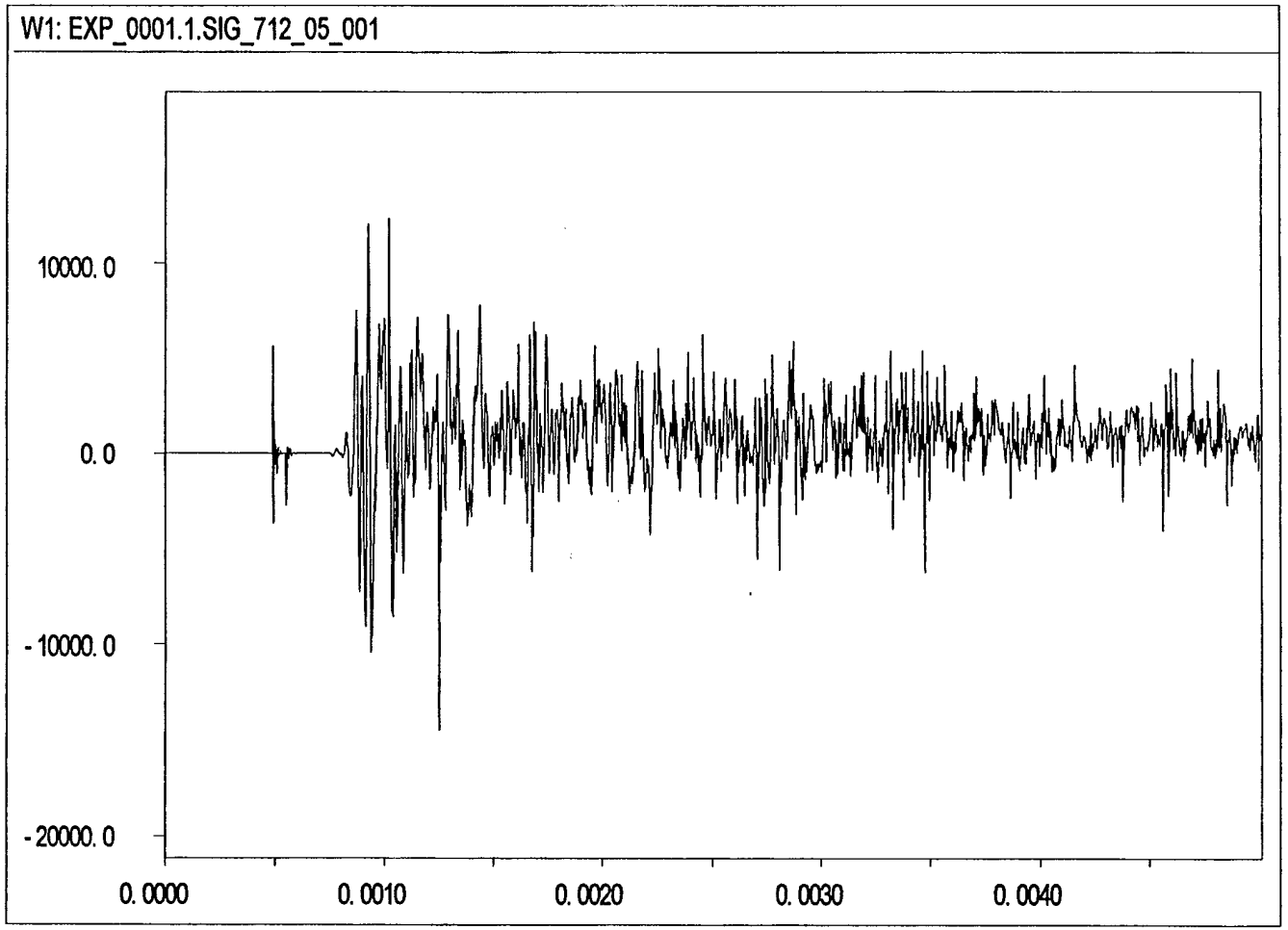


Figure A-53: Calibrated Output of Gauge #5, Shot #712.

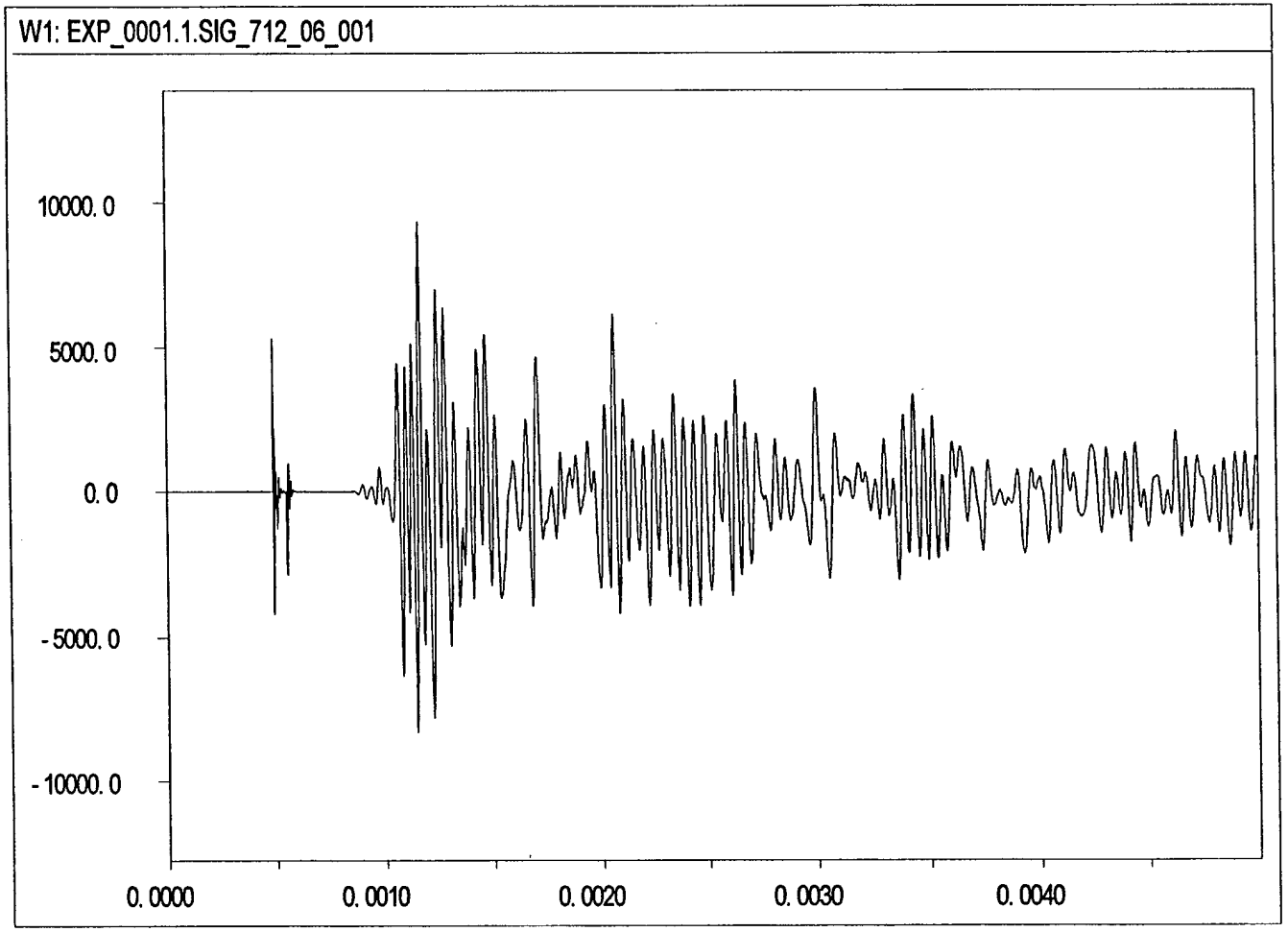


Figure A-54: Calibrated Output of Gauge #6, Shot #712.

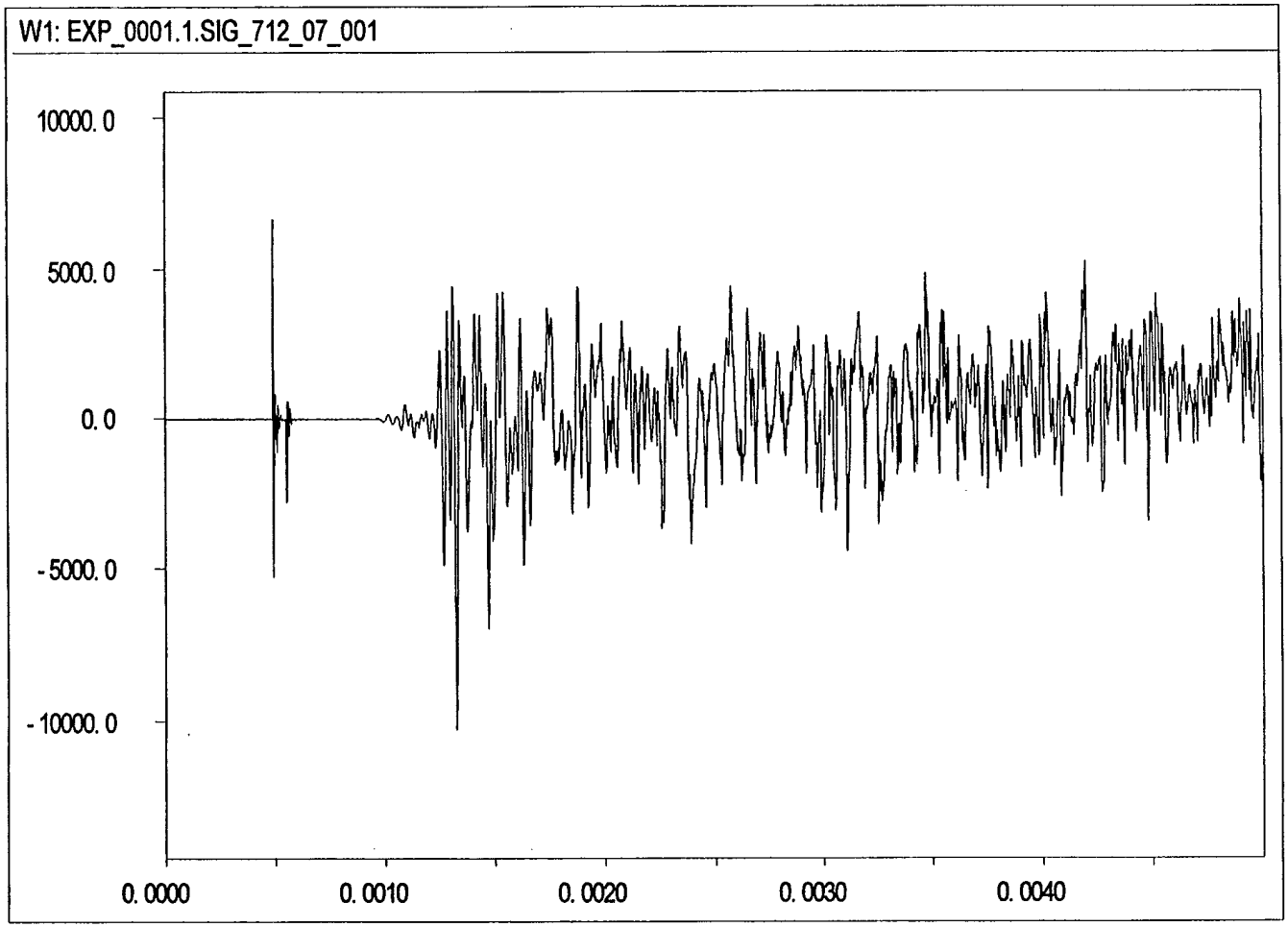


Figure A-55: Calibrated Output of Gauge #7, Shot #712.

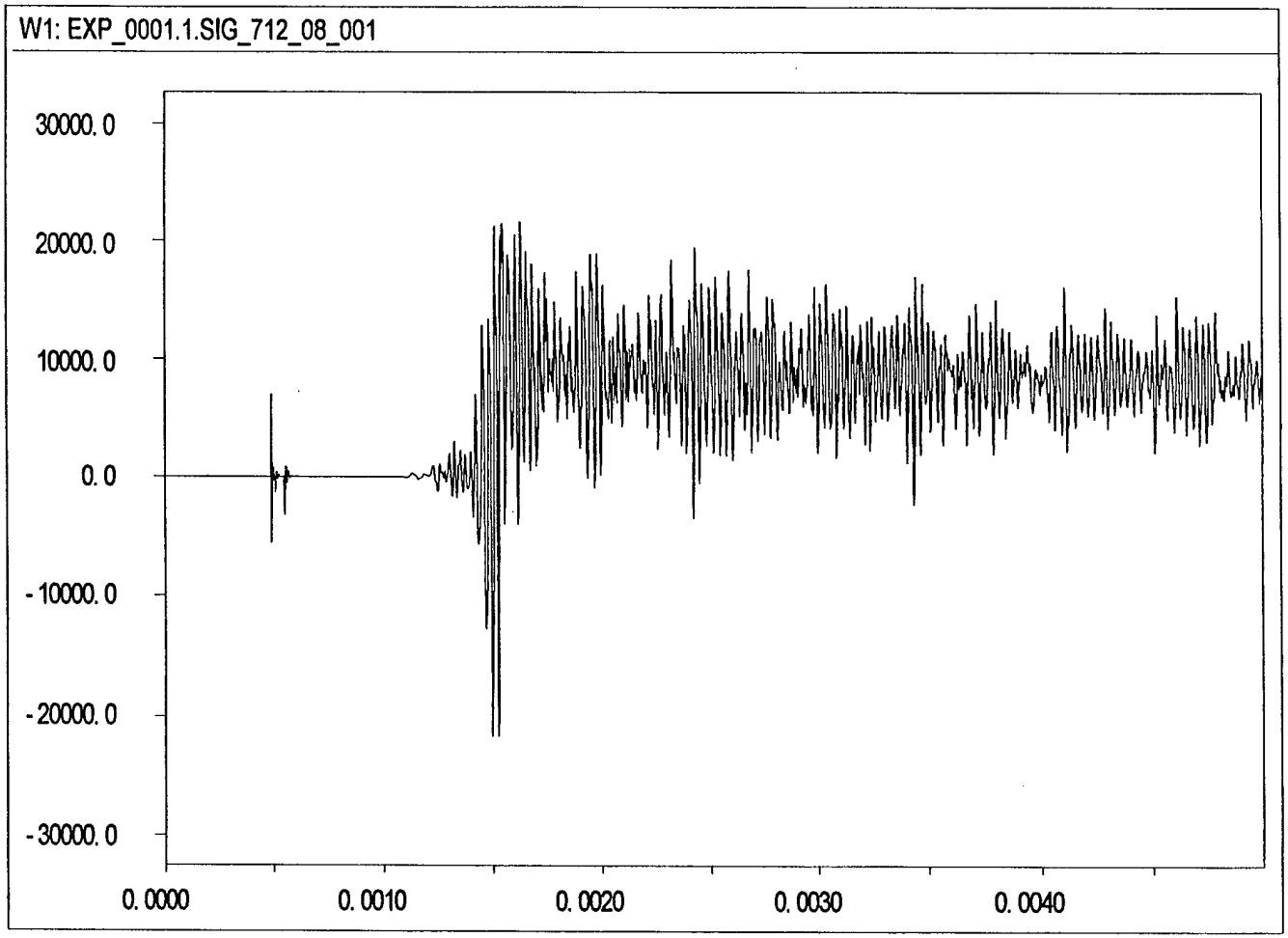


Figure A-56: Calibrated Output of Gauge #8, Shot #712.

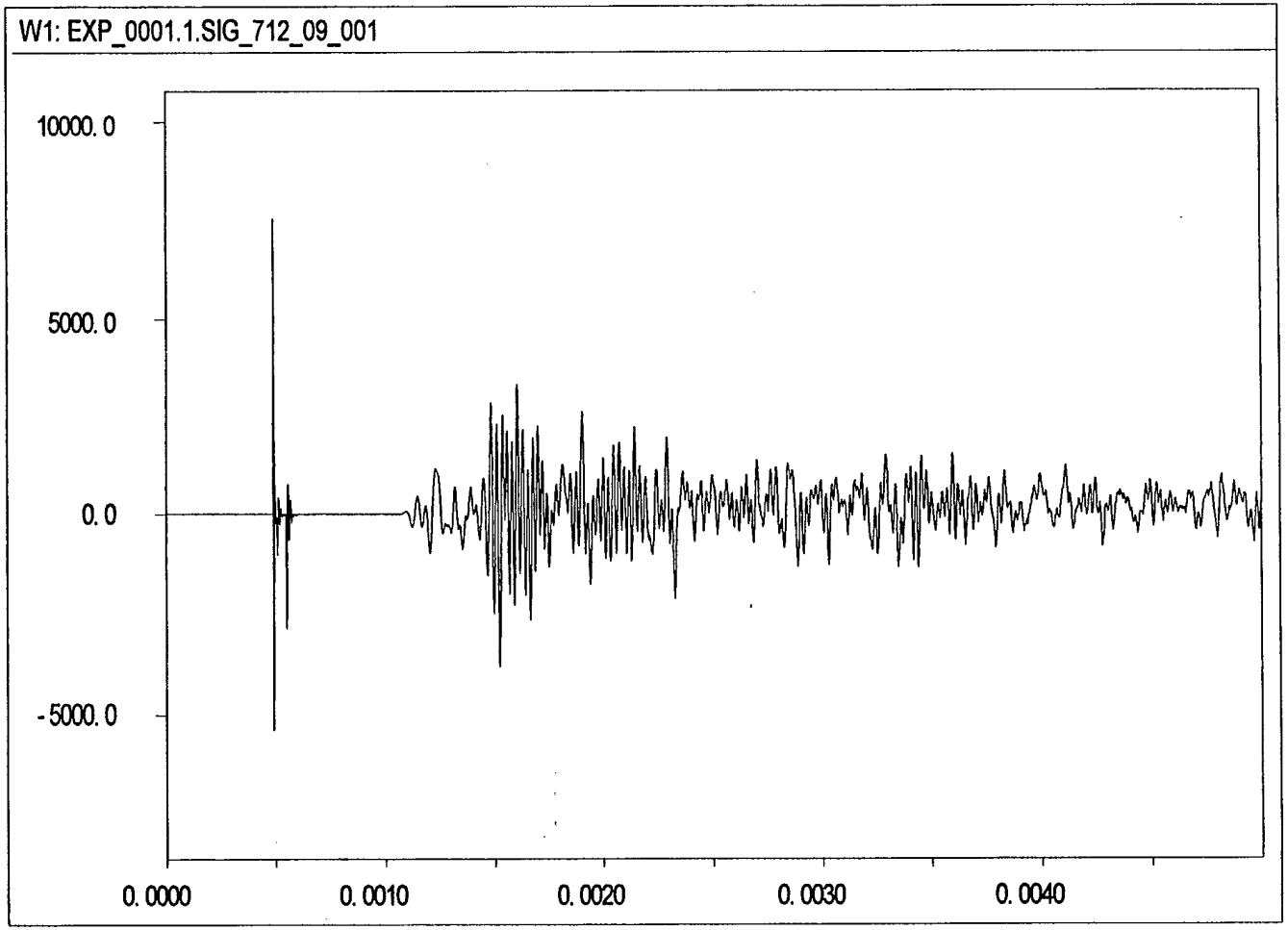


Figure A-57: Calibrated Output of Gauge #9, Shot #712.

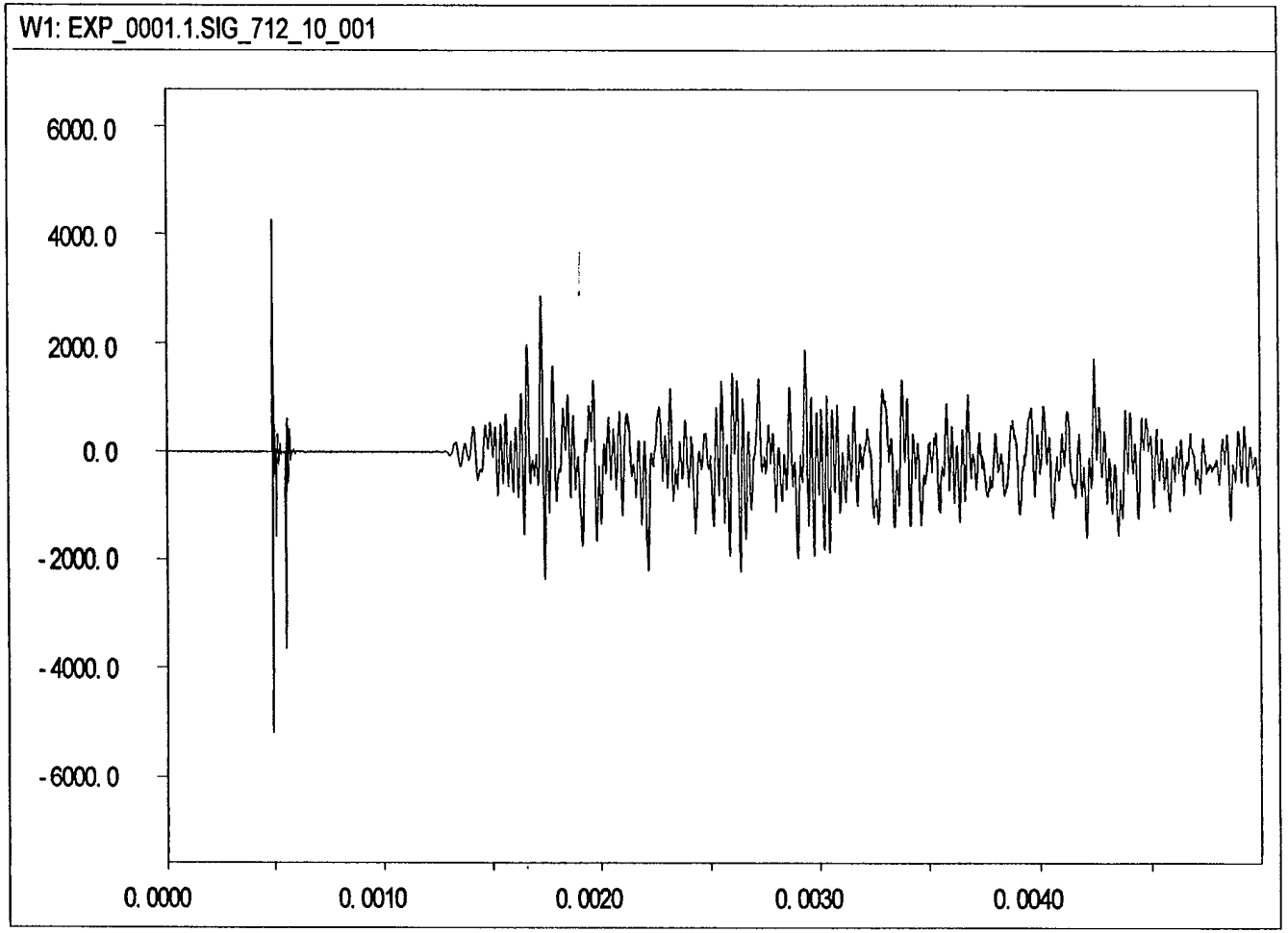


Figure A-58: Calibrated Output of Gauge #10, Shot #712.

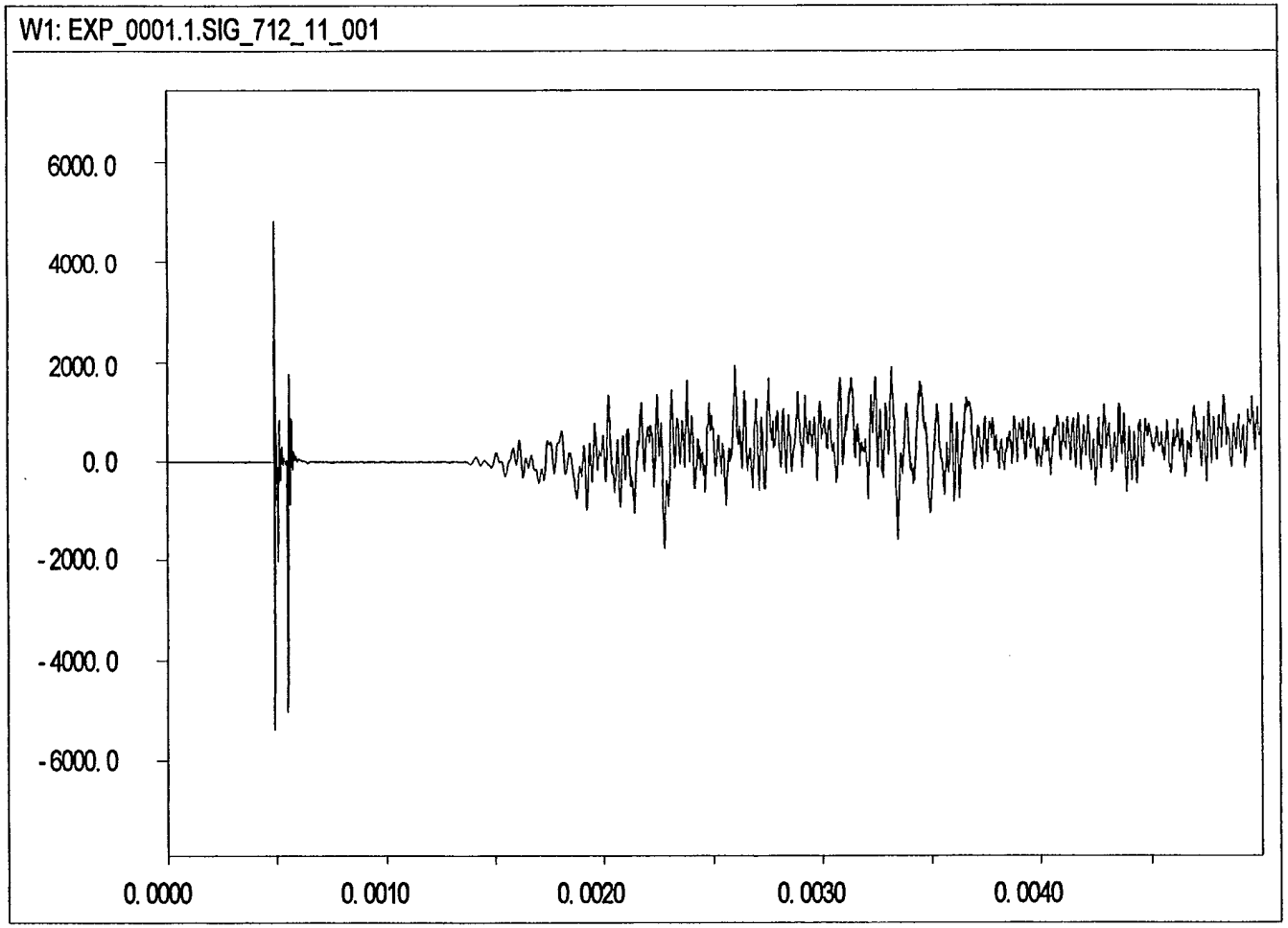


Figure A-59: Calibrated Output of Gauge #11, Shot #712.

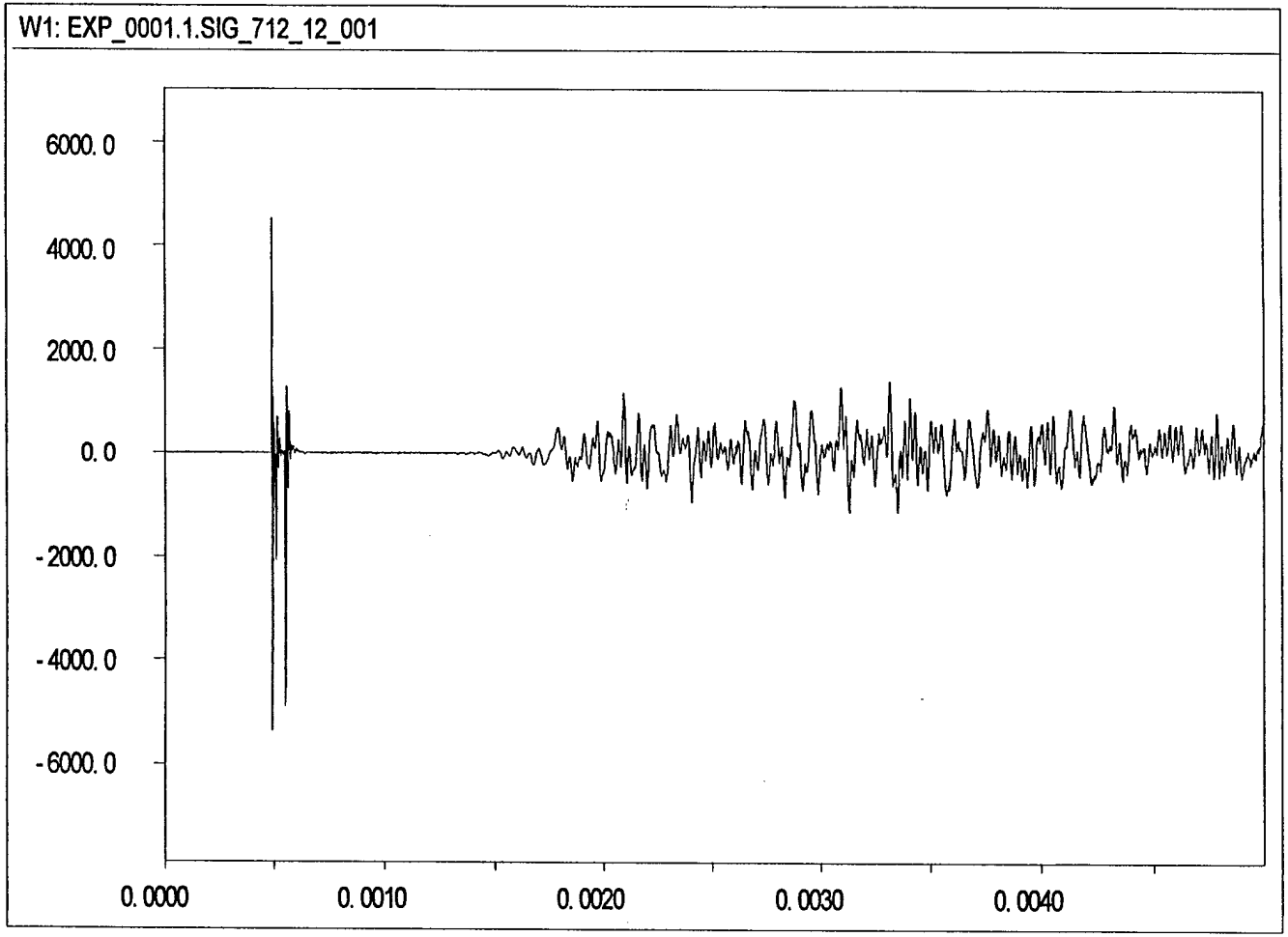


Figure A-60: Calibrated Output of Gauge #12, Shot #712.

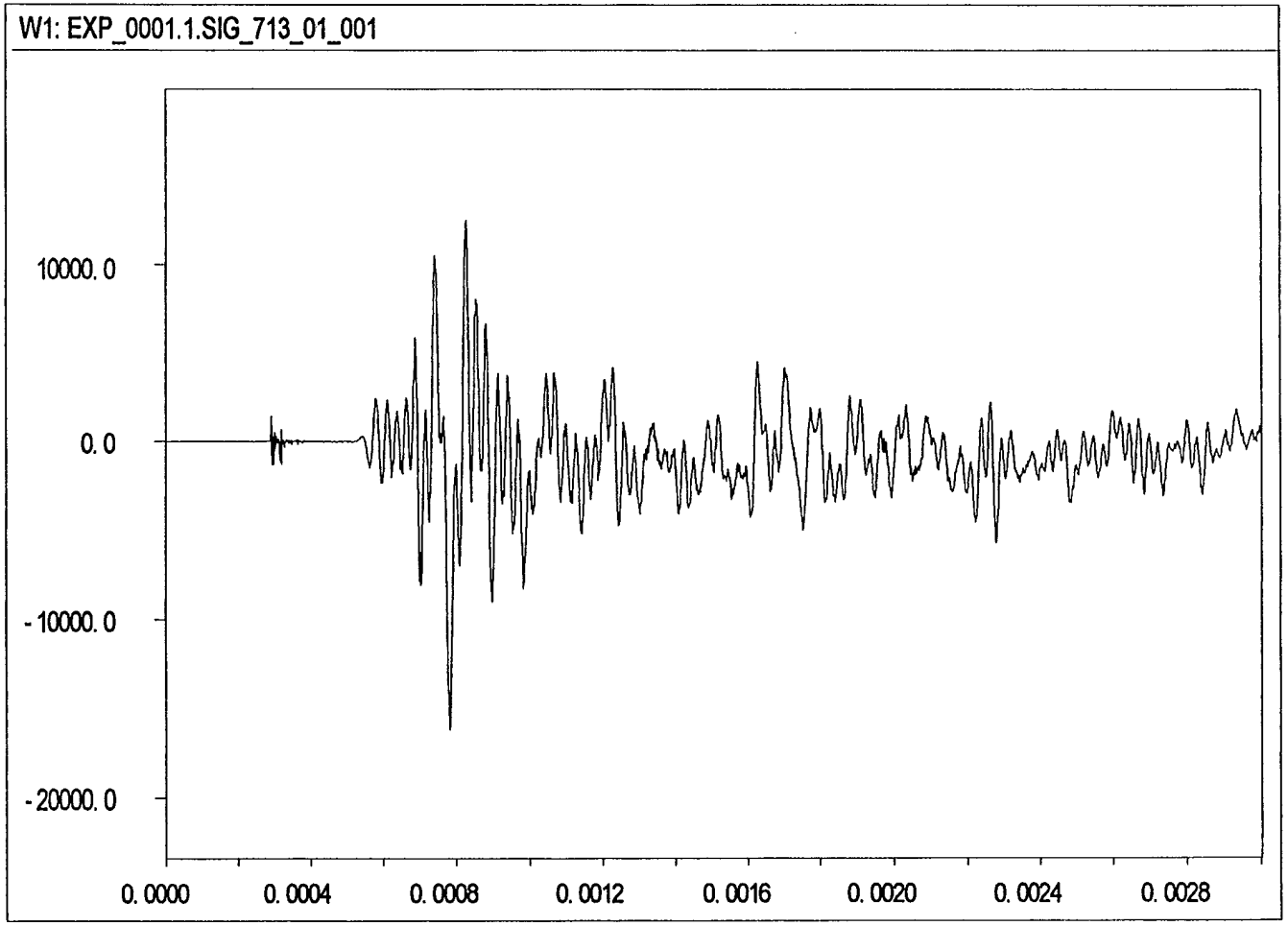


Figure A-61: Calibrated Output of Gauge #1, Shot #713.

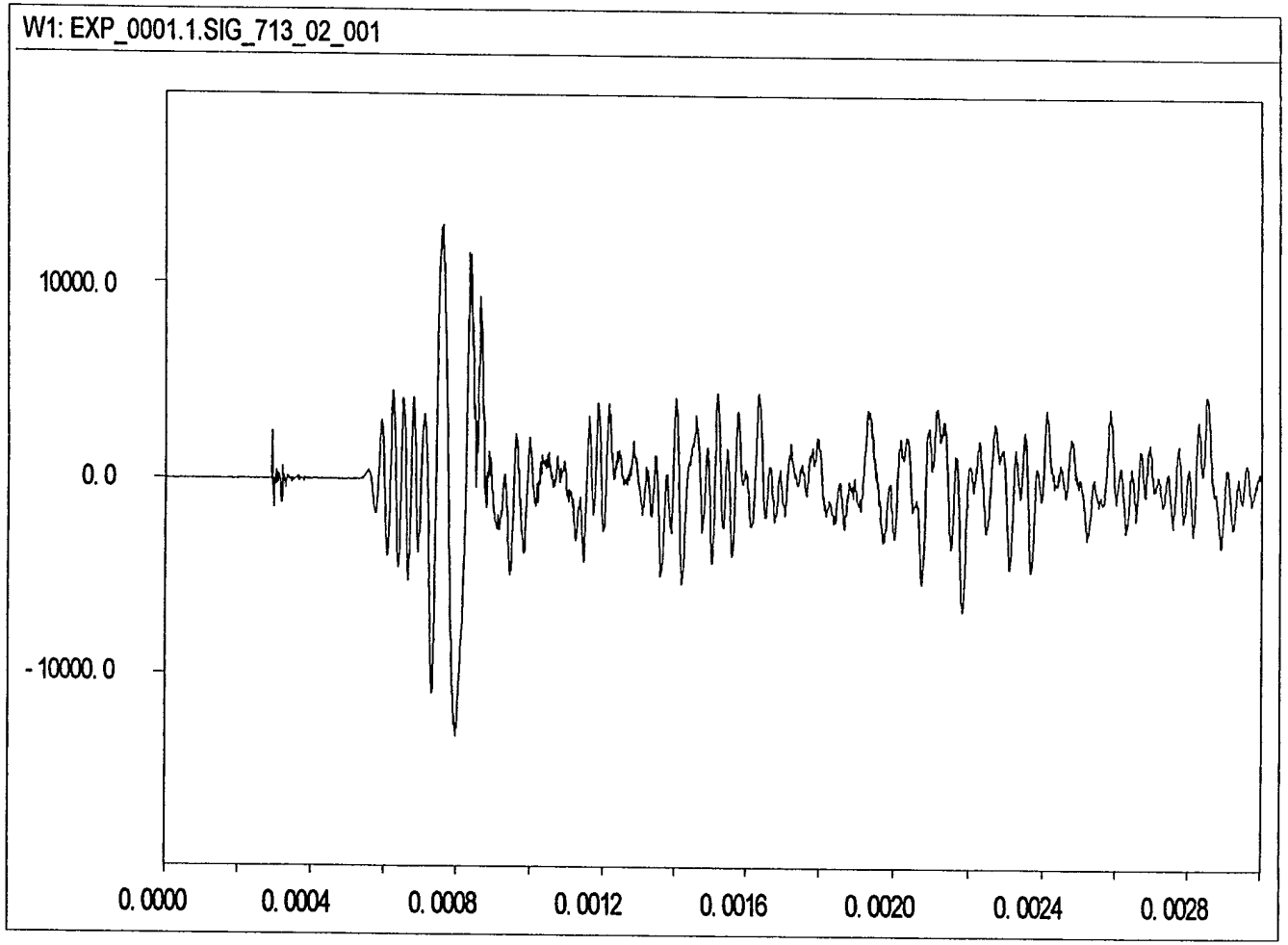


Figure A-62: Calibrated Output of Gauge #2, Shot #713.

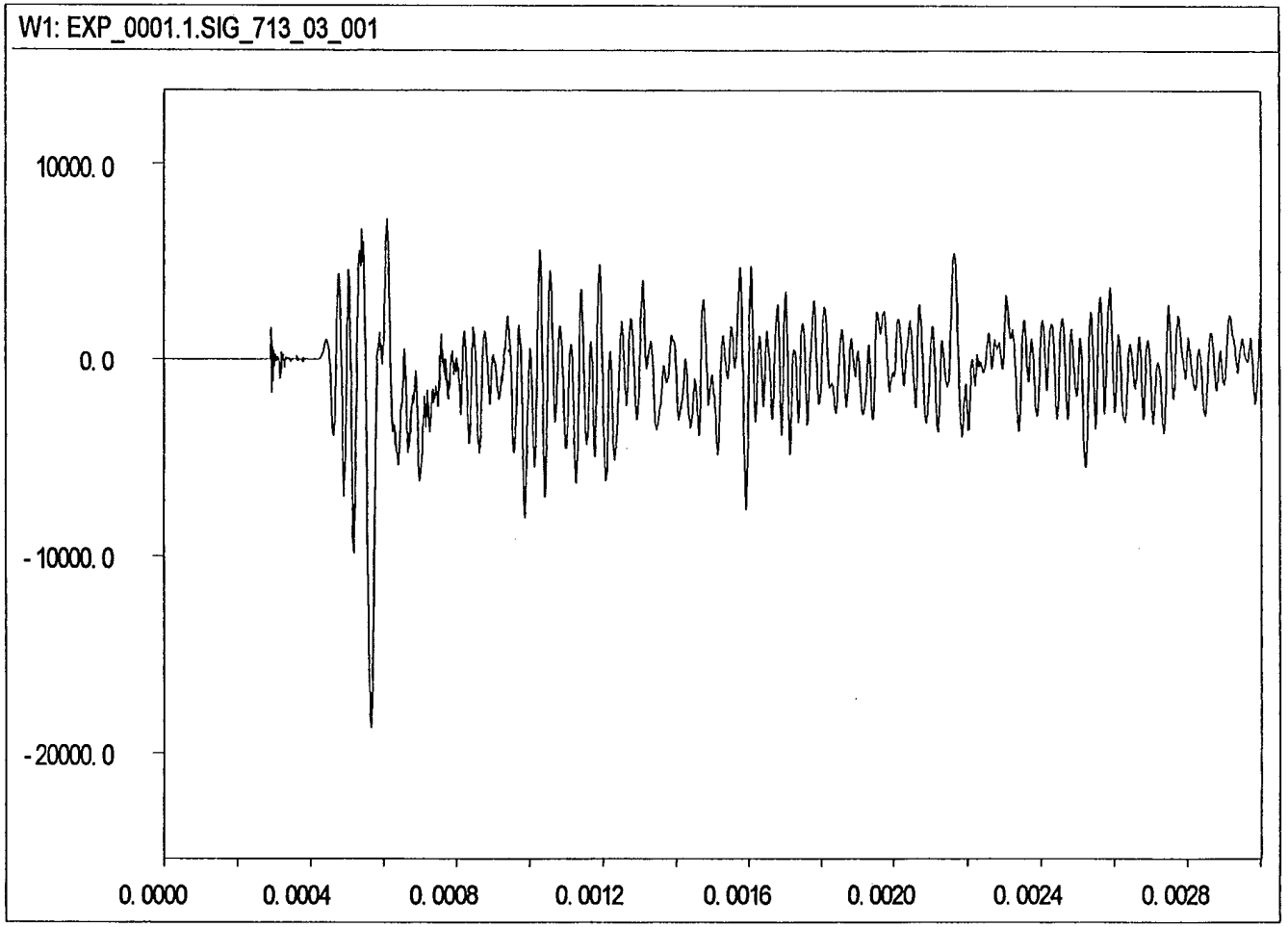


Figure A-63: Calibrated Output of Gauge #3, Shot #713.

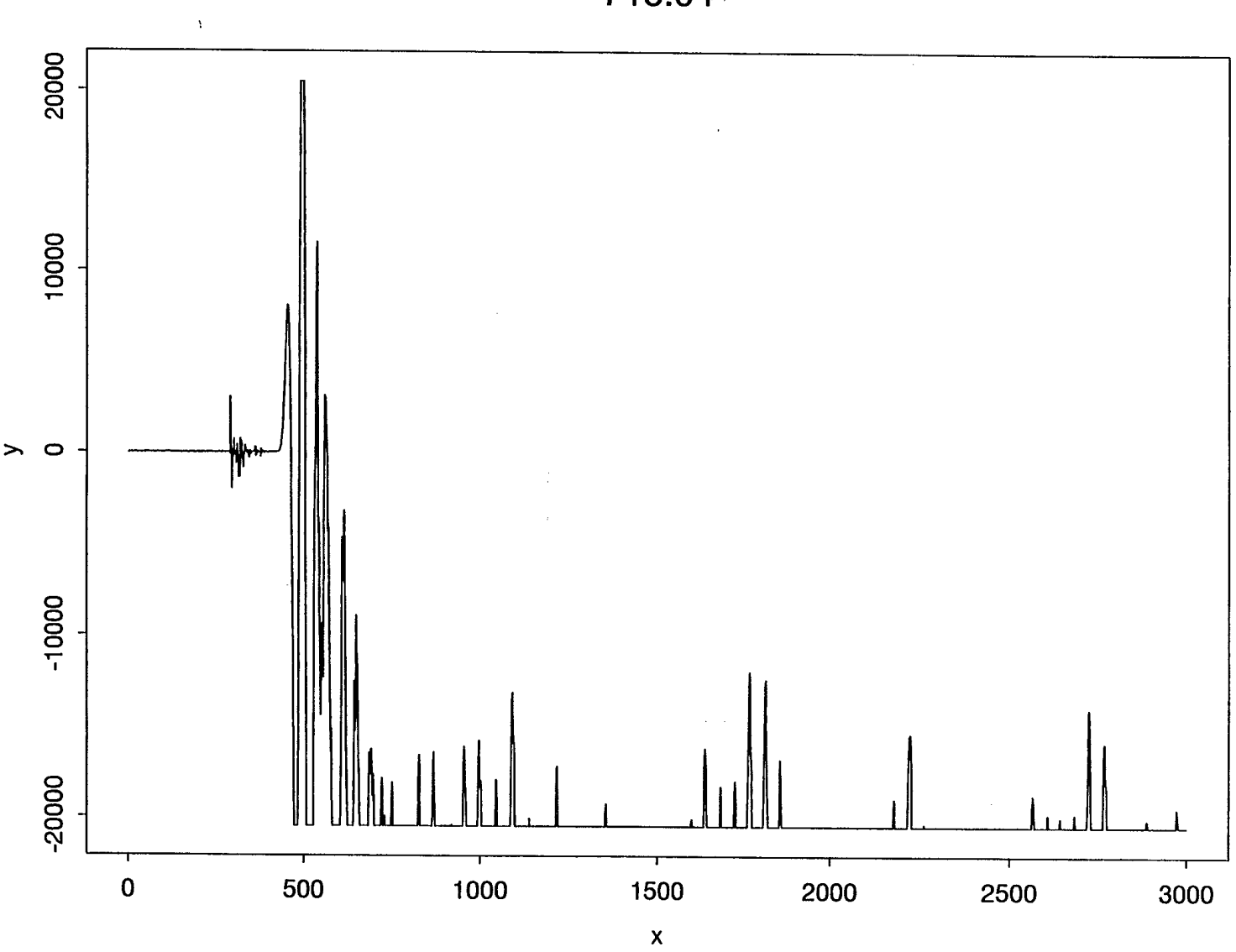


Figure A-64: Calibrated Output of Gauge #4, Shot #713.

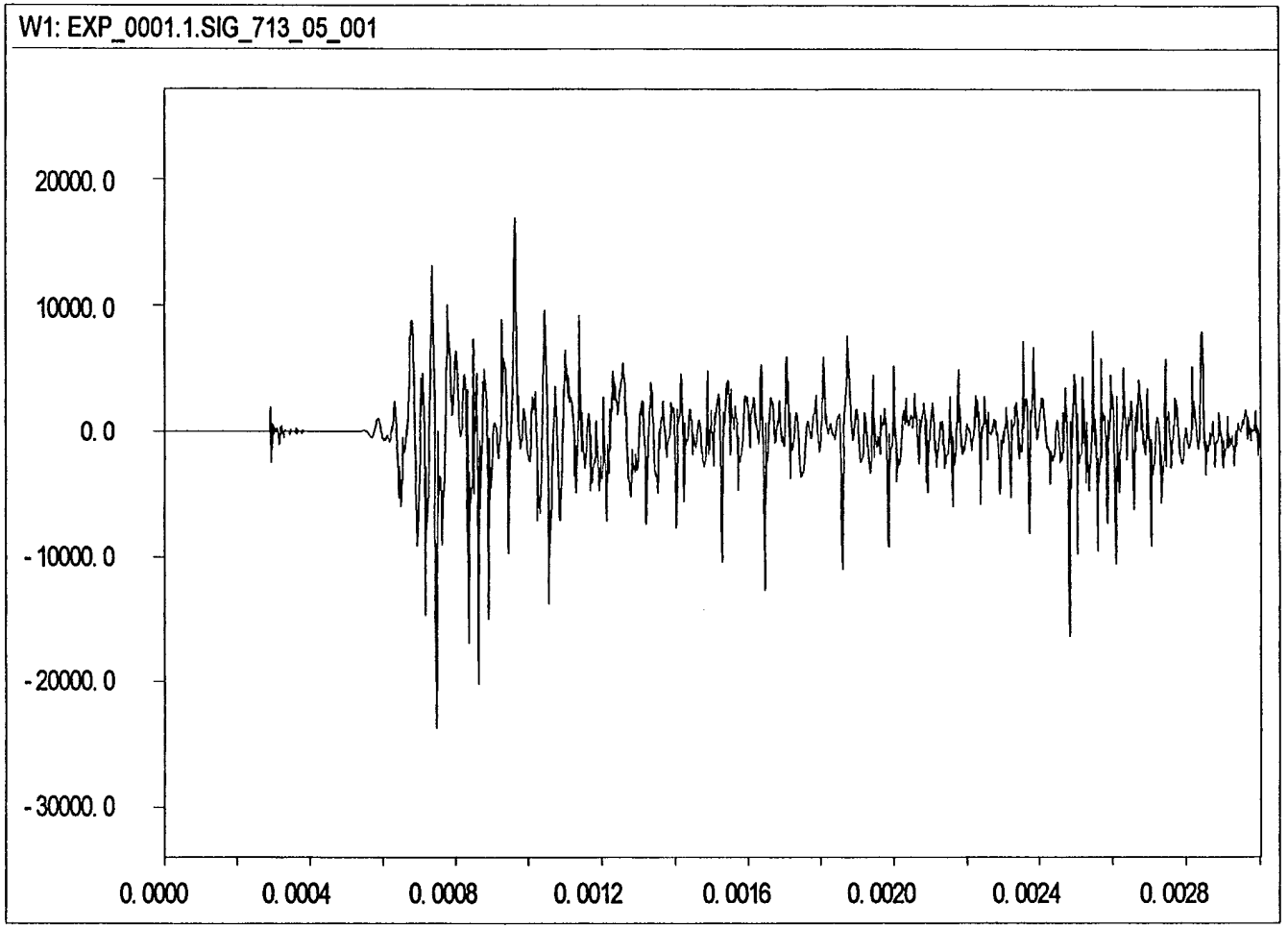


Figure A-65: Calibrated Output of Gauge #5, Shot #713.

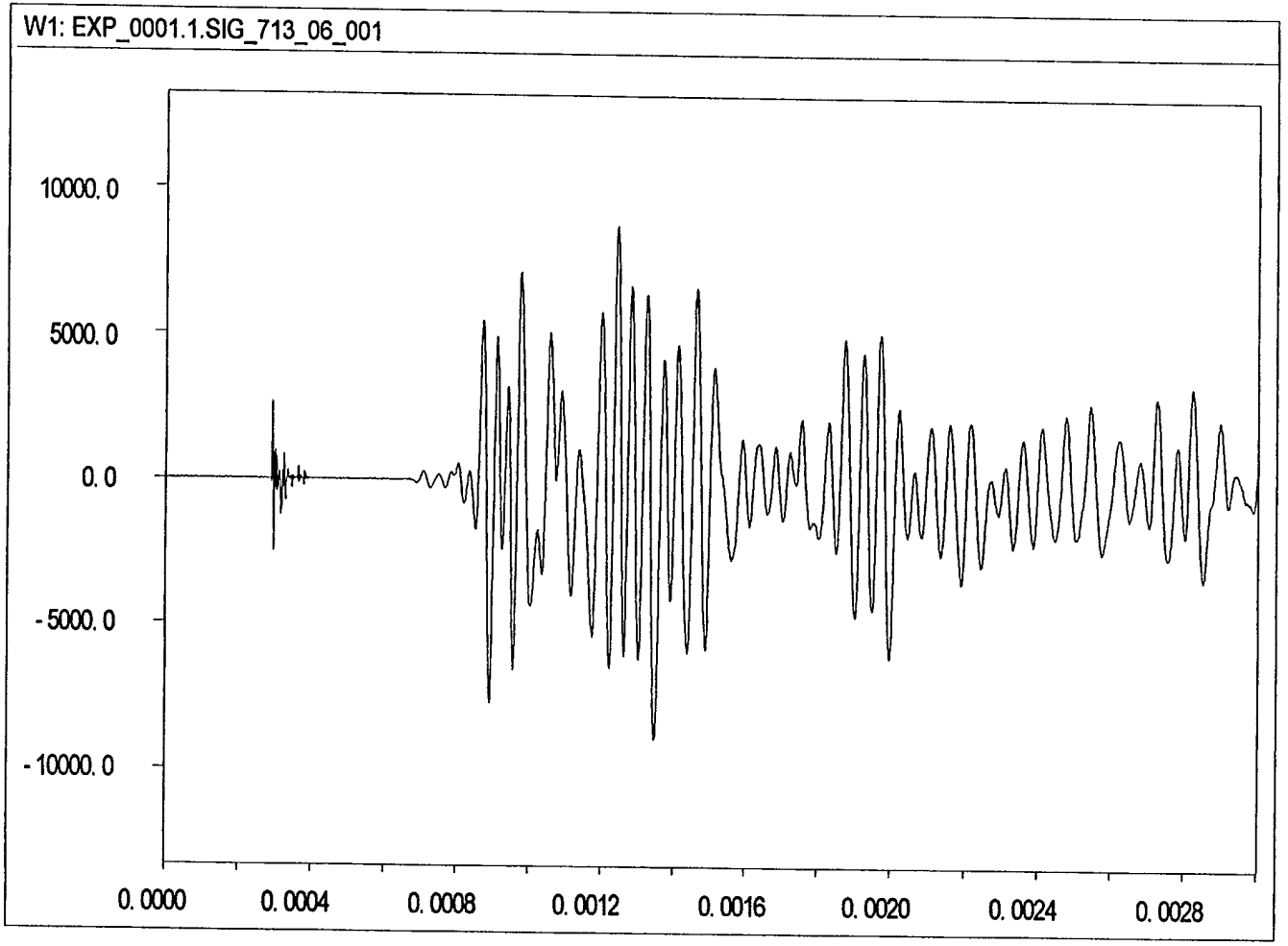


Figure A-66: Calibrated Output of Gauge #6, Shot #713.

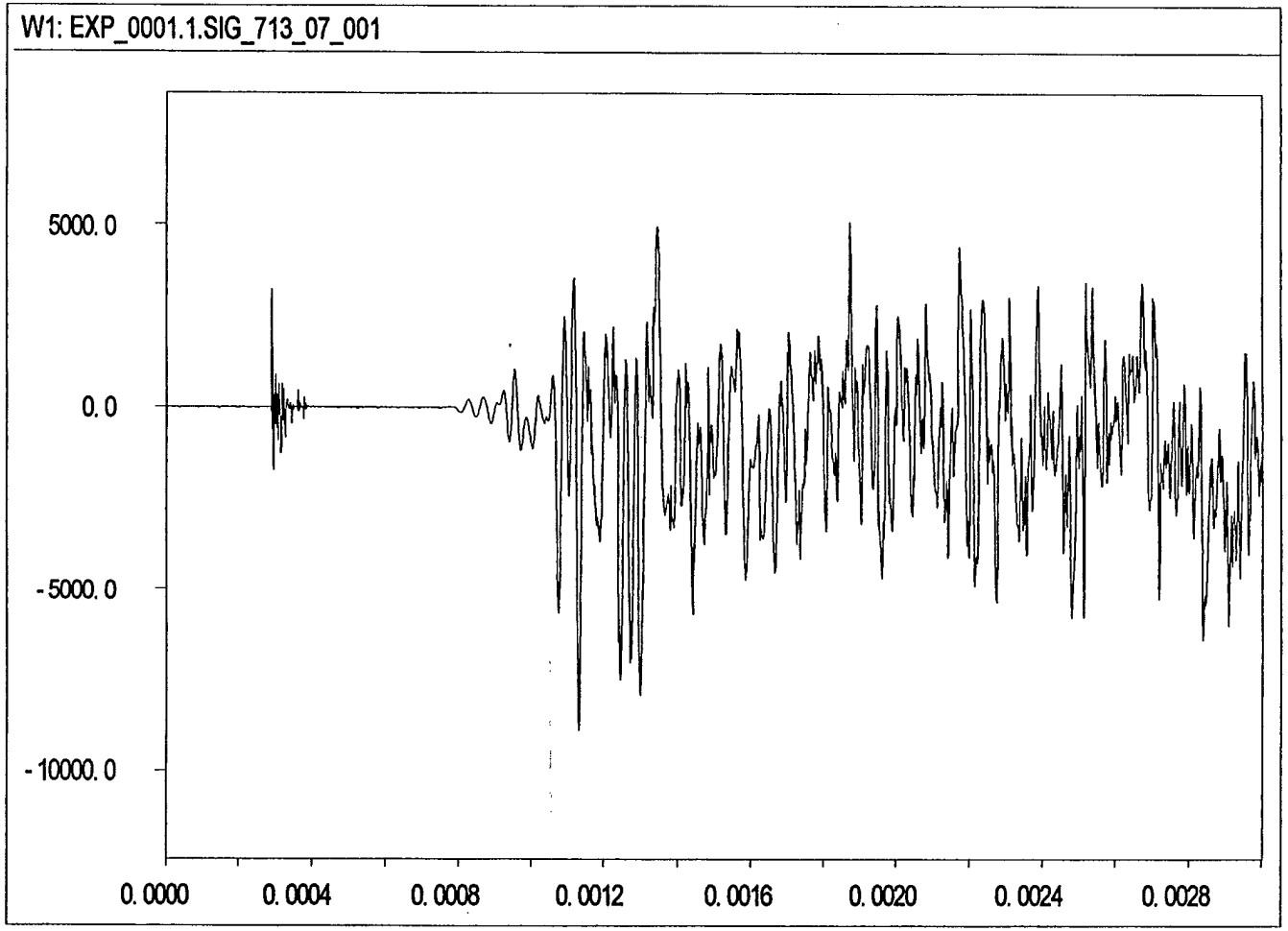


Figure A-67: Calibrated Output of Gauge #7, Shot #713.

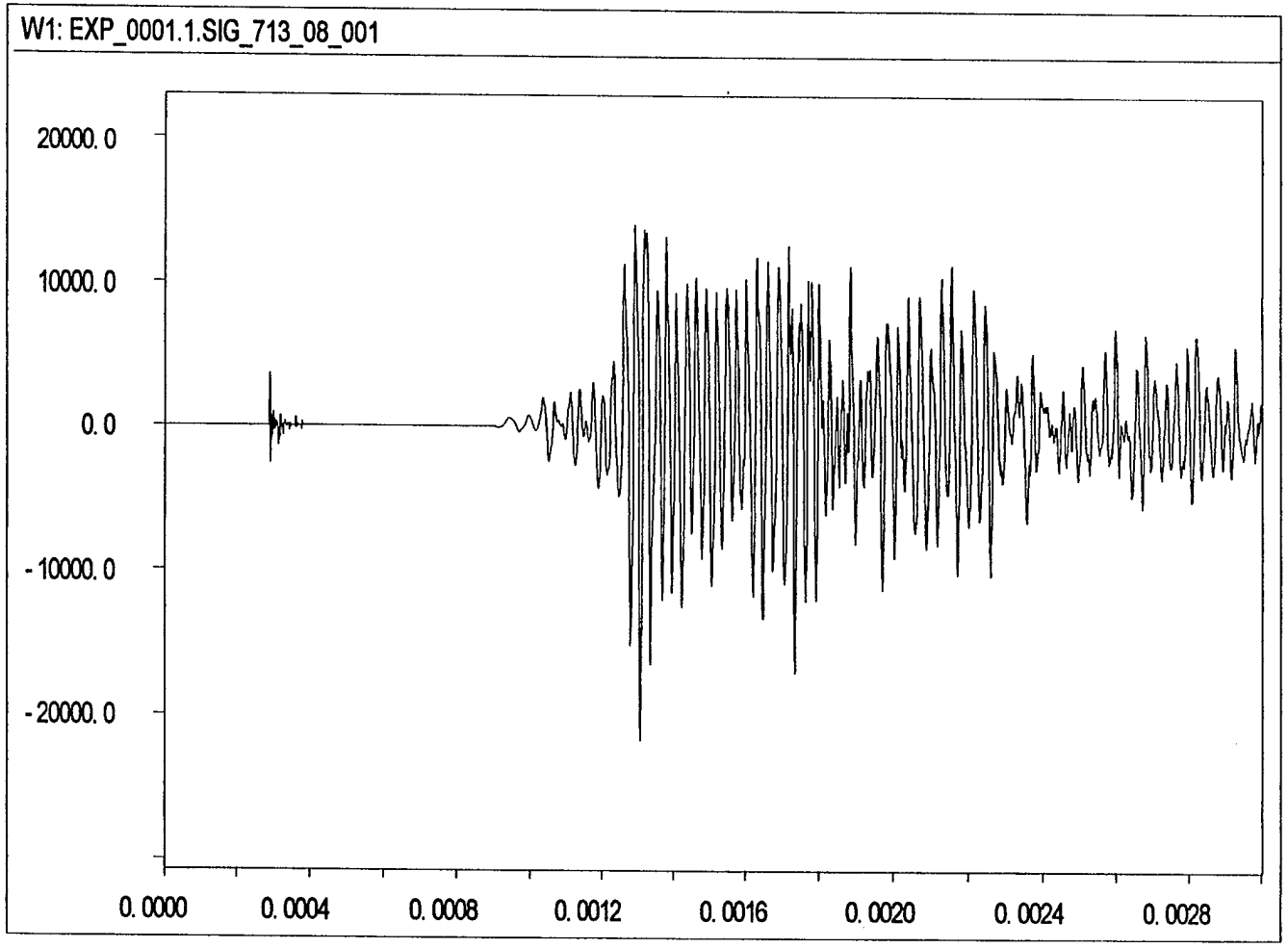


Figure A-68: Calibrated Output of Gauge #8, Shot #713.

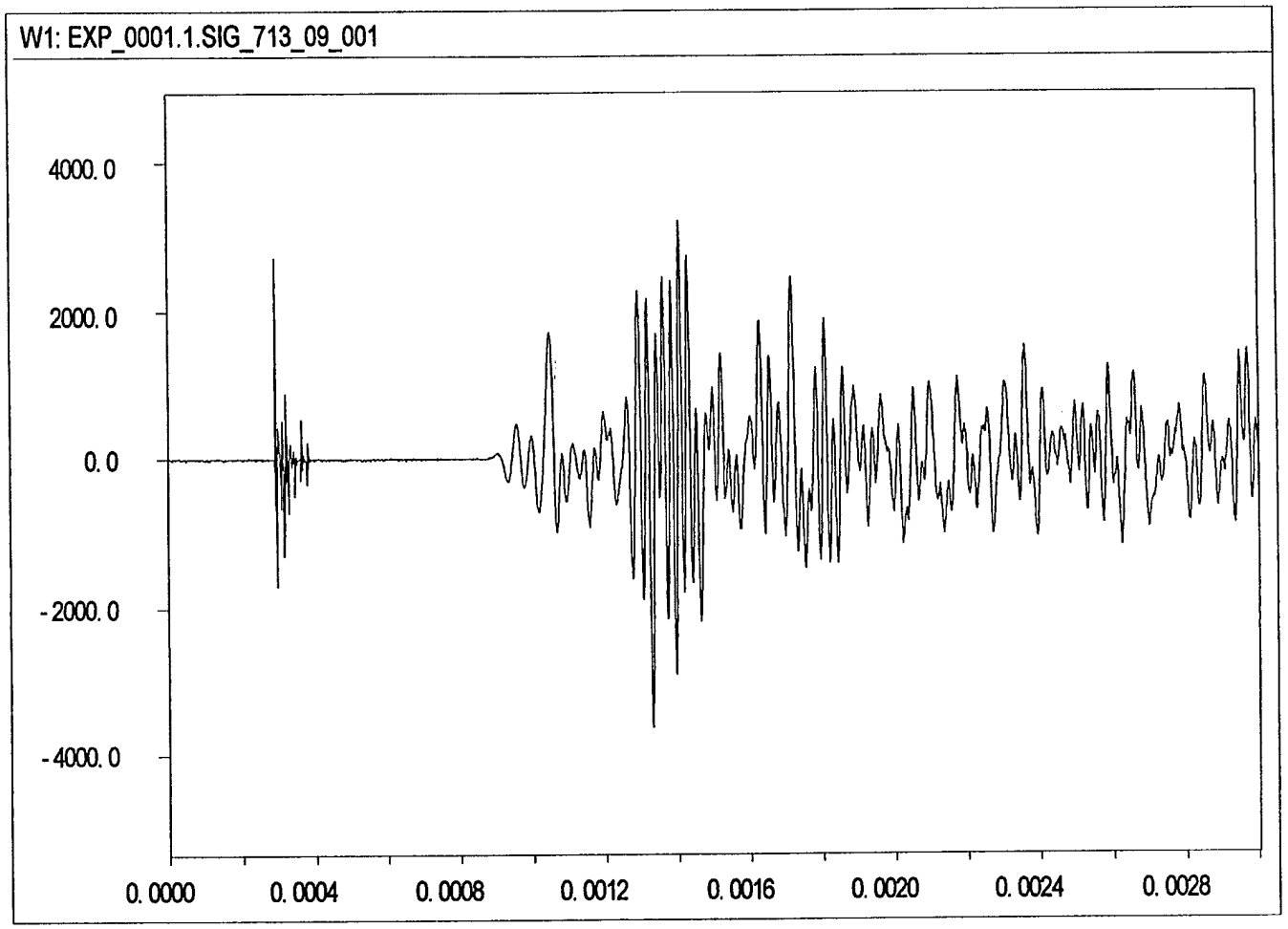


Figure A-69: Calibrated Output of Gauge #9, Shot #713.

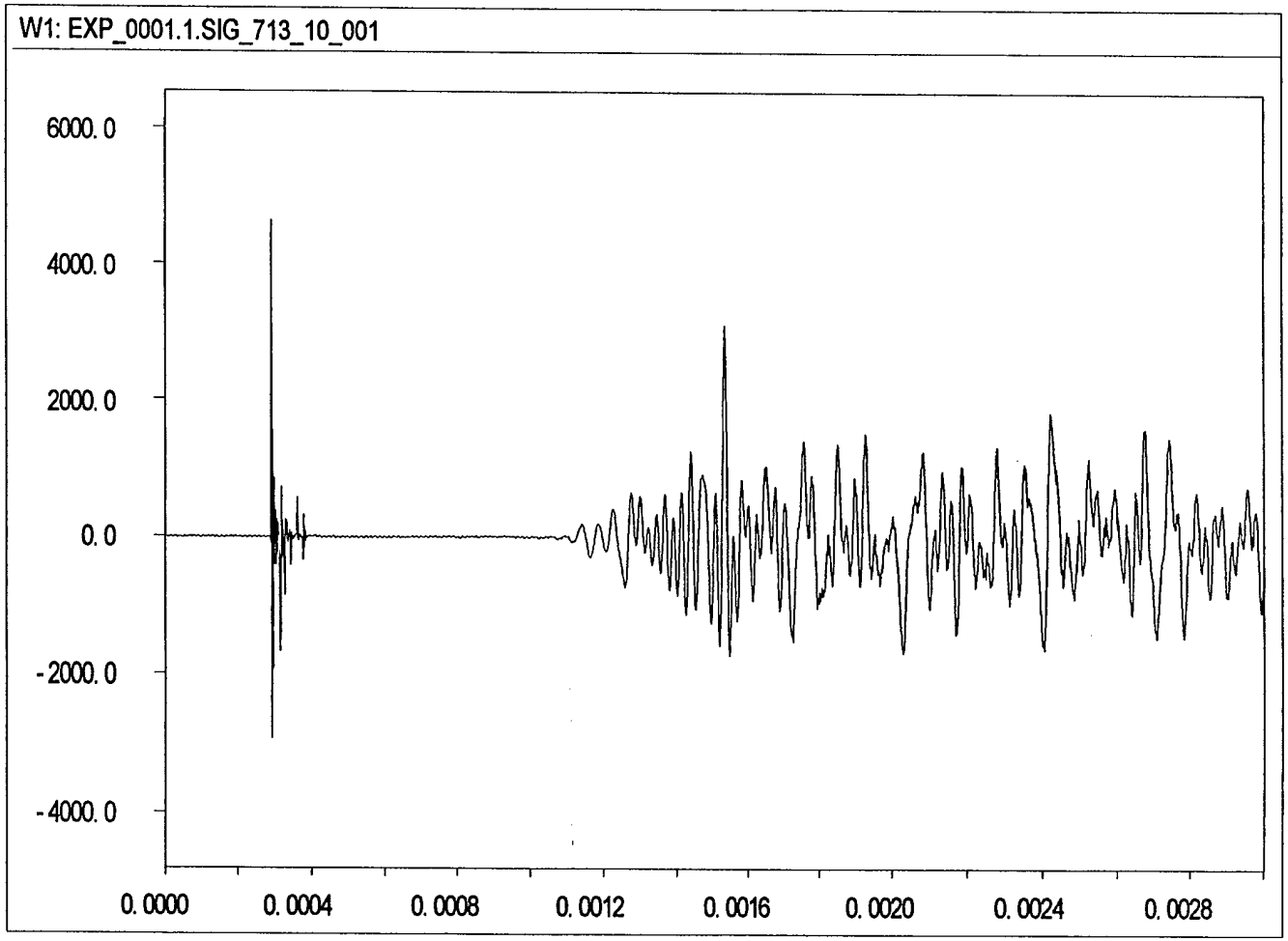


Figure A-70: Calibrated Output of Gauge #10, Shot #713.

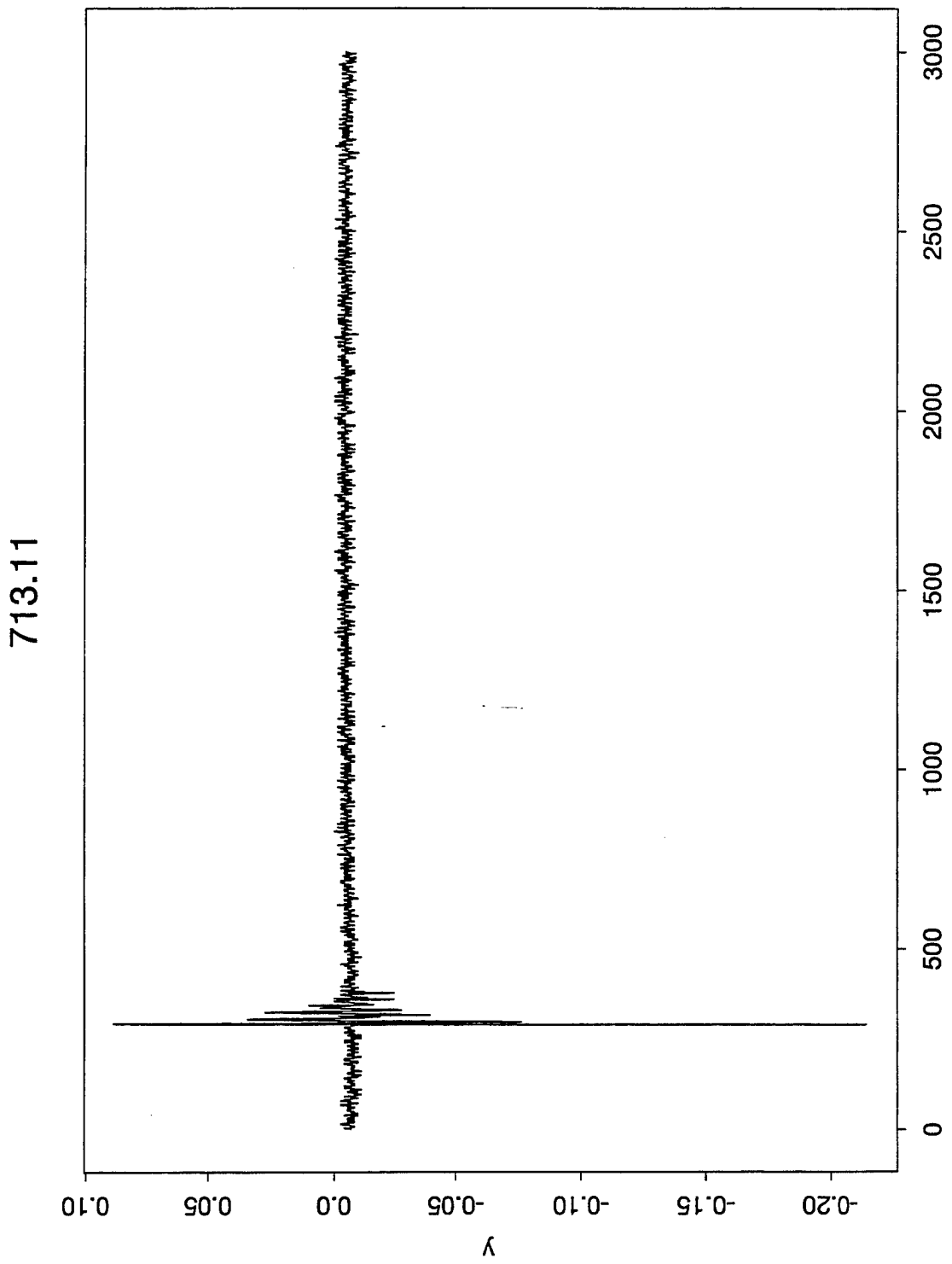


Figure A-71: Calibrated Output of Gauge #11, Shot #713.

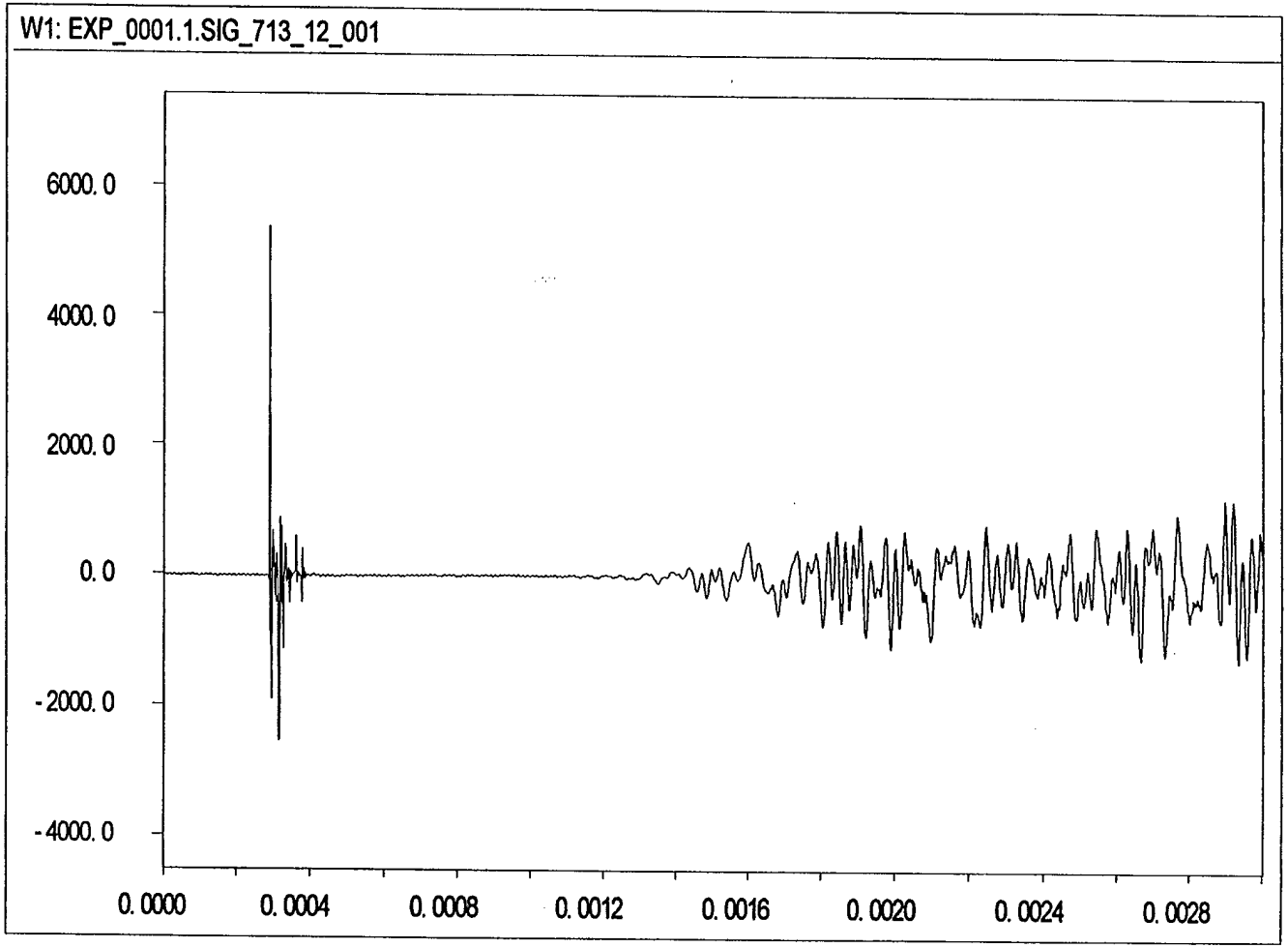


Figure A-72: Calibrated Output of Gauge #12, Shot #713.

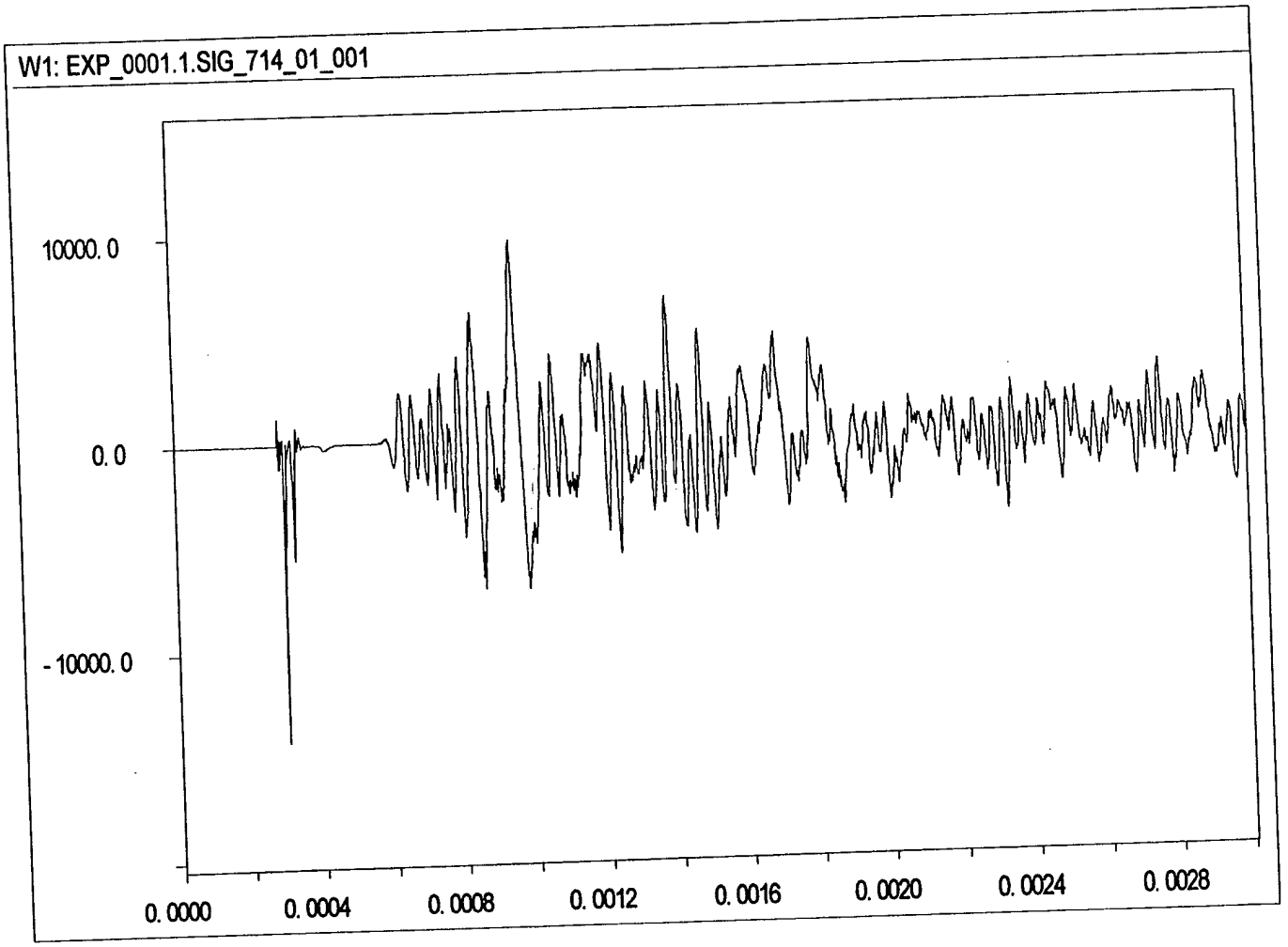


Figure A-73: Calibrated Output of Gauge #1, Shot #714.

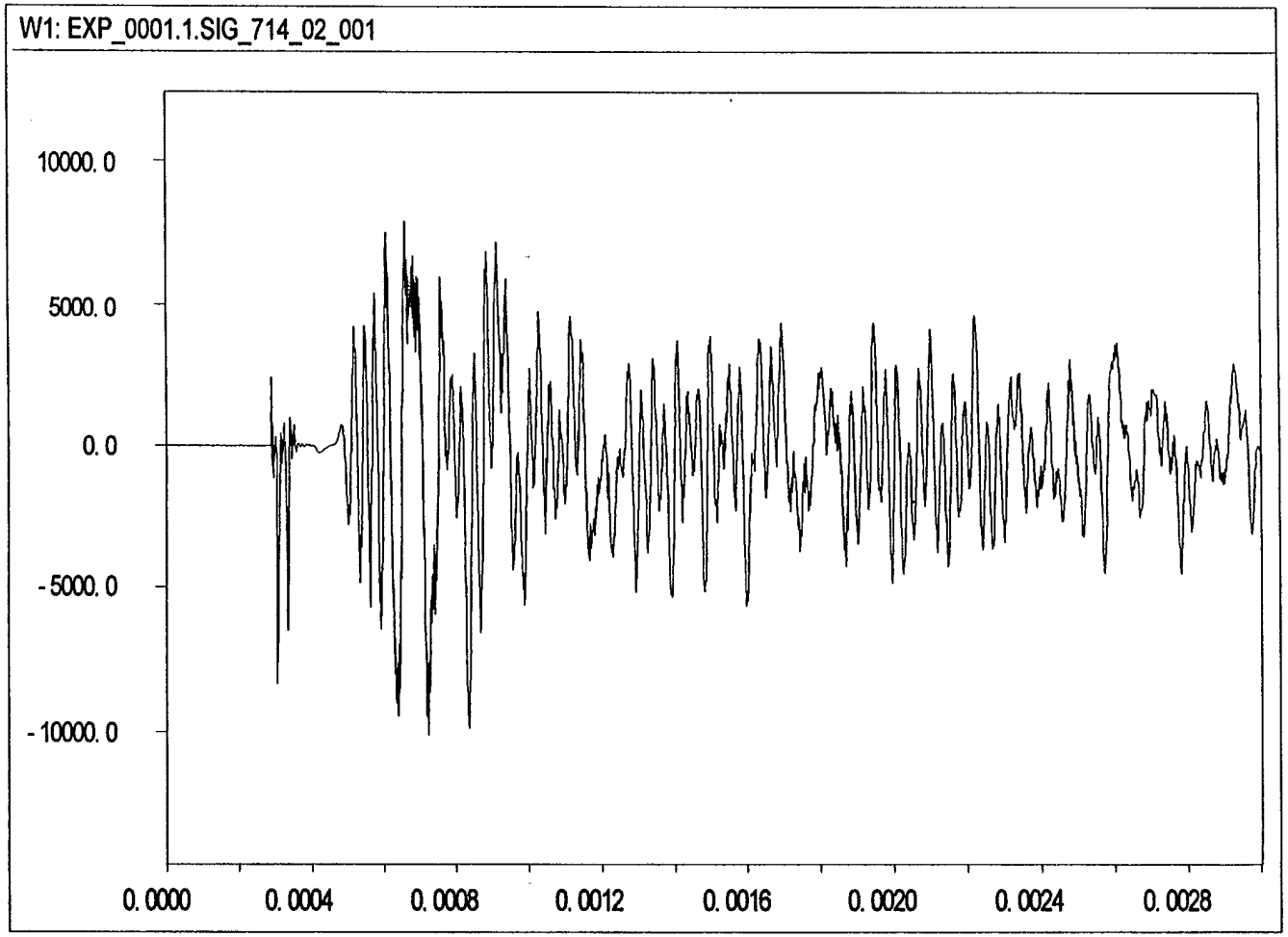


Figure A-74: Calibrated Output of Gauge #2, Shot #714.

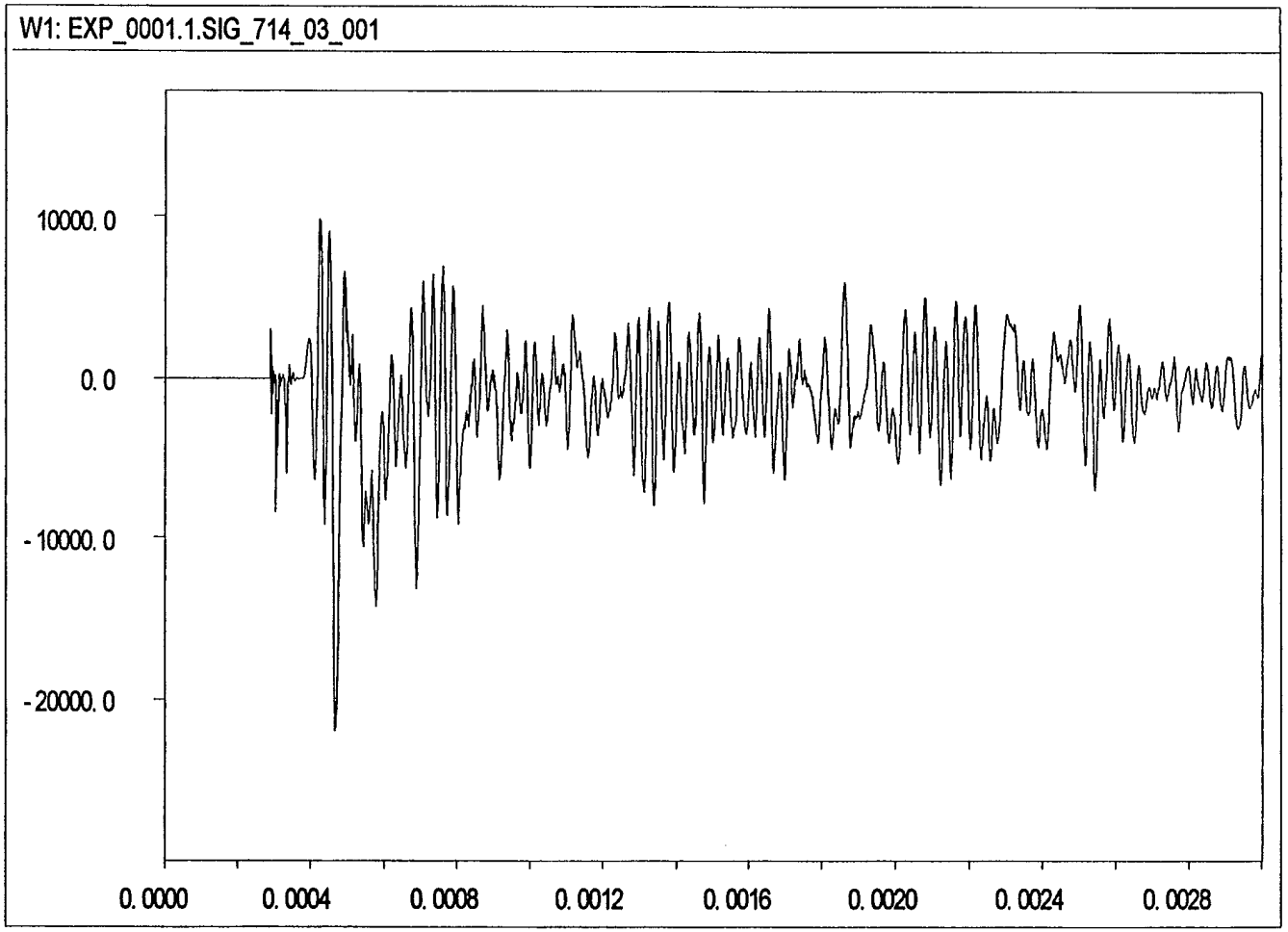


Figure A-75: Calibrated Output of Gauge #3, Shot #714.

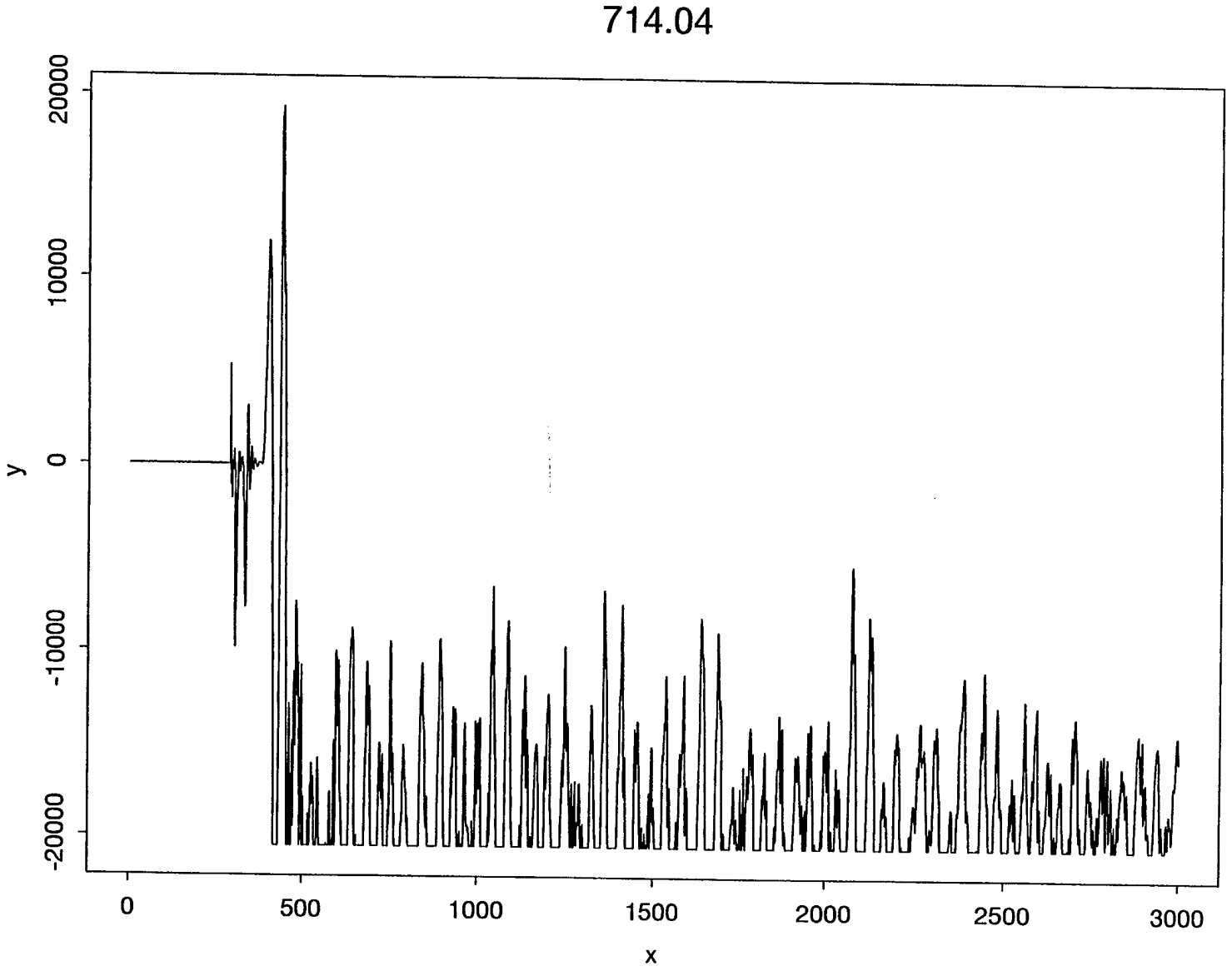


Figure A-76: Calibrated Output of Gauge #4, Shot #714.

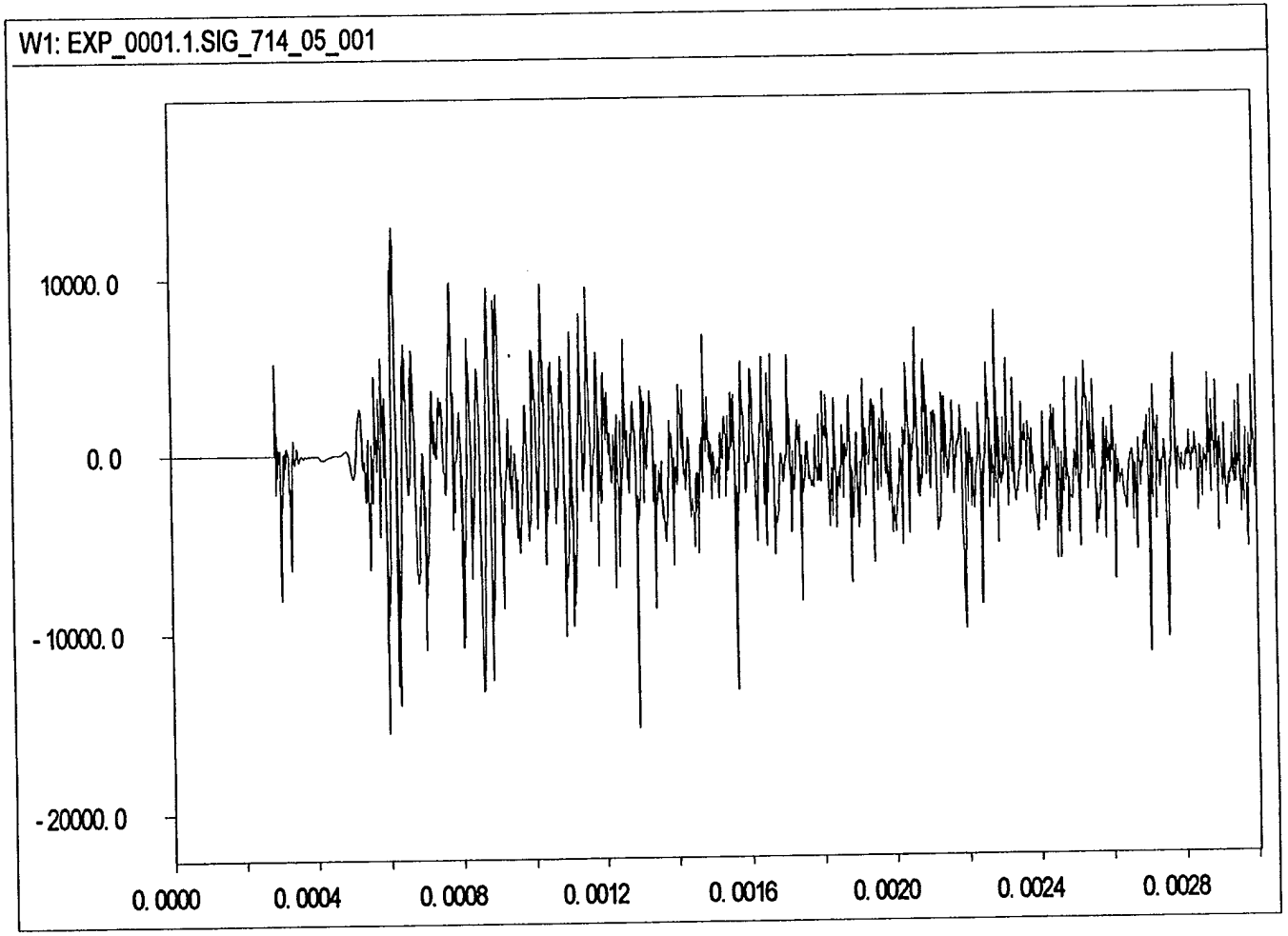


Figure A-77: Calibrated Output of Gauge #5, Shot #714.

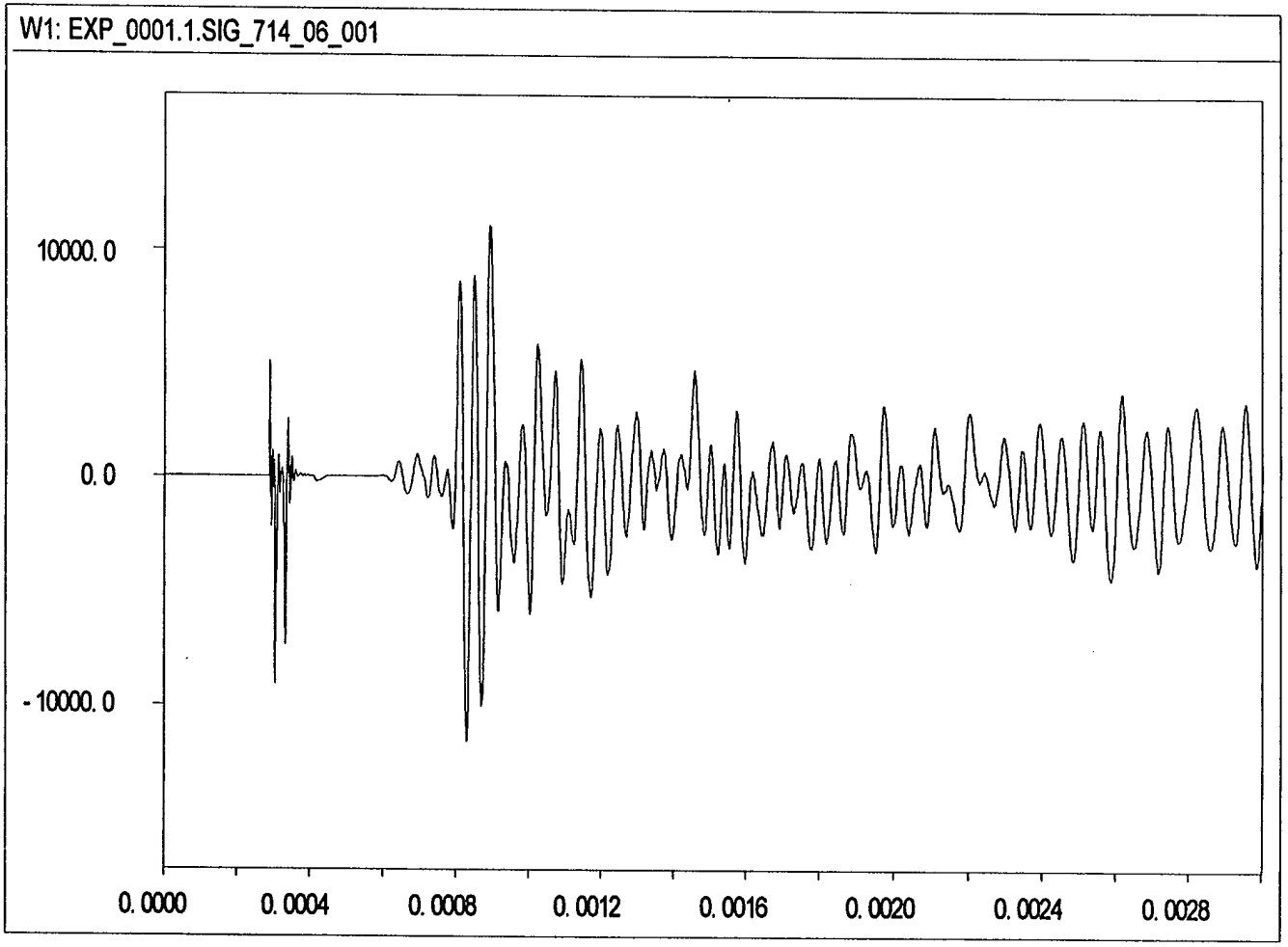


Figure A-78: Calibrated Output of Gauge #6, Shot #714.

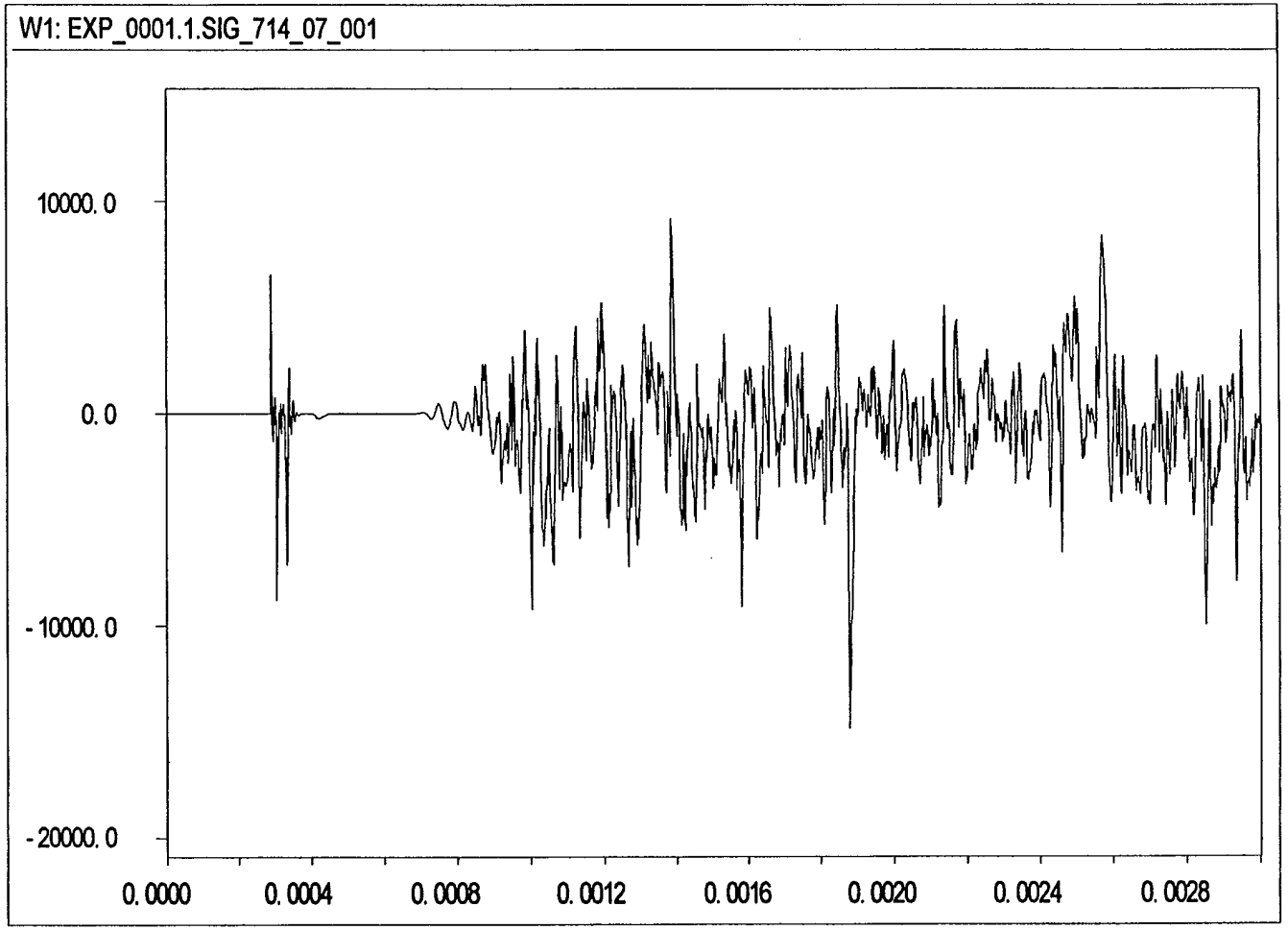


Figure A-79: Calibrated Output of Gauge #7, Shot #714.

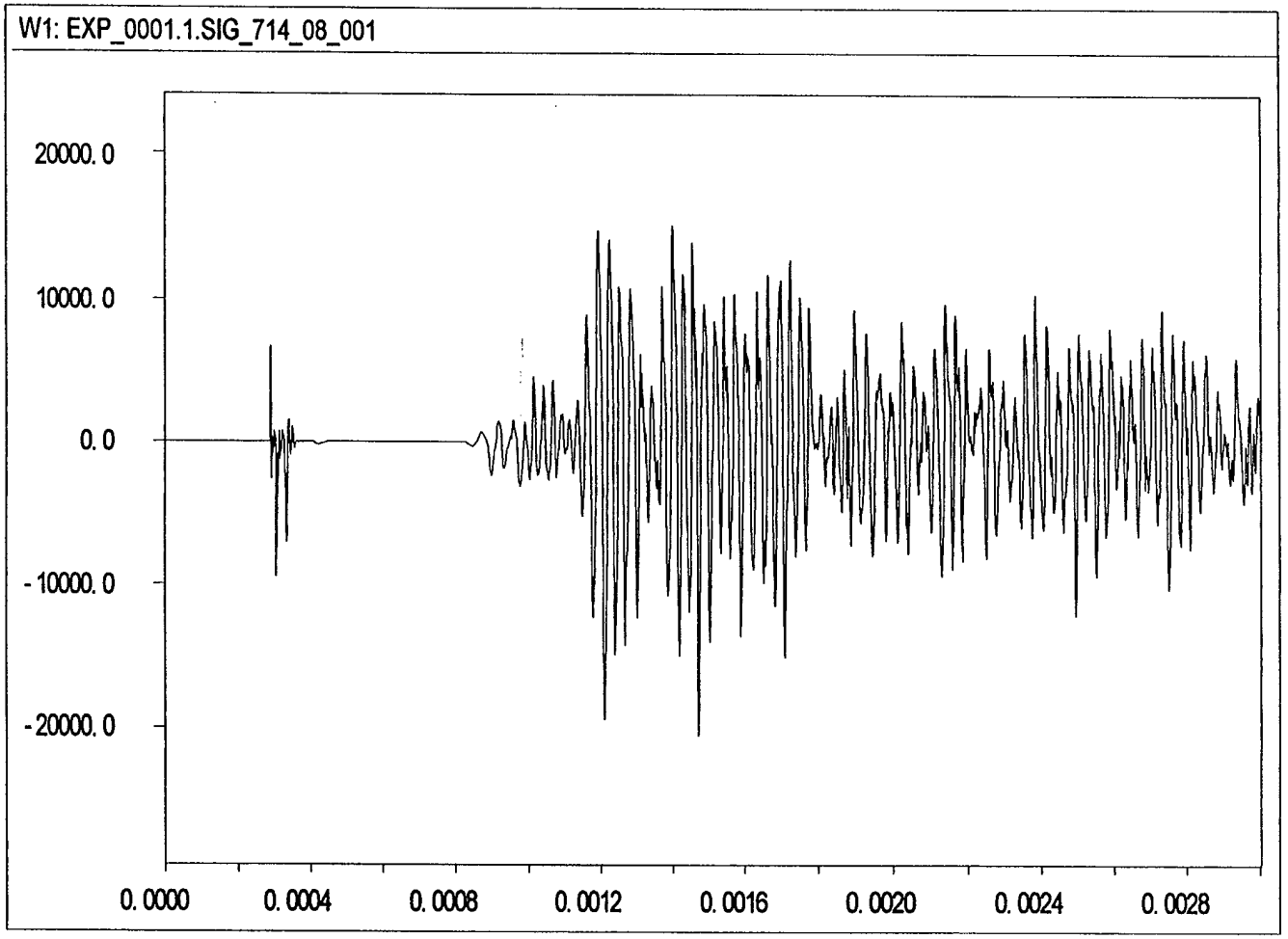


Figure A-80: Calibrated Output of Gauge #8, Shot #714.

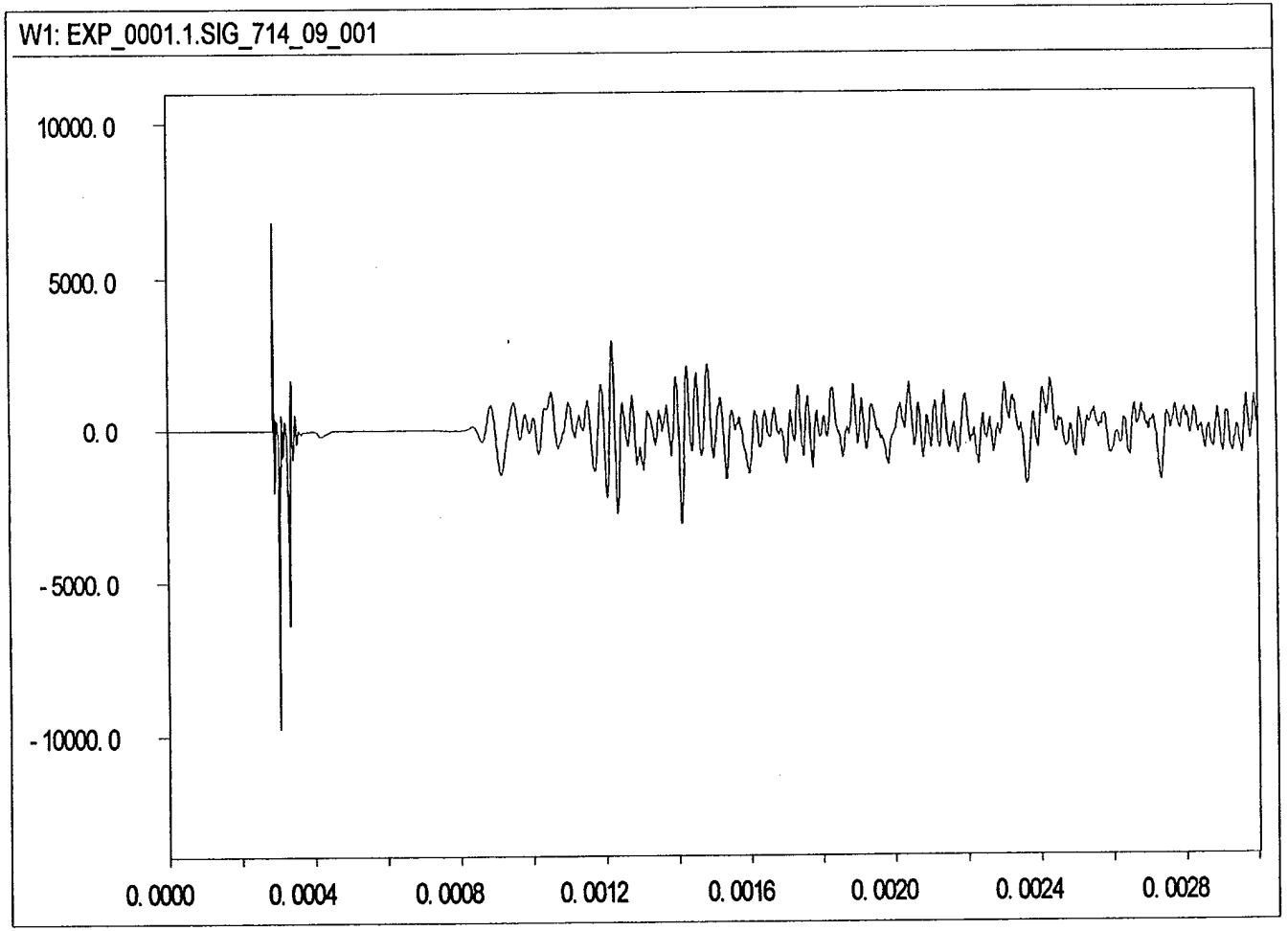


Figure A-81: Calibrated Output of Gauge #9, Shot #714.

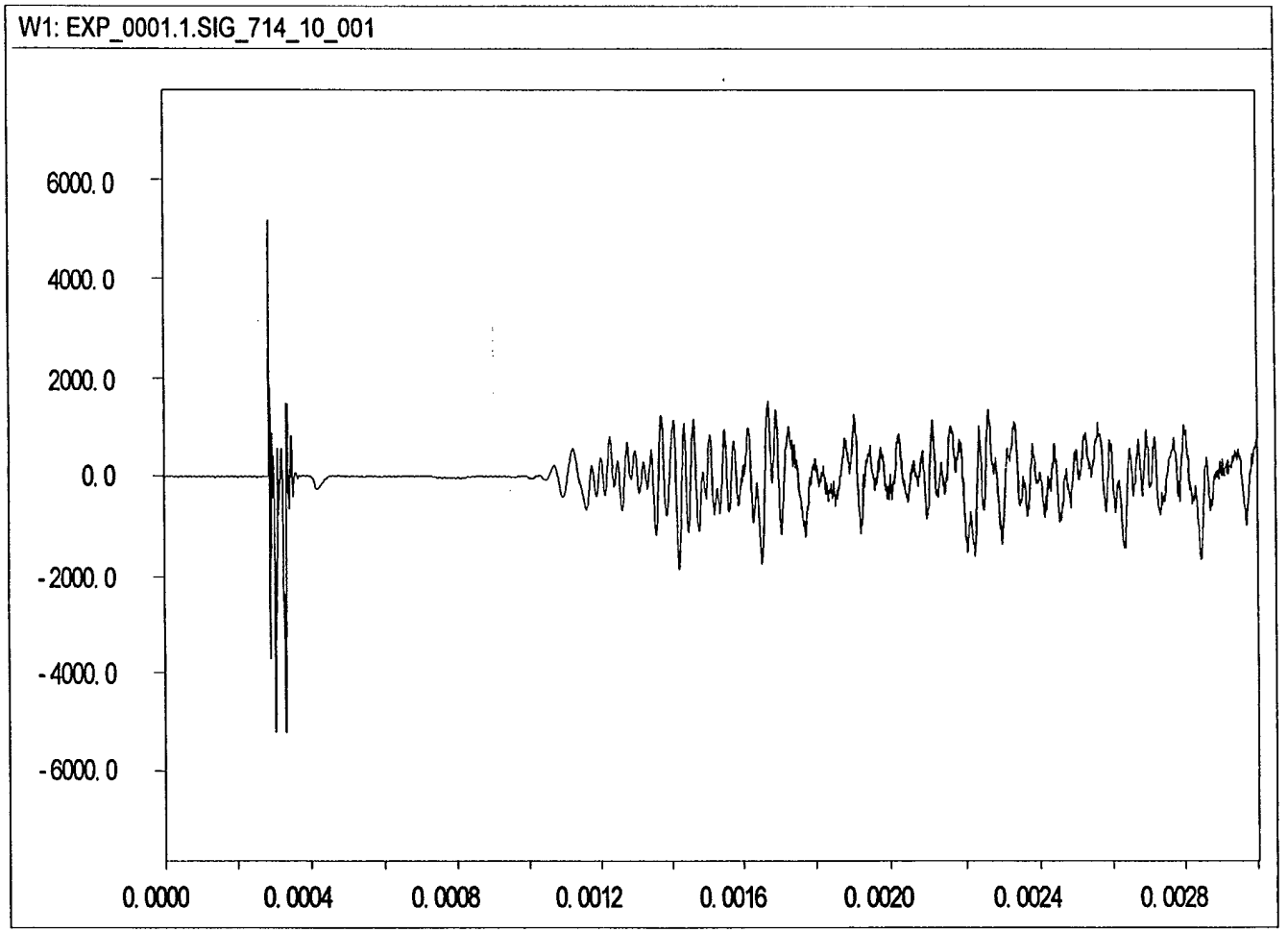


Figure A-82: Calibrated Output of Gauge #10, Shot #714.

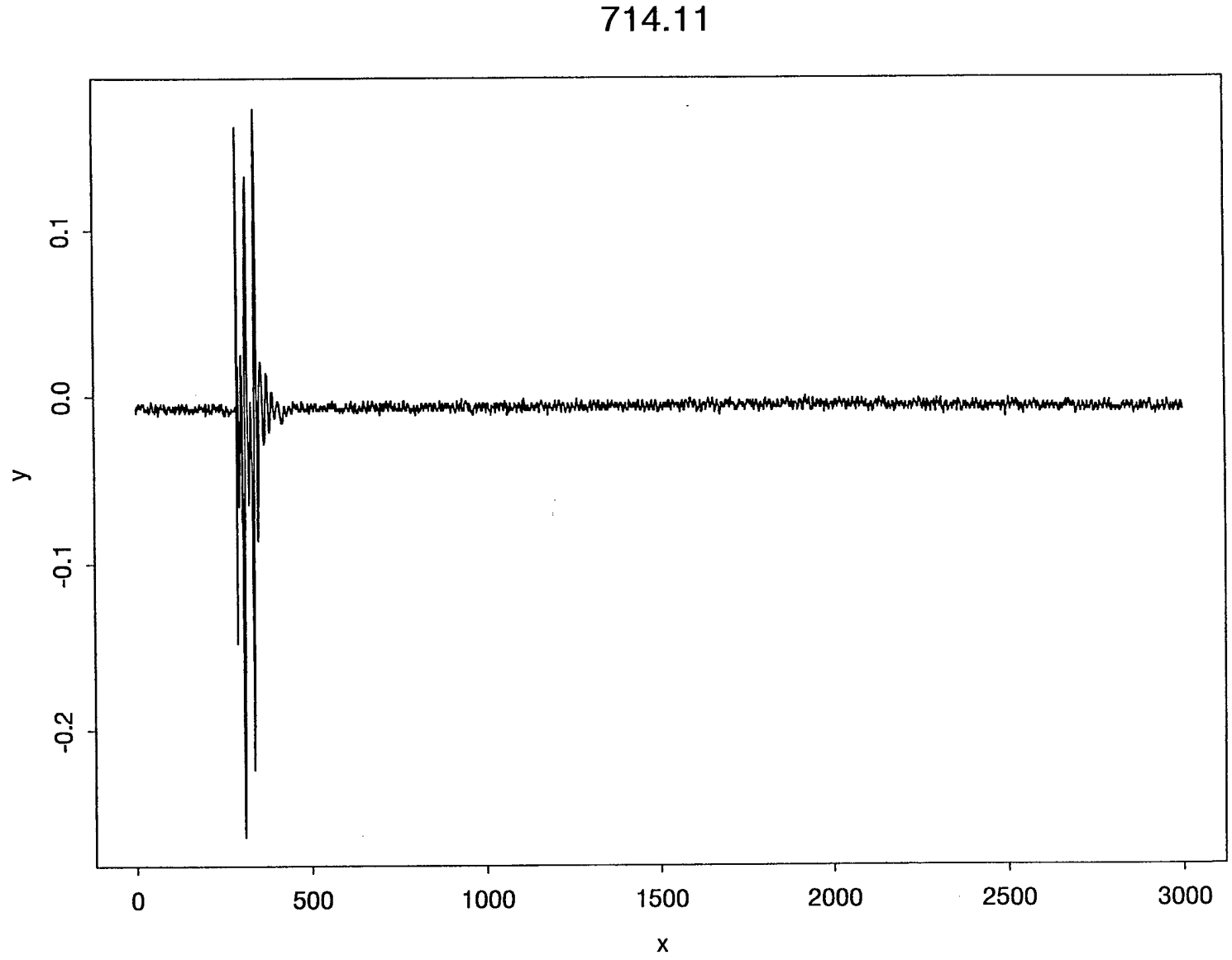


Figure A-83: Calibrated Output of Gauge #11, Shot #714.

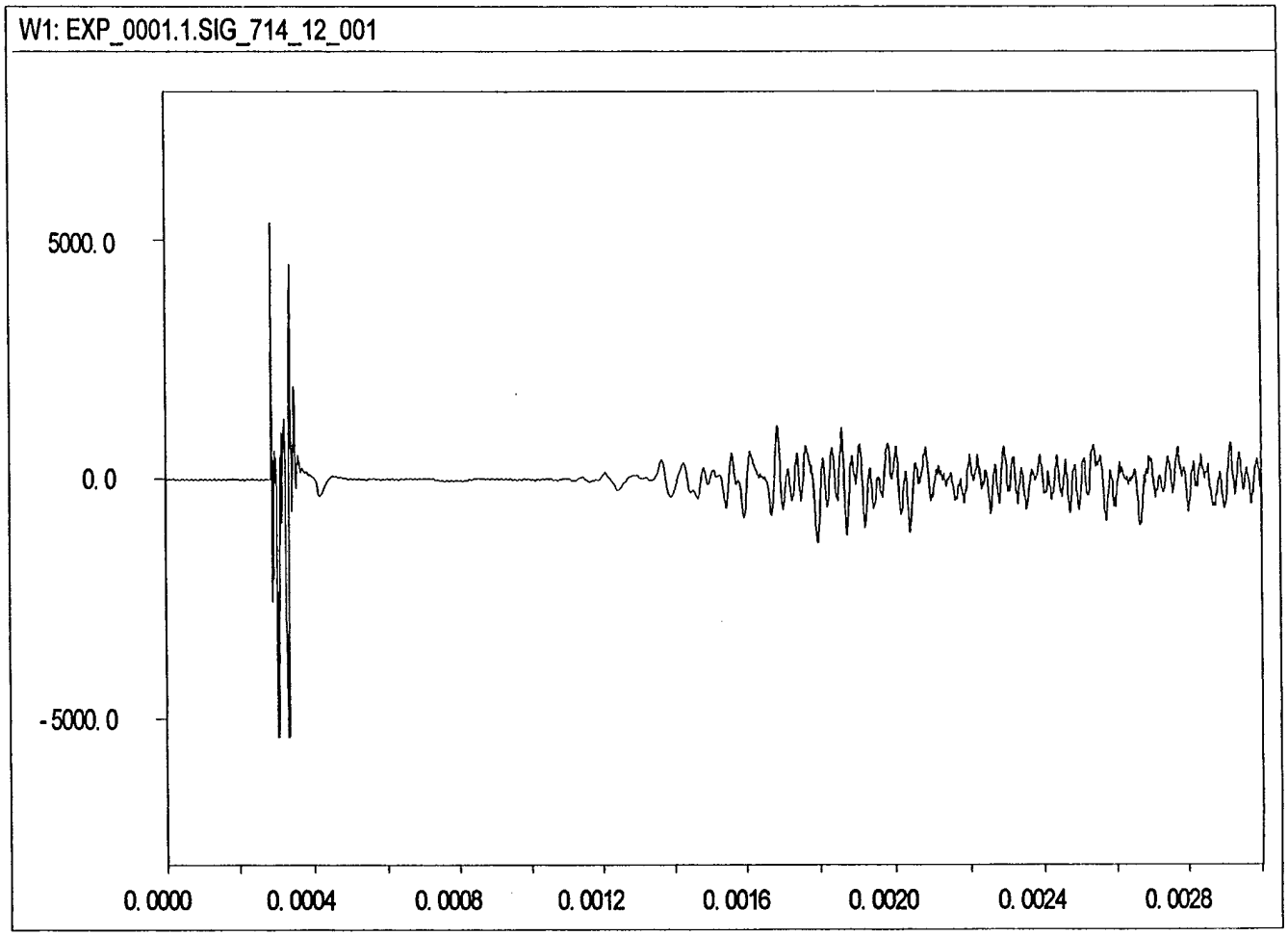


Figure A-84: Calibrated Output of Gauge #12, Shot #714.

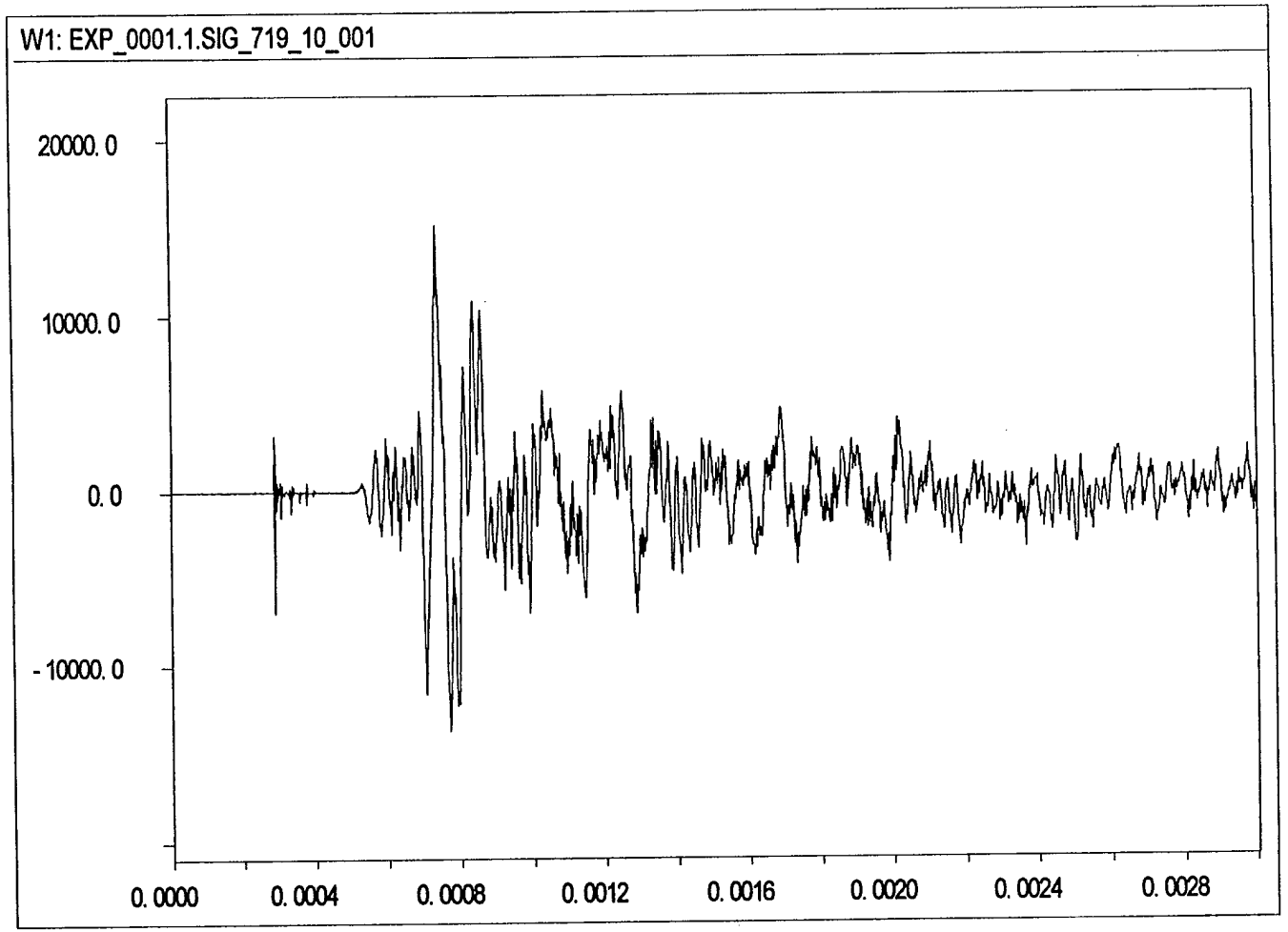


Figure A-85: Calibrated Output of Gauge #10, Shot #719 (Position 1).

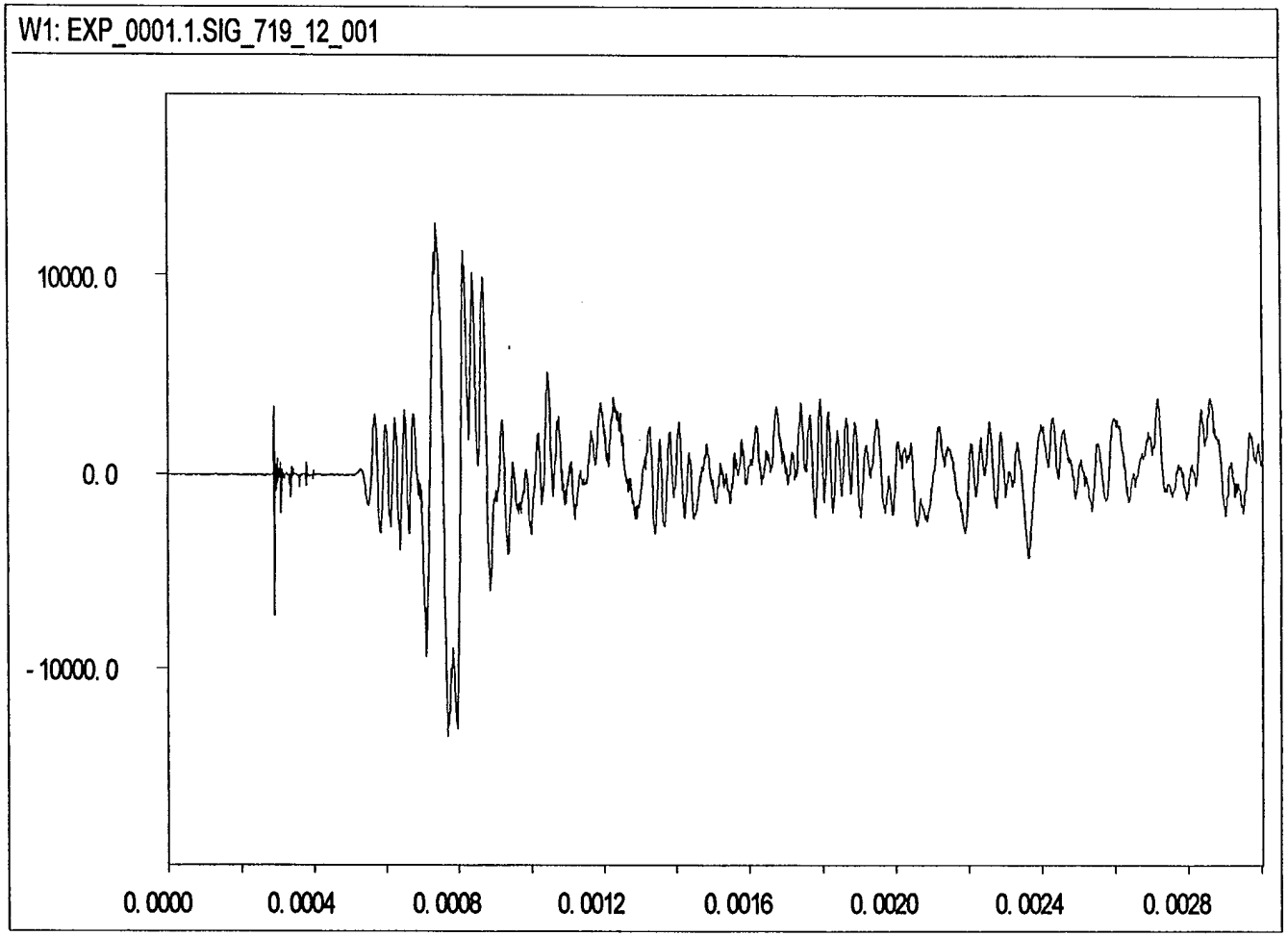


Figure A-86: Calibrated Output of Gauge #12, Shot #719 (Position 2).

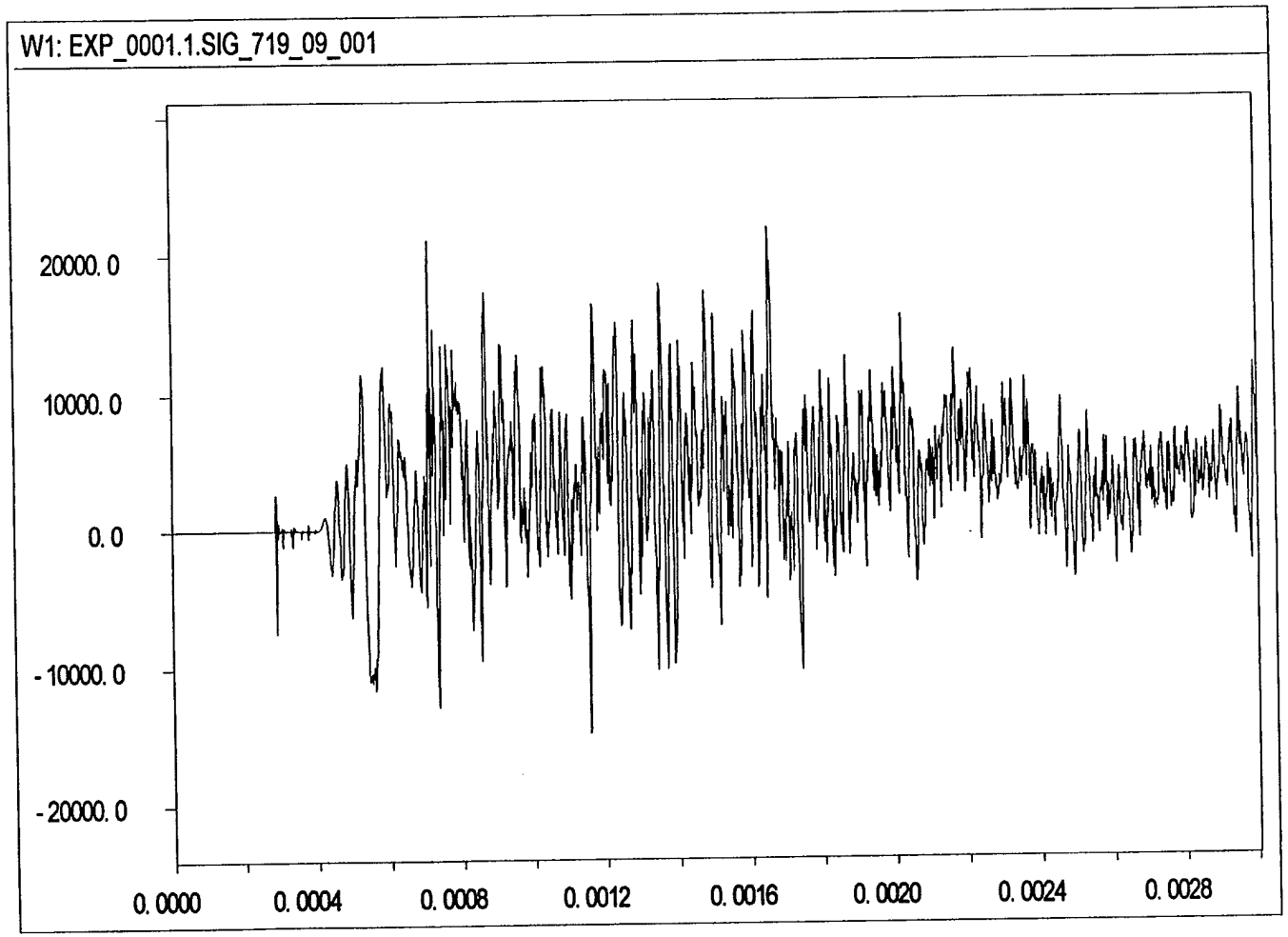


Figure A-87: Calibrated Output of Gauge #9, Shot #719 (Position 3).

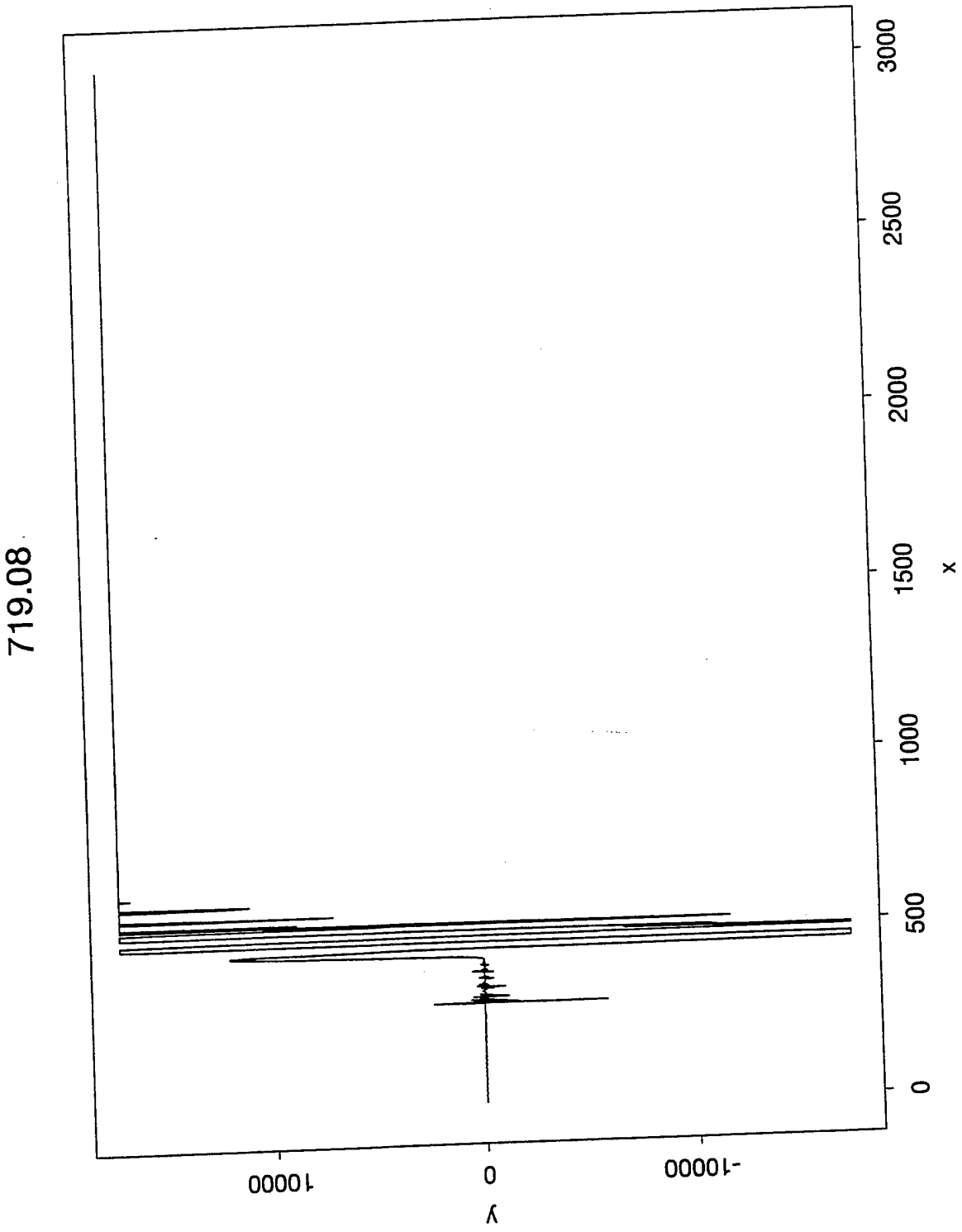


Figure A-88: Calibrated Output of Gauge #8, Shot #719 (Position 4).

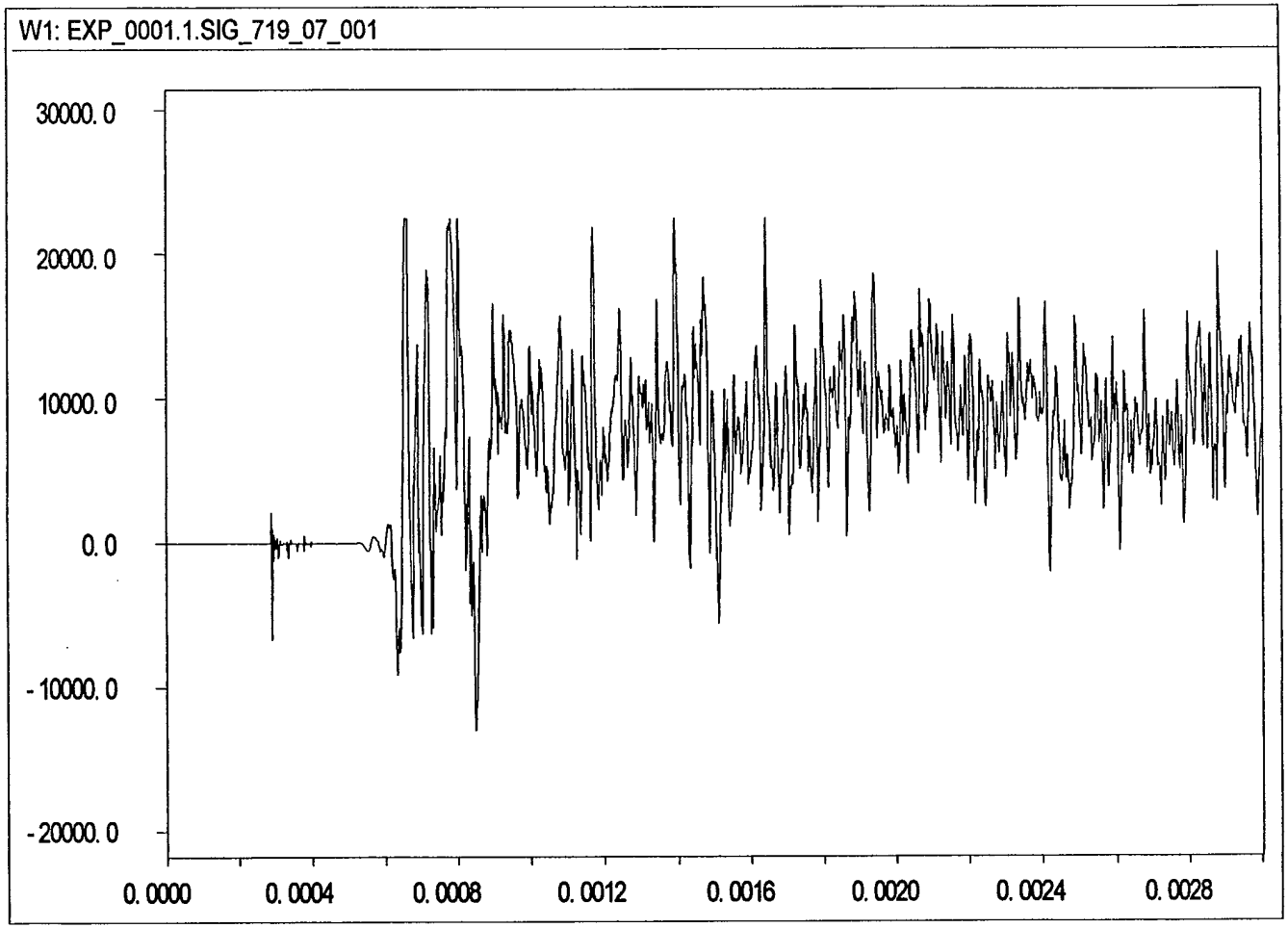


Figure A-89: Calibrated Output of Gauge #7, Shot #719 (Position 5).

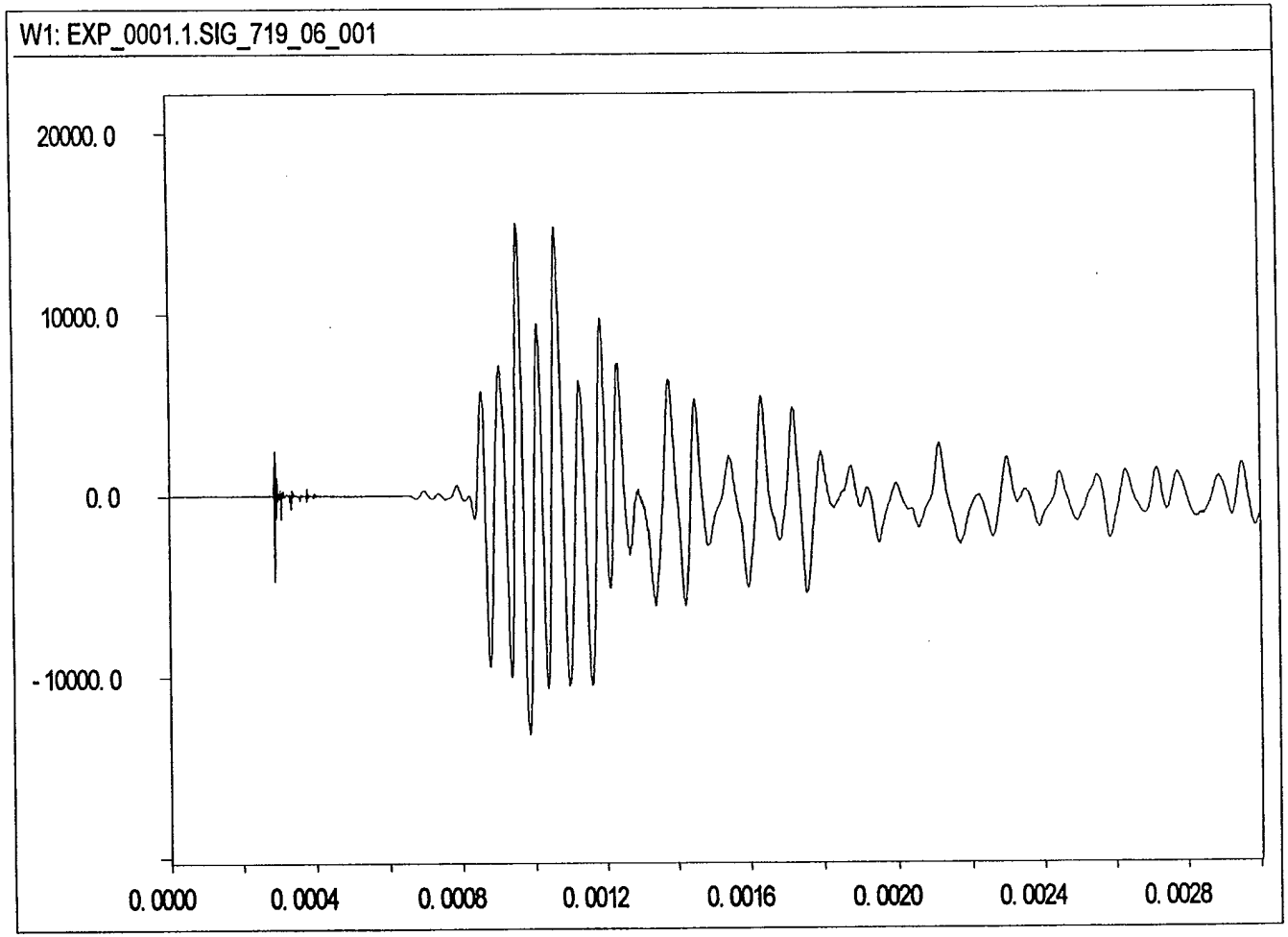


Figure A-90: Calibrated Output of Gauge #6, Shot #719 (Position 6).

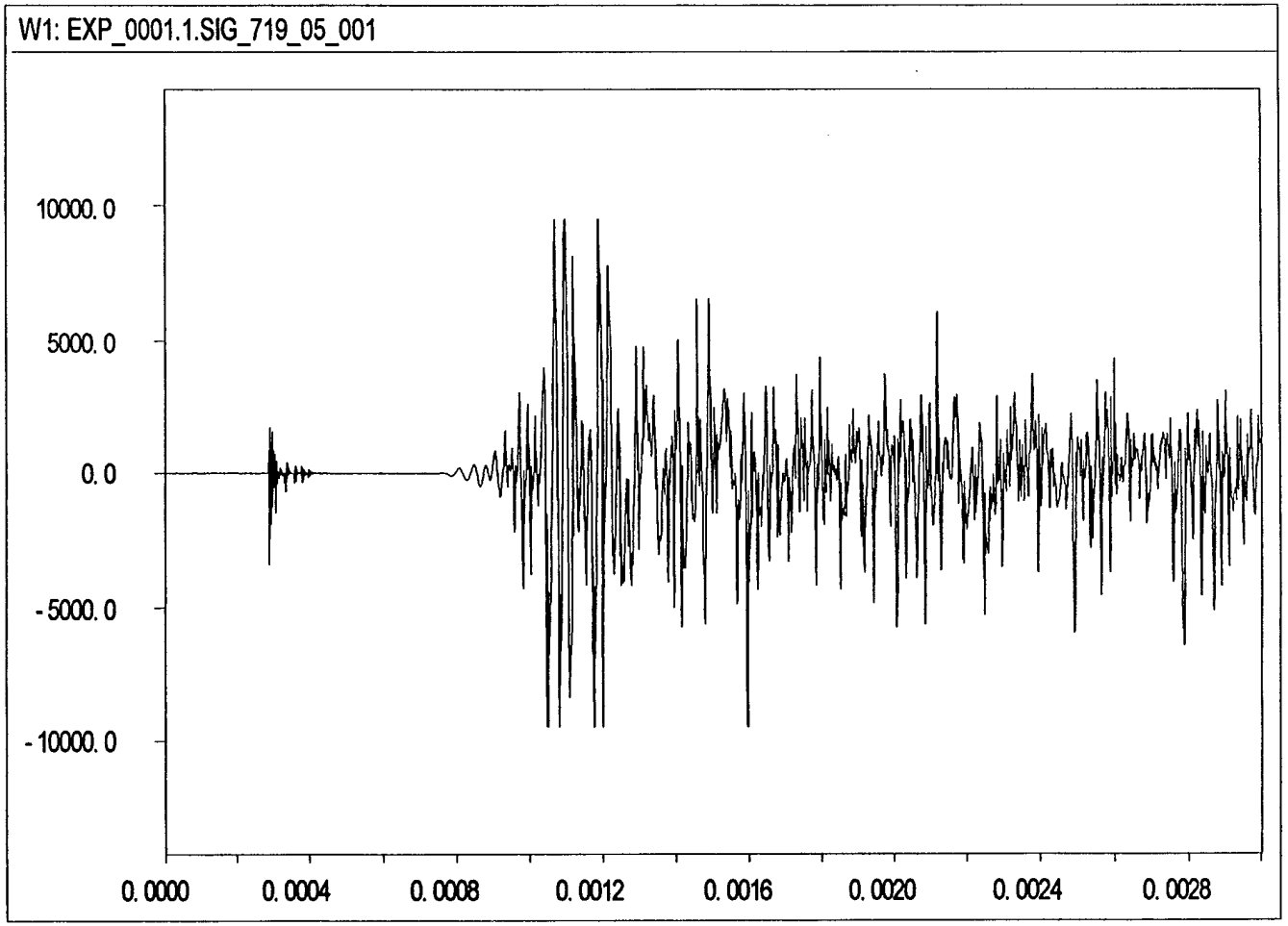


Figure A-91: Calibrated Output of Gauge #5, Shot #719 (Position 7).

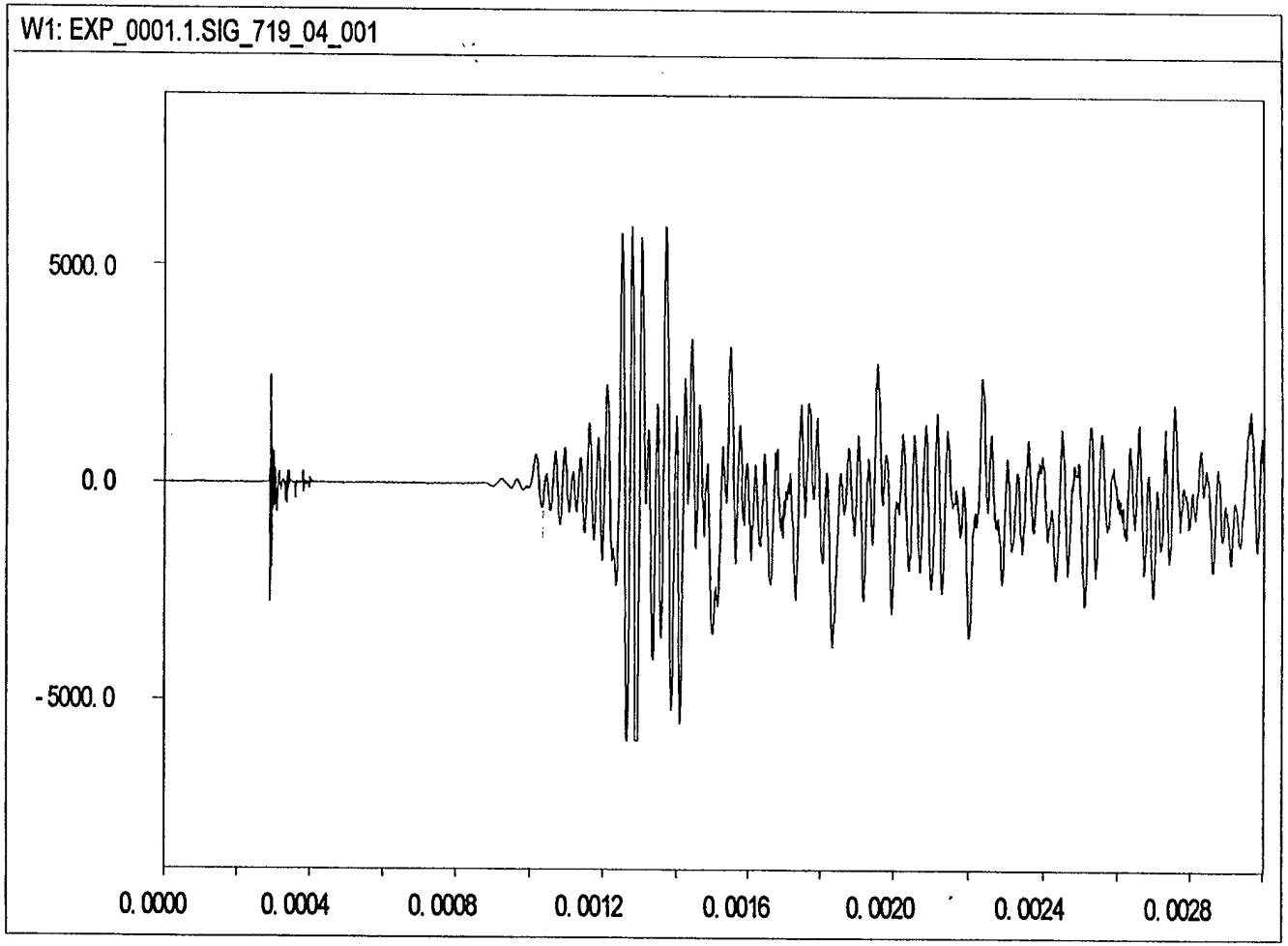


Figure A-92: Calibrated Output of Gauge #4, Shot #719 (Position 8).

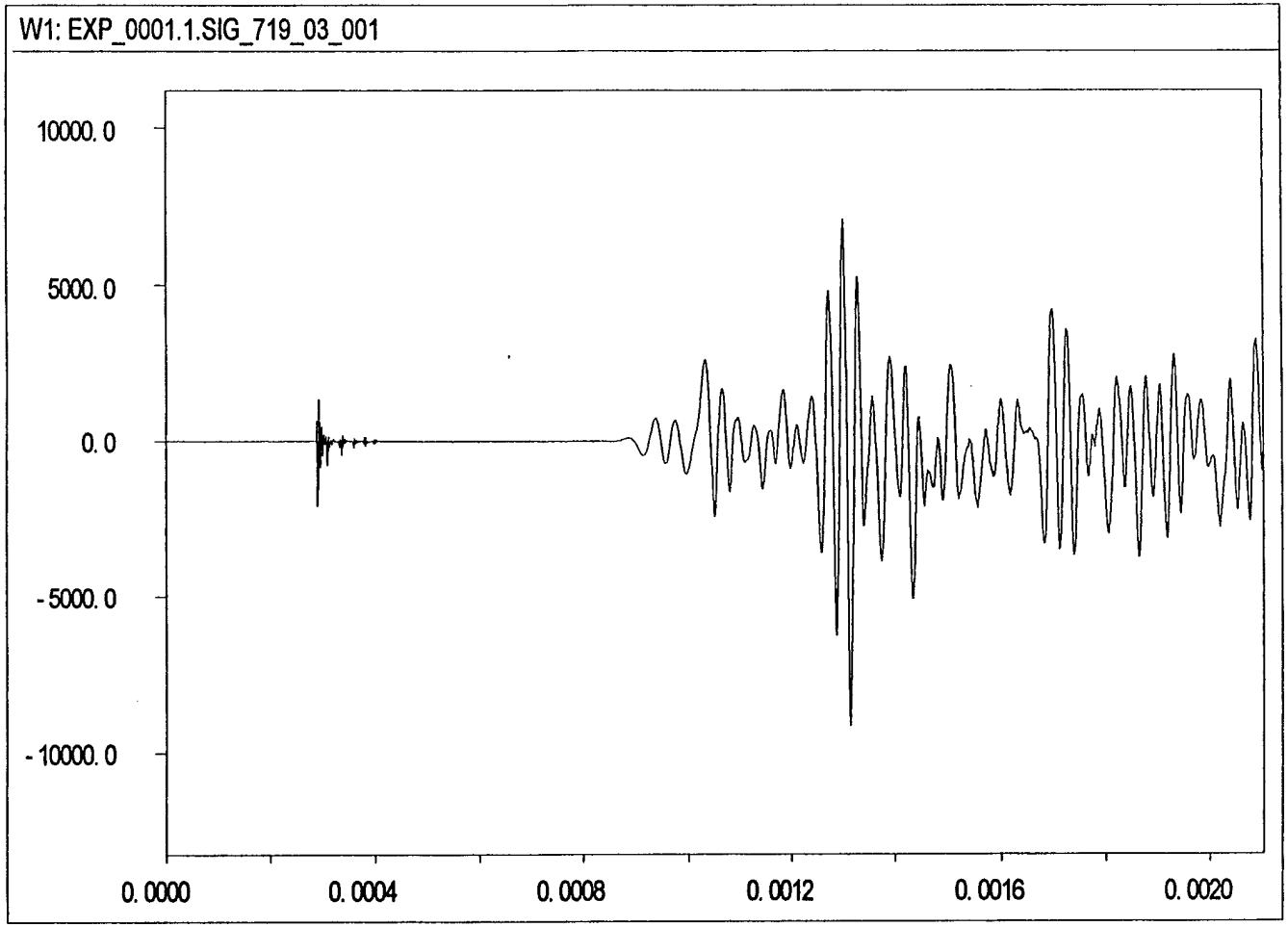


Figure A-93: Calibrated Output of Gauge #3, Shot #719 (Position 9).

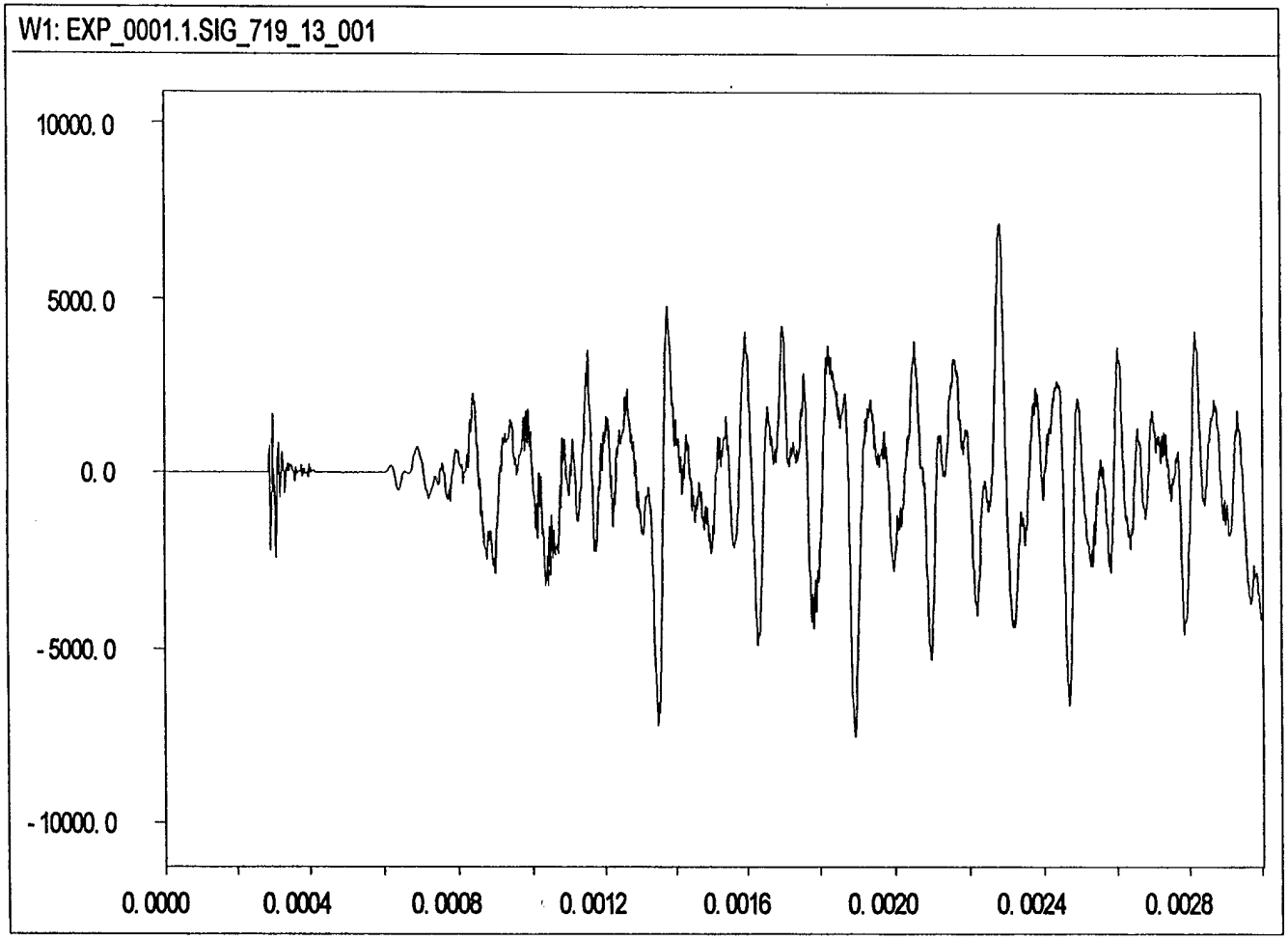


Figure A-94: Calibrated Output of Gauge #13, Shot #719 (Position 10).

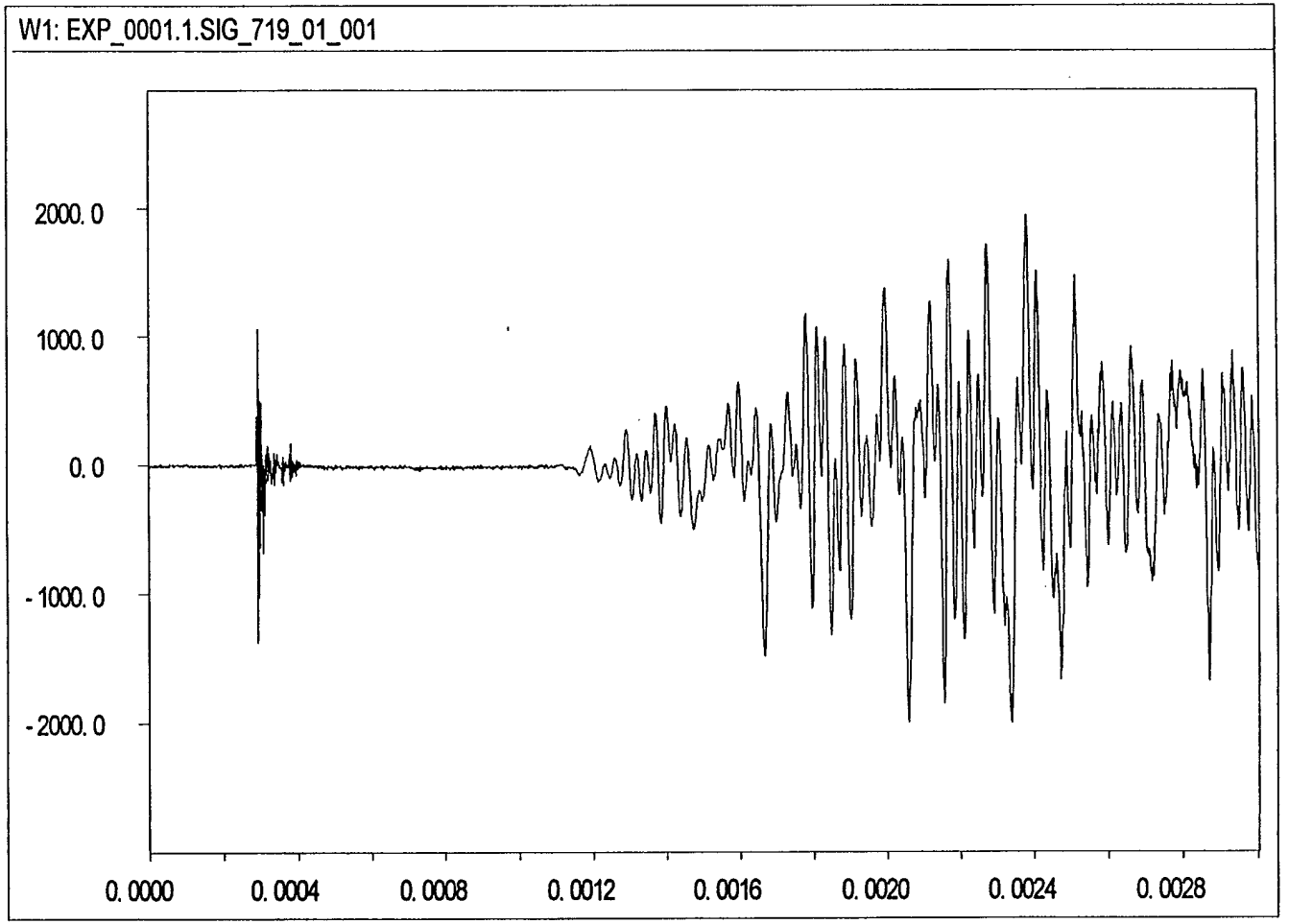


Figure A-95: Calibrated Output of Gauge #1, Shot #719 (Position 11).

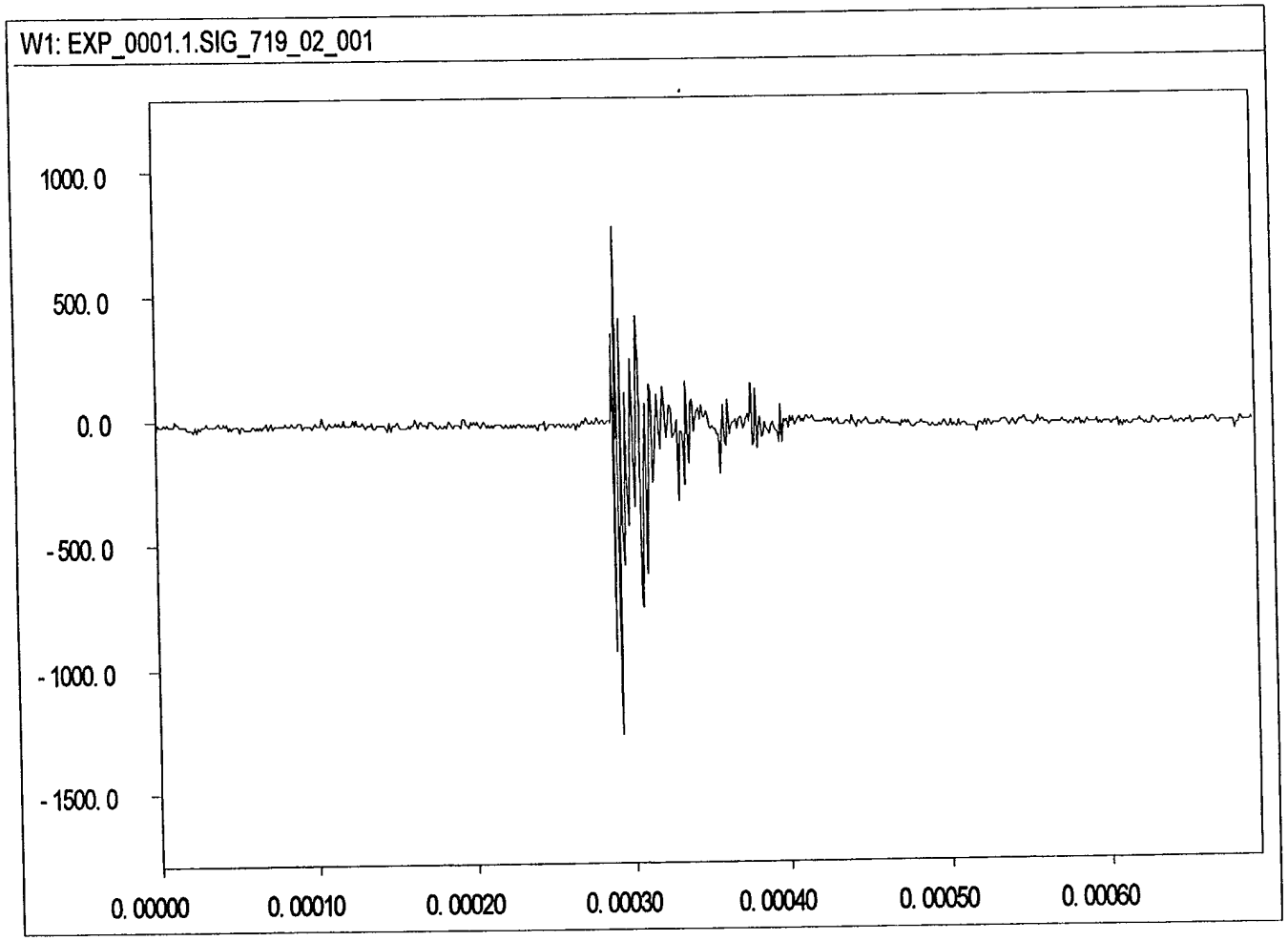


Figure A-96: Calibrated Output of Gauge #2, Shot #719 (Position 12).

# Appendix B

# Normalized Data - Each Shot

This page intentionally left blank

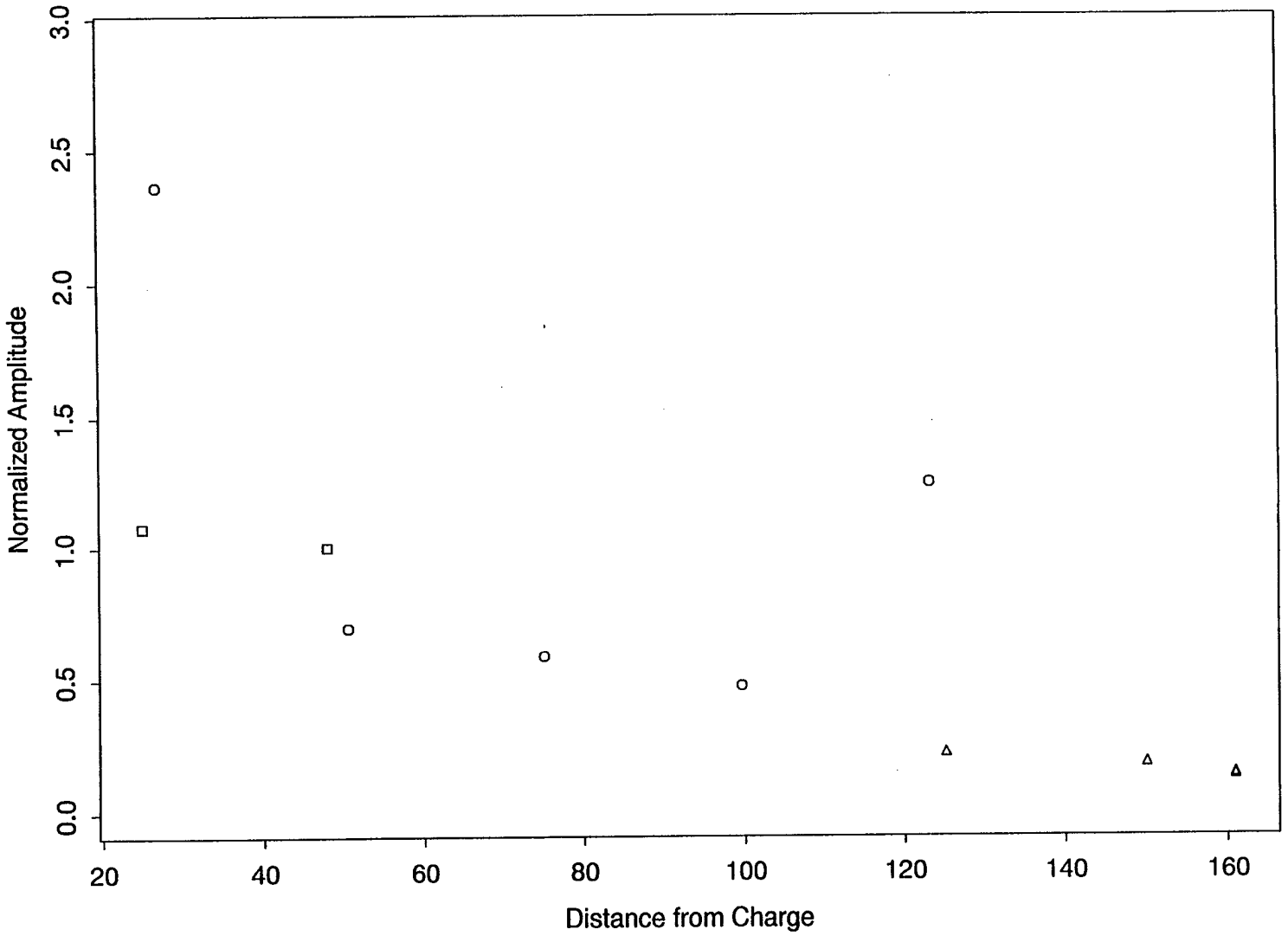


Figure B-1: Normalized Amplitudes by Distance From Shock Point - Shot #695.

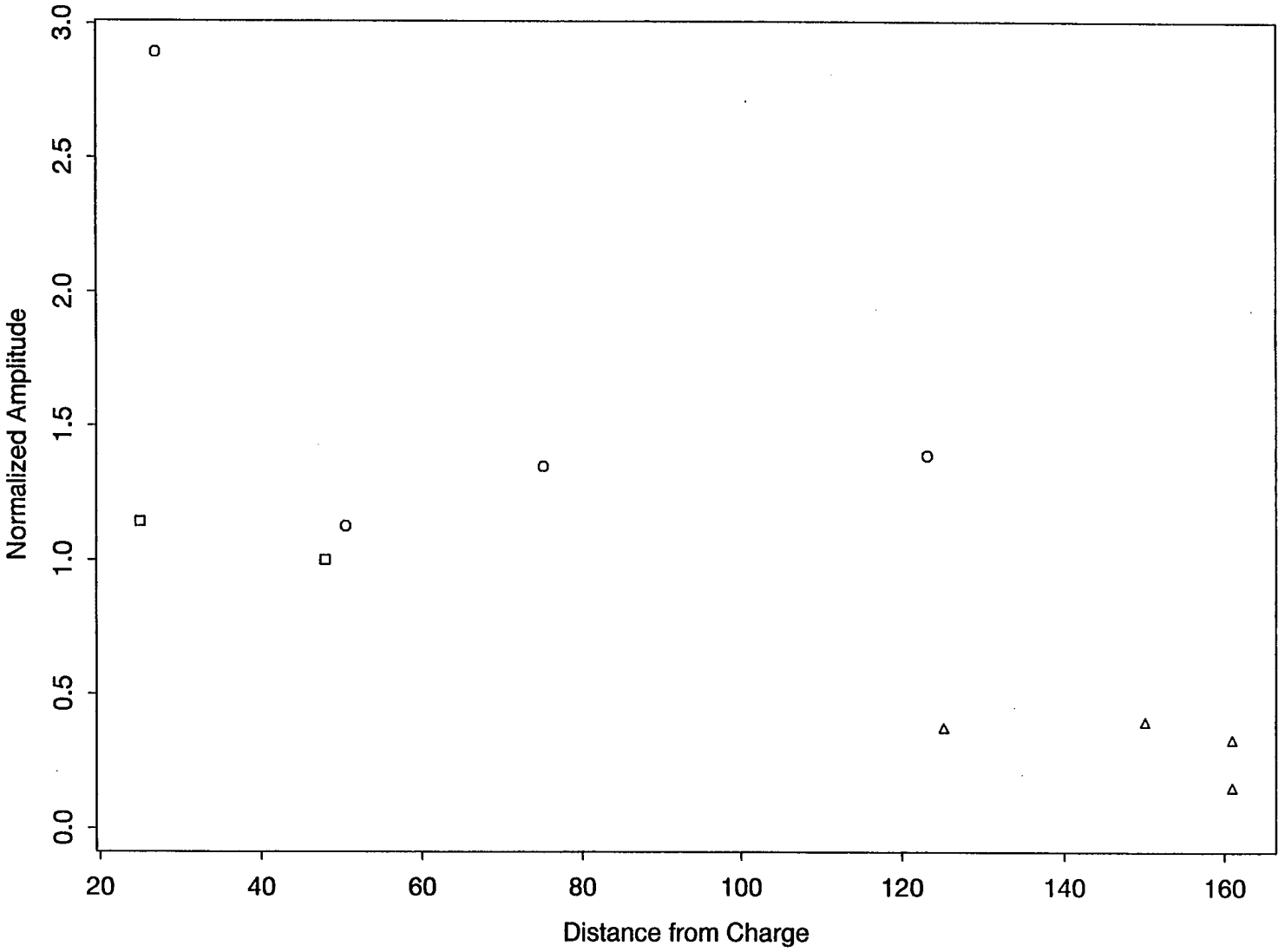


Figure B-2: Normalized Amplitudes by Distance From Shock Point - Shot #698.

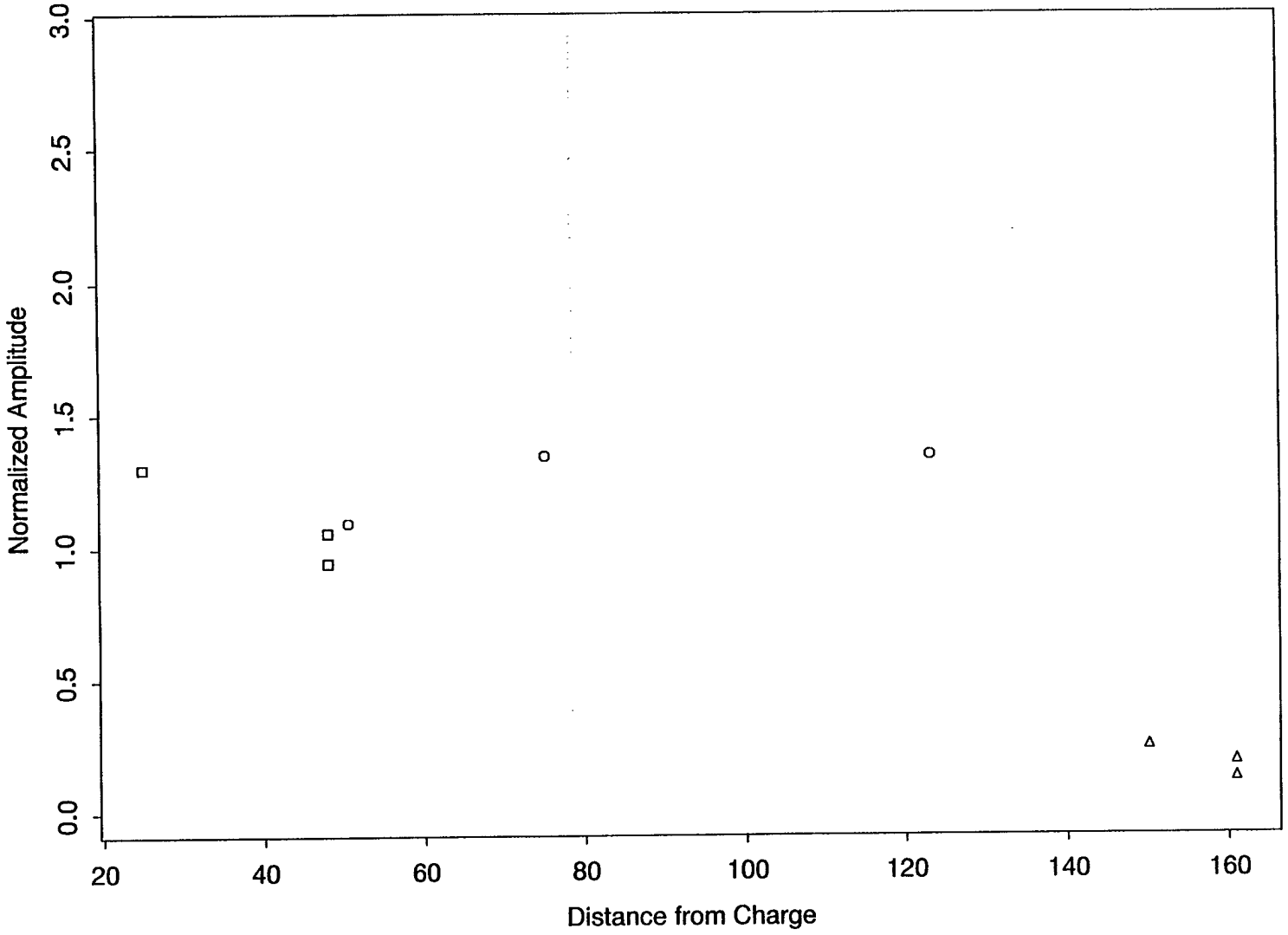


Figure B-3: Normalized Amplitudes by Distance From Shock Point - Shot #708.

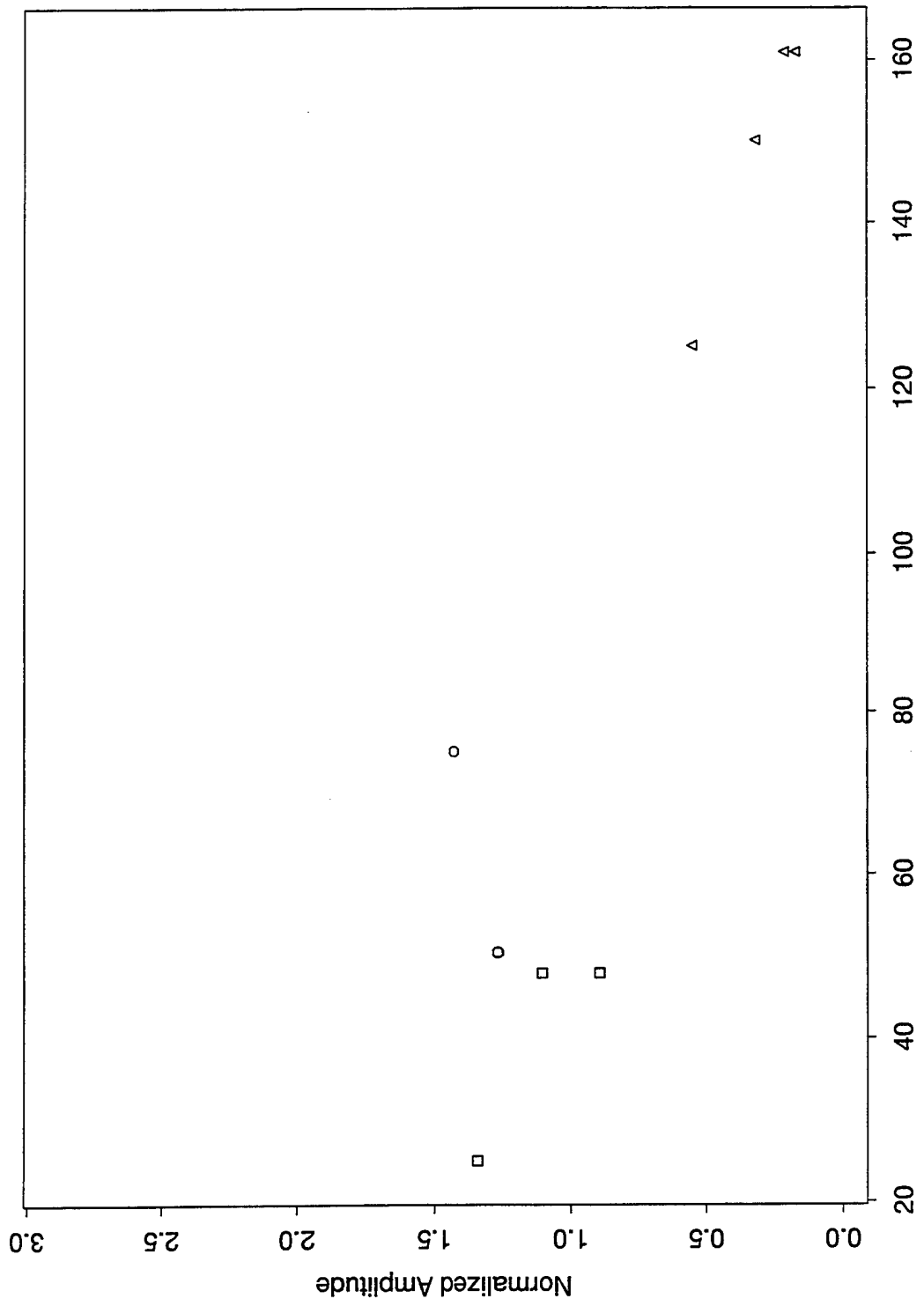


Figure B-4: Normalized Amplitudes by Distance From Shock Point - Shot #709.

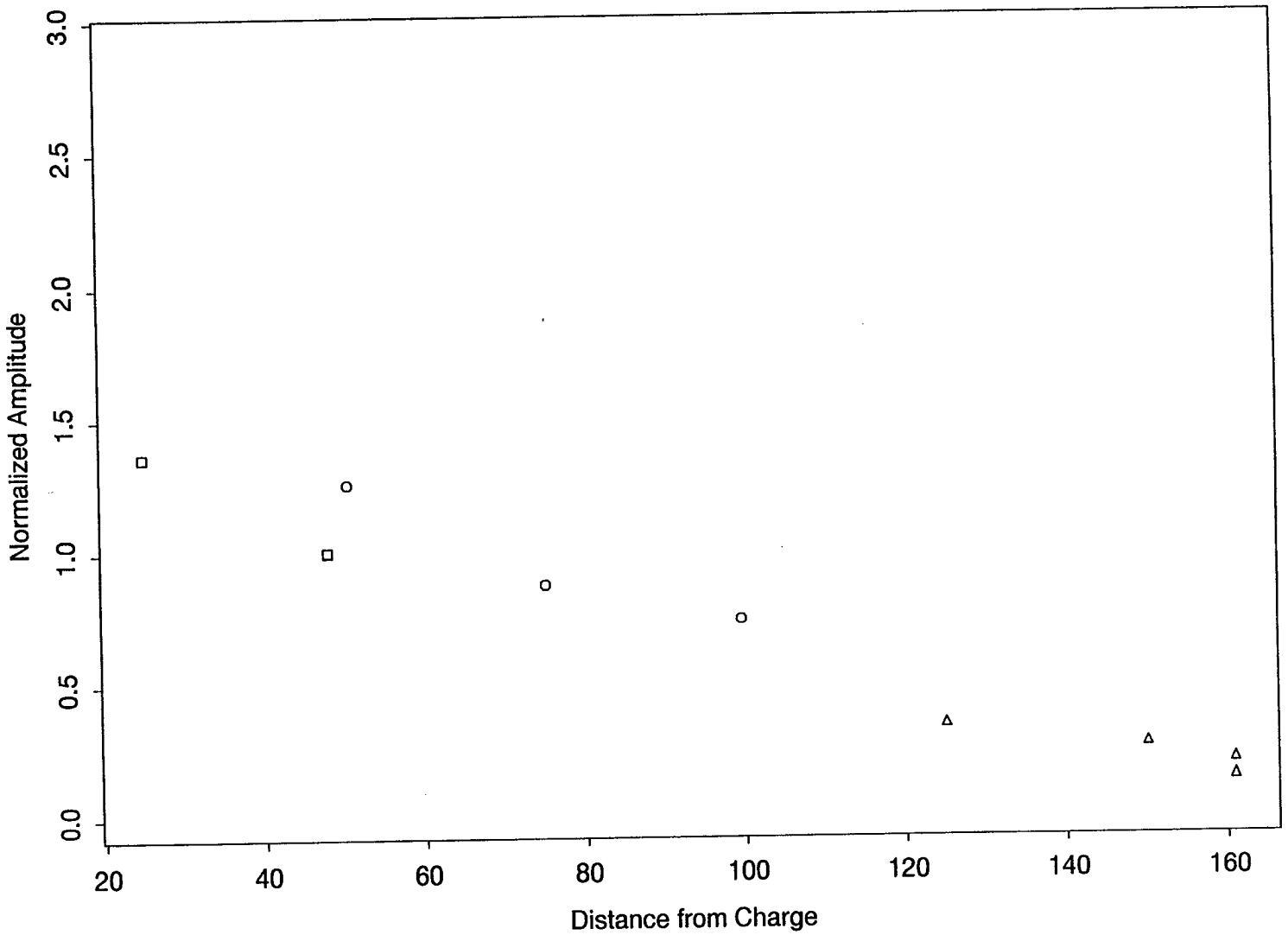


Figure B-5: Normalized Amplitudes by Distance From Shock Point - Shot #712.

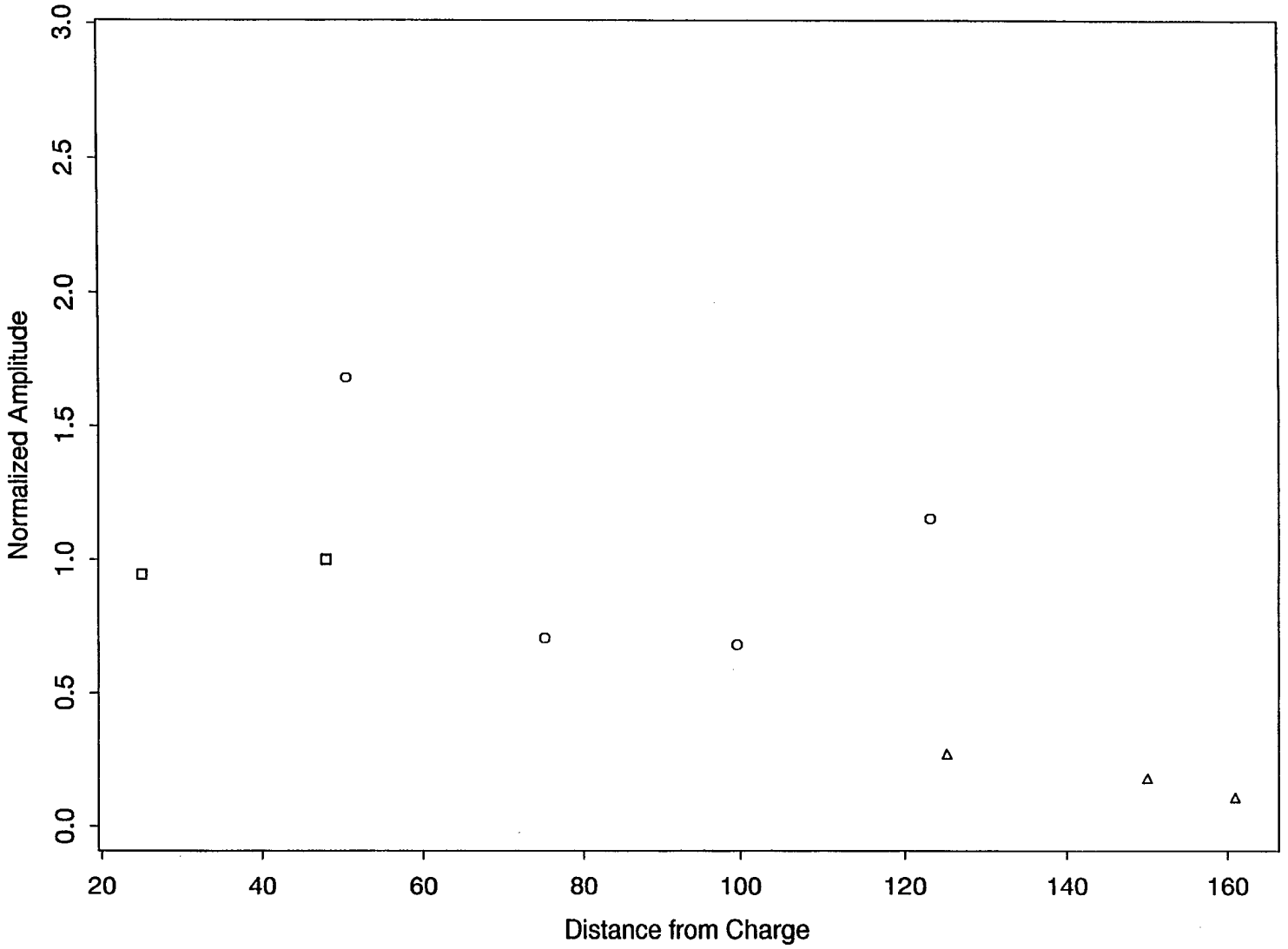


Figure B-6: Normalized Amplitudes by Distance From Shock Point - Shot #713.

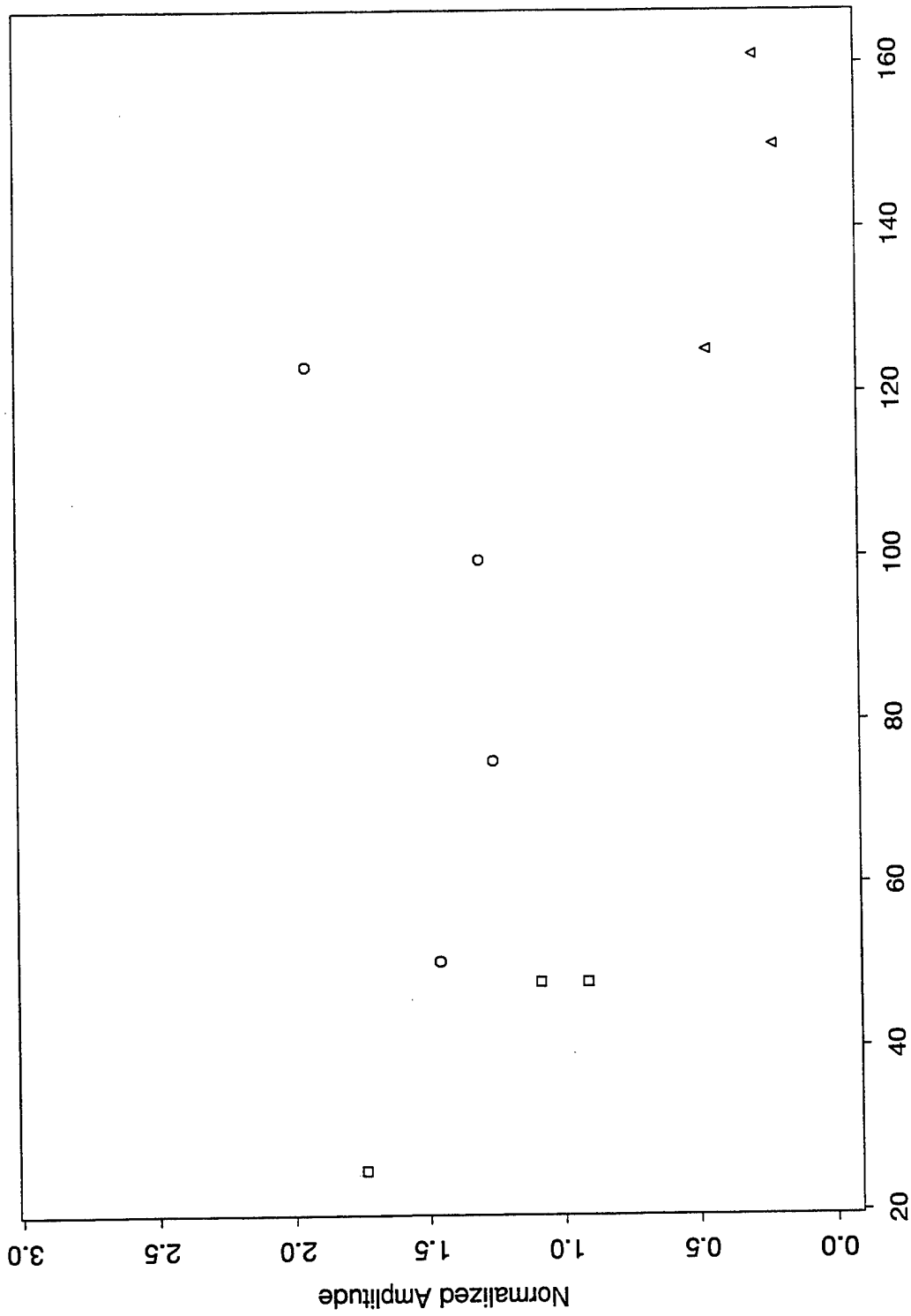


Figure B-7: Normalized Amplitudes by Distance From Shock Point - Shot #714.

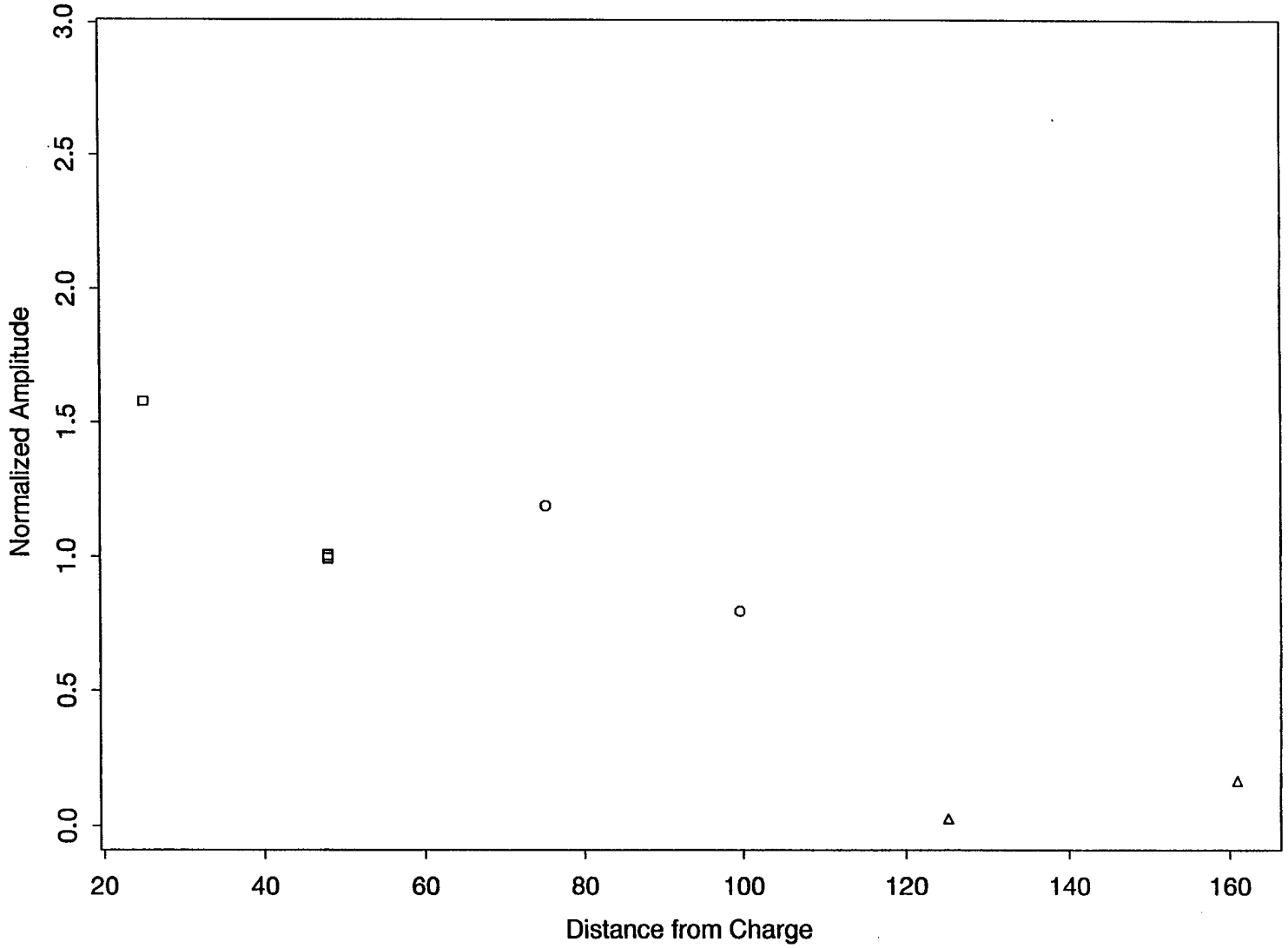


Figure B-8: Normalized Amplitudes by Distance From Shock Point - Shot #719.

NO. OF COPIES ORGANIZATION

2 DEFENSE TECHNICAL INFORMATION CENTER
DTIC DDA
8725 JOHN J KINGMAN RD
STE 0944
FT BELVOIR VA 22060-6218

1 HQDA
DAMO FDQ
DENNIS SCHMIDT
400 ARMY PENTAGON
WASHINGTON DC 20310-0460

1 CECOM
SP & TRRSTRL COMMCTN DIV
AMSEL RD ST MC M
H SOICHER
FT MONMOUTH NJ 07703-5203

1 PRIN DPTY FOR TCHNLGY HQ
US ARMY MATCOM
AMCDCG T
M FISETTE
5001 EISENHOWER AVE
ALEXANDRIA VA 22333-0001

1 PRIN DPTY FOR ACQUSTN HQS
US ARMY MATCOM
AMCDCG A
D ADAMS
5001 EISENHOWER AVE
ALEXANDRIA VA 22333-0001

1 DPTY CG FOR RDE HQS
US ARMY MATCOM
AMCRD
BG BEAUCHAMP
5001 EISENHOWER AVE
ALEXANDRIA VA 22333-0001

1 DPTY ASSIST SCY FOR R&T
SARD TT T KILLION
THE PENTAGON
WASHINGTON DC 20310-0103

1 OSD
OUSD(A&T)/ODDDR&E(R)
J LUPO
THE PENTAGON
WASHINGTON DC 20301-7100

NO. OF COPIES ORGANIZATION

1 INST FOR ADVNCD TCHNLGY
THE UNIV OF TEXAS AT AUSTIN
PO BOX 202797
AUSTIN TX 78720-2797

1 USAASA
MOAS AI W PARRON
9325 GUNSTON RD STE N319
FT BELVOIR VA 22060-5582

1 CECOM
PM GPS COL S YOUNG
FT MONMOUTH NJ 07703

1 GPS JOINT PROG OFC DIR
COL J CLAY
2435 VELA WAY STE 1613
LOS ANGELES AFB CA 90245-5500

1 ELECTRONIC SYS DIV DIR
CECOM RDEC
J NIEMELA
FT MONMOUTH NJ 07703

3 DARPA
L STOTTS
J PENNELLA
B KASPAR
3701 N FAIRFAX DR
ARLINGTON VA 22203-1714

1 SPCL ASST TO WING CMNDR
50SW/CCX
CAPT P H BERNSTEIN
300 O'MALLEY AVE STE 20
FALCON AFB CO 80912-3020

1 USAF SMC/CED
DMA/JPO
M ISON
2435 VELA WAY STE 1613
LOS ANGELES AFB CA
90245-5500

1 US MILITARY ACADEMY
MATH SCI CTR OF EXCELLENCE
DEPT OF MATHEMATICAL SCI
MDN A MAJ DON ENGEN
THAYER HALL
WEST POINT NY 10996-1786

NO. OF
COPIES ORGANIZATION

1 DIRECTOR
US ARMY RESEARCH LAB
AMSRL CS AL TP
2800 POWDER MILL RD
ADELPHI MD 20783-1145

1 DIRECTOR
US ARMY RESEARCH LAB
AMSRL CS AL TA
2800 POWDER MILL RD
ADELPHI MD 20783-1145

3 DIRECTOR
US ARMY RESEARCH LAB
AMSRL CI LL
2800 POWDER MILL RD
ADELPHI MD 20783-1145

ABERDEEN PROVING GROUND

4 DIR USARL
AMSRL CI LP (305)

NO. OF COPIES ORGANIZATION

1 OSD OUSD AT
STRT TAC SYS
DR SCHNEITER
3090 DEFNS PENTAGON RM 3E130
WASHINGTON DC 20301-3090

1 ASST SECY ARMY RESEARCH
DEVELOPMENT ACQUISITION
SARD ZD RM 2E673
103 ARMY PENTAGON
WASHINGTON DC 20310-0103

1 ASST SECY ARMY RESEARCH
DEVELOPMENT ACQUISITION
SARD ZP RM 2E661
103 ARMY PENTAGON
WASHINGTON DC 20310-0103

1 ASST SECY ARMY RESEARCH
DEVELOPMENT ACQUISITION
SARD ZS RM 3E448
103 ARMY PENTAGON
WASHINGTON DC 20310-0103

1 ASST SECY ARMY RESEARCH
DEVELOPMENT ACQUISITION
SARD ZT RM 3E374
103 ARMY PENTAGON
WASHINGTON DC 20310-0103

1 UNDER SEC OF THE ARMY
DUSA OR
RM 2E660
102 ARMY PENTAGON
WASHINGTON DC 20310-0102

1 ASST DEP CHIEF OF STAFF
OPERATIONS AND PLANS
DAMO FDZ RM 3A522
460 ARMY PENTAGON
WASHINGTON DC 20310-0460

1 DEPUTY CHIEF OF STAFF
OPERATIONS AND PLANS
DAMO SW RM 3C630
400 ARMY PENTAGON
WASHINGTON DC 20310-0400

NO. OF COPIES ORGANIZATION

1 ARMY RESEARCH LABORATORY
AMSRL SL
PROGRAMS AND PLANS MGR
WSMR NM 88002-5513

ABERDEEN PROVING GROUND

1 CDR USATECOM
AMSTE-TA

2 DIR USAMSAA
AMXSY-ST
AMXSY-D

4 DIR USARL
AMSRL-SL,
J WADE (433)
M STARKS (433)
AMSRL-SL-C, J BEILFUSS (E3331)
AMSRL-SL-B, P DEITZ (328)

NO. OF COPIES ORGANIZATION

1 DIR OPERATIONAL TEST & EVAL
ERNEST SEGLIE
RM 3E318
1700 DEFENSE PENTAGON
WASHINGTON DC 20301-1700

1 DIR OPERATIONAL TEST & EVAL
JAMES F O'BRYON
RM 1C730A
1700 DEFENSE PENTAGON
WASHINGTON DC 20301-1700

1 ODDRNE AT
DIR WEAPONS TECH
ATTN WES KITCHENS
3080 DEFENSE PENTAGON
WASHINGTON DC 20301-3080

1 UNDER SECY OF THE ARMY
SAUS OR
DANIEL WILLARD
102 ARMY PENTAGON
WASHINGTON DC 20310-0102

1 ASST SECY ARMY RESEARCH
DEVELOPMENT ACQUISITION
SARD ZD DR HERBERT FALLIN
RM 2E673
103 ARMY PENTAGON
WASHINGTON DC 20310-0103

1 ASST SECY ARMY RESEARCH
DEVELOPMENT ACQUISITION
SARD TR TOM KILLION
RM 3E480
103 ARMY PENTAGON
WASHINGTON DC 20310-0103

1 NAVAL SURFACE WARFARE CTR
DAHLGREN DIVISION
GS4 TOM WASMUND
17320 DAHLGREN RD
DAHLGREN VA 22448-5100

NO. OF COPIES ORGANIZATION

1 USAR ASC XRA
HUGH GRIFFIS
BLDG 16
2275D ST SUITE 10
WRIGHT PATTERSON AFB OH
45433-7227

1 USARL WL MNS
LANNY G BURDGE
101 WEST EGLIN BLVD
SUITE 302
EGLIN AFB FL 32542-6810

4 ARMY RESEARCH OFFICE
MATH AND CS DIV
DR J CHANDRA
K CLARK
DR WU
DR MING LING
RESEARCH TRIANGLE PARK NC
27709-2211

1 DEFENSE NUCLEAR AGENCY
WE MICHAEL GILTRUDE
6801 TELEGRAPH RD
ALEXANDRIA VA 22310-3398

1 DEFENSE NUCLEAR AGENCY
ATTN OFTA
DR. MICHAEL SHORE
6801 TELEGRAPH RD
ALEXANDRIA VA 22310-3398

1 DIR LLNL
MILTON FINGER L159
PO BOX 808
LIVERMORE CA 94551

1 DIR LLNL
CONV WEAPON TCHNLGS
JOSEPH REPA MS A133
PO BOX 1663
LOS ALAMOS NM 87545

1 USAMICOM
AMSMI RD
PAUL L JACOBS
REDSTONE ARSENAL AL
35898-5420

NO. OF
COPIES ORGANIZATION

1 NWSCDL
JTCG ME PRGRM OFC G202
GEORGE A WILLIAMS
BLDG 221 RM 245
DAHLGREN VA 22448-5100

1 US MILITARY ACADEMY
DEPT OF MATH SCI
MAJ DAVE OLWELL
THAYER HALL
WEST POINT NY 10996-1786

1 APPLIED RES ASSOC INC
FRANK MAESTAS
SUITE A220
4300 SAN MATEO BLVD
ALBUQUERQUE NM 87110

1 APPLIED RES ASSOC INC
RICH SCUNGIO
219 W BEL AVE SUITE 5
ABERDEEN MD 21001

ABERDEEN PROVING GROUND

1 CDR OPTEC EAC
CSTE EAC BLDG 245
L DELATTRE

15 DIR USARL
ATTN: AMSRL-WM-PD, B. BURNS
AMSRL-WM-TD, D. DIETRICH
AMSRL-WM-M, J. WALBERT
AMSRL-IS-CI, B. BODT
AMSRL-SL, P. TANENBAUM
AMSRL-SL-BE,
D. BELY
R. GROTE
D. PETTY
M. SIVACK
J. T. KLOPCIC
M. MAHAFFEY
AMSRL-SL-BG, A. YOUNG
AMSRL-SL-BL,
M. RITONDO
J. HUNT
AMSRL-SL-BN, D. FARENWALD

INTENTIONALLY LEFT BLANK.

# REPORT DOCUMENTATION PAGE

*Form Approved*
*OMB No. 0704-0188*



| 1. AGENCY USE ONLY *(Leave blank)* | 2. REPORT DATE | 3. REPORT TYPE AND DATES COVERED |
|---|---|---|
| | November 1997 | Final, Jul 95 - Jul 97 |

**4. TITLE AND SUBTITLE**

An Experiment, Analysis, and Model of Ballistic Shock

**5. FUNDING NUMBERS**

AH80

**6. AUTHOR(S)**

J. Terrence Klopcic, Walton T. Robinson, Donald W. Petty, and
Michael R. Sivack

**7. PERFORMING ORGANIZATION NAME(S) AND ADDRESS(ES)**

U.S. Army Research Laboratory
ATTN: AMSRL-SL-BS
Aberdeen Proving Ground, MD 21005-5068

**8. PERFORMING ORGANIZATION REPORT NUMBER**

ARL-MR-368

**9. SPONSORING/MONITORING AGENCY NAMES(S) AND ADDRESS(ES)**

**10.SPONSORING/MONITORING AGENCY REPORT NUMBER**

**11. SUPPLEMENTARY NOTES**

**12a. DISTRIBUTION/AVAILABILITY STATEMENT**

Approved for public release; distribution is unlimited.

**12b. DISTRIBUTION CODE**

**13. ABSTRACT** *(Maximum 200 words)*

This study deals with the propagation of the leading, high-frequency edge of the shock wave emanating from an impact point on an armored vehicle, specifically, in an experiment on an M113 armored personnel carrier subjected to explosive charges.

The amplitude of the transverse wave can be well fit by a semiempirical equation, which accounts for both longitudinal and transverse waves, exponential decrease with distance, mixing of waves at edges, and amplification at points near edges. Comparison of wave speeds with published data confirms the roles of longitudinal and transverse disturbances.

**14. SUBJECT TERMS**

shock, ballistic shock, M113

**15. NUMBER OF PAGES**

146

**16. PRICE CODE**

| 17. SECURITY CLASSIFICATION OF REPORT | 18. SECURITY CLASSIFICATION OF THIS PAGE | 19. SECURITY CLASSIFICATION OF ABSTRACT | 20. LIMITATION OF ABSTRACT |
|---|---|---|---|
| UNCLASSIFIED | UNCLASSIFIED | UNCLASSIFIED | UL |

INTENTIONALLY LEFT BLANK.

## USER EVALUATION SHEET/CHANGE OF ADDRESS

This Laboratory undertakes a continuing effort to improve the quality of the reports it publishes. Your comments/answers to the items/questions below will aid us in our efforts.

1. ARL Report Number/Author ARL-MR-368 (Klopcic) Date of Report November 1997

2. Date Report Received _____

3. Does this report satisfy a need? (Comment on purpose, related project, or other area of interest for which the report will be used.) _____

4. Specifically, how is the report being used? (Information source, design data, procedure, source of ideas, etc.) _____

5. Has the information in this report led to any quantitative savings as far as man-hours or dollars saved, operating costs avoided, or efficiencies achieved, etc? If so, please elaborate. _____

6. General Comments. What do you think should be changed to improve future reports? (Indicate changes to organization, technical content, format, etc.) _____

CURRENT ADDRESS

_____
Organization

_____
Name E-mail Name

_____
Street or P.O. Box No.

_____
City, State, Zip Code

7. If indicating a Change of Address or Address Correction, please provide the Current or Correct address above and the Old or Incorrect address below.

OLD ADDRESS

_____
Organization

_____
Name

_____
Street or P.O. Box No.

_____
City, State, Zip Code

(Remove this sheet, fold as indicated, tape closed, and mail.)

**(DO NOT STAPLE)**

DEPARTMENT OF THE ARMY

OFFICIAL BUSINESS

NO POSTAGE
NECESSARY
IF MAILED
IN THE
UNITED STATES

**BUSINESS REPLY MAIL**
FIRST CLASS PERMIT NO 0001,APG,MD

POSTAGE WILL BE PAID BY ADDRESSEE

DIRECTOR
US ARMY RESEARCH LABORATORY
ATTN AMSRL SL BS
ABERDEEN PROVING GROUND MD 21005-5068